

# NUMERICAL MODELLING OF TRANSPORT IN COMPLEX POROUS MEDIA: METAL FOAMS TO THE HUMAN LUNG

(Spine title: Numerical Modelling of Transport in Complex Porous Media)

(Thesis format: Integrated Article)

by

Christopher T. DeGroot

Graduate Program in Engineering Science

Department of Mechanical and Materials Engineering

A thesis submitted in partial fulfillment

of the requirements for the degree of

Doctor of Philosophy

The School of Graduate and Postdoctoral Studies

The University of Western Ontario

London, Ontario, Canada

© Christopher T. DeGroot 2012

THE UNIVERSITY OF WESTERN ONTARIO  
School of Graduate and Postdoctoral Studies

**CERTIFICATE OF EXAMINATION**

Supervisor

\_\_\_\_\_  
A.G. Straatman

Examiners

\_\_\_\_\_  
J.M. Floryan

\_\_\_\_\_  
J. Yang

\_\_\_\_\_  
A.K. Ray

\_\_\_\_\_  
M. Paraschivoiu

The thesis by

**Christopher Thomas DeGroot**

entitled:

**Numerical Modelling of Transport in Complex Porous Media: Metal  
Foams to the Human Lung**

is accepted in partial fulfillment of the  
requirements for the degree of  
Doctor of Philosophy

\_\_\_\_\_  
Date

\_\_\_\_\_  
Chair of the Thesis Examination Board

# Abstract

Transport in porous media has many practical applications in science and engineering. This work focuses on the development of numerical methods for analyzing porous media flows and uses two major applications, metal foams and the human lung, to demonstrate the capabilities of the methods. Both of these systems involve complex pore geometries and typically involve porous domains of complex shape. Such geometric complexities make the characterization of the relevant effective properties of the porous medium as well as the solution of the governing equations in conjugate fluid-porous domains challenging. In porous domains, there are typically too many individual pores to consider transport processes directly; instead the governing equations are volume-averaged to obtain a new sets of governing equations describing the conservation laws in a bulk sense. There are, however, unknown pore-level terms remaining in the volume-averaged equations that must be characterized using effective properties that account for the effects of processes at the pore level. Once closed, the volume-averaged equations can be solved numerically, however, currently available numerical methods for conjugate domains do not perform well at fluid-porous interfaces when using unstructured grids.

In light of the preceding discussion, the goals of this work are: (i) to develop a finite-volume-based numerical method for solving fluid flow and non-equilibrium heat transfer problems in conjugate fluid-porous domains that is compatible with general unstructured grids, (ii) to characterize the relevant flow and thermal properties of an idealized graphite foam, (iii) to determine the permeability of an alveolated duct, which is considered as a representative element of the respiratory region of the human lung, and (iv) to conduct sim-

---

ulations of airflow in the human lung using a novel fluid-porous description of the domain. Results show that the numerical method that has been developed for conjugate fluid-porous systems is able to maintain accuracy on all grid types, flow directions, and flow speeds considered. This work also introduces a comprehensive set of correlations for the effective properties of graphite foam, which will be useful for studying the performance of devices incorporating this material. In order to model air flow in the lung as a porous medium, the permeability of an alveolated duct is obtained using direct pore-level simulations. Finally, simulations of air flow in the lung are presented which use a novel fluid-porous approach wherein the upper airways are considered as a pure fluid region and the smaller airways and alveoli are considered as a porous domain.

**KEYWORDS:** porous media, volume-averaging, finite volume methods, unstructured grids, heat transfer, thermal dispersion, permeability, metal foams, alveolated duct, human lung

# Co-Authorship Statement

Some content included in this thesis comes from published works that have been co-authored by myself, Christopher DeGroot, and my supervisor, Dr. Anthony Straatman. In all cases, I am the primary author of such publications. All data collection, analysis, and writing of manuscripts was done by myself under the supervision and guidance of Dr. Straatman.

# Acknowledgements

This thesis project, the result of more than three years of hard work, was certainly a challenge, but was also a pleasure to work on. Overall it was an extremely rewarding experience and I am a far better researcher for having been through this journey.

I would like to first gratefully acknowledge the support and guidance of my thesis advisor, Prof. Anthony Straatman, with whom I have worked for more than six years. I also thank all of my current and past colleagues for being such a great group of people to work with. Further, I would like to specifically thank Dr. Lee Betchen for the many insightful conversations that we have shared about all things CFD and otherwise during the years in which we worked together.

Of course, I also thank my family for supporting my puzzling decision to spend eight years in university and understanding that graduate school is indeed a ‘real job’ and requires a lot of hard work and dedication. Michelle, in particular, deserves a lot of credit for any accomplishments that I have achieved.

Finally, I acknowledge the financial support of NSERC, who have funded almost my entire graduate education, and the computing facilities and technical support provided by SHARCNET and Comput/Calcul Canada.

Christopher T. DeGroot

# Contents

Certificate of Examination . . . . .	ii
Abstract . . . . .	iii
Co-Authorship Statement . . . . .	v
Acknowledgements . . . . .	vi
Contents . . . . .	vii
List of Tables . . . . .	viii
List of Figures . . . . .	ix
Nomenclature . . . . .	x
<b>1 Introduction and Literature Review</b>	<b>1</b>
1.1 Background . . . . .	1
1.2 The Method of Volume-Averaging . . . . .	4
1.3 Numerical Modelling of Transport in Conjugate Fluid-Porous Domains . . . . .	12
1.4 Transport in High-Conductivity Metal Foams . . . . .	15
1.5 Transport in the Human Lungs . . . . .	18
1.6 Objectives of the Present Work . . . . .	24
1.7 Thesis Outline . . . . .	27
<b>2 A Numerical Model for Flow in Conjugate Fluid-Porous Domains</b>	<b>41</b>
2.1 Introduction . . . . .	41
2.2 Governing Equations . . . . .	44
2.3 Interface Conditions . . . . .	46

---

2.4	Discretization and Implementation . . . . .	48
2.5	Results and Discussion . . . . .	61
2.6	Conclusions . . . . .	72
<b>3</b>	<b>Numerical Results for the Effective Properties of Graphite Foam</b>	<b>77</b>
3.1	Introduction . . . . .	77
3.2	Governing Equations and Closure . . . . .	80
3.3	Non-dimensionalization and Parameters of Study . . . . .	90
3.4	Simulation Details and Grid Resolution . . . . .	93
3.5	Results for Momentum Closure . . . . .	95
3.6	Results for Energy Closure . . . . .	99
3.7	Comparison of Dispersion Models . . . . .	105
3.8	Summary . . . . .	108
<b>4</b>	<b>Fluid Flow in an Alveolated Duct: A Porous Media Approach</b>	<b>115</b>
4.1	Introduction . . . . .	115
4.2	Governing Equations and Closure . . . . .	118
4.3	Results and Discussion . . . . .	126
4.4	Conclusions . . . . .	135
<b>5</b>	<b>Conjugate Fluid-Porous Flows with Moving Boundaries: Application to the Human Lung</b>	<b>141</b>
5.1	Introduction . . . . .	141
5.2	Governing Equations and Numerical Methods . . . . .	143
5.3	Problem Setup . . . . .	149
5.4	Results and Discussion . . . . .	156
5.5	Summary and Future Directions . . . . .	161

---

<b>6</b>	<b>Summary</b>	<b>169</b>
6.1	Summary of the Present Work . . . . .	169
6.2	Summary of Contributions . . . . .	171
6.3	Suggestions for Future Work . . . . .	174
<b>A</b>	<b>Additional Code Validation and Test Problems</b>	<b>179</b>
A.1	One-dimensional porous plug flow . . . . .	179
A.2	One-dimensional non-equilibrium heat transfer . . . . .	181
A.3	Comparison of porous plug results with those from ANSYS Fluent . . . . .	184
	<b>Vita</b>	<b>187</b>

# List of Tables

2.1	Grid independence study for the porous plug case discretized using hexahedral grids, including the percent difference and grid convergence index (GCI) as defined by Celik et al. [32]. Note that the number of control volumes is given for the porous plug section only and that the pressure difference is given across the full length of the domain. . . . .	64
2.2	Grid independence study for the porous plug case discretized using triangular prismatic grids, including the percent difference and grid convergence index (GCI) as defined by Celik et al. [32]. Note that the number of control volumes is given for the porous plug section only and that the pressure difference is given across the full length of the domain (which is truncated in comparison to the hexahedral grid case). Also note that for all grids, the growth rate was 10% per row with a maximum characteristic grid size of $4\delta_w$ . . . . .	64
3.1	Summary of the dimensionless permeabilities obtained numerically for $\epsilon \in \{0.80, 0.85, 0.90\}$ . . . . .	95
3.2	Summary of the polynomial coefficients for the linear least-squares fits for the non-Darcy drag term, $F_{xx}$ , along with the associated maximum absolute error. . . . .	98

3.3	Summary of the polynomial coefficients for the quadratic least-squares fits for the non-Darcy drag term, $F_{xx}$ , along with the associated maximum absolute error. . . . .	98
3.4	Summary of the average Nusselt number computed using the two dispersion models for $Re_d \in \{50, 100\}$ and the percent difference between them. .	108
4.1	Summary of the maximum and average percent errors between the modelled value of $K/(\epsilon D_H^2)$ and the value obtained using transient simulations in an alveolated duct and Eq. ?? . . . . .	130

# List of Figures

1.1	An illustration of a typical averaging volume, $V$ , for an arbitrary porous medium containing fluid and solid volumes $V_f$ and $V_s$ , respectively. . . . .	4
1.2	An illustration of Taylor dispersion in a tube. The upper drawing shows, from left to right, the velocity profile, the initial concentration, the downstream concentration in the absence of molecular diffusion, and the downstream concentration in the presence of molecular diffusion. The lower drawing plots schematically the distributions of the mean (radially averaged) concentration, $C_m$ , for each of the cases shown in the upper drawing. .	11
1.3	Comparison between the actual graphite foam pore geometry, shown in the electron micrograph images (a) and (b), to the geometric idealization proposed by Yu et al. [82], shown in the rendered images (c) and (d). . . . .	17
1.4	A diagram of the human lung with components of the conducting airways labelled. . . . .	19
1.5	Scanning electron microscope images of (a) the transition from respiratory bronchiole to alveolar duct and (b) alveolar ducts containing many alveoli. These images are obtained from a mouse lung and come from the Lawrence Berkeley National Laboratory Lung Lab Tour, <a href="http://imglib.lbl.gov/ImgLib/COLLECTIONS/LUNG_STRUCTURE/.tour/page1.html">http://imglib.lbl.gov/ImgLib/COLLECTIONS/LUNG_STRUCTURE/.tour/page1.html</a> . . . . .	19
1.6	A sketch of an airway tree. . . . .	21

2.1	An illustration of two adjacent control volumes, $P$ and $nb$ , with the relevant geometric parameters noted. . . . .	51
2.2	An illustration of a control volume, $P$ , with the relevant geometric parameters for evaluating the normal derivative noted. . . . .	55
2.3	An illustration of two control volumes on opposite sides of an fluid-porous interface, $P$ being fluid and $nb$ being porous (indicated by shading), with the relevant partial control volumes indicated with dashed lines. . . . .	58
2.4	A schematic diagram of the porous plug case, where the shaded region indicates the porous subdomain. . . . .	62
2.5	Plots of the (a) hexahedral and (b) triangular prismatic grids, near an interface, used for the porous plug case. . . . .	63
2.6	A plot of the streamwise velocity component for the porous plug problem with $Re_H = 1000$ and $Da = 10^{-2}$ as a function of position along the line $y/H = 0.5$ on the interval $x/H \in [2.5, 12.5]$ using the two grid types in comparison to results from Betchen et al. [18]. . . . .	66
2.7	A plot of the streamwise velocity component for the porous plug problem at $Re_H = 1000$ and $Da = 10^{-2}$ as a function of position along the line $y/H = 0.5$ on the interval $x/H \in [2.5, 12.5]$ for the modified methods of treating the interface pressure and gradients. Note that these cases were run using hexahedral grids. . . . .	68
2.8	A plot of the streamwise velocity component for the porous plug problem at $Re_H = 1000$ as a function of position along the line $y/H = 0.5$ on the interval $x/H \in [2.5, 12.5]$ for $Da \in \{10^{-2}, 10^{-3}, 10^{-4}, 10^{-5}\}$ . . . . .	69
2.9	(a) A schematic diagram of the corrugated heat sink geometry, where the shaded region indicates the porous subdomain and (b) a plot of a selected portion of a 2D section of the computational grid on a plane of constant $z$ which uses both triangular prismatic and hexahedral volumes. . . . .	70

2.10	Contour plots on the plane $z/H = 0.5$ of (a) the dimensionless pressure $\langle p \rangle^f / \rho_f U^2$ along with selected streamlines and (b) the dimensionless fluid temperature $(\langle T_f \rangle^f - T_{in}) / (T_w - T_{in})$ . Note that the porous region is outlined with dashed lines. . . . .	71
3.1	Electron micrograph images of a graphite foam specimen (a,b) in comparison to a CAD model of the idealized pore geometry proposed by Yu et al. [14] (c,d). . . . .	79
3.2	An illustration of a periodic unit-cell for an array of cylinders with the relevant geometric parameters indicated. . . . .	85
3.3	Schematic diagram of the computational domain for direct simulation of the pore-level fields, in this case for a graphite foam with $\varepsilon = 0.85$ . . . . .	92
3.4	A plot of the tetrahedral grids used for the (a) $\varepsilon = 0.8$ and (b) $\varepsilon = 0.9$ cases generated with a grid size at the wall of $\delta_w = 0.0118H$ (where $H$ is the unit-cube size), a growth rate of 8% per row, and a maximum grid size of $\delta_{max} = 3\delta_w$ . . . . .	94
3.5	Plot of the non-Darcy drag term, $F_{xx}$ , as a function of the Reynolds number obtained from the solution of the momentum closure problem in comparison to results obtained directly from the computed pressure field. . . . .	96
3.6	A plot of the dimensionless axial thermal dispersion conductivity as a function of $Re_d^{a_1} Pr^{a_2} (1 - \varepsilon)^{a_3}$ , where the coefficients $(a_1, a_2, a_3)$ are obtained using a least-squares fit of the data. . . . .	100
3.7	A plot of the dimensionless transverse thermal dispersion conductivity as a function of $Pe_d$ . . . . .	101
3.8	Plots of the dimensionless transverse thermal dispersion conductivity as a function of the dimensionless groups $Pe_d^{1.78} (1 - \varepsilon)^{1.37}$ and $Re_d^{1.21} Pr^{0.776} (1 - \varepsilon)^{0.786}$ , obtained by least-squares fits for the regimes (a) $Pe_d < 10$ and (b) $Re_d^{1.21} Pr^{0.776} (1 - \varepsilon)^{0.786} > 30$ , respectively. . . . .	102

3.9	A plot of the dimensionless convecting velocity modification in the flow direction as a function of the Péclet number. . . . .	104
3.10	Plot of the interfacial Nusselt number as a function of the Péclet number. . .	104
3.11	Schematic diagram of the domain under consideration for the volume-averaged simulations. . . . .	106
3.12	Contour plots of the dimensionless fluid temperature, $\theta_f$ , along the center plane defined by $y^* = \frac{1}{2}\frac{L}{d}$ for $Re_d = 50$ using (a) the dispersion model of Calmidi and Mahajan [15] and (b) the present dispersion model. . . . .	109
3.13	Contour plots of the dimensionless fluid temperature, $\theta_f$ , along the center plane defined by $y^* = \frac{1}{2}\frac{L}{d}$ for $Re_d = 100$ using (a) the dispersion model of Calmidi and Mahajan [15] and (b) the present dispersion model. . . . .	109
4.1	A schematic diagram of an idealized geometric model of an alveolated duct.	117
4.2	An illustration of a typical averaging volume, $V$ , for an arbitrary porous medium containing fluid and solid volumes $V_f$ and $V_s$ , respectively. . . . .	118
4.3	A schematic diagram of a periodic unit-cell of the idealized geometric model of an alveolated duct. . . . .	127
4.4	A plot of (a) the dimensionless velocity and (b) the difference between the dimensionless pressure and the dimensionless alveolar pressure, $p^* - p_a^*$ , as functions of the dimensionless coordinate $x^*$ for initial Womersley and Reynolds numbers (at $t^* = 0$ ) of $Wo = Re_{DH} = 0.01$ , $\epsilon_0 = 0.9$ , $\Lambda_\epsilon = 0.1$ , and $\Lambda_{DH} = 0.25$ . . . . .	134
4.5	A plot of the difference between the dimensionless pressure and the dimensionless alveolar pressure, $p^* - p_a^*$ , as a function of the dimensionless time, $t^*$ at $x^* = 5$ for initial Womersley and Reynolds numbers (at $t^* = 0$ ) of $Wo = Re_{DH} = 0.01$ , $\epsilon_0 = 0.9$ , $\Lambda_\epsilon = 0.1$ , and $\Lambda_{DH} = 0.25$ . . . . .	135

---

5.1	An illustration of a control volume, $P$ , with the relevant geometric parameters for evaluating the normal derivative noted. . . . .	148
5.2	An illustration of the combined airway tree (blue) and the lung surfaces (green). . . . .	150
5.3	Plots of the computational meshes for the lung geometry showing (a) the main lung mesh and (b) the trachea extension. . . . .	152
5.4	Plots the blending factor for the lung motion with reference to a 2D section of the lung in its maximally inflated state. . . . .	154
5.5	A plot of the maximum pressure difference within the domain as a function of time, where $t = 0$ represents the beginning of the breath cycle at maximum inflation. . . . .	157
5.6	Contour plots of the pressure in Pascals for the times (a) 0.75, (b) 1.25, (c) 1.75, (d) 2.5, (e) 3.25, (f) 3.75, (g) 4.25, (h) 5.0 seconds from the beginning of the breath cycle. . . . .	158
5.7	Contour plots of velocity vectors in the $xy$ -plane, at times (a,b) 1.25 and (c,d) 3.75 s from the beginning of the breath cycle. . . . .	160
A.1	A plots of the results for the one-dimensional porous plug case obtained using six control volumes in comparison to the analytical solution. . . . .	180
A.2	Plots of the dimensionless temperature difference $\phi/\phi_L$ as a function of the dimensionless position $x/L$ for two values of the parameter $A$ , namely, (a) $A = 5$ and (b) $A = 50$ for different grid densities. . . . .	183
A.3	Plots of the streamwise velocity component for the porous plug problem at $Re_H = 1000$ and (a) $Da = 10^{-2}$ and (b) $Da = 10^{-5}$ computed using the proposed method and ANSYS Fluent. Note that these cases were run using the same hexahedral grids used for the cases presented in Chapter 2. . . . .	186

# Nomenclature

$a$	active coefficient in discretized equation (Chapter 2)
$a$	arbitrarily large value (Chapter 5), $m^{-2}$
$a_{fs}$	specific surface area of porous medium, $m^{-1}$
$\mathbf{a}$	vector used in momentum closure, $m^{-1}$
$A$	area, $m^2$
$A_b$	base area ( $= L \times L$ ), $m^2$
$A_{fe}$	denotes periodic inflow/outflow surfaces
$A_{fs}$	denotes surface of intersection between $V_f$ and $V_s$
$\mathbf{A}$	tensor used in momentum closure
$\mathbf{b}$	vector used in energy closure, $m$
$b$	source term in discretized equation
$c_f$	form drag coefficient for porous medium
$c_{p,f}$	constant pressure specific heat capacity, $J/kg \cdot K$
$c_s$	specific heat capacity for a solid, $J/kg \cdot K$
$\mathbf{c}$	vector used in momentum closure, $m^{-1}$
$\mathbf{C}$	tensor used in momentum closure
$d$	pore diameter (Chapter 3), $m$
$d$	displacement (Chapter 5), $m$
$\hat{d}_{ip}$	factor in advecting velocity equation
$D_H$	hydraulic diameter, $m$
$\mathbf{d}$	vector used in momentum closure, $m$

---

<b>D</b>	tensor used in momentum closure, $m^2$
$\mathbf{D}_{f,ip}$	displacement vector from $\mathbf{x}_P + f_{ip}\mathbf{D}_{P,nb}$ to $\mathbf{x}_{ip}$ , $m$
$\mathbf{D}_{x,y}$	displacement vector from point $x$ to point $y$ , $m$
$Da$	Darcy number based on channel height ( $= K/H^2$ )
$f_{ip}$	parameter for inverse distance interpolations
<b>F</b>	non-Darcy drag tensor
$h_{fs}$	interfacial heat transfer coefficient, $W/m^2 \cdot K$
$H$	channel height (Chapter 2), $m$
$H$	unit-cube size (Chapter 3), $m$
<b>H</b>	tensor used in momentum closure, $m^2$
<b>I</b>	identity matrix
$k$	thermal conductivity, $W/m \cdot K$
$K$	scalar permeability of porous medium, $m^2$
<b>k</b>	thermal conductivity tensor, $W/m \cdot K$
<b>K</b>	permeability tensor of porous medium, $m^2$
$\ell$	length scale of averaging volume, $m$
$L$	length scale of porous domain, $m$
<b>l</b>	vector used in momentum closure, $m$
<b>L</b>	tensor used in momentum closure, $m^2$
$\dot{m}$	mass flux, $kg/s$
<b>m</b>	vector used in momentum closure, $m^{-1}$
<b>M</b>	tensor used in momentum closure
<b>n</b>	unit-normal vector
$\mathbf{n}_{fs}$	unit-normal vector directed from the fluid to solid phase on $A_{fs}$
$Nu_{fs}$	interfacial Nusselt number ( $= a_{fs}h_{fs}d^2/k_f$ )
$\overline{Nu}$	average Nusselt number
$N_{ip}$	number of discrete control surfaces on $\partial\Omega_p$

---

$O()$	denotes an order of magnitude
$p$	pressure, $Pa$
$Pe_d$	Péclet number based on pore diameter ( $= Re_d Pr$ )
$Pr$	Prandtl number ( $= c_{p,f} \mu_f / k_f$ )
$q''$	heat flux, $W/m^2$
$q_{tot}$	overall heat transfer, $W$
$Re_x$	Reynolds number based on length scale $x$ ( $= \rho_f U x / \mu_f$ )
$t$	time, $s$
$T$	temperature, $K$
$\mathbf{u}$	fluid velocity vector ( $= [u, v, w]$ ), $m/s$
$\mathbf{u}_s$	velocity of control surface, $m/s$
$\hat{u}$	advecting velocity, $m/s$
$\tilde{u}$	pseudo-velocity (Chapter 2), $m/s$
$\tilde{u}$	spatial deviation in velocity (Chapters 3–4), $m/s$
$\bar{\mathbf{u}}$	convecting velocity vector, $m/s$
$U$	characteristic velocity, $m/s$
$\mathbf{v}$	vector used in momentum closure (Chapters 3–4)
$\mathbf{v}$	mesh displacement (Chapter 5), $m$
$V$	volume, $m^3$
$Wo$	Womersley number ( $= D_H / 2 \sqrt{\rho_f \omega / \mu_f}$ )
$\mathbf{x}$	position vector ( $= [x, y, z]$ ), $m$
$z_o$	offset value for sigmoid function, $m$
$\langle \rangle$	denotes extrinsic volume-average
$\langle \rangle^k$	denotes intrinsic volume-average with respect to constituent $k \in \{f, s\}$
$\sim$	denotes spatial deviation

**Greek Symbols**

$\Gamma$	diffusion coefficient
$\delta$	characteristic grid spacing
$\delta_{ij}$	Kronecker delta tensor, $\delta_{ij} = 1$ if $i = j$ , $\delta_{ij} = 0$ if $i \neq j$
$\delta V$	swept volume, $m^3$
$\Delta$	denotes a difference
$\varepsilon$	porosity ( $= V_f/V$ )
$\Lambda$	amplitude
$\mu$	dynamic viscosity, $kg/m \cdot s$
$\xi$	scalar used in momentum closure, $Pa$
$\rho$	density, $kg/m^3$
$\sigma_{ij}$	stress tensor, $Pa$
$\phi$	generic scalar quantity
$\psi$	scalar used in energy closure
$\partial\Omega$	denotes a surface bounding a space $\Omega$
$\omega$	angular frequency, $rad/s$
$\Omega$	denotes a three-dimensional space

**Subscripts and Superscripts**

0	reference value or value from previous timestep
<i>a</i>	alveolar
<i>d</i>	dispersion
<i>f</i>	fluid
<i>fe</i>	effective fluid property in porous region
<i>fl</i>	quantity associated with the fluid region
<i>in</i>	inlet
<i>ip</i>	quantity evaluated at or associated with an integration point

<i>nb</i>	quantity evaluated at or associated with a control volume neighbouring <i>P</i>
<i>max</i>	maximum
<i>P</i>	quantity evaluated at or associated with a particular control volume
<i>por</i>	quantity associated with the porous region
<i>s</i>	solid
<i>se</i>	effective solid property in porous region
<i>w</i>	wall
+	approaching from the <i>nb</i> side of an interface
−	approaching from the <i>P</i> side of an interface
*	denotes dimensionless quantity

# Introduction and Literature Review

## 1.1 Background

Transport in porous media, generally defined for the purposes of this work as a solid matrix with fluid-filled voids, has practical applications in a diverse range of fields in science and engineering. The definition of a porous medium is quite broad and includes a wide variety of materials including concrete, limestone, sand, soil, granular crushed rock, fibreglass, metal foams, and even biological tissues. Flow can occur within a porous medium when the void space is interconnected. In many applications it is of interest to predict the flow and other transport processes, such as heat and mass transfer, within a porous medium. For example, in groundwater flows one may seek to determine the flow field in order to predict the migration of contaminants into a water supply. In the field of heat transfer, it may be of interest to obtain the flow and temperature fields within a porous heat sink to predict its heat transfer performance. Such predictions are, however, complicated by the sheer number of pores present in a typical medium. From a computational perspective, it would be prohibitively expensive to simulate the flow and transport processes directly in all pores.

Due to such complexities in the nature of transport processes at the pore level, it is often convenient to model the domain of interest as a porous continuum. This is typically

accomplished using the method of volume-averaging, a procedure by which the governing conservation equations in a general medium are integral-averaged over a representative group of pores within a porous medium to obtain a new set of conservation equations in terms of averaged variables. The difficulty with averaging methods, however, is that some terms in the resulting equations remain in terms of pore-level quantities that are not generally available when solving the volume-averaged equations. Thus, suitable models for the so-called effective properties of the medium must be obtained to characterize the unknown pore-level quantities and close the volume-averaged equations. Difficulties are also encountered when simulating transport processes in a system containing both porous and pure fluid regions because of various difficulties in coupling the volume-averaged model to the standard models for fluid regions. Difficulties range from the theoretical development of appropriate interface conditions to their implementation into a computational algorithm in a manner that is numerically stable.

In this work, both the development of a robust numerical method for computing transport in conjugate fluid-porous domains and the closure of the relevant volume-averaged equations will be considered. Two application areas, metal foams and the human lung, will then be considered to demonstrate the capabilities of the computational methods that have been developed. Metal foams are becoming a popular material for enhanced heat transfer applications and are ideally suited for simulation in a volume-averaged framework. Due to their complex pore shape, however, accurate models for the effective properties of many metal foams are unavailable. Thus, in this work a numerical study will be conducted to determine all of the relevant effective properties for an idealized graphite foam geometry. This work also considers modelling the human lung as a coupled fluid-porous medium, which has many potential applications in the medical field including the study of particle transport, gas exchange, and many other topics. Pore-level simulations will be conducted to determine effective properties for the porous lung model, while volume-averaged simulations will be conducted to predict the air flow in the combined lung and airway tree

geometry.

To summarize, this work encompasses several major topics of relevance in the field of porous media, particularly for porous media with complex pore shapes or systems where the shape of the porous domain is complex. The specific topics that are covered in this work include:

- i. the development of an accurate simulation method for solving the closed forms of the volume-averaged equations for fluid-porous systems,
- ii. the determination of relevant effective properties for closure of the volume-averaged governing equations for graphite foams and the human lung, and
- iii. the simulation of air flow in the human lung, which is to be considered as a complex fluid-porous system.

Thus, the literature review presented in the forthcoming sections will proceed as follows. First, a brief review of the method of volume-averaging will be presented in light of the applications to be considered in this work. The general theory of volume-averaging will be discussed first in order to facilitate subsequent discussions regarding closure of the volume-averaged governing equations. Next, a discussion of the relevant numerical techniques for simulating flow in porous media and, in particular, conjugate fluid-porous systems will be presented. Focus will be placed on fluid-porous interface conditions, which have been a subject of much research over the past several decades. From here, the two main application areas of this work, metal foams and the human lung, are reviewed and discussed. Following the review of the literature will be a discussion of the objectives of the present work and an outline of the thesis.

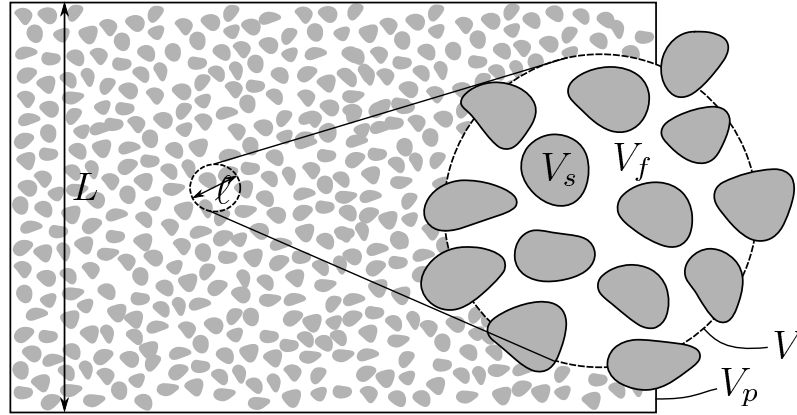


**Figure 1.1:** An illustration of a typical averaging volume,  $V$ , for an arbitrary porous medium containing fluid and solid volumes  $V_f$  and  $V_s$ , respectively.

## 1.2 The Method of Volume-Averaging

### 1.2.1 General Theory

The method of volume-averaging is a procedure by which the governing conservation equations in a general medium are integral-averaged over a representative portion of a porous medium to obtain a new set of governing equations in terms of quantities averaged over many pores. The method of volume-averaging was pioneered by Whitaker [1–3] and Slatery [4, 5] and has been refined by Gray [6]. In the paragraphs to follow, the basics of volume-averaging are briefly described as it is commonly used today. Further details are readily available in the original sources [1–6] as well as more recent reviews [7, 8].

Consider the flow in an arbitrary porous medium composed of both fluid and solid constituents, as depicted in Fig. 1.1. Let  $V_p$  denote the space occupied by the porous medium with length scale  $L$  and let  $V \subset V_p$  define the averaging volume having length scale  $\ell$ . In order to have statistically meaningful averages,  $V$  must be taken large enough that the volume-average at a point is relatively insensitive to the particular choice of  $V$ . Also,  $V$  must be taken small enough that  $\ell \ll L$ , ensuring that the volume-average of a quantity does not vary significantly within  $V$  and can be considered as a constant in integral terms [2, 6–8].

The extrinsic volume-average of a quantity  $\phi_k$ , defined at the centroid of  $V$ , is defined as

$$\langle \phi_k \rangle = \frac{1}{V} \int_{V_k} \phi_k dV, \quad (1.1)$$

where  $k \in \{f, s\}$  denotes the phase in which the quantity  $\phi_k$  is defined with ‘ $f$ ’ and ‘ $s$ ’ indicating the fluid and solid phases, respectively. Alternatively, the intrinsic average is defined as

$$\langle \phi_k \rangle^k = \frac{1}{V_k} \int_{V_k} \phi_k dV, \quad (1.2)$$

which is an average over a single phase only. The intrinsic average may be more convenient for quantities such as pressure because it is the physical quantity that would be measured experimentally. The two types of averages are related through the porosity,  $\varepsilon = V_f/V$ , according to

$$\langle \phi_k \rangle = \begin{cases} \varepsilon \langle \phi_f \rangle^f & \text{if } k = f \\ (1 - \varepsilon) \langle \phi_s \rangle^s & \text{if } k = s \end{cases}. \quad (1.3)$$

Simply applying the integral operator given in Eq. 1.1 to the governing partial differential equations is not sufficient to derive volume-averaged equations that can be solved in practice. The resulting equations would contain averages of derivatives, while derivatives of averages are required for ease of solution. Terms involving spatial derivatives are thus simplified using the ‘spatial averaging theorem’ [1–3, 6–9]. For the gradient operator, this theorem is given as

$$\langle \nabla \phi_k \rangle = \nabla \langle \phi_k \rangle + \frac{1}{V} \int_{A_{kl}} \phi_k \mathbf{n}_{kl} dA, \quad (1.4)$$

where  $k, l \in \{f, s\}$ ,  $k \neq l$ , and the unit normal vector  $\mathbf{n}_{kl}$  is oriented from the  $k$ -phase to the  $l$ -phase.  $A_{kl}$  is the area contained within  $V$  forming the intersection of  $V_k$  and  $V_l$ . In addition to the form given in Eq. 1.4, the spatial averaging theorem may be stated for the divergence of a vector or second-rank tensor,  $\mathbf{a}_k$ , as

$$\langle \nabla \cdot \mathbf{a}_k \rangle = \nabla \cdot \langle \mathbf{a}_k \rangle + \frac{1}{V} \int_{A_{kl}} \mathbf{a}_k \cdot \mathbf{n}_{kl} dA. \quad (1.5)$$

Note that in Eqs. 1.4 and 1.5 the subscripts denote either the fluid or solid phase, thus no summation is implied over repeated indices.

To simplify volume-averages of products of variables, such as those encountered when averaging convection terms, a quantity  $\phi_k$  may be decomposed into its intrinsic volume-average and a pore-level spatial deviation  $\tilde{\phi}_k$ , according to

$$\phi_k = \langle \phi_k \rangle^k + \tilde{\phi}_k, \quad (1.6)$$

leading to the volume-average of a product of variables,  $\phi_{k,1}$  and  $\phi_{k,2}$ , being defined as

$$\langle \phi_{k,1} \phi_{k,2} \rangle = \frac{1}{\varepsilon_k} \langle \phi_{k,1} \rangle \langle \phi_{k,2} \rangle + \langle \tilde{\phi}_{k,1} \tilde{\phi}_{k,2} \rangle, \quad (1.7)$$

where all terms are expressed using extrinsic averages and the  $k$ -phase porosity,  $\varepsilon_k = V_k/V$ , which is introduced so that results are general to both fluid- and solid-phase averages. Note that in arriving at Eq. 1.7 it has been assumed that volume-averaged quantities are constant within a particular averaging volume, which can be shown to be valid provided  $\ell \ll L$ . Additionally, it is assumed that the volume-average of spatial deviations are zero [1, 3, 6, 8].

### 1.2.2 Closure of Volume-Averaged Mass and Momentum Equations

With the theory of volume-averaging discussed in Sec. 1.2.1, one can readily derive the volume-averaged mass and momentum equations required to compute the flow field within a given porous medium. Assuming incompressible flow, the governing equations at the pore level are the standard continuity and Navier-Stokes equations, given as

$$\nabla \cdot \mathbf{u} = 0 \quad (1.8)$$

and

$$\rho_f \left( \frac{\partial \mathbf{u}}{\partial t} + \mathbf{u} \cdot \nabla \mathbf{u} \right) = -\nabla p + \mu_f \nabla^2 \mathbf{u}, \quad (1.9)$$

respectively, where  $\mathbf{u}$  is the velocity vector,  $p$  is the pressure,  $\rho_f$  is the fluid density,  $\mu_f$  is the dynamic viscosity of the fluid, and  $t$  is the time. Volume-averaging Eqs. 1.8 and 1.9, assuming a constant porosity for the purposes of this discussion, results in

$$\nabla \cdot \langle \mathbf{u} \rangle = 0 \quad (1.10)$$

and

$$\begin{aligned} \rho_f \left( \frac{\partial \langle \mathbf{u} \rangle}{\partial t} + \frac{\langle \mathbf{u} \rangle}{\varepsilon} \cdot \nabla \langle \mathbf{u} \rangle \right) &= -\varepsilon \nabla \langle p \rangle^f + \mu_f \nabla^2 \langle \mathbf{u} \rangle \\ &+ \frac{1}{V} \int_{A_{fs}} (-\tilde{p} \mathbf{n}_{fs} + \mu_f \nabla \tilde{\mathbf{u}} \cdot \mathbf{n}_{fs}) dA - \rho_f \nabla \cdot \langle \tilde{\mathbf{u}} \tilde{\mathbf{u}} \rangle \end{aligned} \quad (1.11)$$

in the notation given in Sec. 1.2.1. As a result of the last two terms in Eq. 1.11, which depend on the pore-level spatial deviations  $\tilde{\mathbf{u}}$  and  $\tilde{p}$ , this equation cannot be solved without supplementary information about the pore-level velocity and pressure fields. The typical method for seeking closure of Eq. 1.11 is the semi-empirical approach of Vafai and Tien [10], which seeks to replace the unknown pore-level terms with familiar terms from the extended Darcy equation. Using this approach, Eq. 1.11 becomes

$$\rho_f \left( \frac{\partial \langle \mathbf{u} \rangle}{\partial t} + \frac{\langle \mathbf{u} \rangle}{\varepsilon} \cdot \nabla \langle \mathbf{u} \rangle \right) = -\varepsilon \nabla \langle p \rangle^f + \mu_f \nabla^2 \langle \mathbf{u} \rangle - \frac{\varepsilon \mu_f}{K} \langle \mathbf{u} \rangle - \frac{\varepsilon \rho_f c_f}{\sqrt{K}} |\langle \mathbf{u} \rangle| \langle \mathbf{u} \rangle, \quad (1.12)$$

where the final two terms on the right side of Eq. 1.12 are the resistance terms in the extended Darcy equation. The parameters  $K$  and  $c_f$  are known as the permeability and the Forchheimer (or form drag) coefficient, respectively. This approach to closure is widely used most likely because of its physical relevance, i.e. for steady flow in a fixed porous material without macroscopic velocity gradients, Eq. 1.12 reduces exactly to the extended

Darcy equation,

$$-\nabla\langle p \rangle^f = \frac{\mu_f}{K}\langle \mathbf{u} \rangle + \frac{\rho_f c_f}{\sqrt{K}}|\langle \mathbf{u} \rangle|\langle \mathbf{u} \rangle, \quad (1.13)$$

in the form suggested by Ward [11]. This is a highly desirable feature for a closure method since the extended Darcy equation is widely used and there is a multitude of data available for the parameters  $K$  and  $c_f$  for a wide variety of porous media.

While the closure method proposed by Vafai and Tien [10] provides a convenient way of casting the unknown pore-level terms in a more familiar form, it does not provide a procedure for determining the two parameters that are introduced. One straightforward method of obtaining these parameters is by correlating experimental results where the flow is effectively one-dimensional (i.e. macroscopic boundary layers are of negligible size compared to the size of the sample) and the governing momentum equation reduces to the one-dimensional form of Eq. 1.13 [11–19]. Analogously, one can use numerical simulations to determine the pressure drop across a representative cell of a porous medium as a function of the velocity to correlate  $K$  and  $c_f$  to the calculated pressure drop [20–24].

The difficulty with methods involving correlation of data for pressure drop versus velocity is that it can be difficult to detect certain subtle phenomena such as the cubic dependence of the pressure drop on the velocity for weak inertia flows [22, 25–27]. Thus the closure method of Whitaker [28], which analytically separates the closure problem into flow-independent (Darcy) and flow-dependent (Forchheimer) parts proves useful, since this closure method makes it much simpler to observe non-linear phenomena in the Forchheimer term. It is important that one is aware of the effects of weak inertia on the pressure drop behaviour since it implies that the Forchheimer extension of Darcy’s law is not strictly valid for all flow regimes.

### 1.2.3 Closure of Volume-Averaged Energy Equations

For a porous medium consisting of fluid and solid phases, the governing pore-level energy equations are

$$\rho_f c_{p,f} \left( \frac{\partial T_f}{\partial t} + \mathbf{u} \cdot \nabla T_f \right) = k_f \nabla^2 T_f \quad (1.14)$$

and

$$\rho_s c_s \frac{\partial T_s}{\partial t} = k_s \nabla^2 T_s \quad (1.15)$$

for the fluid and solid phases, respectively, where the subscripts ‘ $f$ ’ and ‘ $s$ ’ again denote quantities associated with either the fluid or solid phase. The specific heat capacities of the fluid and solid are denoted  $c_{p,f}$  and  $c_s$ , respectively, while  $k$  denotes thermal conductivity. Intrinsically volume-averaging these equations according to the procedure described in Sec.

1.2.1 results in

$$\begin{aligned} \rho_f c_{p,f} \left[ \varepsilon \frac{\partial \langle T_f \rangle^f}{\partial t} + \langle \mathbf{u} \rangle \cdot \nabla \langle T_f \rangle^f \right] &= \varepsilon k_f \nabla^2 \langle T_f \rangle^f + \nabla \cdot \left( \frac{1}{V} \int_{A_{fs}} k_f \tilde{T}_f \mathbf{n}_{fs} dA \right) \\ &+ \frac{1}{V} \int_{A_{fs}} k_f \nabla \tilde{T}_f \cdot \mathbf{n}_{fs} dA - \varepsilon \rho_f c_{p,f} \nabla \cdot \langle \tilde{\mathbf{u}} \tilde{T}_f \rangle^f \end{aligned} \quad (1.16)$$

and

$$\begin{aligned} (1 - \varepsilon) \rho_s c_s \frac{\partial \langle T_s \rangle^s}{\partial t} &= (1 - \varepsilon) k_s \nabla^2 \langle T_s \rangle^s + \nabla \cdot \left( \frac{1}{V} \int_{A_{fs}} k_s \tilde{T}_s \mathbf{n}_{sf} dA \right) \\ &+ \frac{1}{V} \int_{A_{fs}} k_s \nabla \tilde{T}_s \cdot \mathbf{n}_{sf} dA. \end{aligned} \quad (1.17)$$

Under certain limiting conditions, one may assume local thermal equilibrium between the fluid and solid phases, i.e.  $\langle T_f \rangle^f = \langle T_s \rangle^s = \langle T \rangle$ , and add Eqs. 1.16 and 1.17 together. In this case, the second last term in Eq. 1.16 and the last term in Eq. 1.17, which represent heat exchange between phases, sum to zero. To characterize the remaining pore-level terms, Vafai and Tien [10] proposed a semi-empirical closure method, wherein the additional terms are treated as a macroscopic heat flux, such that their effects can be characterized as

an augmentation to the thermal conductivity of the medium. Thus, the volume-averaged energy equation under local thermal equilibrium conditions takes on the form

$$[\varepsilon\rho_f c_{p,f} + (1 - \varepsilon)\rho_s c_s] \frac{\partial \langle T \rangle}{\partial t} + \rho_f c_{p,f} \langle \mathbf{u} \rangle \cdot \nabla \langle T \rangle = \nabla \cdot (\mathbf{k}_e \cdot \nabla \langle T \rangle), \quad (1.18)$$

where  $\mathbf{k}_e$  is the effective thermal conductivity tensor of the medium, which takes into account all of the pore-level effects. Typically, the effective conductivity is considered to be made up of three parts: the material, tortuosity, and dispersion conductivities. The tortuosity portion of the effective conductivity takes into account the fact that the conduction path in a porous medium is longer than it would be for a non-porous medium. The thermal dispersion conductivity, which arises from volume-averaging the convection term in the energy equation for the fluid phase, describes the apparent enhancement in conduction within the fluid phase, resulting from pore-level mixing. Since dispersion depends on the flow direction, the dispersion conductivity must generally be considered as a tensor, which leads to an effective conductivity,  $\mathbf{k}_e$ , which is also a tensor.

Dispersion was first studied by Taylor [29] and Aris [30] for a chemical species flowing in a tube. These studies showed that the flowing species is dispersed relative to a plane moving at the mean flow speed with an apparent axial diffusivity equal to the molecular diffusivity plus the dispersion diffusivity, which is proportional to the square of the Péclet number. This phenomenon is illustrated schematically in Fig. 1.2. While this is strictly only valid for flow in a tube, similar Péclet number dependencies have been observed and/or assumed in many other cases of significantly different geometry. However, since dispersion depends on local mixing, any results obtained are particular to the flow configuration for which they are derived. To this end, many experimental and analytical studies have been undertaken to explore dispersion in other porous media such as packed beds of particles and fibrous media, which have revealed a range of behaviours with respect to the Péclet number [31–41]. More recently, numerical studies have been used to investigate tortuosity

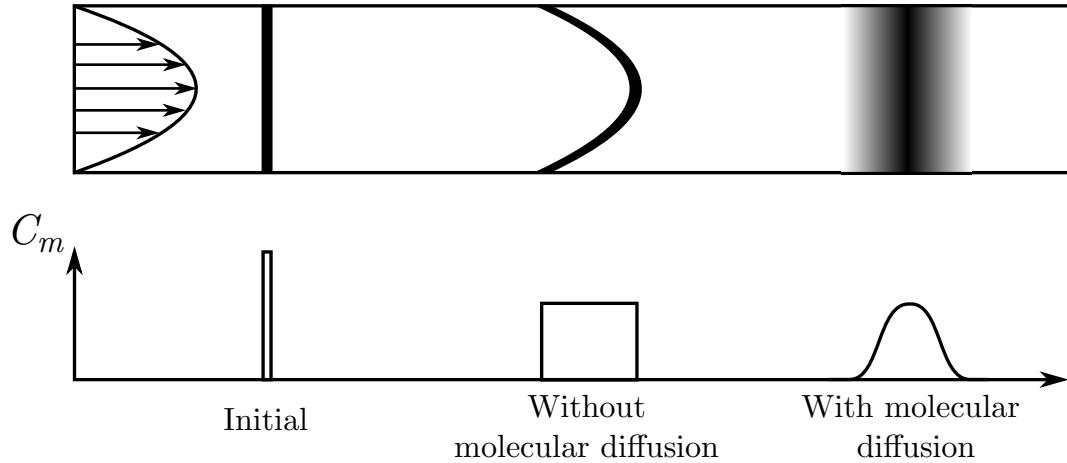


**Figure 1.2:** An illustration of Taylor dispersion in a tube. The upper drawing shows, from left to right, the velocity profile, the initial concentration, the downstream concentration in the absence of molecular diffusion, and the downstream concentration in the presence of molecular diffusion. The lower drawing plots schematically the distributions of the mean (radially averaged) concentration,  $C_m$ , for each of the cases shown in the upper drawing.

and thermal dispersion in porous media. One type of closure method that has been used involves direct calculations of the pore-level flow and thermal fields and integration of the results to obtain the effective conductivity [42–44]. Additionally, there have been closure methods proposed which use numerical calculations of the flow fields as well as additional closure equations used to determine the effective conductivity [45–47].

In all of the literature discussed up to this point, it has been assumed that local thermal equilibrium conditions prevail. However, when the thermal properties of the fluid and solid constituents are substantially different, as in the case of high-conductivity metal foams with air or water as working fluids, it is necessary to consider local thermal non-equilibrium between phases. This can be accomplished empirically using an additional exchange term [48] or more rigorously using constitutive equations to express pore-level quantities in terms of volume-averaged quantities [49]. When constitutive equations are used it can be shown that in addition to the effective thermal conductivity term and an interfacial exchange term, a modification to the convecting velocity is required [49, 50]. The thermal non-

equilibrium energy equations for the fluid and solid constituents are given generally as

$$\rho_f c_{p,f} \left( \varepsilon \frac{\partial \langle T_f \rangle^f}{\partial t} + \bar{\mathbf{u}} \cdot \nabla \langle T_f \rangle^f \right) = \nabla \cdot \left( \mathbf{k}_{fe} \cdot \nabla \langle T_f \rangle^f \right) + a_{fs} h_{fs} \left( \langle T_s \rangle^s - \langle T_f \rangle^f \right) \quad (1.19)$$

and

$$(1 - \varepsilon) \rho_s c_s \frac{\partial \langle T_s \rangle^s}{\partial t} = \nabla \cdot \left( \mathbf{k}_{se} \cdot \nabla \langle T_s \rangle^s \right) - a_{fs} h_{fs} \left( \langle T_s \rangle^s - \langle T_f \rangle^f \right), \quad (1.20)$$

respectively. Note that  $\mathbf{k}_{fe}$  and  $\mathbf{k}_{se}$  are the effective conductivity tensors for the fluid and solid phases, respectively,  $a_{fs}$  is the specific surface area of the porous medium, and  $h_{fs}$  is an interfacial heat transfer coefficient. The convecting velocity  $\bar{\mathbf{u}}$  is typically taken to be the extrinsically averaged velocity,  $\langle \mathbf{u} \rangle$ , however it can be shown that in general it is different from this value [49, 50].

To date, there have been only a small number of studies investigating closure of the volume-averaged energy equations under general thermal non-equilibrium conditions. Quintard et al. [49] were among the first to investigate this problem and formulated an elegant method for determining all of the required effective properties. Their method involved the formulation of constitutive equations for the fluid and solid temperature deviations, which resulted in a set of closure problems, the solutions of which could be integrated to obtain the relevant effective properties. Note that the solution of the closure problems given by Quintard et al. [49] is quite complex. Thus, a simplified model formulated specifically for high-conductivity porous media was recently proposed by DeGroot and Straatman [50]. This model eliminates the need to solve any closure problems in the solid region of the porous medium and thus eliminates coupling of equations at interfaces. Another approach to closure under non-equilibrium conditions, which is an extended version of the closure models employed by Kuwahara et al. [42, 43] for thermal equilibrium conditions, has also been employed [51–55].

### 1.3 Numerical Modelling of Transport in Conjugate Fluid-Porous Domains

From a numerical perspective, solving volume-averaged governing equations is typically no more difficult than solving standard transport equations such as the continuity, Navier-Stokes, and energy equations, since they follow the typical form of a transport equation including transient, convection, diffusion, and source terms. The difficulty comes when one must simulate coupled fluid and porous regions, since the interface must be considered carefully in order to have a numerically stable method that gives physically reasonable results in the neighbourhood of the interface. In this section, literature related to modelling transport in conjugate fluid-porous domains is reviewed, both in terms of theoretical development and numerical implementation.

At fluid-porous interfaces, there is consensus in the literature that the extrinsic velocity on the porous side should be continuous with the velocity on the fluid side [56–74], as shown by Ochoa-Tapia and Whitaker [57]. While the correct interface condition for velocity is straightforward, developing an appropriate condition for the fluid stress, which relates to the velocity gradient, is significantly more challenging because a meaningful averaging volume containing only the porous region cannot be constructed very near an interface. As a result, any averaging volume in the neighbourhood of an interface must necessarily contain both the fluid and porous regions, leading to a potentially important porosity gradient as the averaging volume encompasses more of the fluid region. This effect has been characterized as an effective excess stress at the interface and has been accounted for using a stress-jump interface condition [57, 60, 65, 66]. Although a stress-jump condition is reasonable from a theoretical perspective, it can be inconvenient to use since it requires parameters to be obtained from experiments which may not always be available or straightforward to measure. Additionally, the stress-jump only appears in the component of the stress tangential to the interface, not the normal component. Thus, for flow that is largely

perpendicular to the interface, any jump in tangential stress would be negligible.

Other interface conditions that have been used for the velocity gradient at fluid-porous interfaces include stress continuity [58, 61, 67, 70, 72, 73] and a continuous velocity gradient [64, 68, 69, 74]. While there is little support for the use of a continuous velocity gradient condition, a continuous stress condition may be justified physically and is almost universally accepted as the correct condition for dealing with the normal stress component. Alazmi and Vafai [63] compared the stress-jump, continuous stress, and continuous velocity gradient interface conditions for flow parallel to an interface and found that the continuous stress model gave reasonable results for the velocity profile that were a fair compromise between the cumbersome stress-jump condition and the oversimplified continuous velocity gradient condition. Note that in all of the studies listed above, there is consensus that, like the velocity, the pressure at the interface should be continuous in order to balance the normal stresses at the interface. With these interface conditions established, it becomes possible to conduct numerical simulations in conjugate fluid-porous domains. However, as will be discussed later, the numerical implementation of these interface conditions may be complicated, particularly on non-orthogonal grids and for flows at higher Reynolds numbers.

In addition to interface conditions on velocity, pressure, and the gradient of velocity, it is necessary to devise appropriate conditions for temperature when considering heat transfer. Selection of such conditions first depends on whether one is considering a local thermal equilibrium or non-equilibrium heat transfer model. For equilibrium models the most popular choice for such interface conditions is a continuous temperature and a heat flux balance to determine the gradients on either side of the interface [64, 67, 69–72, 74, 75]. In some cases where the distribution of the solid constituent of the porous medium changes appreciably near the interface, a temperature slip condition may be appropriate along with a heat flux balance [45]. When thermal non-equilibrium energy equations are used, treatment of the interface temperature is more complicated since on the porous side of the inter-

face there are two temperatures to account for, namely  $\langle T_f \rangle^f$  and  $\langle T_s \rangle^s$ , whereas on the fluid side there is only one temperature,  $T_f$ . Typically, the temperature on the fluid side is taken to be continuous with the porosity-weighted temperature on the porous side, i.e.  $T_f = \varepsilon \langle T_f \rangle^f + (1 - \varepsilon) \langle T_s \rangle^s$  on the interface [58, 61, 73]. The temperature gradient on either side of an interface is typically obtained using heat flux balances for each of the fluid and solid phases [61, 73].

Numerically, the greatest difficulty encountered when solving flows in conjugate fluid-porous domains is to maintain coupling between pressure and velocity at the interface. It has been observed that there are significant issues maintaining accuracy in the neighbourhood of interfaces, particularly for internal flows where the average velocity vector is perpendicular to the interface and the Reynolds number is greater than one [61]. Since much of the current literature has focused on flows parallel to interfaces [59, 60, 63, 73, 74], low Reynolds number flows perpendicular to interfaces [59], and external or natural convection flows [58, 62, 64, 66, 76] this problem is not well-studied. Costa et al. [60] proposed a control-volume finite-element model, which is claimed to be accurate near interfaces, however, it is clear from their results that some problems are present at higher Reynolds numbers. As described by Betchen et al. [61], the accuracy problems result primarily from the change in form of the advection term as the medium transitions from fluid to porous, i.e. in the fluid region the advected velocity is a factor of  $\varepsilon$  larger than it is in the porous region, which can lead to a force imbalance at the interface if not properly taken into account. It should also be noted that there have been several numerical models proposed which incorrectly use an advected velocity in the porous region that is a factor of  $\varepsilon$  too large [59, 62, 76], which artificially eliminates this problem, even at higher Reynolds numbers.

The solution proposed by Betchen et al. [61], which introduced a pressure correction at the interface, has been proven effective on structured orthogonal grids, however, some of its robustness appears to be lost when working with non-orthogonal grids [65]. Since

unstructured grids are a requirement for studying porous regions with more complicated geometries, more work needs to be done in order to extend existing methods such that they are robust on general unstructured grids.

## 1.4 Transport in High-Conductivity Metal Foams

Transport in high-conductivity metal foams is of practical importance in many heat transfer applications including compact heat sinks and heat exchangers [12–15, 77–80]. While the effectiveness of high-conductivity porous media as enhanced heat transfer materials has been shown, there are significant challenges involved in simulating the flow and thermal performance of devices incorporating these materials. Since there are generally thousands of pores contained within a given domain of interest, it is impractical to compute the pore-level fields directly. Thus, the method of volume-averaging, discussed in Sec. 1.2.1, is typically employed to derive transport equations governing the averaged flow and thermal fields. Characterization of the pore-level terms remaining in the governing equations (as discussed in Secs. 1.2.2 and 1.2.3) must be carried out in order to determine the required effective properties. Once these terms are properly characterized, it becomes possible to simulate the performance of designs incorporating metal foams using the numerical methods outlined in Sec. 1.3, however, for most porous metals the determination of the correct effective properties remains an open area of research.

Graphite foams are one particular type of porous metal that has been the subject much research over the past decade as a potential material for enhanced heat transfer applications [13–15, 77, 79, 81]. Unique features of graphite foams that make them attractive for heat transfer devices include:

- i. A high solid phase thermal conductivity (800-1900 W/m K), leading to a very high effective solid conductivity (40-160 W/m K) [13].
- ii. A large amount of exposed internal surface area per unit volume available for convec-

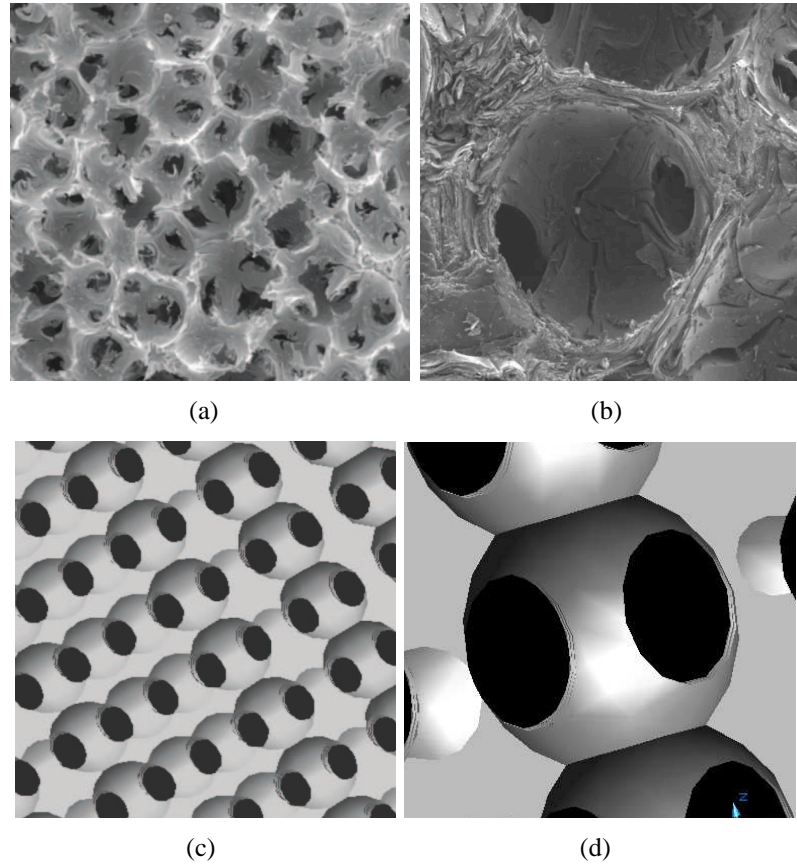


**Figure 1.3:** Comparison between the actual graphite foam pore geometry, shown in the electron micrograph images (a) and (b), to the geometric idealization proposed by Yu et al. [82], shown in the rendered images (c) and (d).

tive heat exchange ( $5000\text{-}50,000\text{ m}^2/\text{m}^3$ ) [13].

While the heat transfer characteristics of graphite foams have been investigated experimentally [13, 14, 79, 81], there have been relatively few attempts to determine the relevant effective properties such that the performance of designs incorporating graphite foams can be accurately simulated numerically using volume-averaged simulations. Although there exist numerical methods to solve these equations, the accuracy of such simulations is limited by the accuracy of the effective properties specified for the foam region. Further complicating matters is the fact that the extremely high solid phase conductivity necessitates the consideration of local thermal non-equilibrium between the fluid and solid phases.

Many of the required geometric parameters of graphite foams can be obtained from

the idealized geometric model of the pore structure proposed by Yu et al. [82], shown in Fig. 1.3 in comparison to images of actual foam. From this geometric model, many important parameters such as the effective thermal conductivity of the solid matrix can be obtained. Using the model of Yu et al. [82] and experimental data, Straatman et al. [13] used volume-averaged simulations to calibrate an interstitial exchange model to match experimental results. Note that in this work, thermal dispersion was modelled simply using the correlation of Calmidi and Mahajan [83] for aluminum foams and was not part of the calibration procedure. Recent work by Karimian and Straatman [23] used direct simulations of flow and heat transfer at the pore level to investigate axial dispersion using a simplified model. Since the development of accurate closure methods is now quite mature and the computational tools exist to readily solve the pore-level flow field and the associated closure problems, the effective properties of new metal foam materials, including graphite foam, can be determined such that volume-averaged simulations may be conducted.

## 1.5 Transport in the Human Lungs

### 1.5.1 Lung Structure and Function

The human lungs perform the essential task of providing oxygen from the atmosphere to the bloodstream while removing excess carbon dioxide from the blood and expelling it into the atmosphere. Breathing is driven by the thoracic diaphragm, a sheet of muscle extending across the bottom of the rib cage, which is able to expand the lung causing air to flow in through the oral and nasal cavities. The internal structure of the lung is generally characterized as a network of bifurcating airways that become smaller in both length and diameter with each bifurcation, or ‘generation’. In all there are approximately 23 generations in the human lung. The first sixteen generations comprise the ‘conducting’ region of the lung, shown in Fig. 1.4, which is primarily responsible for warming and humidifying the air before it enters the ‘respiratory’ region where most of the gas exchange occurs. The

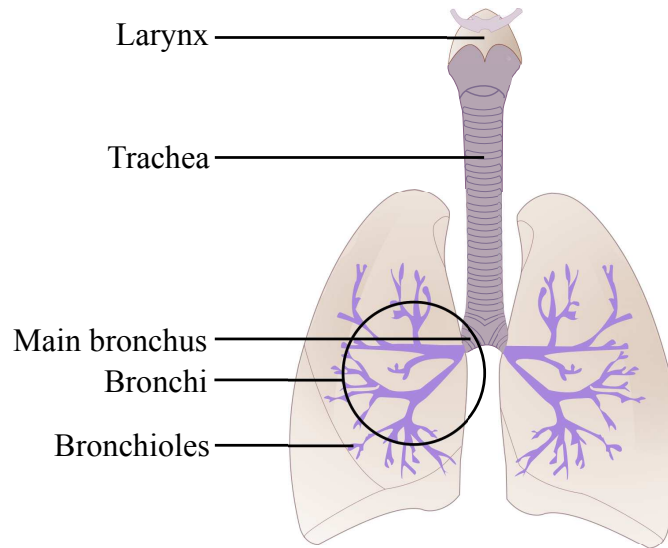


**Figure 1.4:** A diagram of the human lung with components of the conducting airways labelled.

respiratory region of the lung includes all airway generations beyond the conducting region and are known as the respiratory bronchioles, alveolar ducts, and alveolar sacs. This region is also commonly referred to as the lung ‘parenchyma’ since it is the ‘functional’ part of the lung, taking part in gas exchange. As seen in Figs. 1.5a and 1.5b, the respiratory bronchioles and alveolar ducts are tube-like while the alveolar sacs (or ‘alveoli’) are sponge-like in their appearance. Overall there are approximately 300 million alveoli in the human lung with a surface area of approximately  $70 \text{ m}^2$  available for exchange. For further details on lung structure and function, see West [84].

In order to simulate transport in the human lung, a geometric model is required. Traditionally, the pulmonary anatomy has been described using idealized models based upon direct measurements of cadaver lungs. The classical model in this category is the model proposed by Weibel in 1963 [85]. Based on extensive measurements, Weibel was able to determine many quantities of interest, such as the total number of alveoli and the overall surface-to-volume ratio of the lung. In addition, a model for the lengths and diameters of each airway generation was given. Horsfield et al. [86] studied a resin cast of a human lung and proposed a similar model which took into account the asymmetry of the airway tree.

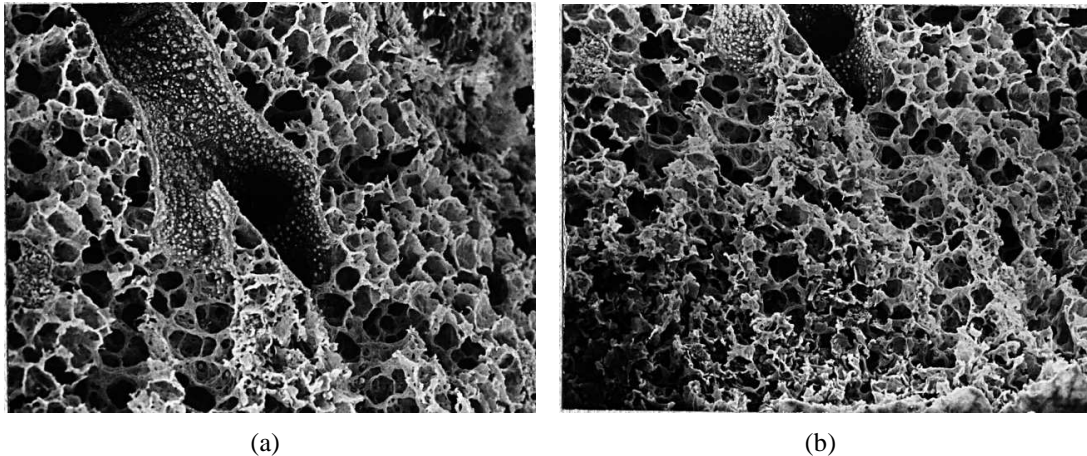


**Figure 1.5:** *Scanning electron microscope images of (a) the transition from respiratory bronchiole to alveolar duct and (b) alveolar ducts containing many alveoli. These images are obtained from a mouse lung and come from the Lawrence Berkeley National Laboratory Lung Lab Tour; [http://imglib.lbl.gov/ImgLib/COLLECTIONS/LUNG\\_STRUCTURE/.tour/page1.html](http://imglib.lbl.gov/ImgLib/COLLECTIONS/LUNG_STRUCTURE/.tour/page1.html).*

While these models are extremely useful, they represent somewhat of an ‘average’ lung, not the lung of a specific individual. To perform simulations for a specific individual, more detailed anatomical data is needed. Fortunately, medical imaging has emerged as a method of extracting information regarding the anatomy of an individual’s lungs, making it possible to perform personalized simulations of lung function. Some specific numerical studies that have employed either idealized or subject-specific geometric models of the airway tree will be discussed in the following section.

### 1.5.2 Simulation of Transport in Conducting Airways

With the continual increase in computational power, it has become a major topic of research to numerically simulate air flow and transport processes in the lung using computational fluid dynamics (CFD) methods [87–104]. Numerical simulations are an attractive method for analyzing transport in the lung since measuring such phenomena experimentally would be exceptionally challenging. Additionally, numerical simulations can typically provide resolution not possible with most experiments. Some specific applications where CFD

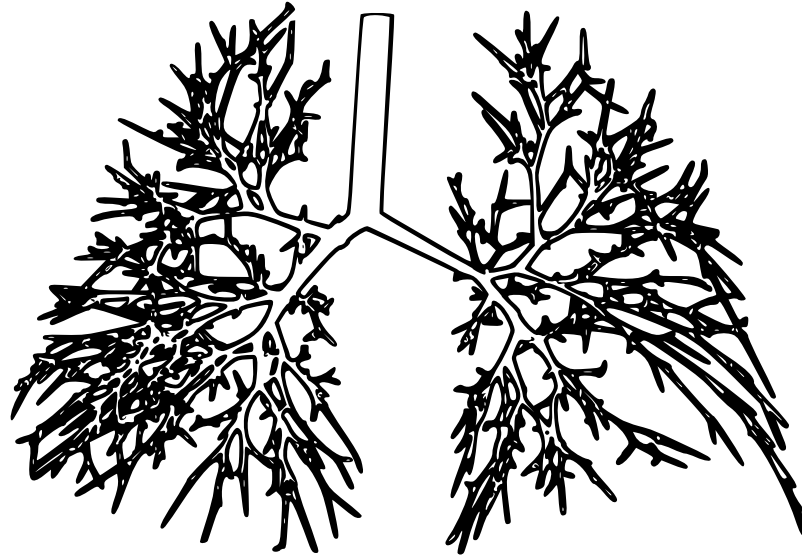


**Figure 1.6:** *A sketch of an airway tree.*

simulations can benefit the study of the human lung include particle or aerosol transport and deposition [87, 89–91, 94, 95, 100, 103], heat and mass transfer [88, 104], and the general study of the flow behaviour within the lung [92, 96–99, 101, 102].

There have been many computational fluid dynamics studies conducted in which the flow is computed in idealized or subject-specific airway geometries for a fixed number of airway bifurcations within the conducting region of the lung. The trouble with this approach is that the computational requirements grow rapidly as more airway generations are added to the model, as can be inferred from Fig. 1.6 which shows a sketch of a fairly extensive airway tree. As a result, most direct simulation studies to date have focussed on the upper six or seven generations, although some work has been done to include more generations with only partial resolution. One of the earliest attempts to simulate flow in the human airway tree was by Comer et al. [89] in 2000, who were able to compute the three-dimensional flow field within an idealized tree containing two bifurcations in order to study aerosol transport and deposition. Shortly thereafter, Zhang et al. [90] and Zhang and Kleinstreuer [87] studied airflow and particle transport in four-generation airway models based on the Weibel geometry model for steady and unsteady inspiration, respectively.

Both studies considered the third to sixth airway generations. Zhang and Kleinstreuer [88] later considered a similar four-generation model with the addition of an idealized mouth, pharynx, and larynx model to simulate heat and mass transfer in the zeroth to third generations.

In an effort to study particle transport in a more realistic geometry than the Weibel model, Calay et al. [99] and van Ertbruggen et al. [91] computed solutions using the geometric model of Horsfield et al. [86] in the upper four and seven airway generations, respectively. Luo and Liu [92] used computed tomography (CT) images to construct a subject-specific airway model to simulate flow in the upper five generations. In an effort to use an even more realistic geometric model, Lin et al. [93] conducted a study of flow in subject-specific airway geometries, based on CT images for upper airways and an idealized model for lower airways. Yin et al. [102] used a subject-specific airway tree along with subject-specific boundary conditions based on regional ventilation patterns measured using CT imaging techniques.

At this point in time, the computational methods for simulating flow in the upper airways are well established, however, present computational capabilities limit the number of airway generations that may be considered. In an effort to reduce computational costs, Nowak et al. [94] and Zhang et al. [95] simulated flow in smaller subsections of the lung using the outlet condition of one subunit as an inlet condition to the next. Nowak et al. [94] simulated twenty-three airway generations using this approach, although beyond sixteen generations it is questionable whether the Weibel geometry model [85] is accurate due to the presence of alveoli in the respiratory region. Zhang et al. [95] simulated flow in sixteen airway generations, or the full conducting region, using this method. The downside of this method is that for each subsection the outlet boundary condition must be specified *a priori*, which is not a straightforward task.

Ma and Lutchen [96] proposed a hybrid model of direct simulation in the upper six airway generations and a simple impedance model to specify time-dependent pressures at

the outlets of a subject-specific airway model. Gemci et al. [97] directly simulated flow in a seventeen generation model, although only 1453 branches were included, rather than the  $2^{17} = 131,072$  required for a fully-resolved model. Thus, many of the branches were truncated, and the computational grids used were insufficient for grid-independent results. Also, the authors used a constant pressure boundary condition at all outlets, which is not appropriate in general. Recently, Walters and Luke [98] followed an approach similar to Gemci et al. [97] in which many generations could be simulated by truncating one of the branches at each bifurcation, resulting in a significantly smaller computational domain. To prescribe boundary conditions at the truncated branches, they proposed a stochastic coupling of pressures at truncated outlets with corresponding locations in resolved flow paths.

In summary, much work has been done to model transport in the upper airways of the human lung. The major challenge that remains, regardless of whether one employs idealized or subject-specific airway models, is that the total number of airway branches that can be simulated is limited by the available computational resources. As a result there must necessarily be information about the transport processes that occur in the missing branches that is lost. Thus, an important area of research is to develop novel methods to simulate transport in the lung in as much detail as possible, without directly simulating the flow in every individual branch of the airway tree, such that all important influences on the transport are properly accounted for.

### 1.5.3 Simulation of Transport in Respiratory Airways

In addition to simulating flow and transport in the conducting airways, much attention has been paid to transport in the respiratory region of the lung, particularly in alveolated ducts (shown previously in Fig. 1.5) [105–116]. Earlier works have considered fairly simple geometric models such as a circular duct with a toroidal alveolus [105, 106], a circular duct with a series of orifice plates [107, 116], or a circular duct with chambers shaped as

partial annular rings [116]. More recently, fully three-dimensional model geometries such as a circular duct with spherical alveoli [108, 110] and space-filling alveolar structures [110, 111, 115] have been explored. Some studies have even looked at several consecutive branches of alveolated ducts using space-filling [110] or spherical alveoli [114].

The above-mentioned studies of transport in alveolated ducts were typically focused on the analysis of particle transport and the physics of the flow fields. As a result of the sponge-like nature of the respiratory region of the lung, it has been suggested that flow in the lung parenchyma can be modelled as a porous medium [117, 118]. Owen and Lewis [117] considered coupled fluid flow and solid displacement in alveolar tissue during high-frequency ventilation, which is a form of mechanical ventilation occurring at high frequency and low tidal volume. To transform the equations governing the fluid flow and solid displacement at the alveolar level, homogenization was used to expand the solution as an asymptotic power series in terms of the small parameter  $\delta = \ell/L$ , which is the ratio of the microscopic length scale to the macroscopic length scale. The resulting equations were, however, expressed in terms of coefficients which depend on the unit-cell geometry. Proper determination of these closure coefficients was not considered in this work; only rough estimates were made in order to obtain selected one-dimensional results.

Despite the lack of accurate effective properties, the work of Owen and Lewis [117] was an important step because it was the first attempt to model coupled flow of air and viscoelastic solid displacements in lung tissue as a porous medium. They did not, however, attempt to couple their macroscopic model for the respiratory region with models for the flow in the larger conducting airways to form a model for the whole lung. Additionally, their geometric model of the alveoli was very much simplified, and further work should be undertaken to consider more realistic geometries, such as those used for simulations of alveolated duct flow. Finally, since the perturbation approach is only valid for small departures from the reference solution, further work should be done to obtain more general results for more typical breathing conditions.

## 1.6 Objectives of the Present Work

The overall goal of this work is to develop methods for analyzing transport in porous media with complex pore and/or porous domain geometries and to apply these methods in relevant applications. To work towards this overall goal, the following specific objectives have been identified:

- i. to develop a suitable numerical method for computing fluid flow and heat transport in conjugate fluid-porous domains, based on the finite-volume method, that incorporates robust and accurate fluid-porous interface conditions that are effective for all flow speeds and grid types,
- ii. to study the closure of volume-averaged momentum and energy equations in order to characterize the effective properties of porous media with complex pore shapes with specific applications to convective heat transfer in graphite foams and air flow in alveolated ducts within the human lung, and
- iii. to further extend the proposed computational model to utilize moving unstructured grids and to apply the model to the study of air flow in the human lung, which is to be considered as a fluid-porous system wherein a subset of the upper airway tree is taken as a pure fluid region and the remainder of the lung volume is modelled as a porous medium.

The primary motivation for this work is the development of useful computational tools for treating transport in systems involving porous media that have clear applications in science and engineering. While two specific applications are chosen to demonstrate the capabilities of the tools developed in this work, these computational techniques are in no way limited to these particular applications. The development of a general framework for solving conjugate fluid-porous transport problems, described in objective (i), is of relevance not only to the applications considered in this work but also in a diverse range of applications

encompassing tissue engineering scaffolds, desiccant drying, etc. Similarly, with regards to objective (ii) listed above, closure of volume-averaged equations is critically important for obtaining accurate results for transport in all porous media. With regards to objective (iii), the extension to moving unstructured grids represents an important capability for transport in many biomedical applications which are inherently dynamic processes.

While the first objective deals with the development of a general computational framework that is to be used in the remainder of the work, the final two objectives involve specific applications that have been chosen to demonstrate the capabilities of the computational model. Closure of volume-averaged equations is first considered for a graphite foam pore geometry and all effective properties required for computing fluid flow and heat transfer are obtained by numerically solving the relevant closure problems over a wide range of parameters. While the pore geometry for graphite foam has a rigid structure, the alveolated duct geometry considered for flow in the human lung changes in time, which adds an additional level of complexity to the closure approach and is considered in this work. Following from the work on closure of the volume-averaged momentum equation for flow in the human lung, objective (iii) relates to the extension of the computational model to moving unstructured grids which is applied to computing air flow in the human lung using a coupled fluid-porous approach, wherein the airway tree is considered as a pure fluid region and the parenchyma is considered as a connected porous region. As air flow in the lung is driven primarily by the motion of the diaphragm the additional capability of mesh motion is a required addition to the computational model in order to allow the motion of the porous region drive the flow in the remainder of the lung and airway tree.

To summarize, the overall goal of this work, to develop useful computational tools for the study of transport in complex porous systems, has lead to the objectives of developing a general computational framework for solving flows in conjugate fluid-porous domains, the study of closure of the volume-averaged governing equations, and the implementation of a moving grid framework. In this work, the computational tools will be applied to convective

heat transfer in graphite foams and air flow in the human lung, however, the computational techniques are developed generally and are applicable to many problems beyond those considered in this work.

## 1.7 Thesis Outline

The remaining chapters of this thesis detail the steps taken to meet the objectives described in §1.6. Chapters will be presented as follows:

- *Chapter 2:* A finite-volume method for computing fluid flow and heat transfer in conjugate fluid-porous domains is presented. The key development presented in this chapter is the set of robust conditions for fluid-porous interfaces that allow the use of unstructured grids, which are required to discretize complex geometries such as the human lung. Although this chapter considers heat transfer problems, the proposed model is equally applicable to mass transfer, which is also of relevance in applications involving the human lung.
- *Chapter 3:* A comprehensive set of results for the effective flow and thermal properties of an idealized graphite foam pore geometry is presented. The results are obtained using advanced constitutive equation-based closure methods and 198 individual numerical simulations. The key outcome of this chapter is a set of correlations for the effective properties of graphite foam that can be used for conducting volume-averaged simulations of devices incorporating this material, which was previously not fully characterized in this manner. Additionally, volume-averaged calculations are presented to demonstrate the impact of the choice of dispersion model on overall heat transfer predictions.
- *Chapter 4:* Numerical results for the permeability of the lung parenchyma are presented using the same closure approach as in Chapter 3 for closure of the momentum

equation. The pore geometry is taken to be an idealized model of a fully alveolated duct, since this structure makes up the majority of the volume of the parenchyma. Although the alveolar walls are moving and breathing is a transient process, it is shown in this chapter using rigorous scaling arguments, which are validated using further numerical simulations, that the closure problem reduces to that of the steady case for physiologically relevant values of the key parameters. The results of this chapter enable volume-averaged calculations of flow in the human lung.

- *Chapter 5:* Simulations of flow in the human lung are conducted using a conjugate fluid-porous model, wherein a truncated airway tree is considered as a fluid region and the remainder of the lung volume is considered as a coupled porous region. The permeability of the lung parenchyma used within the volume-averaged model comes from the results of Chapter 4. The geometries of both the airway tree and the remaining lung volume are based on CT images and are thus physically realistic. The flow is considered to be driven by the motion of the diaphragm, which requires the governing equations to be solved on a moving mesh. The key outcome of this chapter is the novel method of treating the human lung as a conjugate medium and the numerical solution of such a complex system.
- *Chapter 6:* A summary of the present work and its key contributions is given along with suggestions for future work.

# References

- [1] Whitaker, S., 1967, "Diffusion and dispersion in porous media," A.I.Ch.E. J., **13**, pp. 420–427.
- [2] Whitaker, S., 1969, "Advances in theory of fluid motion in porous media," Ind. Engin. Chem., **61**, pp. 14–28.
- [3] Whitaker, S., 1973, "The transport equations for multi-phase systems," Chem. Eng. Sci., **28**, pp. 139–147.
- [4] Slattery, J. C., 1967, "Flow of viscoelastic fluids through porous media," A.I.Ch.E. J., **13**, pp. 1066–1071.
- [5] Slattery, J. C., 1970, "Two-phase flow through porous media," A.I.Ch.E. J., **16**, pp. 345–352.
- [6] Gray, W. G., 1975, "A derivation of the equations for multi-phase transport," Chem. Eng. Sci., **30**, pp. 229–233.
- [7] Kaviany, M., 1995, *Principles of Heat Transfer in Porous Media*, Springer-Verlag, New York, NY, 2nd ed.
- [8] Whitaker, S., 1997, *Volume Averaging of Transport Equations*, chap. 1, Fluid Transport in Porous Media, Springer-Verlag, Southampton, UK, pp. 1–59.
- [9] Howes, F. A. and Whitaker, S., 1985, "The spatial averaging theorem revisited," Chem. Eng. Sci., **40**, pp. 1387–1392.

- 
- [10] Vafai, K. and Tien, C. L., 1981, "Boundary and inertia effects on flow and heat transfer in porous media," *Int. J. Heat Mass Transfer*, **24**, pp. 195–203.
- [11] Ward, J. C., 1964, "Turbulent flow in porous media," *J. Hydraul. Div. A.S.C.E.*, **90**, pp. 1–12.
- [12] Bhattacharya, A., Calmidi, V. V., and Mahajan, R. L., 2002, "Thermophysical properties of high porosity metal foams," *Int. J. Heat Mass Transfer*, **45**, pp. 1017–1031.
- [13] Straatman, A. G., Gallego, N. C., Yu, Q., Betchen, L. J., and Thompson, B. E., 2007, "Forced convection heat transfer and hydraulic losses in graphitic foam," *J. Heat Transfer*, **129**, pp. 1237–1245.
- [14] Straatman, A. G., Gallego, N. C., Yu, Q., and Thompson, B. E., 2007, "Characterization of porous carbon foam as a material for compact recuperators," *J. Eng. Gas Turb. Power*, **129**, pp. 326–330.
- [15] Leong, K. C., Li, H. Y., Jin, L. W., and Chai, J. C., 2010, "Numerical and experimental study of forced convection in graphite foams of different configurations," *Appl. Therm. Eng.*, **30**, pp. 520–532.
- [16] Ergun, S., 1952, "Fluid flow through packed columns," *Chem. Eng. Prog.*, **48**, pp. 85–92.
- [17] Dullien, F. A. L., 1975, "Single phase flow through porous media and pore structure," *Chem. Eng. J.*, **10**, pp. 1–34.
- [18] Macdonald, I. F., El-Sayed, M. S., Mow, K., and Dullien, F. A. L., 1979, "Flow through porous media—the Ergun equation revisited," *Ind. Eng. Chem. Fundam.*, **18**, pp. 199–208.
- [19] Dukhan, N. and Patel, P., 2008, "Equivalent particle diameter and length scale for pressure drop in porous media," *Exp. Therm. Fluid Sci.*, **32**, pp. 1059–1067.

- [20] Nakayama, A., Kuwahara, F., and Hayashi, T., 2004, “Numerical modelling for three-dimensional heat and fluid flow through a bank of cylinders in yaw,” *J. Fluid Mech.*, **498**, pp. 139–159.
- [21] Krishnan, S., Murthy, J. Y., and Garimella, S. V., 2006, “Direct simulation of transport in open-cell metal foam,” *J. Heat Transfer*, **128**, pp. 793–799.
- [22] Karimian, S. A. M. and Straatman, A. G., 2007, “CFD study of the hydraulic and thermal behavior of spherical-void-phase porous materials,” *Int. J. Heat Fluid Flow*, **29**, pp. 292–305.
- [23] Karimian, S. A. M. and Straatman, A. G., 2009, “Numerical modeling of multi-directional flow and heat transfer in graphitic foams,” *J. Heat Transfer*, **131**, pp. 052602–1–11.
- [24] Souto, H. P. A. and Moyne, C., 1997, “Dispersion in two-dimensional periodic porous media. Part I. Hydrodynamics,” *Phys. Fluids*, **9**, pp. 2243–2252.
- [25] Mei, C. C. and Auriault, J. L., 1991, “The effect of weak inertia on flow through a porous medium,” *J. Fluid Mech.*, **222**, pp. 647–663.
- [26] Firdaouss, M., Guermond, J. L., and Quéré, P. L., 1997, “Nonlinear corrections to Darcy’s law at low Reynolds numbers,” *J. Fluid Mech.*, **343**, pp. 331–351.
- [27] Rojas, S. and Koplik, J., 1998, “Nonlinear flow in porous media,” *Phys. Rev. E*, **58**, pp. 4776–4782.
- [28] Whitaker, S., 1996, “The Forchheimer equation: A theoretical development,” *Transport Porous Med.*, **25**, pp. 27–61.
- [29] Taylor, G., 1953, “Dispersion of soluble matter in solvent flowing slowly through a tube,” *Proc. R. Soc. A*, **219**, pp. 186–203.

- [30] Aris, R., 1956, "On the dispersion of a solute in a fluid flowing through a tube," Proc. R. Soc. A, **235**, pp. 67–77.
- [31] Yagi, S., Kunii, D., and Wakao, N., 1960, "Studies on axial effective thermal conductivities in packed beds," A.I.Ch.E. J., **6**, pp. 543–207.
- [32] Hunt, M. L. and Tien, C. L., 1988, "Effects of thermal dispersion on forced convection in fibrous media," Int. J. Heat Mass Transfer, **31**, pp. 301–309.
- [33] Koch, D. L. and Brady, J. F., 1985, "Dispersion in fixed beds," J. Fluid Mech., **154**, pp. 399–427.
- [34] Koch, D. L. and Brady, J. F., 1985, "The effective diffusivity of fibrous media," A.I.Ch.E. J., **32**, pp. 575–591.
- [35] Saffman, P. G., 1959, "A theory of dispersion in a porous medium," J. Fluid Mech., **6**, pp. 321–349.
- [36] Gunn, D. J. and Pryce, C., 1969, "Dispersion in packed beds," Trans. Instn. Chem. Engrs., **47**, pp. 341–350.
- [37] Gunn, D. J., 1969, "Theory of axial and radial dispersion in packed beds," Trans. Instn. Chem. Engrs., **47**, pp. 351–359.
- [38] Hsu, C. T. and Cheng, P., 1990, "Thermal dispersion in a porous medium," Int. J. Heat Mass Transfer, **33**, pp. 1587–1597.
- [39] Gunn, D. J. and Khalid, M., 1975, "Thermal dispersion and wall heat transfer in packed beds," Chem. Eng. Sci., **30**, pp. 261–267.
- [40] Brenner, H., 1980, "Dispersion resulting from flow through spatially periodic porous media," Philos. T. Roy. Soc. A, **297**, pp. 81–133.

- [41] Koch, D. L., Cox, R. G., Brenner, H., and Brady, J. F., 1989, "The effect of order on dispersion in porous media," *J. Fluid Mech.*, **200**, pp. 173–188.
- [42] Kuwahara, F., Nakayama, A., and Koyama, H., 1996, "A numerical study of thermal dispersion in porous media," *J. Heat Transfer*, **118**, pp. 756–761.
- [43] Kuwahara, F. and Nakayama, A., 1999, "Numerical determination of thermal dispersion coefficients using a periodic porous structure," *J. Heat Transfer*, **121**, pp. 160–163.
- [44] Pedras, M. H. J. and de Lemos, M. J. S., 2008, "Thermal dispersion in porous media as a function of the solid-fluid conductivity ratio," *Int. J. Heat Mass Transfer*, **51**, pp. 5359–5367.
- [45] Sahraoui, M. and Kaviany, M., 1994, "Slip and no-slip temperature boundary conditions at the interface of porous, plain media: Convection," *Int. J. Heat Mass Transfer*, **37**, pp. 1029–1044.
- [46] Souto, H. P. A. and Moyne, C., 1997, "Dispersion in two-dimensional periodic porous media. Part II. Dispersion tensor," *Phys. Fluids*, **9**, pp. 2253–2263.
- [47] Saada, M. A., Chikh, S., and Campo, A., 2006, "Analysis of hydrodynamic and thermal dispersion in porous media by means of a local approach," *Heat Mass Transfer*, **42**, pp. 995–1006.
- [48] Amiri, A., Vafai, K., and Kuzay, T. M., 1995, "Effects of boundary conditions of non-darcian heat transfer through porous media and experimental comparisons," *Numer. Heat Tr. A-Appl.*, **27**, pp. 651–664.
- [49] Quintard, M., Kaviany, M., and Whitaker, S., 1997, "Two-medium treatment of heat transfer in porous media: Numerical results for effective properties," *Adv. Water Resour.*, **20**, pp. 77–94.

- [50] DeGroot, C. T. and Straatman, A. G., 2011, "Closure of non-equilibrium volume-averaged energy equations in high-conductivity porous media," *Int. J. Heat Mass Transfer*, **54**, pp. 5039–5048.
- [51] Moghari, M., 2008, "A numerical study of non-equilibrium convective heat transfer in porous media," *J. Enhanc. Heat Transf.*, **15**, pp. 81–99.
- [52] Kuwahara, F., Shirota, M., and Nakayama, A., 2001, "A numerical study of interfacial convective heat transfer coefficient in two-energy equation model for convection in porous media," *Int. J. Heat Mass Transfer*, **44**, pp. 1153–1159.
- [53] Saito, M. B. and de Lemos, M. J. S., 2006, "A correlation for interfacial heat transfer coefficient for turbulent flow over an array of square rods," *J. Heat Transfer*, **128**, pp. 444–452.
- [54] Alshare, A. A., Strykowski, P. J., and Simon, T. W., 2010, "Modeling of unsteady and steady fluid flow, heat transfer and dispersion in porous media using unit cell scale," *Int. J. Heat Mass Transfer*, **53**, pp. 2294–2310.
- [55] Pathak, M. G. and Ghiaasiaan, S. M., 2011, "Convective heat transfer and thermal dispersion during laminar pulsating flow in porous media," *Int. J. Thermal Sci.*, **50**, pp. 440–448.
- [56] Vafai, K. and Kim, S. J., 1995, "On the limitations of the Brinkman-Forchheimer-extended Darcy equation," *Int. J. Heat Fluid Flow*, **16**, pp. 11–15.
- [57] Ochoa-Tapia, J. A. and Whitaker, S., 1995, "Momentum transfer at the boundary between a porous medium and a homogeneous fluid – I. Theoretical development," *Int. J. Heat Mass Transfer*, **38**, pp. 2635–2646.
- [58] Phanikumar, M. S. and Mahajan, R. L., 2002, "Non-Darcy natural convection in high porosity metal foams," *Int. J. Heat Mass Transfer*, **45**, pp. 3781–3793.

- [59] Costa, V. A. F., Oliveira, L. A., Baliga, B. R., and Sousa, A. C. M., 2004, "Simulation of coupled flows in adjacent porous and open domains using a control-volume finite-element method," *Numer. Heat Tranf. A-Appl.*, **45**, pp. 675–697.
- [60] Costa, V. A. F., Oliveira, L. A., and Baliga, B. R., 2008, "Implementation of the stress jump condition in a control-volume finite-element method for the simulation of laminar coupled flows in adjacent open and porous domains," *Numer. Heat Tr. B-Fund.*, **53**, pp. 383–411.
- [61] Betchen, L. J., Straatman, A. G., and Thompson, B. E., 2006, "A nonequilibrium finite-volume model for conjugate fluid/solid/porous domains," *Numer. Heat Tr. A-Appl.*, **49**, pp. 543–565.
- [62] Chikh, S., Boumedien, A., Bouhadef, K., and Lauriat, G., 1998, "Analysis of fluid flow and heat transfer in a channel with intermittent heated porous blocks," *Heat Mass Transfer*, **33**, pp. 405–413.
- [63] Alazmi, B. and Vafai, K., 2001, "Analysis of fluid flow and heat transfer interfacial conditions between a porous medium and a fluid layer," *Int. J. Heat Mass Transfer*, **44**, pp. 1735–1749.
- [64] Fu, W. S. and Chen, S. F., 2002, "A numerical study of heat transfer of a porous block with the random porosity model in a channel flow," *Heat Mass Transfer*, **38**, pp. 695–704.
- [65] Yu, P., Lee, T. S., Zeng, Y., and Low, H. T., 2007, "A numerical method for flows in porous and homogeneous fluid domains coupled at the interface by stress jump," *Int. J. Numer. Meth. Fluids*, **53**, pp. 1755–1775.
- [66] Chen, X. B., Yu, P., Winoto, S. H., and Low, H. T., 2009, "Numerical analysis for the flow past a porous trapezoidal-cylinder based on the stress-jump interfacial-conditions," *Int. J. Numer. Method. H.*, **19**, pp. 223–241.

- 
- [67] Kim, S. J. and Choi, C. Y., 1996, "Convection heat transfer in porous and overlying layers heated from below," *Int. J. Heat Mass Transfer*, **39**, pp. 319–329.
- [68] Vafai, K. and Kim, S. J., 1990, "Fluid mechanics of the interface region between a porous medium and a fluid layer—an exact solution," *Int. J. Heat Fluid Flow*, **11**, pp. 254–256.
- [69] Vafai, K. and Kim, S. J., 1990, "Analysis of surface enhancement by a porous substrate," *J. Heat Transfer*, **112**, pp. 700–706.
- [70] Neale, G. and Nader, W., 1974, "Practical significance of Brinkman's extension of Darcy's law: Coupled parallel flows within a channel and a bounding porous medium," *Can. J. Chem. Eng.*, **52**, pp. 475–478.
- [71] Vafai, K. and Thiyagaraja, R., 1987, "Analysis of flow and heat transfer at the interface region of a porous medium," *Int. J. Heat Mass Transfer*, **30**, pp. 1391–1405.
- [72] Poulikakos, D. and Kazmierczak, M., 1987, "Forced convection in a duct partially filled with a porous material," *J. Heat Transfer*, **109**, pp. 653–662.
- [73] Martins-Costa, M. L. and da Gama, R. M. S., 1994, "A local model for the heat transfer process in two distinct flow regions," *Int. J. Heat Fluid Flow*, **15**, pp. 477–485.
- [74] Jang, J. Y. and Chen, J. L., 1992, "Forced convection in a parallel plate channel partially filled with a high porosity medium," *Int. Comm. Heat Mass Transfer*, **19**, pp. 263–273.
- [75] Ochoa-Tapia, J. A. and Whitaker, S., 1997, "Heat transfer at the boundary between a porous medium and a homogeneous fluid," *Int. J. Heat Mass Transfer*, **40**, pp. 2691–2707.

- [76] Ould-Amer, Y., Chikh, S., Bouhadeb, K., and Lauriat, G., 1998, "Forced convection cooling enhancement by use of porous materials," *Int. J. Heat Fluid Flow*, **19**, pp. 251–258.
- [77] Gallego, N. C. and Klett, J. W., 2003, "Carbon foams for thermal management," *Carbon*, **41**, pp. 1461–1466.
- [78] Boomsma, K., Poulikakos, D., and Zwick, F., 2003, "Metal foams as compact high performance heat exchangers," *Mech. Mater.*, **35**, pp. 1161–1176.
- [79] Straatman, A. G., Gallego, N. C., Thompson, B. E., and Hangan, H., 2006, "Thermal characterization of porous carbon foam – convection in parallel flow," *Int. J. Heat Mass Transfer*, **49**, pp. 1991–1998.
- [80] DeGroot, C., Straatman, A., and Betchen, L., 2009, "Modeling Forced Convection in Finned Metal Foam Heat Sinks," *J. Electron. Packag.*, **131**, pp. 021001–1–021001–10.
- [81] Sultan, K., DeGroot, C. T., Straatman, A. G., Gallego, N. C., and Hangan, H., 2009, "Thermal characterization of porous graphitic foam – convection in impinging flow," *Int. J. Heat Mass Transfer*, **52**, pp. 4296–4301.
- [82] Yu, Q., Thompson, B. E., and Straatman, A. G., 2006, "A unit cube-based model for heat transfer and fluid flow in porous carbon foam," *J. Heat Transfer*, **128**, pp. 352–360.
- [83] Calmidi, V. V. and Mahajan, R. L., 2000, "Forced convection in high porosity metal foams," *J. Heat Transfer*, **122**, pp. 557–565.
- [84] West, J. B., 1995, *Respiratory physiology – the essentials*, Williams & Wilkins, Baltimore, MD, 5th ed.

- 
- [85] Weibel, E. R., 1963, *Morphometry of the human lung*, Springer-Verlag, New York, NY.
- [86] Horsfield, K., Dart, G., Olson, D. E., Filley, G. F., and Cumming, G., 1971, "Models of the human bronchial tree," *J. Appl. Physiol.*, **31**, pp. 207–217.
- [87] Zhang, Z. and Kleinstreuer, C., 2002, "Transient airflow structures and particle transport in a sequentially branching lung airway model," *Phys. Fluids*, **14**, pp. 862–880.
- [88] Zhang, Z. and Kleinstreuer, C., 2003, "Species heat and mass transfer in a human upper airway model," *Int. J. Heat Mass Transfer*, **46**, pp. 4755–4768.
- [89] Comer, J. K., Kleinstreuer, C., Hyun, S., and Kim, C. S., 2000, "Aerosol transport and deposition in sequentially bifurcating airways," *J. Biomech. Eng.*, **122**, pp. 152–158.
- [90] Zhang, Z., Kleinstreuer, C., and Kim, C. S., 2001, "Flow structure and particle transport in a triple bifurcation airway model," *J. Fluids Eng.*, **123**, pp. 320–330.
- [91] van Ertbruggen, C., Hirsch, C., and Paiva, M., 2005, "Anatomically based three-dimensional model of airways to simulate flow and particle transport using computational fluid dynamics," *J. Appl. Physiol.*, **98**, pp. 970–980.
- [92] Luo, H. Y. and Liu, Y., 2008, "Modeling the bifurcating flow in a CT-scanned human lung airway," *J. Biomech.*, **41**, pp. 2681–2688.
- [93] Lin, C., Tawhai, M. H., Lennan, G. M., and Hoffman, E. A., 2009, "Multiscale simulation of gas flow in subject-specific models of the human lung," *IEEE Eng. Med. Biol. Mag.*, **28**, pp. 25–33.
- [94] Nowak, N., Kakade, P. P., and Annappagada, A. V., 2003, "Computational fluid dynamics simulation of airflow and aerosol deposition in human lungs," *Ann. Biomed. Eng.*, **31**, pp. 374–390.

- [95] Zhang, Z., Kleinstreuer, C., and Kim, C. S., 2008, “Airflow and nanoparticle deposition in a 16-generation tracheobronchial airway model,” *Ann. Biomed. Eng.*, **36**, pp. 2095–2110.
- [96] Ma, B. and Lutchen, K. R., 2006, “An anatomically based hybrid computational model of the human lung and its application to low frequency oscillatory mechanics,” *Ann. Biomed. Eng.*, **34**, pp. 1691–1704.
- [97] Gemci, T., Ponyavin, V., Chen, Y., Chen, H., and Collins, R., 2008, “Computational model of airflow in upper 17 generations of human respiratory tract,” *J. Biomech.*, **41**, pp. 2047–2054.
- [98] Walters, D. K. and Luke, W. H., 2010, “A method for three-dimensional Navier-Stokes simulations of large-scale regions of the human lung,” *J. Fluids Eng.*, **132**, pp. 051101–1–8.
- [99] Calay, R. K., Kurujareon, J., and Holdø, A. E., 2002, “Numerical simulation of respiratory flow patterns within human lung,” *Respir. Physiol. Neuro.*, **130**, pp. 201–221.
- [100] Nazridoust, K. and Asgharian, B., 2008, “Unsteady-state airflow and particle deposition in a three-generation human lung geometry,” *Inhal. Toxicol.*, **20**, pp. 595–610.
- [101] Comerford, A., Förster, C., and Wall, W. A., 2010, “Structured tree impedance outflow boundary conditions for 3D lung simulations,” *J. Biomech. Eng.*, **132**, pp. 081002–1–10.
- [102] Yin, Y., Choi, J., Hoffman, E. A., Tawhai, M. H., and Lin, C.-L., 2010, “Simulation of pulmonary air flow with a subject-specific boundary condition,” *J. Biomech.*, **43**, pp. 2159–2163.

- [103] Walters, D. K. and Luke, W. H., 2011, "Computational fluid dynamics simulations of particle deposition in large-scale multigenerational lung models," *J. Biomech. Eng.*, **133**, pp. 011003–1–8.
- [104] Saksono, P. H., Nithiarasu, P., and Sazonov, I., 2012, "Numerical prediction of heat transfer patterns in a subject-specific human upper airway," *J. Heat Transfer*, **134**, pp. 031022–1–9.
- [105] Tsuda, A., Henry, F. S., and Butler, J. P., 1995, "Chaotic mixing of alveolated duct flow in rhythmically expanding pulmonary acinus," *J. Appl. Physiol.*, **79**, pp. 1055–1063.
- [106] Lee, D. Y. and Lee, J. W., 2003, "Characteristics of particle transport in an expanding or contracting alveolated tube," *J. Aerosol Sci.*, **34**, pp. 1193–1215.
- [107] Karl, A., Henry, F. S., and Tsuda, A., 2004, "Low Reynolds number viscous flow in an alveolated duct," *J. Biomech. Eng.*, **126**, pp. 420–429.
- [108] Sznitman, J., Heimsch, F., Heimsch, T., Rusch, D., and Rösgen, T., 2007, "Three-dimensional convective alveolar flow induced by rhythmic breathing motion of the pulmonary acinus," *J. Biomech. Eng.*, **129**, pp. 658–665.
- [109] Tsuda, A., Henry, F. S., and Butler, J. P., 2008, "Gas and aerosol mixing in the acinus," *Respir. Physiol. Neuro.*, **163**, pp. 139–149.
- [110] Sznitman, J., Heimsch, T., Wildhaber, J. H., Tsuda, A., and Rösgen, T., 2009, "Respiratory flow phenomena and gravitational deposition in a three-dimensional space-filling model of the pulmonary acinar tree," *J. Biomech. Eng.*, **131**, pp. 031010–1–031010–16.
- [111] Kumar, H., Tawhai, M. H., Hoffman, E. A., and Lin, C.-L., 2009, "The effects of

- geometry on airflow in the acinar region of the human lung,” *J. Biomech.*, **42**, pp. 1635–1642.
- [112] Harding, E. M. and Robinson, R. J., 2010, “Flow in a terminal alveolar sac model with expanding walls using computational fluid dynamics,” *Inhal. Toxicol.*, **22**, pp. 669–678.
- [113] Li, Z. and Kleinstreuer, C., 2011, “Airflow analysis in the alveolar region using the lattice-Boltzmann method,” *Med. Biol. Eng. Comput.*, **49**, pp. 441–451.
- [114] Ma, B. and Darquenne, C., 2011, “Aerosol deposition characteristics in distal acinar airways under cyclic breathing conditions,” *J. Appl. Physiol.*, **110**, pp. 1271–1282.
- [115] Kumar, H., Tawhai, M. H., Hoffman, E. A., and Lin, C.-L., 2011, “Steady streaming: A key mixing mechanism in low-Reynolds-number acinar flows,” *Phys. Fluids*, **23**, pp. 041092–1–21.
- [116] Darquenne, C. and Paiva, M., 1996, “Two- and three-dimensional simulations of aerosol transport and deposition in alveolar zone of human lung,” *J. Appl. Physiol.*, **80**, pp. 1401–1414.
- [117] Owen, M. R. and Lewis, M. A., 2001, “The mechanics of lung tissue under high-frequency ventilation,” *SIAM J. Appl. Math.*, **61**, pp. 1731–1761.
- [118] Lande, B. and Mitzner, W., 2005, “Analysis of lung parenchyma as a parametric porous medium,” *J. Appl. Physiol.*, **101**, pp. 926–933.

# A Numerical Model for Flow in Conjugate Fluid-Porous Domains<sup>†</sup>

## 2.1 Introduction

Problems involving fluid flow and heat transfer in domains containing both fluid and porous regions have many applications in areas such as filtration, packed bed reactors, and thermal management. In recent years there has been significant interest in the use of high-porosity, high-conductivity metallic foams for heat transfer enhancement [1–8]. In order to effectively simulate the performance of such devices, there is a need to develop robust mathematical and numerical models, which are capable of accurately computing the flow and thermal fields in fluid and porous regions as well as maintaining coupling at interfaces between these regions. While the equations governing heat and fluid flow in porous media are readily derived using the method of volume-averaging [9] in conjunction with suitable closure models such as the empirically-based models of Vafai and Tien [10], it often remains challenging to obtain physically reasonable solutions in the vicinity of fluid-porous interfaces.

---

<sup>†</sup>A version of this chapter entitled “A finite-volume model for fluid flow and nonequilibrium heat transfer in conjugate fluid-porous domains using general unstructured grids” has been published in *Numerical Heat Transfer, Part B*, vol. 60, pp. 252–277, 2011.

Several different numerical models have been proposed for the simulation of flow and heat transfer in conjugate domains using staggered, orthogonal finite-volume grids, either under the assumption of local thermal equilibrium [11–13] or non-equilibrium [14]. While equilibrium models are appropriate where the fluid and solid conductivities are similar, it is necessary to consider local thermal non-equilibrium and solve separate, coupled energy equations for each constituent when the conductivities are substantially different as in many heat transfer applications [14, 15]. As a result, Phanikumar and Mahajan [14] extended the applicability of earlier conjugate models by considering local thermal non-equilibrium between the fluid and solid constituents. While all of these algorithms were successful for their specific applications, which were two-dimensional and easily discretized using orthogonal grids, it is quite challenging to implement a staggered grid formulation for more general three-dimensional problems where non-orthogonal grids are required.

More recently there have been models proposed which utilize collocated grids, where the grids used for pressure and velocity calculations are identical. For example, Costa et al. [16, 17] proposed a control-volume finite-element model for conjugate domains that was developed generally for arbitrary unstructured grids, however, the model was only tested for relatively simple geometries that were discretized using orthogonal grids. Thus, it is unclear how the model would perform for non-orthogonal grids. Betchen et al. [18] proposed a collocated finite-volume model and introduced an improved estimate of the interface pressure, which allowed results to be obtained at high Reynolds numbers for interfaces perpendicular to the flow direction. As described in this work, it is much more challenging to obtain physically reasonable solutions in the neighbourhood of a porous-fluid interface when the flow is perpendicular to that interface as a result of the change in the form of the advected momentum flux across the interface. At high flow rates, this results in a significant change in pressure in the immediate vicinity of the interface in order to satisfy a momentum balance on the fluid side of the interface [18]. This effect is most pronounced for internal flows where the fluid is forced to pass through the porous medium,

as opposed to external flows where much of the fluid flows around the porous region.

The idea of a pressure correction at interfaces has not been well-studied in the literature, due in part to the fact that many previous studies have focussed on low Reynolds number flows where the change in pressure as a result of the change in the advected velocity is indeed negligible. Additionally, there have been several models proposed [11, 12, 16] which use an advected velocity in the porous region that is a factor of  $\varepsilon$  too large, which artificially eliminates this problem even at higher Reynolds numbers. It is clear that high Reynolds number flows in porous media are of great practical importance in heat transfer applications, so it is important that accurate results be obtained in the presence of fluid-porous interfaces. The pressure condition proposed by Betchen et al. [18], which takes into account the rapid change in pressure resulting from the change in the advected velocity at the interface, is capable of obtaining results for high Reynolds numbers without spurious oscillations in the pressure or velocity fields. Costa et al. [17] have also reported some simulations with perpendicular interfaces at moderate Reynolds numbers, however, there still appear to be issues with spurious oscillations in pressure at the interface (as seen in Fig. 9(c) of Ref. [17]), which is likely due to a force imbalance as a result of the change in the advected velocity across the interface without an appropriate change in pressure.

The main disadvantage of the model of Betchen et al. [18] is that it has been developed specifically for geometries which can be discretized using orthogonal grids. Yu et al. [19] implemented the interface pressure condition proposed by Betchen et al. [18] into their model which uses multi-block, body-fitted meshes, however, their model cannot produce smooth solutions for Reynolds numbers as high as those considered by Betchen et al. [18]. This difference could stem from a multitude of factors, including the gradient reconstruction at the interface or the treatment of the advecting and advected velocities at the interface, which are not described in detail in Ref. [19]. In any case, these results highlight the special difficulties encountered with non-orthogonal grids that must be dealt with in order to have a robust model.

In summary, it is clear that the model proposed by Betchen et al. [18] is very robust and is able to produce physically reasonable solutions for all Reynolds and Darcy numbers considered, however, there are some difficulties encountered when extending the model for use on non-orthogonal grids [19]. While the model of Costa et al. [16, 17] was developed for general unstructured grids, it thus far remains largely untested for non-orthogonal grids. Additionally, even with orthogonal grids, the model of Costa et al. [16, 17] seems to produce some small unphysical oscillations in the solution fields near interfaces. Thus, the goal of this work is to develop a robust finite-volume-based algorithm for computing conjugate fluid-porous flows using general unstructured, non-orthogonal grids that is able to obtain smooth solutions for all laminar Reynolds numbers.

In this chapter, we first outline the relevant governing equations in the fluid region and briefly outline the volume-averaging procedure that is used to derive the governing equations for the porous region. This is followed by a discussion of the interface conditions imposed at the intersection of the fluid and porous subdomains. Subsequently, the discretization of the governing equations and interface conditions and their implementation into a finite-volume computational fluid dynamics code is described. Finally, we present two relevant cases which illustrate the performance of the model.

## 2.2 Governing Equations

In this work, we consider fluid flow and heat transfer in a conjugate domain,  $\Omega$ , which consists of pure fluid and porous regions,  $\Omega_{fl}$  and  $\Omega_{por}$ , respectively. In  $\Omega_{fl}$ , the flow is governed by the continuity and Navier-Stokes equations, given by

$$\nabla \cdot \mathbf{u} = 0 \tag{2.1}$$

and

$$\rho_f \left[ \frac{\partial \mathbf{u}}{\partial t} + \nabla \cdot (\mathbf{u}\mathbf{u}) \right] = -\nabla p + \mu_f \nabla^2 \mathbf{u}, \quad (2.2)$$

respectively. The energy equation in the fluid region is given as

$$\rho_f c_{p,f} \left[ \frac{\partial T}{\partial t} + \nabla \cdot (\mathbf{u}T) \right] = k_f \nabla^2 T, \quad (2.3)$$

where the effects of viscous dissipation and heat generation are considered negligible since we are considering only laminar flows where the Eckert number is generally low and it is assumed that there are no internal heat sources.

While we do not consider pure solid regions in this work, we do require an energy equation for the solid constituent of the porous region for volume-averaging. This is given as

$$\rho_s c_s \frac{\partial T}{\partial t} = k_s \nabla^2 T. \quad (2.4)$$

In  $\Omega_{por}$  the flow is governed by the volume-averaged counterparts of Eqs. 2.1–2.4. Let us define an averaging volume occupying the space  $V$  which contains fluid and solid, occupying the spaces  $V_f$  and  $V_s$ , respectively. Then, the volume-averaging operator is defined as

$$\langle \phi_k \rangle = \frac{1}{V} \int_{V_k} \phi_k dV \quad (2.5)$$

or

$$\langle \phi_k \rangle^k = \frac{1}{V_k} \int_{V_k} \phi_k dV \quad (2.6)$$

for extrinsic and intrinsic averages, respectively, where  $k \in \{f, s\}$  denotes the phase in which the generic quantity  $\phi_k$  is defined. Clearly, the two averages are related through the porosity  $\varepsilon = V_f/V$ .

Extrinsically averaging the continuity equation, Eq. 2.1, in accordance with the definitions above, we have [10, 20]

$$\nabla \cdot \langle \mathbf{u} \rangle = 0. \quad (2.7)$$

The extrinsically averaged momentum equation, arising from Eq. 2.2 with certain length-scale constraints [20] and the assumption of a constant porosity, is expressed as [10]

$$\rho_f \left( \frac{\partial \langle \mathbf{u} \rangle}{\partial t} + \frac{1}{\varepsilon} \nabla \cdot (\langle \mathbf{u} \rangle \langle \mathbf{u} \rangle) \right) = -\varepsilon \nabla \langle p \rangle^f + \mu_f \nabla^2 \langle \mathbf{u} \rangle - \frac{\varepsilon \mu_f}{K} \langle \mathbf{u} \rangle - \frac{\varepsilon \rho_f c_f}{\sqrt{K}} |\langle \mathbf{u} \rangle| \langle \mathbf{u} \rangle, \quad (2.8)$$

where the final two terms on the right side of Eq. 2.8, known as the Darcy and Forchheimer terms, have been used empirically to close the set of equations as suggested by Vafai and Tien [10]. These terms describe the viscous and form drag interaction between the fluid and solid constituents in terms of volume-averaged quantities, rather than the pore-level quantities that arise directly from the averaging procedure.

The energy equations in  $\Omega_{por}$  are derived under the assumption of local thermal non-equilibrium, leading to separate energy equations for the fluid and solid regions. These equations are given for the fluid and solid regions, respectively, as [21]

$$\rho_f c_{p,f} \left( \varepsilon \frac{\partial \langle T_f \rangle^f}{\partial t} + \nabla \cdot (\langle \mathbf{u} \rangle \langle T_f \rangle^f) \right) = k_{fe} \nabla^2 \langle T_f \rangle^f + h_{fs} a_{fs} (\langle T_s \rangle^s - \langle T_f \rangle^f) \quad (2.9)$$

and

$$(1 - \varepsilon) \rho_s c_s \frac{\partial \langle T_s \rangle^s}{\partial t} = k_{se} \nabla^2 \langle T_s \rangle^s - h_{fs} a_{fs} (\langle T_s \rangle^s - \langle T_f \rangle^f). \quad (2.10)$$

Here, the effective fluid and solid conductivities,  $k_{fe}$  and  $k_{se}$ , are used to close the set of equations and may include a component to account for the effects of thermal dispersion. The final term in each of Eq. 2.9 and Eq. 2.10 accounts for the convective heat exchange between the fluid and solid constituents within the porous medium.

## 2.3 Interface Conditions

The treatment of fluid-porous interfaces has been well-studied over the years [14, 16–18, 22–25]. There is consensus in the literature that the most appropriate condition for the

velocity at the interface,  $\partial\Omega_{fl,por} = \Omega_{fl} \cap \Omega_{por}$ , is to enforce its continuity, i.e.

$$\mathbf{u}|_{fl} = \langle \mathbf{u} \rangle|_{por} \text{ on } \partial\Omega_{fl,por} \quad (2.11)$$

which was shown by Ochoa-Tapia and Whitaker [24]. Developing an appropriate condition for stress at the interface is more complicated, since it becomes difficult to construct a proper averaging volume containing only the fluid or only the porous region very near the interface. In this case, some terms involving the spatial porosity gradient, which are neglected in arriving at Eq. 2.8, may become important and lead to excess stresses at the interface. A stress-jump condition has been used successfully [17, 24], however, this approach requires parameters to be obtained from experimental data which may be unavailable for a particular flow configuration of interest. For interfaces parallel to the flow direction, Alazmi and Vafai [25] showed that taking the fluid stress to be continuous at the interface gave good results for the velocity profile and represented a reasonable compromise between the somewhat cumbersome stress-jump condition and the simplistic approximation of a constant velocity gradient on both sides of the interface. Thus, for the purposes of this work, we require that the stress carried by the fluid is continuous at the interface.

The stress tensors in the fluid and porous regions, in indicial notation, are given as

$$\sigma_{ij} = \mu_f \left( \frac{\partial u_i}{\partial x_j} + \frac{\partial u_j}{\partial x_i} \right) - p \delta_{ij} \quad (2.12)$$

and

$$\langle \sigma_{ij} \rangle = \mu_f \left( \frac{\partial \langle u_i \rangle}{\partial x_j} + \frac{\partial \langle u_j \rangle}{\partial x_i} \right) - \varepsilon \langle p \rangle^f \delta_{ij}. \quad (2.13)$$

The stress on the pure fluid side of the interface, however, is carried partially by the fluid and partially by the solid constituent within the porous medium. Therefore, only a fraction  $\varepsilon$  of the stress on the pure fluid side is balanced by the fluid portion of the porous medium,

resulting in the interface conditions [18, 23]

$$p|_{fl} = \langle p \rangle^f \Big|_{por} \quad \text{on } \partial\Omega_{fl,por} \quad (2.14)$$

and

$$\mu_f \frac{\partial \mathbf{u}}{\partial \mathbf{n}} \Big|_{fl} = \frac{\mu_f}{\varepsilon} \frac{\partial \langle \mathbf{u} \rangle}{\partial \mathbf{n}} \Big|_{por} \quad \text{on } \partial\Omega_{fl,por}, \quad (2.15)$$

where  $\mathbf{n}$  is the unit-normal vector at the fluid-porous interface.

In the energy equations, we take the temperature on the fluid side to be continuous with the average temperature on the porous side. Additionally, we require an energy balance over the surface to be satisfied. These conditions are stated mathematically as [18]

$$T|_{fl} = \left( \varepsilon \langle T_f \rangle^f + (1 - \varepsilon) \langle T_s \rangle^s \right)_{por} \quad \text{on } \partial\Omega_{fl,por} \quad (2.16)$$

and

$$\left( k_f \frac{\partial T}{\partial \mathbf{n}} \right)_{fl} = \left( k_{fe} \frac{\partial \langle T_f \rangle^f}{\partial \mathbf{n}} + k_{se} \frac{\partial \langle T_s \rangle^s}{\partial \mathbf{n}} \right)_{por} \quad \text{on } \partial\Omega_{fl,por}. \quad (2.17)$$

## 2.4 Discretization and Implementation

### 2.4.1 Governing Equations

Discretization of the relevant governing equations is carried out for general, unstructured grids with arbitrary cell topology using a cell-centred finite-volume method. As such, we integrate the governing equations over an arbitrary control volume  $\Omega_P$  having volume  $V_P$  which is bounded by the control surface  $\partial\Omega_P$ . It is assumed that  $\partial\Omega_P$  may be expressed as the union of the discrete control surfaces  $\partial\Omega_{ip}$  each of area  $A_{ip}$ , where  $ip \in \{1, 2, \dots, N_{ip}\}$  and  $N_{ip}$  is the number of discrete control surfaces. For the governing equations in the fluid

region, Eqs. 2.1–2.3, this results in

$$\sum_{ip=1}^{N_{ip}} \dot{m}_{ip} = 0, \quad (2.18)$$

$$\rho_f V_P \frac{\partial \mathbf{u}_P}{\partial t} + \sum_{ip=1}^{N_{ip}} \dot{m}_{ip} (\mathbf{u}_{ip} - \mathbf{u}_P) = - \sum_{ip=1}^{N_{ip}} p_{ip} \mathbf{n}_{ip} A_{ip} + \sum_{ip=1}^{N_{ip}} \mu_f \nabla \mathbf{u}|_{ip} \cdot \mathbf{n}_{ip} A_{ip}, \quad (2.19)$$

and

$$\rho_f c_{p,f} V_P \frac{\partial T_P}{\partial t} + \sum_{ip=1}^{N_{ip}} \dot{m}_{ip} (T_{ip} - T_P) = \sum_{ip=1}^{N_{ip}} k_f \nabla T|_{ip} \cdot \mathbf{n}_{ip} A_{ip}. \quad (2.20)$$

Note that Eq. 2.18 multiplied by  $\mathbf{u}_P$  and  $T_P$  has been subtracted from the discretized forms of Eqs. 2.2–2.3, respectively, to ensure a conservative method. Similarly, the discretized governing equations in the porous region arising from Eqs. 2.7–2.10 are given as

$$\sum_{ip=1}^{N_{ip}} \dot{m}_{ip} = 0, \quad (2.21)$$

$$\begin{aligned} \rho_f V_P \frac{\partial \langle \mathbf{u} \rangle_P}{\partial t} + \sum_{ip=1}^{N_{ip}} \frac{\dot{m}_{ip}}{\varepsilon} (\langle \mathbf{u} \rangle_{ip} - \langle \mathbf{u} \rangle_P) = & - \sum_{ip=1}^{N_{ip}} \varepsilon \langle p \rangle_{ip}^f \mathbf{n}_{ip} A_{ip} + \sum_{ip=1}^{N_{ip}} \mu_f \nabla \langle \mathbf{u} \rangle|_{ip} \cdot \mathbf{n}_{ip} A_{ip} \\ & - \frac{\varepsilon V_P \mu_f}{K} \langle \mathbf{u} \rangle_P - \frac{\varepsilon \rho_f V_P c_f}{\sqrt{K}} |\langle \mathbf{u} \rangle_P| \langle \mathbf{u} \rangle_P, \end{aligned} \quad (2.22)$$

$$\begin{aligned} \varepsilon \rho_f c_{p,f} V_P \frac{\partial \langle T_f \rangle_P^f}{\partial t} + \sum_{ip=1}^{N_{ip}} c_{p,f} \dot{m}_{ip} (\langle T_f \rangle_{ip}^f - \langle T_f \rangle_P^f) = & \sum_{ip=1}^{N_{ip}} k_{fe} \nabla \langle T_f \rangle^f|_{ip} \cdot \mathbf{n}_{ip} A_{ip} \\ & + h_{fs} a_{fs} V_P (\langle T_s \rangle_P^s - \langle T_f \rangle_P^f), \end{aligned} \quad (2.23)$$

and

$$(1 - \varepsilon) \rho_s c_s V_P \frac{\partial \langle T_s \rangle_P^s}{\partial t} = \sum_{ip=1}^{N_{ip}} k_{se} \nabla \langle T_s \rangle^s|_{ip} \cdot \mathbf{n}_{ip} A_{ip} - h_{fs} a_{fs} V_P (\langle T_s \rangle_P^s - \langle T_f \rangle_P^f). \quad (2.24)$$

Equations 2.18–2.24, presently in semi-discrete form, are second-order accurate in space provided the points  $P$  and  $ip$  are taken to be at the centroids of the control volume and discrete control surfaces, respectively. Thus, to maintain a second-order method, all remaining interpolations used to cast the equations in fully-discrete form must be accurate to a minimum of second-order. In general, interpolations will be in terms of both the cell-centred values of the dependent variables as well as their gradients. Terms involving the cell-centred values may be incorporated implicitly into the coefficient matrix describing the linearized problem, while other terms must be added explicitly to the right side of the linear system  $\mathbf{Ax} = \mathbf{b}$ . Generally, we aim to include as much implicit information as possible to enhance stability and convergence of the linearized problem to a solution of the non-linear problem.

To obtain second-order accuracy in time, all partial derivatives with respect to time are computed using second-order backward differences, with the value at the present time-step being implicit. The only exception to this is at the first time-step in which first-order backward differences must be used. For the spatial interpolations, the gradient vectors and Hessian tensors are reconstructed using the method proposed by Betchen and Straatman [26], which provides second-order accurate gradients and first-order accurate Hessian tensors. Convection terms are discretized using second-order upwind interpolations with the flux-limiter of Venkatakrishnan [27], which was chosen because of its excellent convergence properties in comparison to many other limiters. The pressure terms in Eqs. 2.19 and 2.22 are evaluated using third-order accurate spatial interpolations to obtain the pressure at the integration points. In general, a third-order interpolation using cell-centred values of a quantity  $\phi$  and its derivatives is expressed as [26]

$$\begin{aligned} \phi_{ip} = & (1 - f_{ip})\phi_P + f_{ip}\phi_{nb} + \mathbf{D}_{f,ip} \cdot [(1 - f_{ip})\nabla\phi|_P + f_{ip}\nabla\phi|_{nb}] \\ & + \frac{1}{2} [\mathbf{D}_{f,ip}\mathbf{D}_{f,ip} - f_{ip}(1 - f_{ip})\mathbf{D}_{P,nb}\mathbf{D}_{P,nb}] : [(1 - f_{ip})\nabla\nabla\phi|_P + f_{ip}\nabla\nabla\phi|_{nb}] + O(\delta^3) \end{aligned} \quad (2.25)$$

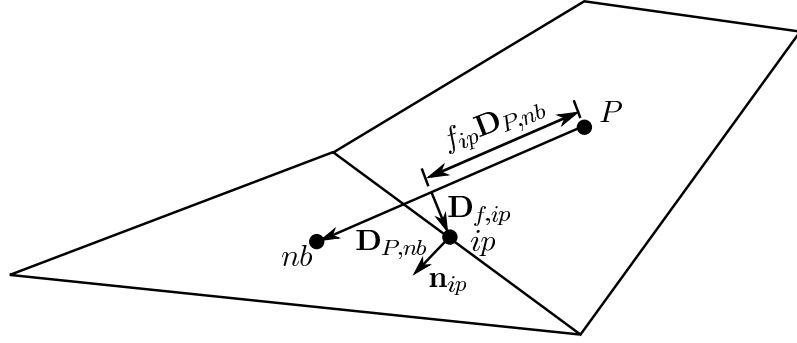


**Figure 2.1:** An illustration of two adjacent control volumes,  $P$  and  $nb$ , with the relevant geometric parameters noted.

where the relevant displacement vectors are defined in Fig. 2.1. Note that we have taken  $f_{ip}$  such that  $\mathbf{D}_{P,nb} \cdot \mathbf{D}_{f,ip} = 0$ , as suggested by Betchen and Straatman [26] in order to minimize the size of the correction associated with the interpolation from the point  $\mathbf{x}_P + f_{ip} \mathbf{D}_{P,nb}$  to the point  $\mathbf{x}_{ip}$ .

Diffusion terms must be considered carefully since in the form given in Eqs. 2.19–2.20 and Eqs. 2.22–2.24 there is no dependence on the cell-centred values and thus cannot be considered implicitly. One option is to decompose the diffusion term into normal and cross diffusion terms [28] or to use the approach of Demirdžić and Muzaferija [29] where a higher-order estimate of the gradient is used and the low-order estimate is subtracted explicitly. We employ a formulation similar to Demirdžić and Muzaferija [29] where the normal derivative at the integration point for a scalar  $\phi$  is estimated with second-order accuracy as

$$\nabla\phi|_{ip} \cdot \mathbf{n}_{ip} = \overline{\nabla\phi}|_{ip} \cdot \mathbf{n}_{ip} + \left[ \frac{\phi_{nb} - \phi_P}{\mathbf{D}_{P,nb} \cdot \mathbf{n}_{ip}} - \frac{((1 - f_{ip})\nabla\phi|_P + f_{ip}\nabla\phi|_{nb}) \cdot \mathbf{D}_{P,nb}}{\mathbf{D}_{P,nb} \cdot \mathbf{n}_{ip}} \right] + O(\delta^2), \quad (2.26)$$

where  $\overline{\nabla\phi}|_{ip}$  denotes a second-order interpolation of  $\nabla\phi$  to the integration point, given generally as

$$\overline{\nabla\phi}|_{ip} = (1 - f_{ip})\nabla\phi|_P + f_{ip}\nabla\phi|_{nb} + \mathbf{D}_{f,ip} \cdot [(1 - f_{ip})\nabla\nabla\phi|_P + f_{ip}\nabla\nabla\phi|_{nb}] + O(\delta^2). \quad (2.27)$$

In Eq. 2.26, the first term in square brackets is a first-order estimate of the gradient at the integration point and may be treated implicitly, bringing stability to the solution method. Further, it may easily be shown using Taylor series that

$$\phi_{nb} - \phi_P = ((1 - f_{ip})\nabla\phi|_P + f_{ip}\nabla\phi|_{nb}) \cdot \mathbf{D}_{P,nb} + O(\delta^3) \quad (2.28)$$

such that the term in square brackets in Eq. 2.26 is of the order  $\delta^2$  as required to maintain the second-order accuracy of the given interpolation. Note that in this work, an inverse distance approximation of the gradient is employed in the last term of Eq. 2.26, rather than a simple mean as in Ref. [29], although both result in the same truncation error.

The mass flux through the discrete control surfaces, required to form the continuity equations and the convection terms, is computed as

$$\dot{m}_{ip} = \rho_f A_{ip} \langle \hat{\mathbf{u}} \rangle_{ip} \cdot \mathbf{n}_{ip}, \quad (2.29)$$

noting that  $\langle \mathbf{u} \rangle_{ip} = \mathbf{u}_{ip}$  in the fluid region. The advecting velocity,  $\langle \hat{\mathbf{u}} \rangle_{ip}$ , is computed using the approach of Rhie and Chow [30] which uses a specially constructed momentum equation to ensure coupling between the velocity and pressure fields. As an illustration, let us consider the  $x$ -momentum equation, given for the control volume  $P$ :

$$a_P \langle u \rangle_P = \sum_{ip=1}^{N_{ip}} a_{nb,ip} \langle u \rangle_{nb,ip} + b_P - \varepsilon V_P \left. \frac{\partial \langle p \rangle^f}{\partial x} \right|_P = \langle \tilde{u} \rangle_P - \varepsilon V_P \left. \frac{\partial \langle p \rangle^f}{\partial x} \right|_P, \quad (2.30)$$

where  $\varepsilon = 1$  in the fluid region. Similarly, for the volume  $nb$  sharing an integration point  $ip$  with the volume  $P$ , we may write

$$a_{nb} \langle u \rangle_{nb} = \langle \tilde{u} \rangle_{nb} - \varepsilon V_{nb} \left. \frac{\partial \langle p \rangle^f}{\partial x} \right|_{nb}. \quad (2.31)$$

By analogy, we may write a similar equation for a ‘virtual’ control volume centred about

the integration point  $ip$ , to obtain an estimate of the advecting velocity  $\langle \hat{u} \rangle_{ip}$ , given as

$$\langle \hat{u} \rangle_{ip} = \frac{\langle \tilde{u} \rangle_{ip}}{a_{ip}} - \frac{\varepsilon V_{ip}}{a_{ip}} \left. \frac{\partial \langle p \rangle^f}{\partial x} \right|_{ip}, \quad (2.32)$$

where  $V_{ip} = (V_P + V_{nb})/2$  and  $a_{ip} = (a_P + a_{nb})/2$ . The value of  $\langle \tilde{u} \rangle_{ip}$  is then found by interpolation using the values of  $\langle \tilde{u} \rangle_P$  and  $\langle \tilde{u} \rangle_{nb}$  at the surrounding control volumes. When  $P$  and  $nb$  are both located in the same region (i.e. they are both porous or both fluid), we may assume that  $a_P \approx a_{nb} \approx a_{ip}$  and  $V_P \approx V_{nb} \approx V_{ip}$  in Eqs. 2.30–2.31 then interpolate  $\langle \tilde{u} \rangle$  to the integration point from the values at the neighbouring control volumes. This results in

$$\langle \hat{u} \rangle_{ip} = \overline{\langle \tilde{u} \rangle}_{ip} - \frac{\varepsilon V_{ip}}{a_{ip}} \left( \left. \frac{\partial \langle p \rangle^f}{\partial x} \right|_{ip} - \overline{\left. \frac{\partial \langle p \rangle^f}{\partial x} \right|}_{ip} \right), \quad (2.33)$$

where the overbar again indicates a second-order interpolation to the integration point. Forming similar equations for the advecting velocity in the remaining directions, we may compute the mass flux as

$$\dot{m}_{ip} = \rho_f A_{ip} \left[ \overline{\langle \mathbf{u} \rangle}_{ip} \cdot \mathbf{n}_{ip} - \varepsilon \hat{d}_{ip} \left( \left. \nabla \langle p \rangle^f \right|_{ip} - \overline{\left. \nabla \langle p \rangle^f \right|}_{ip} \right) \cdot \mathbf{n}_{ip} \right], \quad (2.34)$$

where  $\hat{d}_{ip}$  is the average of  $V_{ip}/a_{ip}$  in each of the coordinate directions, weighted by the magnitude of the normal vector in that direction. Then, using Eq. 2.26 for  $\left. \nabla \langle p \rangle^f \right|_{ip} \cdot \mathbf{n}_{ip}$  the second-order interpolation of the pressure gradient to the interface cancels out leaving

$$\dot{m}_{ip} = \rho_f A_{ip} \left[ \overline{\langle \mathbf{u} \rangle}_{ip} \cdot \mathbf{n}_{ip} - \varepsilon \hat{d}_{ip} \left( \frac{\langle p \rangle_{nb}^f - \langle p \rangle_P^f}{\mathbf{D}_{P,nb} \cdot \mathbf{n}_{ip}} - \frac{((1 - f_{ip}) \nabla \langle p \rangle^f|_P + f_{ip} \nabla \langle p \rangle^f|_{nb}) \cdot \mathbf{D}_{P,nb}}{\mathbf{D}_{P,nb} \cdot \mathbf{n}_{ip}} \right) \right]. \quad (2.35)$$

Thus, we have now managed to incorporate the pressure into the calculation of the mass flux at the integration point, which allows us to express the continuity equation in terms of both velocity and pressure. During the solution procedure, the pressure term in Eq. 2.35

acts to smooth out spurious oscillations in the pressure field, while in a converged solution, this term will vanish to within the second-order truncation error of the numerical scheme. It should also be noted that we solve the mass and momentum equations simultaneously as a coupled set rather than solve in a segregated manner as in Refs. [28, 31].

### 2.4.2 Interface Conditions

At the interface between a fluid and porous region, care must be taken in obtaining estimates of the pressure, advecting velocity, as well as the diffusive and advective fluxes to ensure they are physically reasonable and do not induce spurious oscillations in any of the solution fields. When estimating the advecting velocity in either the pure fluid or porous regions, we are able to assume that the active coefficients,  $a_p$  and  $a_{nb}$ , on either side of a control surface are approximately equal, simplifying the expression for  $\langle \hat{u} \rangle_{ip}$  substantially. In the case where one of the volumes is fluid and the other is porous, this simplification is invalid as a result of the potentially large Darcy and Forchheimer terms present on the porous side of the interface. Additionally, the advective momentum flux on the fluid side of an interface takes on the form  $\dot{m}_{ip} \langle \mathbf{u} \rangle_{ip} / \varepsilon$ , while in the remainder of the fluid region it is of the form  $\dot{m}_{ip} \langle \mathbf{u} \rangle_{ip}$ . As a result, special consideration must be made for the pressure at the interface to account for its rapid change as the fluid approaches the interface, such that the pressure forces balance the differing advective fluxes at the interface in comparison to that a small distance away from the interface. Also, the values of velocity and temperature at the interface must be calculated such that they correctly satisfy the proper diffusion balance equation.

Since we are developing special methods for estimating the velocity, temperature, and pressure at the interface, it is important to ensure that these values are taken into account when reconstructing the gradient vectors and Hessian tensors. As a result, any fluid-porous interfaces are effectively treated as boundaries in the gradient and Hessian reconstruction, in which the value of the independent variable is specified and the gradient is extrapolated

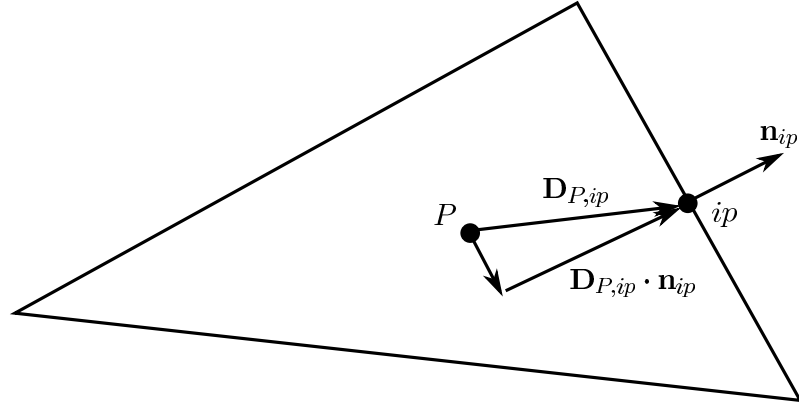


**Figure 2.2:** An illustration of a control volume,  $P$ , with the relevant geometric parameters for evaluating the normal derivative noted.

in the same manner described by Betchen and Straatman [26] for standard boundaries. However, as will be described later, the interface value used in the gradient and Hessian reconstruction is not always the same as that used for other purposes, such as advective fluxes or pressure forces.

### Diffusive and advective terms

Let us first consider a general diffusion balance at an interface between two regions, given as

$$\Gamma_P \nabla \phi|_{ip,P} \cdot \mathbf{n}_{ip} = \Gamma_{nb} \nabla \phi|_{ip,nb} \cdot \mathbf{n}_{ip}, \quad (2.36)$$

where  $\Gamma_i$  is the diffusion coefficient for the volume  $i$  and the subscript  $ip, i$  denotes a quantity evaluated at the integration point, from the side of volume  $i$ . The normal derivative at the integration point can be formed by extrapolating the cell-centred value at point  $P$  to a point which is located on a line through the integration point, in the direction of the normal to the face as illustrated in Fig. 2.2. Using a finite difference approximation along this line for the volume  $P$ , it is determined that a second-order approximation of the normal derivative at the integration point is given as

$$\nabla \phi|_{ip,P} \cdot \mathbf{n}_{ip} = \frac{\phi_{ip} - [\phi_P + \nabla \phi|_P \cdot (\mathbf{D}_{P,ip} - (\mathbf{D}_{P,ip} \cdot \mathbf{n}_{ip}) \mathbf{n}_{ip})]}{\mathbf{D}_{P,ip} \cdot \mathbf{n}_{ip}} + O(\delta^2), \quad (2.37)$$

where  $\mathbf{D}_{P,ip} = \mathbf{x}_{ip} - \mathbf{x}_P$ . Then, considering two volumes,  $P$  and  $nb$ , on opposite sides of an interface, we may formulate an expression for the value of  $\phi$  at the integration point which satisfies the diffusion balance by substituting the expression given in Eq. 2.37 and an analogous expression for the volume  $nb$  into the general diffusion balance given in Eq. 2.36. As a result, it is shown that

$$\begin{aligned} \phi_{ip} = & \frac{\Gamma_{nb}(\mathbf{D}_{P,ip} \cdot \mathbf{n}_{ip})}{\Gamma_{nb}(\mathbf{D}_{P,ip} \cdot \mathbf{n}_{ip}) - \Gamma_P(\mathbf{D}_{nb,ip} \cdot \mathbf{n}_{ip})} \phi_{nb} - \frac{\Gamma_P(\mathbf{D}_{nb,ip} \cdot \mathbf{n}_{ip})}{\Gamma_{nb}(\mathbf{D}_{P,ip} \cdot \mathbf{n}_{ip}) - \Gamma_P(\mathbf{D}_{nb,ip} \cdot \mathbf{n}_{ip})} \phi_P \\ & + \frac{\Gamma_{nb}(\mathbf{D}_{P,ip} \cdot \mathbf{n}_{ip})(\mathbf{D}_{nb,ip} - (\mathbf{D}_{nb,ip} \cdot \mathbf{n}_{ip})\mathbf{n}_{ip})}{\Gamma_{nb}(\mathbf{D}_{P,ip} \cdot \mathbf{n}_{ip}) - \Gamma_P(\mathbf{D}_{nb,ip} \cdot \mathbf{n}_{ip})} \cdot \nabla \phi|_{nb} \\ & - \frac{\Gamma_P(\mathbf{D}_{nb,ip} \cdot \mathbf{n}_{ip})(\mathbf{D}_{P,ip} - (\mathbf{D}_{P,ip} \cdot \mathbf{n}_{ip})\mathbf{n}_{ip})}{\Gamma_{nb}(\mathbf{D}_{P,ip} \cdot \mathbf{n}_{ip}) - \Gamma_P(\mathbf{D}_{nb,ip} \cdot \mathbf{n}_{ip})} \cdot \nabla \phi|_P + O(\delta^2), \quad (2.38) \end{aligned}$$

where  $\mathbf{D}_{nb,ip} = \mathbf{x}_{ip} - \mathbf{x}_{nb}$ . Equation 2.38 may then be substituted back into Eq. 2.37 to obtain the normal derivative, which is used in forming the diffusion terms. The result is summarized as

$$\begin{aligned} \nabla \phi|_{ip,P \cdot \mathbf{n}_{ip}} = & \frac{\phi_{nb} - \phi_P}{(\mathbf{D}_{P,ip} \cdot \mathbf{n}_{ip}) - \frac{\Gamma_P}{\Gamma_{nb}}(\mathbf{D}_{nb,ip} \cdot \mathbf{n}_{ip})} + \frac{(\mathbf{D}_{nb,ip} - (\mathbf{D}_{nb,ip} \cdot \mathbf{n}_{ip})\mathbf{n}_{ip})}{(\mathbf{D}_{P,ip} \cdot \mathbf{n}_{ip}) - \frac{\Gamma_P}{\Gamma_{nb}}(\mathbf{D}_{nb,ip} \cdot \mathbf{n}_{ip})} \cdot \nabla \phi|_{nb} \\ & - \frac{(\mathbf{D}_{P,ip} - (\mathbf{D}_{P,ip} \cdot \mathbf{n}_{ip})\mathbf{n}_{ip})}{(\mathbf{D}_{P,ip} \cdot \mathbf{n}_{ip}) - \frac{\Gamma_P}{\Gamma_{nb}}(\mathbf{D}_{nb,ip} \cdot \mathbf{n}_{ip})} \cdot \nabla \phi|_P + O(\delta^2). \quad (2.39) \end{aligned}$$

Note that the first two terms in Eq. 2.38 and the first term in Eq. 2.39 are equivalent to those given by Betchen et al. [18], while the remaining terms ensure second-order accuracy when the grid is non-orthogonal. In cases where the grid is orthogonal  $\mathbf{D}_{P,ip} - (\mathbf{D}_{P,ip} \cdot \mathbf{n}_{ip})\mathbf{n}_{ip} = \mathbf{D}_{nb,ip} - (\mathbf{D}_{nb,ip} \cdot \mathbf{n}_{ip})\mathbf{n}_{ip} = 0$ , so these additional terms will be identically zero. When using Eq. 2.39 in diffusive terms, the first term is treated implicitly, while the remaining terms must be treated explicitly.

For the particular case of the stress balance at the interface, we may take  $\Gamma_P = \mu_f$  and  $\Gamma_{nb} = \mu_f/\varepsilon$  when volume  $P$  is on the fluid side, or the reverse when volume  $P$  is on the porous side of the interface. Substituting these values into Eq. 2.39, yields the appropriate

value of the normal derivative at the interface, which is used to compute the diffusion terms in the momentum equation. Additionally, the value of the velocity at the integration point is computed using Eq. 2.38, which is used to provide a physically realistic estimate of the advective momentum transfer through the control surface located at an interface.

In the energy equations, we implement the parallel conduction model proposed by Betchen et al. [18], given for an arbitrarily oriented interface as:

$$q_f'' = \varepsilon k_f \nabla T|_{fl} \cdot \mathbf{n}_{ip} = k_{fe} \nabla \langle T_f \rangle^f|_{por} \cdot \mathbf{n}_{ip} \text{ on } \partial\Omega_{fl,por} \quad (2.40)$$

and

$$q_s'' = (1 - \varepsilon)k_f \nabla T|_{fl} \cdot \mathbf{n}_{ip} = k_{se} \nabla \langle T_s \rangle^s|_{por} \cdot \mathbf{n}_{ip} \text{ on } \partial\Omega_{fl,por}, \quad (2.41)$$

for the conduction heat flux within the fluid and solid constituents, respectively. Note that the addition of Eqs. 2.40–2.41 satisfy the interfacial heat flux balance given by Eq. 2.17 and may be implemented quite simply using Eqs. 2.38–2.39 to obtain the advected temperature at an interface. These equations are also used in forming diffusive fluxes at interfaces, however, it must be noted that on the fluid side of the interface, the heat flux through the interface is the sum of  $q_f''$  and  $q_s''$  given in Eqs. 2.40–2.41. Additionally, when computing the fluid temperature gradients and Hessians, the interface temperature on the fluid side of the interface is defined by the average given in Eq. 2.16, while on the porous side it is defined in the same way as the advected temperature.

### Interface pressure

In order to compute the pressure forces in the momentum equations as well as the mass flux at the integration points for volumes adjacent to interfaces, the interface pressure must be considered carefully. The first issue that arises is the generally discontinuous nature of the pressure gradient across the interface as a result of the presence of the Darcy and Forchheimer terms on the porous side, which results in a greater pressure gradient required to drive the flow. Additionally, as a result of reduction in flow area as the fluid flows from the

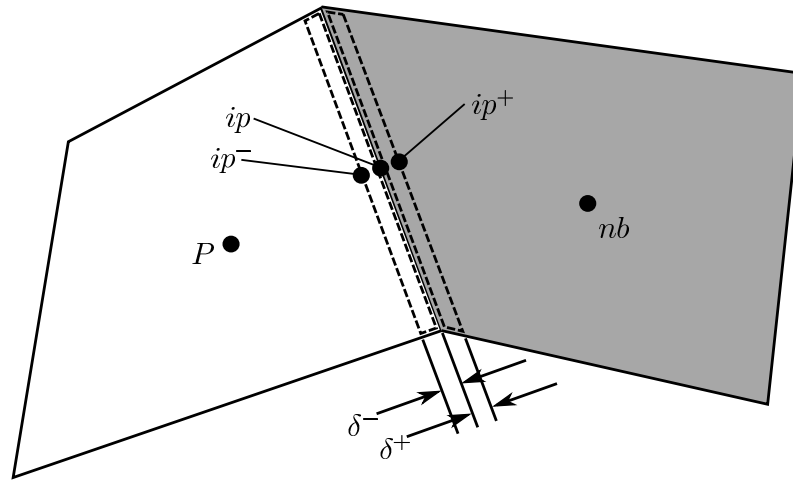


**Figure 2.3:** An illustration of two control volumes on opposite sides of a fluid-porous interface,  $P$  being fluid and  $nb$  being porous (indicated by shading), with the relevant partial control volumes indicated with dashed lines.

fluid region into the porous region, the advecting velocity undergoes a rapid change, which must be balanced by appropriate pressure forces. Let us consider an example, illustrated in Fig. 2.3, in which fluid is flowing into a porous region from a pure fluid region. Following a momentum balance on the narrow control volume on the fluid side of the interface, neglecting any mass flux from the sides of width  $\delta^-$ , the pressure at  $ip$  is found to be [18]

$$p_{ip} = p_{ip^-} - \frac{1 - \varepsilon}{\varepsilon} \frac{\dot{m}_{ip} \langle \mathbf{u} \rangle_{ip} \cdot \mathbf{n}_{ip}}{A_{ip}}, \quad (2.42)$$

while a similar momentum balance on the porous side of the interface indicates

$$p_{ip} = p_{ip^+}, \quad (2.43)$$

where  $p_{ip^-}$  and  $p_{ip^+}$  are computed using third-order Taylor series extrapolations from  $P$  and  $nb$ , respectively. Then, letting  $\delta^-, \delta^+ \rightarrow 0$  gives us an estimate of the interface pressure at an infinitesimally small distance from  $ip$  on either side of the interface that accounts for the change in advecting velocity at the interface. Clearly, this means that a different pressure will be used in the fluid and porous regions to compute the pressure forces in

the momentum equations. Thus, while we do not directly enforce the pressure continuity condition listed in Eq. 2.14, it is implied that it is satisfied at  $ip$ , however we evaluate the pressure forces using pressures very small distances away from  $ip$  to avoid any difficulties associated with the discontinuous gradient at this point. As will be shown, it has been found that this approach is necessary on non-orthogonal grids to avoid spurious oscillations in the velocity field.

When computing the gradients at the cell centroids, however, it does not make physical sense to take the pressure at the integration point to be the interface pressure computed above, since this would artificially change the magnitude of the gradient in the fluid region. While Betchen et al. [18] were able to use the corrected pressure in computing gradients, this is due to the structured, orthogonal framework of that code, which blends this estimate with an estimate of the gradient from the other side of the control volume. In the present non-orthogonal code, the gradient and Hessian tensors in each region are tightly coupled together meaning that an over- or under-estimate of the gradient adjacent to the interface will propagate itself throughout that domain. Therefore, when computing the gradients and Hessians at volumes adjacent to an interface, we take the pressures on either side to be the pressures extrapolated using third-order Taylor series to the points  $ip^-$  and  $ip^+$  with  $\delta^-, \delta^+ \rightarrow 0$ . From a physical perspective, this gives a better estimate of the gradient and Hessian over the control volume as a whole, since the rapid change in pressure described by Eq. 2.42 occurs over such a small portion of that volume. Again, we will show that this method is required to obtain a realistic estimate of the pressure gradient in volumes adjacent to interfaces and to avoid spurious oscillations in the velocity field.

### **Advecting velocity**

At fluid-porous interfaces, special consideration must also be given to the advecting velocity since the assumption  $a_P \approx a_{nb} \approx a_{ip}$  is not valid due to the potentially large Darcy and Forchheimer terms on the porous side of the interface. In this case, the interpolation of

$\langle \tilde{u} \rangle$  to the integration point based on Eqs. 2.30 and 2.31 takes on the form

$$\begin{aligned} \langle \tilde{u} \rangle_{ip} = & (1 - f_{ip})a_P \langle u \rangle_P + f_{ip}a_{nb} \langle u \rangle_{nb} \\ & + \mathbf{D}_{f,ip} \cdot \left( (1 - f_{ip})a_P \nabla \langle u \rangle|_P + f_{ip}a_{nb} \nabla \langle u \rangle|_{nb} \right) + \overline{\left( \varepsilon V \frac{\partial \langle p \rangle^f}{\partial x} \right)} \Big|_{ip}, \end{aligned} \quad (2.44)$$

where again the overbar indicates a second-order interpolation to the integration point.

Using this expression in Eq. 2.32 results in

$$\begin{aligned} \langle \hat{u} \rangle_{ip} = & (1 - f_{ip}) \frac{a_P}{a_{ip}} \langle u \rangle_P + f_{ip} \frac{a_{nb}}{a_{ip}} \langle u \rangle_{nb} + \mathbf{D}_{f,ip} \cdot \left( (1 - f_{ip}) \frac{a_P}{a_{ip}} \nabla \langle u \rangle|_P + f_{ip} \frac{a_{nb}}{a_{ip}} \nabla \langle u \rangle|_{nb} \right) \\ & - \frac{V_{ip}}{a_{ip}} \left( \varepsilon_{ip} \frac{\partial \langle p \rangle^f}{\partial x} \Big|_{ip} - \frac{1}{V_{ip}} \overline{\left( \varepsilon V \frac{\partial \langle p \rangle^f}{\partial x} \right)} \Big|_{ip} \right). \end{aligned} \quad (2.45)$$

Since  $\partial \langle p \rangle^f / \partial x$  is generally expected to be discontinuous across fluid-porous interfaces we make the following assumption regarding the pressure gradient at the integration point

$$\varepsilon_{ip} \frac{\partial \langle p \rangle^f}{\partial x} \Big|_{ip} = \frac{1}{2V_{ip}} \left( \varepsilon_P V_P \frac{\partial \langle p \rangle^f}{\partial x} \Big|_{ip^-} + \varepsilon_{nb} V_{nb} \frac{\partial \langle p \rangle^f}{\partial x} \Big|_{ip^+} \right), \quad (2.46)$$

which is a volume-weighted average of the porosity multiplied by the pressure gradient, estimated from either side of the integration point. Additionally, the interpolated pressure gradient term in Eq. 2.45 is treated simply as the mean of the values on either side of the integration point, i.e.

$$\overline{\left( \varepsilon V \frac{\partial \langle p \rangle^f}{\partial x} \right)} \Big|_{ip} = \frac{1}{2} \left( \varepsilon_P V_P \frac{\partial \langle p \rangle^f}{\partial x} \Big|_{ip^-} + \varepsilon_{nb} V_{nb} \frac{\partial \langle p \rangle^f}{\partial x} \Big|_{ip^+} \right). \quad (2.47)$$

Combining Eqs. 2.46 and 2.47 with Eq. 2.45 and forming similar equations in the remaining coordinate directions, we arrive at an estimate of the mass flux at the integration point, given

as

$$\begin{aligned} \dot{m}_{ip} = \rho_f A_{ip} \left[ \overline{\langle \mathbf{u} \rangle}'_{ip} \cdot \mathbf{n}_{ip} - \hat{d}_{ip} \left( \frac{1}{2} \frac{\varepsilon_P V_P}{V_{ip}} \left( \nabla \langle p \rangle^f |_{ip^-} - \overline{\nabla \langle p \rangle^f} |_{ip^-} \right) \cdot \mathbf{n}_{ip} \right. \right. \\ \left. \left. + \frac{1}{2} \frac{\varepsilon_{nb} V_{nb}}{V_{ip}} \left( \nabla \langle p \rangle^f |_{ip^+} - \overline{\nabla \langle p \rangle^f} |_{ip^+} \right) \cdot \mathbf{n}_{ip} \right) \right], \quad (2.48) \end{aligned}$$

where  $\overline{\langle \mathbf{u} \rangle}'_{ip}$  is a special interpolation to the integration point which is weighted by the active coefficients and is defined as

$$\begin{aligned} \overline{\langle \mathbf{u} \rangle}'_{ip} = (1 - f_{ip}) \frac{a_P}{a_{ip}} \langle \mathbf{u} \rangle_P + f_{ip} \frac{a_{nb}}{a_{ip}} \langle \mathbf{u} \rangle_{nb} \\ + \mathbf{D}_{f,ip} \cdot \left( (1 - f_{ip}) \frac{a_P}{a_{ip}} \nabla \langle \mathbf{u} \rangle|_P + f_{ip} \frac{a_{nb}}{a_{ip}} \nabla \langle \mathbf{u} \rangle|_{nb} \right) \quad (2.49) \end{aligned}$$

As before, the pressure gradients in the direction of the unit-normal at the integration point are estimated using Eq. 2.26, resulting in

$$\begin{aligned} \dot{m}_{ip} = \rho_f A_{ip} \left[ \overline{\langle \mathbf{u} \rangle}'_{ip} \cdot \mathbf{n}_{ip} - \hat{d}_{ip} \left( \frac{1}{2} \frac{\varepsilon_P V_P}{V_{ip}} \left( \frac{\langle p \rangle^f_{ip} - \langle p \rangle^f_P}{\mathbf{D}_{P,ip} \cdot \mathbf{n}_{ip}} - \frac{\nabla \langle p \rangle^f|_P \cdot \mathbf{D}_{P,ip}}{\mathbf{D}_{P,ip} \cdot \mathbf{n}_{ip}} \right) \right. \right. \\ \left. \left. + \frac{1}{2} \frac{\varepsilon_{nb} V_{nb}}{V_{ip}} \left( \frac{\langle p \rangle^f_{ip} - \langle p \rangle^f_{nb}}{\mathbf{D}_{nb,ip} \cdot \mathbf{n}_{ip}} - \frac{\nabla \langle p \rangle^f|_{nb} \cdot \mathbf{D}_{nb,ip}}{\mathbf{D}_{nb,ip} \cdot \mathbf{n}_{ip}} \right) \right) \right]. \quad (2.50) \end{aligned}$$

## 2.5 Results and Discussion

In this section, we consider two particular configurations involving coupled fluid and porous regions and solve the flows using the numerical model described previously. The first problem to be solved is that of plane flow through a parallel plate channel with a porous plug inserted some distance from the inlet. At high Reynolds numbers ( $Re_H \geq O(100)$ ), this problem is typically quite challenging to solve numerically and special consideration of the interface conditions is necessary [18]. In this case we solve for  $Re_H = 1000$  and find that accurate results are obtained at all locations, including the interface. This problem is used

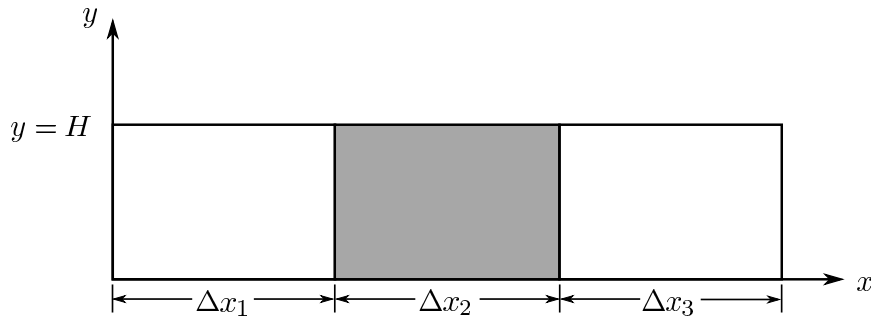


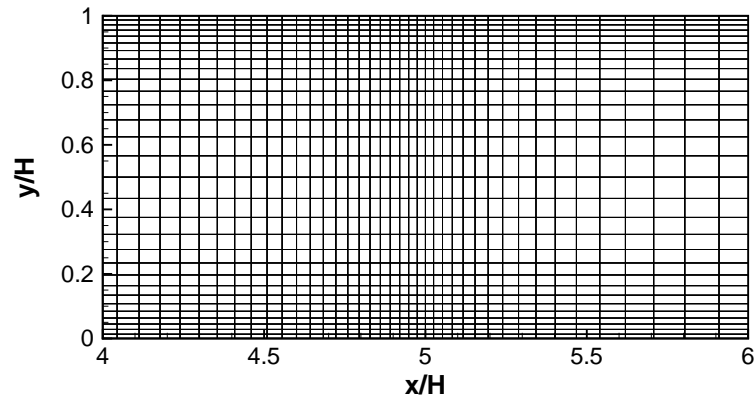
**Figure 2.4:** A schematic diagram of the porous plug case, where the shaded region indicates the porous subdomain.

to demonstrate the effectiveness of the present formulation on non-orthogonal grids as well as to show the problems that occur when modified formulations are employed, even on orthogonal grids. The second problem involves a porous heat sink, which demonstrates the effectiveness of the conjugate heat transfer model in geometries that cannot be discretized using orthogonal grids.

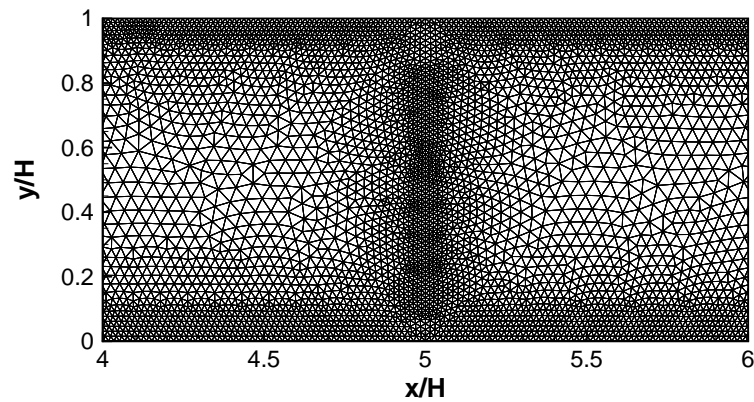
### 2.5.1 Porous Plug Flow

The porous plug problem considered here is identical to that considered by Betchen et al. [18] and is illustrated schematically in Fig. 2.4. In this case we are interested in computing the flow field for  $Re_H = 1000$  and  $Da = 10^{-2}$  since the pressure correction term given in Eq. 2.42 will be rather large and thus challenging to solve numerically. This particular case is discretized using both hexahedral and triangular prismatic volumes, shown in Fig. 2.5, in order to demonstrate the effectiveness of the non-orthogonal correction terms introduced in this paper, since these terms will be relatively large in the case of the triangular prismatic grids and identically zero in the case of the hexahedral grids.

The cases using hexahedral grids are configured in the same way as in Ref. [18], where the lengths shown in Fig. 3.11 were specified as  $\Delta x_1 = \Delta x_2 = 5H$  and  $\Delta x_3 = 50H$ . In this case the large value of  $\Delta x_3$  is chosen to ensure fully developed conditions at the outlet. Although this case is two-dimensional, it is discretized using three-dimensional grids



(a)



(b)

**Figure 2.5:** Plots of the (a) hexahedral and (b) triangular prismatic grids, near an interface, used for the porous plug case.

with a single row of volumes in the  $z$ -direction with symmetry conditions imposed on the planes of constant  $z$ . The velocity boundary conditions consist of a fully-developed plane channel flow specified at the inlet boundary,  $x = 0$ , fully-developed conditions at the outlet boundary,  $x = 60H$ , and zero velocity at the channel walls,  $y = 0$  and  $y = H$ . The pressure was specified as zero at the outlet boundary to set the pressure level, while pressure was extrapolated to all other boundaries.

Using hexahedral grids, it is possible to create volumes near the outlet boundary which are very long in the flow direction in order to greatly reduce the number of volumes in the

**Table 2.1:** Grid independence study for the porous plug case discretized using hexahedral grids, including the percent difference and grid convergence index (GCI) as defined by Celik et al. [32]. Note that the number of control volumes is given for the porous plug section only and that the pressure difference is given across the full length of the domain.

$N_x \times N_y$	$\Delta p$	% difference	GCI	$u(2.5H, 0.5H)/U$	% difference	GCI
$35 \times 21$	1463.41	N/A	N/A	1.476	N/A	N/A
$50 \times 30$	1466.36	0.2	0.6	1.494	1.2	3.5
$70 \times 42$	1469.27	0.2	0.6	1.497	0.2	0.6

portion of the domain downstream of the porous plug. Although these volumes have a very high aspect ratio, accuracy is maintained since the flow is nearly fully-developed. With triangular prismatic grids this approach is not practical, thus a great number of volumes are required to compute the downstream flow, which is not generally of interest. To avoid this issue we instead choose  $\Delta x_3 = 5H$  and implement a velocity boundary condition based upon an application of the continuity equation at the outlet face. In this case, since the primary flow is in the  $x$ -direction, the velocity components in the  $y$ - and  $z$ -directions are simply extrapolated to the outlet, while the pressure is set to zero. Based on the continuity equation we may state

$$\left. \frac{\partial u}{\partial x} \right|_{ip} = - \left( \frac{\partial v}{\partial y} + \frac{\partial w}{\partial z} \right)_{ip}. \quad (2.51)$$

Then, since  $\mathbf{n}_{ip} = \mathbf{i}$ , Eq. 2.37 may be applied to find  $\partial u / \partial x$  at the integration point which results in an expression for the integration point velocity, given as

$$u_{ip} = u_P + \nabla u|_P \cdot (\mathbf{D}_{P,ip} - (\mathbf{D}_{P,ip} \cdot \mathbf{i})\mathbf{i}) - \left( \frac{\partial v}{\partial y} + \frac{\partial w}{\partial z} \right)_{ip} (\mathbf{D}_{P,ip} \cdot \mathbf{i}), \quad (2.52)$$

which is used to specify the velocity component in the  $x$ -direction at the outlet boundary.

Grid independence studies were performed for each volume type, where the total number of volumes was repeatedly doubled until all quantities of interest were independent of the grid resolution to within a certain tolerance. In this case, we wish to obtain results which are grid independent to within 1% and have an acceptable grid convergence index

**Table 2.2:** *Grid independence study for the porous plug case discretized using triangular prismatic grids, including the percent difference and grid convergence index (GCI) as defined by Celik et al. [32]. Note that the number of control volumes is given for the porous plug section only and that the pressure difference is given across the full length of the domain (which is truncated in comparison to the hexahedral grid case). Also note that for all grids, the growth rate was 10% per row with a maximum characteristic grid size of  $4\delta_w$ .*

$\delta_w$	$N_{por}$	$\Delta p$	% diff.	GCI	$u(2.5H, 0.5H)/U$	% diff.	GCI
0.0375	4644	1382.83	N/A	N/A	1.486	N/A	N/A
0.0227	9272	1394.43	0.8	2.5	1.490	0.3	0.8
0.0129	18726	1400.07	0.4	1.2	1.494	0.3	0.8

[32]. The results of the present grid independence studies are summarized in Tables 2.1 and 2.2. In general, it was found that obtaining an overall pressure drop across the domain that was grid independent did not always yield velocity fields which were also grid independent. Thus, in addition to the pressure drop across the domain, we also consider the velocity at the point  $(2.5H, 0.5H)$ , which is associated with how well momentum diffusion is resolved in the upstream channel and should approach 1.5 as the solution is well-resolved. Using hexahedral grids it was found that using  $35 \times 21$  control volumes in the porous region, with similar grid densities in the fluid regions, was sufficient to obtain grid independent results for the pressure drop, but that further refinement was required to obtain grid independent velocity results. A grid with  $50 \times 30$  volumes in the porous region was found to be sufficiently refined for the velocity field to be grid independent, therefore this grid is used for all subsequent calculations. Note that in all of these cases, the volumes adjacent to the interface and walls were refined in comparison to those in the interior of the domain, as shown in Fig. 2.5(a).

Using the prismatic grids, shown in Fig. 2.5(b), it was found that about 4644 volumes were needed to discretize the porous region in order to achieve results for pressure and velocity fields that were grid independent, in comparison to the 1500 volumes for the hexahedral grids. This is reasonable, however, due to the non-orthogonal nature of these grids as well as the smaller area occupied by a triangle in comparison to a square of the same

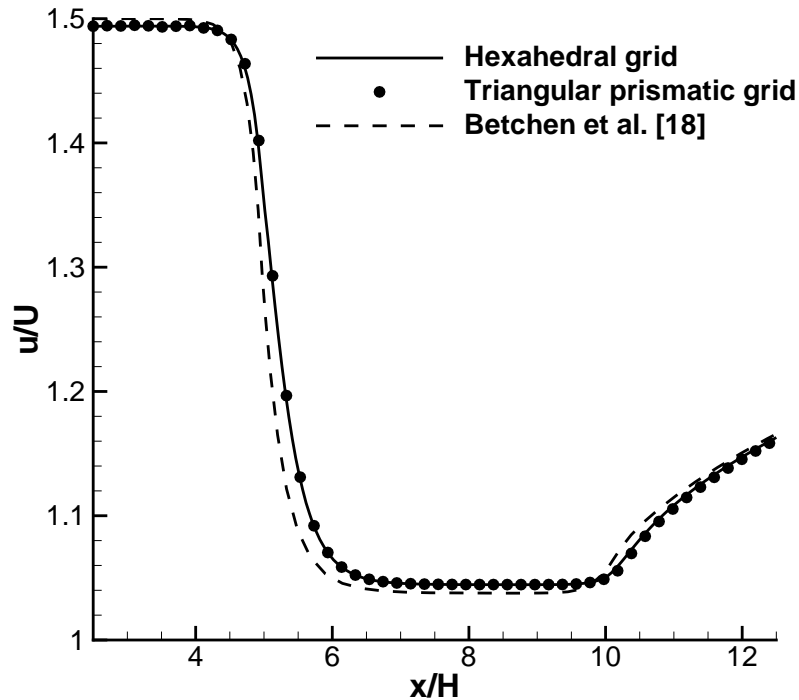


**Figure 2.6:** A plot of the streamwise velocity component for the porous plug problem with  $Re_H = 1000$  and  $Da = 10^{-2}$  as a function of position along the line  $y/H = 0.5$  on the interval  $x/H \in [2.5, 12.5]$  using the two grid types in comparison to results from Betchen et al. [18].

characteristic dimension. While the prismatic grid containing 4644 volumes was sufficient to obtain grid independent results, it proved challenging in some locations to interpolate a smooth curve along the channel centreline. As a result, the grid containing 9272 volumes in the porous region has been used for subsequent calculations since the volumes near the centreline are smaller and lead to more accurate interpolations for plotting purposes.

Figure 2.6 shows the results computed using the two different grid types described above for the streamwise velocity component along the line  $y/H = 0.5$  on the interval  $x/H \in [2.5, 12.5]$  in addition to the results obtained by Betchen et al. [18]. It is clear from this figure that the results obtained using the two different grid types are in quite good agreement with one another, indicating that the terms which account for the non-orthogonality of the grid are accurate. Additionally, comparing to the results given by Betchen et al. [18] for the same case, we see similar results, although the profiles near the interfaces are slightly different due to the different treatment of the pressure at the interface.

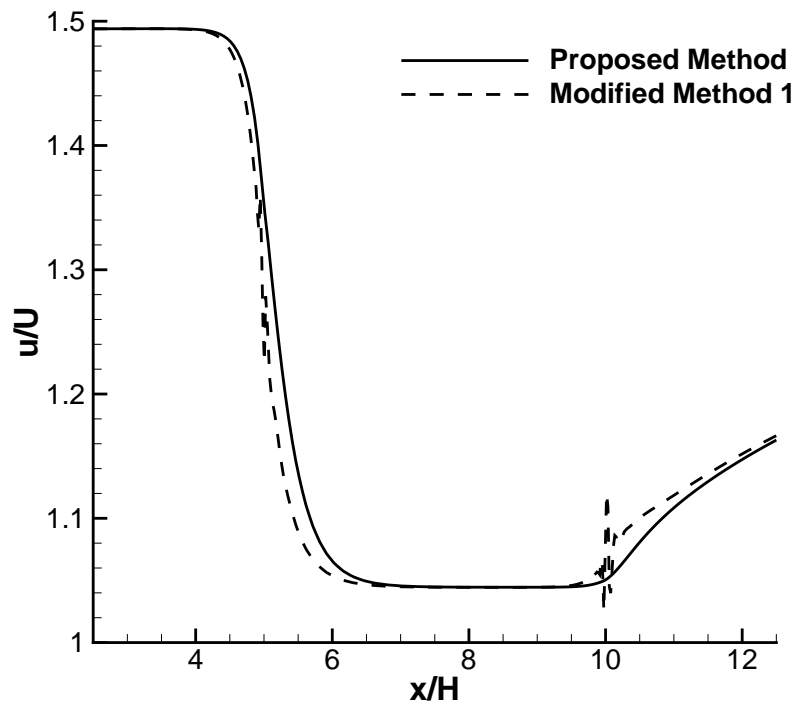
While Betchen et al. [18] blends the pressure obtained using Eqs. 2.42 and 2.43 to arrive at an estimate for the interface pressure and uses this pressure to find the pressure gradient, we use different interface pressures on either side of the interface and do not use the corrected pressure to reconstruct the pressure gradient field. Thus, the pressure forces on the fluid at the interface are slightly different leading to a slight difference in the velocity field.

In addition to evaluating the effects of grid type, we also wish to evaluate the impact of the present form of the pressure correction in comparison to other possible treatments of the interface pressure. To do so, we introduce the modified schemes:

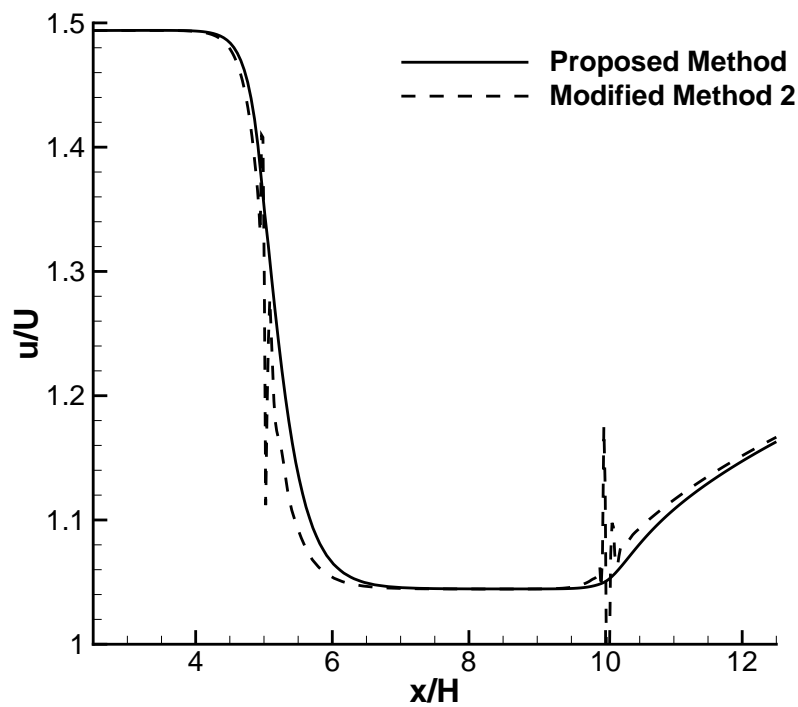
1. Use a standard second-order interpolation for  $p_{ip}$  at interfaces and perform no special pressure correction in the momentum equations.
2. Take the interface pressure to be the average of the estimates given in Eqs. 2.42 and 2.43 (as in Ref. [18]) and use this pressure for both the gradient reconstruction and the pressure forces in the momentum equations.

Results shown in Figs. 2.7(a) and 2.7(b) indicate that the use of either of these modified schemes yields highly unrealistic results in the vicinity of the interface and it is clear that the velocity has become quite decoupled from the pressure field. The failure of the first modified method indicates that a pressure correction is indeed required, while failure of the second modified method shows that the corrected pressure should not be used for reconstructing the gradients for reasons described previously. In summary, this indicates that the interface pressure conditions proposed in this work are indeed required to obtain reasonable results for high  $Re_H$  on unstructured grids, even if orthogonal, due to issues associated with the gradient reconstruction.

It should also be noted that the convergence of the proposed method is not significantly slower than the first modified method and that it is significantly faster than the second modified method. All cases were solved using a single large time-step with a non-linear residual tolerance, normalized by the average magnitude of the given field, specified as



(a)



(b)

**Figure 2.7:** A plot of the streamwise velocity component for the porous plug problem at  $Re_H = 1000$  and  $Da = 10^{-2}$  as a function of position along the line  $y/H = 0.5$  on the interval  $x/H \in [2.5, 12.5]$  for the modified methods of treating the interface pressure and gradients. Note that these cases were run using hexahedral grids.

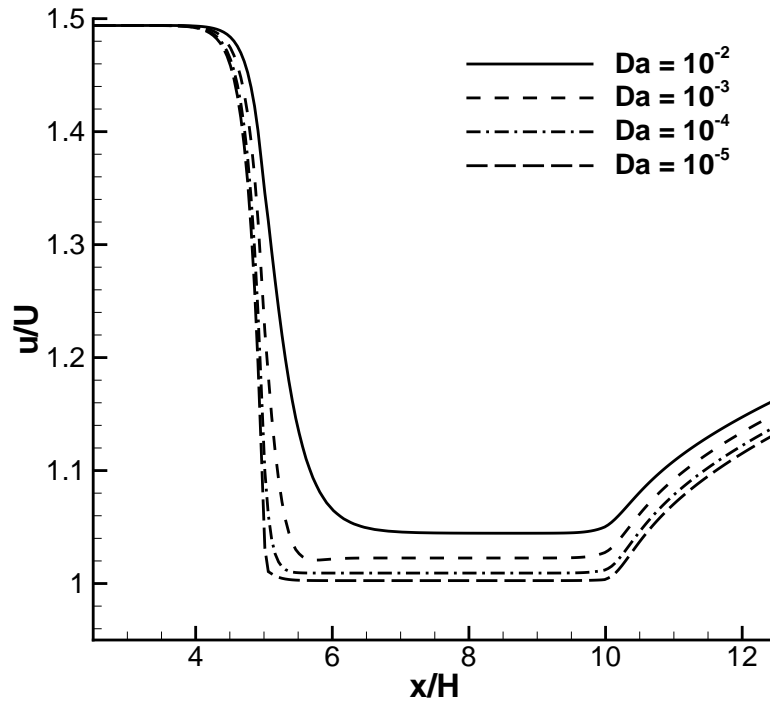


**Figure 2.8:** A plot of the streamwise velocity component for the porous plug problem at  $Re_H = 1000$  as a function of position along the line  $y/H = 0.5$  on the interval  $x/H \in [2.5, 12.5]$  for  $Da \in \{10^{-2}, 10^{-3}, 10^{-4}, 10^{-5}\}$ .

$10^{-6}$ . The proposed scheme converged in 43 iterations, while the two modified methods converged in 31 and 135 iterations, respectively. Thus, in addition to adding significant accuracy, the proposed method maintains good convergence properties.

Finally, we have computed results for  $Da \in \{10^{-3}, 10^{-4}, 10^{-5}\}$  and  $Re_H = 1000$  to demonstrate the robustness of the model over a wide range of Darcy numbers with high Reynolds number. Results for the streamwise velocity component along the line  $y/H = 0.5$  on the interval  $x/H \in [2.5, 12.5]$  are plotted in Fig. 2.8 and indicate that the model is capable of obtaining physically reasonable results for porous materials with low permeability.

## 2.5.2 Graphite Foam Heat Sink

Recently, there has been interest in creating graphite foam heat sinks with unique structures intended to balance the excellent heat transfer properties of graphite foam with its generally poor hydrodynamic properties which lead to very high pressure losses when forcing

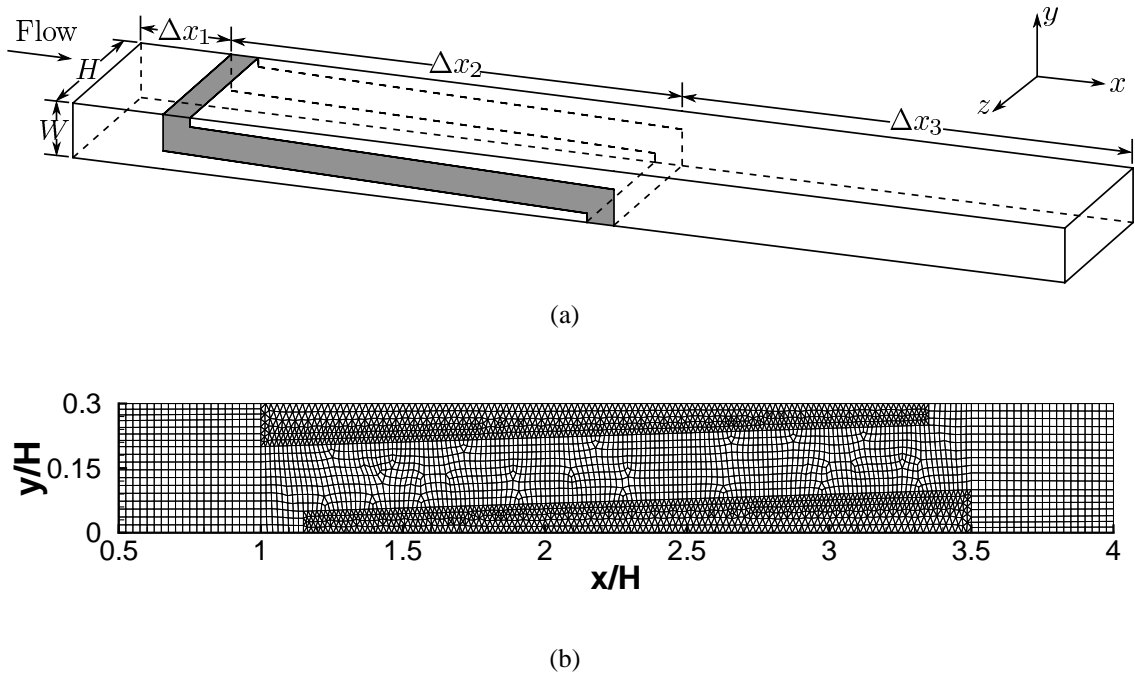


**Figure 2.9:** (a) A schematic diagram of the corrugated heat sink geometry, where the shaded region indicates the porous subdomain and (b) a plot of a selected portion of a 2D section of the computational grid on a plane of constant  $z$  which uses both triangular prismatic and hexahedral volumes.

fluid through the foam structure. Heat sinks proposed by Leong et al. [7] and Wu et al. [8] employ corrugated foam structures to allow fluid to pass relatively easily through the narrow porous regions while still obtaining some of its heat transfer benefits. The heat sink described in Ref. [8] is of particular relevance to this work because of its V-shaped corrugations, or ‘porous fins’, which cannot be discretized by orthogonal grids. With the present model, these heat sinks may be readily analyzed to determine their heat transfer characteristics and to perform optimization of their structure. While a complete parametric study is beyond the scope of this work, we shall demonstrate, using one particular flow configuration, the ability of the present model to solve the flow and thermal fields in such applications and show that the results are physically reasonable.

A schematic diagram of the geometry under consideration is given in Fig. 2.9(a). This geometry is a simplified version of the heat sink considered by Wu et al. [8], obtained by considering only one symmetric section of the heat sink and flattening the curved surfaces.

Note that we have added fluid sections upstream and downstream of the heat sink in order to allow the fluid to enter and exit in a natural way. As in Ref. [8], the height of the heat sink was taken to be  $H = 20$  mm. Additionally, we prescribed the dimensions  $\Delta x_1/H = \Delta x_3/H = 1$ ,  $\Delta x_2/H = 2.5$ , and  $W/H = 0.3$ . The thickness of the porous fins was taken to be  $W/2$  and the slope of the fin was taken such that the fluid gap at the inlet of the heat sink is double the minimum gap size, occurring at  $x/H = 3.35$ .

A uniform inflow condition was imposed at  $x/H = 0$  along with the mass-based outlet condition described in the previous section at  $x/H = 4.5$ . On the upper and lower walls,  $z/H = 0$  and  $z/H = 1$ , a no-slip condition was imposed, while on the symmetry planes,  $y/W = 0$  and  $y/W = 1$ , zero-derivative conditions were applied. The pressure was set to a reference value of zero at the outlet and was extrapolated to all other non-symmetric boundaries. On the symmetry planes, the derivative of pressure normal to the plane was set to zero. At the inlet and at the heated base,  $x/H \in [1, 3.5]$ , the uniform temperatures  $T_{in}$  and  $T_w$  were applied, respectively. At all remaining boundaries, adiabatic conditions were imposed. All graphite foam properties were taken from Straatman et al. [3] for POCO foam and fluid properties were taken as standard properties of air.

A plot of a selected portion of the computational grid is given in Fig. 2.9(b), which shows the use of multiple volume types. Results for  $Re_H = 100$  are given in Fig. 2.10 for the dimensionless pressure and temperature fields as well as some selected streamlines in the plane  $z/H = 0.5$ . Based on the results for the dimensionless pressure, coupled with the plotted streamlines, we clearly see how the high pressure on one side of the porous region coupled with the low pressure on the other side leads to a fair amount of fluid being drawn directly through the foam. The dimensionless temperature plot clearly shows the rapid increase in temperature as the fluid picks up heat from the solid constituent of the graphite foam and exits the heat sink at nearly the wall temperature. It should also be noted that although this grid is relatively coarse near interfaces, smooth results are still obtained.

The results given in this section are one example of a new class of problems that may

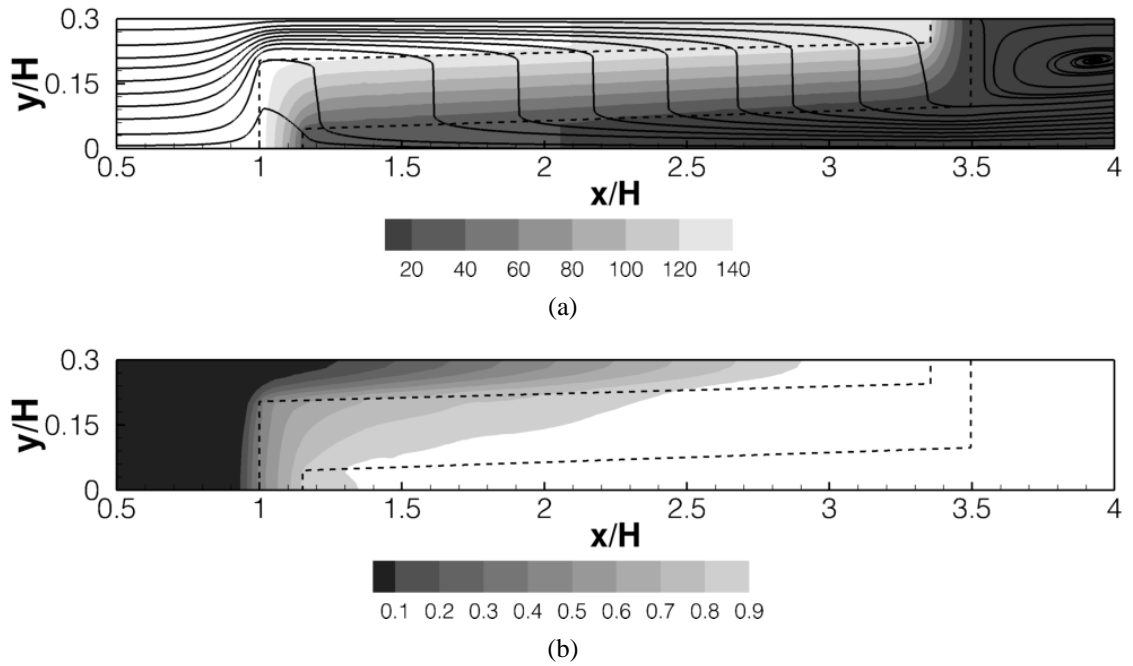


**Figure 2.10:** Contour plots on the plane  $z/H = 0.5$  of (a) the dimensionless pressure  $\langle p \rangle^f / \rho_f U^2$  along with selected streamlines and (b) the dimensionless fluid temperature  $(\langle T_f \rangle^f - T_{in}) / (T_w - T_{in})$ . Note that the porous region is outlined with dashed lines.

now be solved numerically using the newly developed model for heat and fluid flow in conjugate fluid-porous domains. In this case, the geometry cannot be discretized using orthogonal grids, due to the sloped fins. The present model, however, is capable of obtaining physically reasonable results for this type of heat sink, although to compare directly with the experimental results of Wu et al. [8] a turbulence model would be required in the fluid regions due to the higher Reynolds numbers considered in that work. Nevertheless, we have demonstrated that smooth results are obtained through the interface and in future work more rigorous validation may be pursued for this and other cases.

## 2.6 Conclusions

A numerical model for computing fluid flow and heat transfer in conjugate fluid-porous domains using unstructured, non-orthogonal grids has been proposed. Novel, physically-reasoned interface conditions have been proposed which are shown to be very robust at

high laminar Reynolds numbers and induce no spurious oscillations in any of the solution fields. The major contribution of this model is the ability to use non-orthogonal grids to discretize complex geometries without affecting the robustness of the model or having any significant impact on the computational time required to obtain a solution.

## References

- [1] Bhattacharya, A., Calmidi, V. V., and Mahajan, R. L., 2002, “Thermophysical properties of high porosity metal foams,” *Int. J. Heat Mass Transfer*, **45**, pp. 1017–1031.
- [2] Boomsma, K., Poulikakos, D., and Zwick, F., 2003, “Metal foams as compact high performance heat exchangers,” *Mech. Mater.*, **35**, pp. 1161–1176.
- [3] Straatman, A. G., Gallego, N. C., Yu, Q., Betchen, L. J., and Thompson, B. E., 2007, “Forced convection heat transfer and hydraulic losses in graphitic foam,” *J. Heat Transfer*, **129**, pp. 1237–1245.
- [4] Straatman, A. G., Gallego, N. C., Yu, Q., and Thompson, B. E., 2007, “Characterization of porous carbon foam as a material for compact recuperators,” *J. Eng. Gas Turb. Power*, **129**, pp. 326–330.
- [5] Betchen, L. J. and Straatman, A. G., 2008, “The development of a volume-averaged entropy-generation function for nonequilibrium heat transfer in high-conductivity porous foams,” *Numer. Heat Tr. B-Fund.*, **53**, pp. 412–436.
- [6] DeGroot, C. T., Straatman, A. G., and Betchen, L. J., 2009, “Modeling forced convection in finned metal foam heat sinks,” *J. Electron. Packag.*, **131**, pp. 021001–1–10.
- [7] Leong, K. C., Li, H. Y., Jin, L. W., and Chai, J. C., 2010, “Numerical and experimental study of forced convection in graphite foams of different configurations,” *Appl. Therm. Eng.*, **30**, pp. 520–532.

- 
- [8] Wu, W., Du, J. H., Lin, Y. R., Chow, L. C., Bostanci, H., Saarloos, B. A., and Rini, D. P., 2011, "Evaluation of compact and effective air-cooled carbon foam heat sink," *J. Heat Transfer*, **133**, pp. 054504–1–5.
- [9] Whitaker, S., 1967, "Diffusion and dispersion in porous media," *A.I.Ch.E. J.*, **13**, pp. 420–427.
- [10] Vafai, K. and Tien, C. L., 1981, "Boundary and inertia effects on flow and heat transfer in porous media," *Int. J. Heat Mass Transfer*, **24**, pp. 195–203.
- [11] Ould-Amer, Y., Chikh, S., Bouhadeif, K., and Lauriat, G., 1998, "Forced convection cooling enhancement by use of porous materials," *Int. J. Heat Fluid Flow*, **19**, pp. 251–258.
- [12] Chikh, S., Boumediene, A., Bouhadeif, K., and Lauriat, G., 1998, "Analysis of fluid flow and heat transfer in a channel with intermittent heated porous blocks," *Heat Mass Transfer*, **33**, pp. 405–413.
- [13] Fu, W. S. and Chen, S. F., 2002, "A numerical study of heat transfer of a porous block with the random porosity model in a channel flow," *Heat Mass Transf.*, **38**, pp. 695–704.
- [14] Phanikumar, M. S. and Mahajan, R. L., 2002, "Non-Darcy natural convection in high porosity metal foams," *Int. J. Heat Mass Transfer*, **45**, pp. 3781–3793.
- [15] Calmidi, V. V. and Mahajan, R. L., 2000, "Forced convection in high porosity metal foams," *J. Heat Transfer*, **122**, pp. 557–565.
- [16] Costa, V. A. F., Oliveira, L. A., Baliga, B. R., and Sousa, A. C. M., 2004, "Simulation of coupled flows in adjacent porous and open domains using a control-volume finite-element method," *Numer. Heat Tr. A-Appl.*, **45**, pp. 675–697.

- [17] Costa, V. A. F., Oliveira, L. A., and Baliga, B. R., 2008, "Implementation of the stress jump condition in a control-volume finite-element method for the simulation of laminar coupled flows in adjacent open and porous domains," *Numer. Heat Tr. B-Fund.*, **53**, pp. 383–411.
- [18] Betchen, L. J., Straatman, A. G., and Thompson, B. E., 2006, "A nonequilibrium finite-volume model for conjugate fluid/solid/porous domains," *Numer. Heat Tr. A-Appl.*, **49**, pp. 543–565.
- [19] Yu, P., Lee, T. S., Zeng, Y., and Low, H. T., 2007, "A numerical method for flows in porous and homogeneous fluid domains coupled at the interface by stress jump," *Int. J. Numer. Meth. Fl.*, **53**, pp. 1755–1775.
- [20] Whitaker, S., 1997, *Volume Averaging of Transport Equations*, chap. 1, Fluid Transport in Porous Media, Springer-Verlag, Southampton, UK, pp. 1–59.
- [21] Amiri, A., Vafai, K., and Kuzay, T. M., 1995, "Effects of boundary conditions of non-darcian heat transfer through porous media and experimental comparisons," *Numer. Heat Tr. A-Appl.*, **27**, pp. 651–664.
- [22] Martins-Costa, M. L. and da Gama, R. M. S., 1994, "A local model for the heat transfer process in two distinct flow regions," *Int. J. Heat Fluid Flow*, **15**, pp. 477–485.
- [23] Vafai, K. and Kim, S. J., 1995, "On the limitations of the Brinkman-Forchheimer-extended Darcy equation," *Int. J. Heat Fluid Flow*, **16**, pp. 11–15.
- [24] Ochoa-Tapia, J. A. and Whitaker, S., 1995, "Momentum transfer at the boundary between a porous medium and a homogeneous fluid – I. Theoretical development," *Int. J. Heat Mass Transfer*, **38**, pp. 2635–2646.

- 
- [25] Alazmi, B. and Vafai, K., 2002, "Analysis of fluid flow and heat transfer interfacial conditions between a porous medium and a fluid layer," *Int. J. Heat Mass Transfer*, **44**, pp. 1735–1749.
- [26] Betchen, L. J. and Straatman, A. G., 2010, "An accurate gradient and Hessian reconstruction method for cell-centered finite volume discretizations on general unstructured grids," *Int. J. Numer. Meth. Fl.*, **62**, pp. 945–962.
- [27] Venkatakrishnan, V., 1995, "Convergence to steady-state solutions of the Euler equations on unstructured grids with limiters," *J. Comput. Phys.*, **118**, pp. 120–130.
- [28] Dalal, A., Eswaran, V., and Biswas, G., 2008, "A finite-volume method for Navier-Stokes equations on unstructured grids," *Numer. Heat Tr. B-Fund.*, **54**, pp. 238–259.
- [29] Demirdžić, I. and Muzaferija, S., 1995, "Numerical method for coupled fluid flow, heat transfer and stress analysis using unstructured moving meshes with cells of arbitrary topology," *Comput. Methods Appl. Mech. Engrg.s*, **125**, pp. 235–255.
- [30] Rhie, C. M. and Chow, W. L., 1983, "Numerical study of the turbulent-flow past an airfoil with trailing edge separation," *AIAA J.*, **21**, pp. 1525–1532.
- [31] Moradi Larmaei, M., Behzadi, J., and Mahdi, T.-F., 2010, "Treatment of checkerboard pressure in the collocated unstructured finite-volume scheme," *Numer. Heat Tr. B-Fund.*, **58**, pp. 121–144.
- [32] Celik, I. B., Ghia, U., Roache, P. J., Freitas, C. J., Coleman, H., and Raad, P. E., 2008, "Procedure for estimation and reporting of uncertainty due to discretization in CFD applications," *J. Fluids Eng.*, **130**, pp. 078001–1–078001–4.

# Numerical Results for the Effective Properties of Graphite Foam<sup>†</sup>

## 3.1 Introduction

High-conductivity porous materials, such as aluminum and graphite foams, have been the subject of much research over the past decade as a potential material for enhanced heat transfer devices [1–9]. In particular, graphite foams have been of significant interest due to its extremely high solid-phase thermal conductivity (800–1900 W/m·K), which leads to a very high effective solid conductivity (40–160 W/m·K) [5]. This enables heat to penetrate deeply into the foam structure leading to significant thermal non-equilibrium between the fluid and solid, creating potential for convective exchange. Combined with the large amount of exposed internal surface area, which can be as high as 5,000–50,000 m<sup>2</sup>/m<sup>3</sup>, there is little resistance to convective exchange and good heat transfer performance can be obtained.

Experimentally, the heat transfer characteristics of graphite foams in various configurations have been explored [4–6, 8], however, the ability to study the performance of devices

---

<sup>†</sup>A version of this chapter entitled “Numerical results for the effective flow and thermal properties of graphite foam” has been published in *Journal of Heat Transfer*, vol. 134, art. 042603, 2012.

incorporating graphite foams numerically remains challenging due to incomplete knowledge of its effective properties. Since any practical domain of interest will contain a large number of pores, the pore-level flow and thermal fields are not computed directly. Rather, volume-averaged governing equations [10] are solved to obtain results for the average fields. While numerical methods exist to solve these equations [11–13], the accuracy of the simulations depends on the accuracy of the models for the relevant effective properties such as the permeability and thermal dispersion conductivity.

To obtain many of the required geometric parameters of graphite foams, Yu et al. [14] developed an idealized geometric model, shown in Fig. 3.1 in comparison to images of an actual foam. Additionally, Yu et al. [14] proposed a simplified analytical model for the effective thermal conductivity of the solid constituent of the foam and used experimental data to develop models for the permeability and Forchheimer coefficient. Straatman et al. [5] used further experimental data to obtain results for the permeability and Forchheimer coefficient and used volume-averaged simulations to calibrate an interstitial heat exchange model of the form  $Nu_\ell = h_{fs}\ell/k_f = CRe_\ell^m Pr^n$ , where  $\ell$  is an appropriate length scale, to match experimental results. Thermal dispersion was modeled as in Calmidi and Mahajan [15] for aluminum foams as a linear function of the Péclet number. However, recent work by Karimian and Straatman [16], involving direct simulation of the pore-level flow and thermal fields in graphite foams, indicates that the Nusselt number and thermal dispersion conductivity correlations may be more complicated than those considered by Straatman et al. [5].

While there have been a number of studies undertaken to explore the effective properties of graphite foam, there have been no comprehensive studies that have computed all of the required properties to obtain a fully closed volume-averaged model. In particular, thermal dispersion in graphite foams has not been well-studied and is very important for flow at high Péclet numbers. While Karimian and Straatman [16] obtained some results for the axial dispersion conductivity, there is a need to study the transverse dispersion conductivity

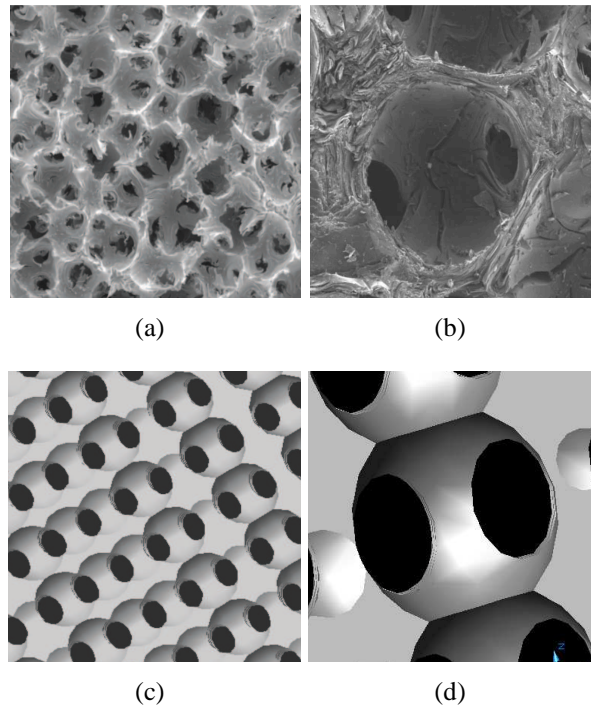


**Figure 3.1:** *Electron micrograph images of a graphite foam specimen (a,b) in comparison to a CAD model of the idealized pore geometry proposed by Yu et al. [14] (c,d).*

and to obtain functions which relate the dispersion conductivity to the flow conditions. Recently, a general method for obtaining all of the required effective thermal properties for high-conductivity media has been proposed based on numerical simulation of the pore-level flow fields [17]. Similarly, a method has been proposed by Whitaker [18] to obtain the relevant effective flow properties required for closure of the volume-averaged momentum equation. Thus, with these two methods, it is possible to obtain all of the relevant effective properties to fully characterize graphite foams and perform volume-averaged simulations of their flow and thermal behaviour.

Thus, the purpose of the present work is to obtain direct simulation results for an idealized spherical void phase foam geometry, proposed by Yu et al. [14], and then apply the closure methods proposed in DeGroot and Straatman [17] and Whitaker [18] to obtain results for all relevant effective properties. As such, we will first outline the relevant governing equations and the associated closure problems which must be solved to close the

volume-averaged equations. Next, we will present results for the closure of the momentum equation which results in the permeability and non-Darcy drag terms. Of particular interest is the non-Darcy drag term, which is typically modeled as a quadratic function of the Reynolds number and is characterized using the Forchheimer coefficient, since there is some evidence that this term may in fact be cubic with respect to Reynolds number [19–21]. We then present results for the effective thermal properties, which are the thermal dispersion conductivity tensor, the modified convecting velocity, and the interfacial Nusselt number. Special attention is paid to modeling thermal dispersion since it is typically modeled as a simple function of the Péclet number and there is evidence that this may be an oversimplification of the physics for complex three-dimensional structures such as graphite foams [16]. Finally, results based on volume-averaged simulations are presented to compare the present dispersion model with that of Calmidi and Mahajan [15] to highlight the differences arising from the different models.

## 3.2 Governing Equations and Closure

### 3.2.1 Pore-Level Governing Equations

At the pore level, the flow and thermal fields are governed by the standard mass, momentum, and energy conservation equations for a general continuum. The continuity and Navier-Stokes equations are given by

$$\nabla \cdot \mathbf{u} = 0 \quad (3.1)$$

and

$$\rho_f \left( \frac{\partial \mathbf{u}}{\partial t} + \mathbf{u} \cdot \nabla \mathbf{u} \right) = -\nabla p + \mu_f \nabla^2 \mathbf{u} \quad (3.2)$$

and are used to directly compute the pore-level flow field required for closure of the relevant volume-averaged equations. The equations governing the conservation of energy in the

fluid and solid phases are given as

$$\rho_f c_{p,f} \left( \frac{\partial T_f}{\partial t} + \mathbf{u} \cdot \nabla T_f \right) = k_f \nabla^2 T_f \quad (3.3)$$

and

$$\rho_s c_s \frac{\partial T_s}{\partial t} = k_s \nabla^2 T_s, \quad (3.4)$$

respectively, where viscous dissipation in the fluid phase is neglected. Also note that Eqs. 3.1–3.4 are the pore-level governing equations from which the volume-averaged equations are to be derived.

### 3.2.2 The Method of Volume-Averaging

The method of volume-averaging is a procedure by which the partial differential equations describing the flow and thermal fields in a general medium may be integral-averaged over many pores of a porous medium to obtain a new set of governing equations in terms of quantities averaged over many pores. In the paragraphs to follow, the basic definitions relevant to volume-averaging transport equations are briefly outlined. For further details regarding the method of volume averaging, see [10, 17, 22–25].

The definition of the extrinsic volume-average of a quantity  $\phi_k$ , over the volume  $V$  containing fluid and solid volumes  $V_f$  and  $V_s$ , is given by

$$\langle \phi_k \rangle = \frac{1}{V} \int_{V_k} \phi_k dV, \quad (3.5)$$

where  $k \in \{f, s\}$  denotes the phase in which the quantity  $\phi_k$  is defined. Alternatively, the intrinsic average is defined as

$$\langle \phi_k \rangle^k = \frac{1}{V_k} \int_{V_k} \phi_k dV, \quad (3.6)$$

which is an average over a single phase only. The two types of averages are related through

the porosity,  $\varepsilon = V_f/V$ , according to

$$\langle \phi_k \rangle = \begin{cases} \varepsilon \langle \phi_f \rangle^f & \text{if } k = f \\ (1 - \varepsilon) \langle \phi_s \rangle^s & \text{if } k = s \end{cases}. \quad (3.7)$$

To convert averages of derivatives to derivatives of averages, the ‘spatial averaging theorem’ [10, 24, 25] is employed. For the gradient operator, this theorem is stated as

$$\langle \nabla \phi_k \rangle = \nabla \langle \phi_k \rangle + \frac{1}{V} \int_{A_{kl}} \phi_k \mathbf{n}_{kl} dA, \quad (3.8)$$

where  $k, l \in \{f, s\}$ ,  $k \neq l$ , and the unit-normal vector  $\mathbf{n}_{kl}$  is oriented from the  $k$ -phase to the  $l$ -phase and  $A_{kl}$  is the area contained within  $V$  forming the intersection of  $V_k$  and  $V_l$ . Analogous to Eq. 3.8, the spatial averaging theorem for the divergence of a vector or second-rank tensor,  $\mathbf{a}_k$ , is given as

$$\langle \nabla \cdot \mathbf{a}_k \rangle = \nabla \cdot \langle \mathbf{a}_k \rangle + \frac{1}{V} \int_{A_{kl}} \mathbf{a}_k \cdot \mathbf{n}_{kl} dA. \quad (3.9)$$

Note that in Eqs. 3.8 and 3.9 the subscripts denote either the fluid or solid phase, thus no summation is implied over repeated indices.

To simplify volume-averages of products of variables a quantity  $\phi_k$  may be decomposed into its intrinsic volume-average and a pore-level spatial deviation  $\tilde{\phi}_k$ . The quantity  $\phi_k$  is then expressed as

$$\phi_k = \langle \phi_k \rangle^k + \tilde{\phi}_k, \quad (3.10)$$

leading to the volume-average of a product of variables,  $\phi_{k,1}$  and  $\phi_{k,2}$ , being defined as

$$\langle \phi_{k,1} \phi_{k,2} \rangle = \frac{1}{\varepsilon_k} \langle \phi_{k,1} \rangle \langle \phi_{k,2} \rangle + \langle \tilde{\phi}_{k,1} \tilde{\phi}_{k,2} \rangle, \quad (3.11)$$

where all terms are expressed using extrinsic averages and the  $k$ -phase porosity,  $\varepsilon_k = V_k/V$ , which is introduced so that results are general to both fluid- and solid-phase averages.

### 3.2.3 Volume-Averaged Mass and Momentum Equations

To obtain the volume-averaged mass and momentum equations, Eqs. 3.1 and 3.2 are extrinsically volume-averaged, for a constant-porosity medium, to yield [25]

$$\nabla \cdot \langle \mathbf{u} \rangle = 0 \quad (3.12)$$

and

$$\begin{aligned} \rho_f \left( \frac{\partial \langle \mathbf{u} \rangle}{\partial t} + \frac{\langle \mathbf{u} \rangle}{\varepsilon} \cdot \nabla \langle \mathbf{u} \rangle \right) = & -\varepsilon \nabla \langle p \rangle^f + \mu_f \nabla^2 \langle \mathbf{u} \rangle \\ & + \frac{1}{V} \int_{A_{fs}} (-\tilde{p} \mathbf{n}_{fs} + \mu_f \nabla \tilde{\mathbf{u}} \cdot \mathbf{n}_{fs}) dA - \rho_f \nabla \cdot \langle \tilde{\mathbf{u}} \tilde{\mathbf{u}} \rangle. \end{aligned} \quad (3.13)$$

Note that the spatial averaging theorem as well as the spatial decomposition given in Eq. 3.11 are required to arrive at Eq. 3.13. In its present form, Eq. 3.13 is of limited practical value because it depends on the unknown pore-level spatial deviations  $\tilde{p}$  and  $\tilde{\mathbf{u}}$ . The closure of these equations, which involves characterization of these unknown terms will be discussed next.

### 3.2.4 Closure of the Volume-Averaged Momentum Equation

To close Eq. 3.13, we follow the approach of Whitaker [18] in which transport equations for the spatial deviations are derived by subtracting Eq. 3.12 from Eq. 3.1 and subtracting Eq. 3.13, divided by  $\varepsilon$ , from Eq. 3.2. Various scaling arguments are made and the following equation is derived for the pressure and velocity deviations:

$$\rho_f \mathbf{u} \cdot \nabla \tilde{\mathbf{u}} = -\nabla \tilde{p} + \mu_f \nabla^2 \tilde{\mathbf{u}} - \frac{1}{V_f} \int_{A_{fs}} (-\tilde{p} \mathbf{n}_{fs} + \mu_f \nabla \tilde{\mathbf{u}} \cdot \mathbf{n}_{fs}) dA. \quad (3.14)$$

Then, Whitaker [18] has proposed the following constitutive equations for  $\tilde{\mathbf{u}}$  and  $\tilde{p}$ :

$$\tilde{\mathbf{u}} = \mathbf{M} \cdot \langle \mathbf{u} \rangle^f + \mathbf{v}, \quad \tilde{p} = \mu_f \mathbf{m} \cdot \langle \mathbf{u} \rangle^f + \xi, \quad (3.15a,b)$$

where  $\mathbf{M}$  is a second-rank tensor and  $\mathbf{m}$  is a vector, both of which are functions of position. Whitaker [18] proves that  $\mathbf{v}$  is zero and  $\xi$  is constant, such that it does not pass through any integrals and is therefore inconsequential to the solution of the closure problem. Whitaker [18] then makes substitutions which separate the problem into a part which depends only on pore geometry and a part which depends on the flow field. These substitutions are summarized as

$$\mathbf{m} = \mathbf{a} + \mathbf{c}, \quad \mathbf{M} = \mathbf{A} + \mathbf{C}, \quad (3.16a,b)$$

where  $\mathbf{a}$  and  $\mathbf{A}$  are by definition only dependent on the pore geometry since the inertial terms are dropped from the equations governing the  $\mathbf{a}$  and  $\mathbf{A}$  fields. Further, in order to eliminate integral terms from the closure problems, Whitaker [18] makes substitutions as follows:

$$\mathbf{d} = \varepsilon^{-1} \mathbf{a} \cdot \mathbf{K}, \quad \mathbf{D} = \varepsilon^{-1} (\mathbf{A} + \mathbf{I}) \cdot \mathbf{K}, \quad \mathbf{H}^{-1} = \mathbf{K}^{-1} \cdot (\mathbf{I} + \mathbf{F}), \quad (3.17a,b,c)$$

$$\mathbf{l} = \varepsilon^{-1} \mathbf{m} \cdot \mathbf{H}, \quad \mathbf{L} = \varepsilon^{-1} (\mathbf{M} + \mathbf{I}) \cdot \mathbf{H}, \quad (3.17d,e)$$

where  $\mathbf{I}$  is the identity matrix,  $\mathbf{K}$  is the Darcian permeability tensor, and  $\mathbf{F}$  is the non-Darcy drag tensor. Then, to obtain  $\mathbf{K}$  we first solve the boundary-value problem

$$\nabla \cdot \mathbf{D} = \mathbf{0} \quad (3.18a)$$

$$-\nabla \mathbf{d} + \nabla^2 \mathbf{D} + \mathbf{I} = \mathbf{0}, \quad (3.18b)$$

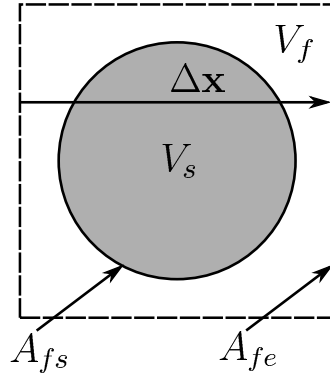


**Figure 3.2:** An illustration of a periodic unit-cell for an array of cylinders with the relevant geometric parameters indicated.

subject to the boundary conditions

$$\mathbf{D} = \mathbf{0}, \text{ on } A_{fs} \quad (3.19a)$$

$$\mathbf{D}(\mathbf{x}_{in} + \Delta\mathbf{x}) = \mathbf{D}(\mathbf{x}_{in}), \text{ on } A_{fe} \quad (3.19b)$$

$$\mathbf{d}(\mathbf{x}_{in} + \Delta\mathbf{x}) = \mathbf{d}(\mathbf{x}_{in}), \text{ on } A_{fe}, \quad (3.19c)$$

where  $A_{fe}$  is the area on the periodic faces of the unit-cell under consideration and  $\Delta\mathbf{x}$  refers to the spatial period, as shown in Fig. 3.2. The permeability tensor is then obtained through integration of the computed  $\mathbf{D}$  field according to

$$\mathbf{K} = \varepsilon \langle \mathbf{D} \rangle^f. \quad (3.20)$$

To obtain the non-Darcy drag tensor, we solve

$$\nabla \cdot \mathbf{L} = \mathbf{0} \quad (3.21a)$$

$$\left( \frac{\rho_f \mathbf{u}}{\mu_f} \right) \cdot \nabla \mathbf{L} = -\nabla \mathbf{I} + \nabla^2 \mathbf{L} + \mathbf{I}, \quad (3.21b)$$

subject to the boundary conditions

$$\mathbf{L} = \mathbf{0}, \text{ on } A_{fs} \quad (3.22a)$$

$$\mathbf{L}(\mathbf{x}_{in} + \Delta\mathbf{x}) = \mathbf{L}(\mathbf{x}_{in}), \text{ on } A_{fe} \quad (3.22b)$$

$$\mathbf{l}(\mathbf{x}_{in} + \Delta\mathbf{x}) = \mathbf{l}(\mathbf{x}_{in}), \text{ on } A_{fe}, \quad (3.22c)$$

such that the non-Darcy drag tensor,  $\mathbf{F}$ , is defined by the equations:

$$\mathbf{H} = \varepsilon \langle \mathbf{L} \rangle^f, \quad \mathbf{F} = \mathbf{K} \cdot \mathbf{H}^{-1} - \mathbf{I}. \quad (3.23a,b)$$

Note that the closure problems given in Eqs. 3.18 and 3.21 are similar in form to the steady forms of the Stokes and Navier-Stokes equations with source terms, respectively, such that any solution technique for these equations that incorporates periodic boundary conditions can easily be adapted to the solution of Eqs. 3.18 and 3.21.

Whitaker [18] has shown that  $\mathbf{K}$  must be symmetric. In the case where pore geometries exhibit symmetry about all three coordinate planes, it can be further shown that  $\mathbf{K}$  is diagonal. Additionally, if the flow field is similar in all three coordinate directions (i.e. flow is at a 45 degree angle to all positive axes), then the tensor  $\mathbf{H}$  will also be symmetric with all diagonal components being equal to one another and all off-diagonal components being equal to one another. In such cases with geometric as well as flow field symmetry, only a single row or column of the tensors  $\mathbf{D}$  and  $\mathbf{L}$  needs to be evaluated using solutions to Eqs. 3.18 and 3.21 in order to obtain the diagonal components of  $\mathbf{K}$  as well as the value of the diagonal and off-diagonal components of  $\mathbf{H}$ .

Once  $\mathbf{K}$  and  $\mathbf{F}$  are evaluated, the closed form of the volume-averaged momentum equa-

tion is given as

$$\rho_f \left( \frac{\partial \langle \mathbf{u} \rangle}{\partial t} + \frac{\langle \mathbf{u} \rangle}{\varepsilon} \cdot \nabla \langle \mathbf{u} \rangle \right) = -\varepsilon \nabla \langle p \rangle^f + \mu_f \nabla^2 \langle \mathbf{u} \rangle - \varepsilon \mu_f \mathbf{K}^{-1} \cdot \langle \mathbf{u} \rangle - \varepsilon \mu_f \mathbf{K}^{-1} \cdot \mathbf{F} \cdot \langle \mathbf{u} \rangle, \quad (3.24)$$

where the  $\rho_f \nabla \cdot \langle \tilde{\mathbf{u}} \tilde{\mathbf{u}} \rangle$  term has been neglected since in regions away from bounding surfaces,  $\langle \tilde{\mathbf{u}} \tilde{\mathbf{u}} \rangle$  is constant from cell-to-cell when the flow is periodic. Also note that if  $\mathbf{K}$  and  $\mathbf{F}$  are diagonal and  $\mathbf{F}$  is a linear function of  $\langle \mathbf{u} \rangle$ , the empirically closed equation of Vafai and Tien [26] is recovered by defining the Forchheimer coefficient,  $c_f$ , according to

$$F_{xx} = \frac{\rho_f |\langle \mathbf{u} \rangle| \sqrt{K}}{\mu_f} c_f = Re_K c_f, \quad (3.25)$$

where  $F_{xx}$  is the diagonal component of  $\mathbf{F}$  when the flow is in the  $x$ -direction and  $Re_K$  is the Reynolds number based on the square root of the permeability as the length-scale.

The advantages of the approach described in this section are twofold: (i) the computed permeability tensor represents the “true permeability” in that it depends only on pore geometry, and is thus not influenced by the effects of inertia and (ii) the non-Darcy drag tensor, representing the remaining drag, is computed in general terms making it quite simple to determine its dependence on Reynolds number.

### 3.2.5 Volume-Averaged Energy Equations

The volume-averaged energy equations are derived by averaging Eqs. 3.3 and 3.4, yielding

$$\rho_f c_{p,f} \left[ \varepsilon \frac{\partial \langle T_f \rangle^f}{\partial t} + \langle \mathbf{u} \rangle \cdot \nabla \langle T_f \rangle^f \right] = \varepsilon k_f \nabla^2 \langle T_f \rangle^f + \frac{1}{V} \int_{A_{fs}} k_f \nabla \tilde{T}_f \cdot \mathbf{n}_{fs} dA - \varepsilon \rho_f c_{p,f} \nabla \langle \tilde{\mathbf{u}} \tilde{T}_f \rangle^f \quad (3.26)$$

and

$$(1 - \varepsilon)\rho_s c_s \frac{\partial \langle T_s \rangle^s}{\partial t} = (1 - \varepsilon)k_s \nabla^2 \langle T_s \rangle^s + \nabla \cdot \left( \frac{1}{V} \int_{A_{fs}} k_s \tilde{T}_s \mathbf{n}_{sf} dA \right) + \frac{1}{V} \int_{A_{fs}} k_s \nabla \tilde{T}_s \cdot \mathbf{n}_{sf} dA, \quad (3.27)$$

where the simplifications listed in [17] based on the high solid-to-fluid phase conductivity ratio have been made in the fluid energy equation. Note that the final term in Eq. 3.26 represents thermal dispersion, while the second last term in Eq. 3.26 and the last term in Eq. 3.27 represent heat exchange between phases. Also note that the tortuosity term has been neglected in the fluid energy equation since convection dominates conduction in the fluid [17, 27]. In the solid energy equation, the tortuosity term is retained (as the second last term in Eq. 3.27) since this term can be significant in forming the effective solid conductivity [28]. Again, these equations are not particularly amiable to solution, since they depend on the unresolved pore-level fields. Closure of the energy equations will be discussed next.

### 3.2.6 Closure of the Volume-Averaged Energy Equations

As in the closure of the volume-averaged momentum equations, we subtract the volume-averaged energy equation for the fluid phase, divided by  $\varepsilon$ , from the energy equation for a fluid continuum. This equation is simplified using the scaling arguments given in [17], resulting in

$$\rho_f c_{p,f} \left( \mathbf{u} \cdot \nabla \tilde{T}_f + \tilde{\mathbf{u}} \cdot \nabla \langle T_f \rangle^f \right) = k_f \nabla^2 \tilde{T}_f - \frac{1}{V_f} \int_{A_{fs}} k_f \nabla \tilde{T}_f \cdot \mathbf{n}_{fs} dA. \quad (3.28)$$

The constitutive equation for the temperature deviations is given as [17]

$$\tilde{T}_f = \mathbf{b} \cdot \nabla \langle T_f \rangle^f + \psi \left( T_w - \langle T_f \rangle^f \right), \quad (3.29)$$

where  $T_w$  is the constant wall temperature on  $A_{fs}$ . The resulting closure problems that must be solved for the two closure parameters  $\mathbf{b}$  and  $\psi$  are given as [17]

$$\rho_f c_{p,f} (\tilde{\mathbf{u}} + \mathbf{u} \cdot \nabla \mathbf{b}) = k_f \nabla^2 \mathbf{b} - \frac{1}{V_f} \int_{A_{fs}} k_f \nabla \mathbf{b} \cdot \mathbf{n}_{fs} dA, \quad (3.30)$$

subject to

$$\mathbf{b} = \mathbf{0}, \text{ on } A_{fs} \quad (3.31a)$$

$$\mathbf{b}(\mathbf{x}_{in} + \Delta \mathbf{x}) = \mathbf{b}(\mathbf{x}_{in}), \text{ on } A_{fe} \quad (3.31b)$$

$$\langle \mathbf{b} \rangle^f = \mathbf{0}, \quad (3.31c)$$

as well as

$$\rho_f c_{p,f} \mathbf{u} \cdot \nabla \psi = k_f \nabla^2 \psi - \frac{1}{V_f} \int_{A_{fs}} k_f \nabla \psi \cdot \mathbf{n}_{fs} dA, \quad (3.32)$$

subject to

$$\psi = 1, \text{ on } A_{fs} \quad (3.33a)$$

$$\psi(\mathbf{x}_{in} + \Delta \mathbf{x}) = \psi(\mathbf{x}_{in}), \text{ on } A_{fe} \quad (3.33b)$$

$$\langle \psi \rangle^f = 0. \quad (3.33c)$$

Noting that  $T_w = \langle T_s \rangle^s$  within any averaging volume, the closed volume-averaged energy equation in the fluid phase is given by

$$\rho_f c_{p,f} \left( \varepsilon \frac{\partial \langle T_f \rangle^f}{\partial t} + \bar{\mathbf{u}} \cdot \nabla \langle T_f \rangle^f \right) = \nabla \cdot \left( \mathbf{k}_{fe} \cdot \nabla \langle T_f \rangle^f \right) + a_{fs} h_{fs} \left( \langle T_s \rangle^s - \langle T_f \rangle^f \right), \quad (3.34)$$

where the convecting velocity is defined by

$$\bar{\mathbf{u}} = \langle \mathbf{u} \rangle - \varepsilon \langle \tilde{\mathbf{u}} \psi \rangle^f - \frac{\varepsilon}{V_f} \int_{A_{fs}} \frac{k_f}{\rho_f c_{p,f}} \nabla \mathbf{b} \cdot \mathbf{n}_{fs} dA \quad (3.35)$$

and the effective conductivity tensor is defined by

$$\mathbf{k}_{fe} = \varepsilon k_f \mathbf{I} + \varepsilon \mathbf{k}_d, \quad (3.36)$$

where the dispersion conductivity tensor is given by

$$\mathbf{k}_d = -\rho_f c_{p,f} \langle \tilde{\mathbf{u}} \mathbf{b} \rangle^f. \quad (3.37)$$

Finally, the interfacial heat transfer coefficient is defined by

$$a_{fs} h_{fs} = \frac{\varepsilon}{V_f} \int_{A_{fs}} k_f \nabla \psi \cdot \mathbf{n}_{fs} dA. \quad (3.38)$$

Note that due to the fact that the solid region of graphite foams may be highly anisotropic and that the solid phase effective conductivity can differ quite substantially from  $(1 - \varepsilon)k_s$ , it is recommended that the solid energy equation be closed using an appropriate empirical or analytical model for the effective solid conductivity which takes into account the tortuosity term and any anisotropy in the material. The interfacial exchange term, however, is closed using Eq. 3.38 as in the fluid energy equation. The closed form of the volume-averaged energy equation in the solid phase is then given by

$$(1 - \varepsilon) \rho_s c_s \frac{\partial \langle T_s \rangle^s}{\partial t} = \nabla \cdot (\mathbf{k}_{se} \cdot \nabla \langle T_s \rangle^s) - a_{fs} h_{fs} (\langle T_s \rangle^s - \langle T_f \rangle^f), \quad (3.39)$$

where  $\mathbf{k}_{se}$  is the effective solid conductivity tensor.

### 3.3 Non-dimensionalization and Parameters of Study

In order to provide more general results and to provide guidance regarding the relevant parameters of study, the volume-averaged governing equations, given by Eqs. 3.12, 3.24, and 3.34 are non-dimensionalized. Neglecting unsteady terms, the required dimensionless

variables are

$$\mathbf{x}^* = \frac{\mathbf{x}}{d}, \quad \langle \mathbf{u} \rangle^* = \frac{\langle \mathbf{u} \rangle}{U}, \quad \bar{\mathbf{u}}^* = \frac{\bar{\mathbf{u}}}{U}, \quad \langle p \rangle^{f*} = \frac{\langle p \rangle^f}{\rho_f U^2}, \quad (3.40a,b,c,d)$$

$$\theta_f = \frac{\langle T_f \rangle^f - T_{in}}{T_w - T_{in}}, \quad \theta_s = \frac{\langle T_s \rangle^s - T_{in}}{T_w - T_{in}}. \quad (3.40e,f)$$

The resulting dimensionless equations are then:

$$\nabla^* \cdot \mathbf{u}^* = 0, \quad (3.41)$$

$$\frac{\langle \mathbf{u} \rangle^*}{\varepsilon} \cdot \nabla^* \langle \mathbf{u} \rangle^* = -\varepsilon \nabla^* \langle p \rangle^{f*} + \frac{1}{Re_d} [\nabla^{*2} \langle \mathbf{u} \rangle^* - \varepsilon d^2 \mathbf{K}^{-1} \cdot (\mathbf{I} + \mathbf{F}) \cdot \langle \mathbf{u} \rangle^*], \quad (3.42)$$

$$\bar{\mathbf{u}}^* \cdot \nabla^* \theta_f = \frac{1}{Re_d Pr} \left[ \nabla^* \cdot \left( \frac{\mathbf{k}_{fe}}{k_f} \cdot \nabla^* \theta_f \right) + Nu_{fs} (\theta_s - \theta_f) \right], \quad (3.43)$$

and

$$\nabla^* \cdot \left( \frac{\mathbf{k}_{se}}{k_f} \cdot \nabla^* \theta_s \right) = Nu_{fs} (\theta_s - \theta_f), \quad (3.44)$$

where  $\nabla^* = \partial/\partial x_1^* \mathbf{i} + \partial/\partial x_2^* \mathbf{j} + \partial/\partial x_3^* \mathbf{k}$  is the dimensionless gradient operator and the relevant dimensionless groups are

$$Re_d = \frac{\rho_f U d}{\mu_f}, \quad Pr = \frac{c_{p,f} \mu_f}{k_f}, \quad Nu_{fs} = \frac{a_{fs} h_{fs} d^2}{k_f}. \quad (3.45a,b,c)$$

By inspection of Eqs. 3.41 to 3.44 we note nine dimensionless parameters, namely,  $Re_d$ ,  $Pr$ ,  $Nu_{fs}$ ,  $d^2 \mathbf{K}^{-1}$ ,  $\mathbf{F}$ ,  $\bar{\mathbf{u}}^*$ ,  $\mathbf{k}_{fe}/k_f$ ,  $\mathbf{k}_{se}/k_f$ , and  $\varepsilon$ . By specifying the pore geometry, fluid properties, and boundary conditions, the parameters  $\varepsilon$ ,  $Re_d$ , and  $Pr$  are fixed. As mentioned, the effective solid conductivity is determined by an appropriate model, fixing  $\mathbf{k}_{se}/k_f$ . The remaining parameters,  $Nu_{fs}$ ,  $d^2 \mathbf{K}^{-1}$ ,  $\mathbf{F}$ ,  $\bar{\mathbf{u}}^*$ , and  $\mathbf{k}_{fe}/k_f$ , are defined by the solutions to the closure problems.

In this study, we consider three different Prandtl numbers,  $Pr \in \{1, 5, 10\}$ , which cover the range of typical fluids encountered in heat transfer applications (i.e. air, water, and

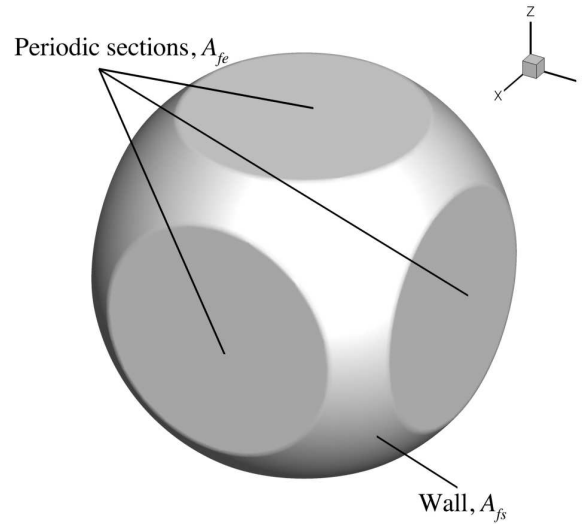


**Figure 3.3:** Schematic diagram of the computational domain for direct simulation of the pore-level fields, in this case for a graphite foam with  $\varepsilon = 0.85$ .

refrigerants). The range of Reynolds numbers considered is  $Re_d \in [1, 100]$ . Creeping flows where  $Re_d \ll 1$  are not considered herein since they are of limited practical value in heat transfer, while flows above  $Re_d = 100$  are not considered due to the onset of transient/turbulent effects.

The pore geometry under consideration is based on an idealized model of the pore structure for graphite foams, proposed by Yu et al. [14] and shown previously in Fig. 3.1. This model considers the pore shape as a repeating cubic structure of size  $H$ , wherein the solid region is formed by removing a spherical void region of diameter  $d$  from the cube. A schematic diagram of the computational domain is shown in Fig. 3.3. In this study, porosities  $\varepsilon \in \{0.80, 0.85, 0.90\}$  are considered, which cover the primary region of interest for heat transfer applications. Below  $\varepsilon = 0.80$ , the smaller pore windows lead to an exceedingly high pressure drop, while above  $\varepsilon = 0.90$ , foams are difficult to manufacture as the ligaments become small. For the porosities considered, the ratios of the pore diameters to the unit-cube size are  $d/H \in \{1.2018, 1.2491, 1.3051\}$ .

### 3.4 Simulation Details and Grid Resolution

In all, the flow field and momentum closure problem is solved for 66 cases and the thermal closure problem is solved for 198 cases (as a result of the three Prandtl numbers considered). For each unique pair of porosity and Reynolds number, the first case involved the solution of the flow field as well as the thermal and momentum closure problems. For the subsequent Prandtl number cases, the flow solution was read from the previously generated data files and only the thermal closure problem was solved. Generally, cases were run using 64 processors in parallel. Cases in which the flow field and both closure problems were solved took about 8–10 hours, while only solving the thermal closure problem took about 2–3 hours. Thus, the total computational time expended obtaining the present results is approximately 6–8 CPU years (i.e. the time taken to run all cases sequentially on a single processor).

One factor leading to the large computational requirements is the sensitivity of the closure problems to the accuracy of the flow field computation, which require that the specified tolerances be set quite restrictively. The maximum normalized non-linear residual in a converged solution was specified as  $10^{-10}$ , the maximum relative difference between the actual and specified mass flux through the periodic faces was set to  $10^{-9}$ , and the maximum value of  $\langle \mathbf{b} \rangle^f$  and  $\langle \psi \rangle^f$  in the root-finding algorithm to obtain the correct source terms (as described in [17]), was specified as  $10^{-12}$ . Thus, all solutions presented herein are well-converged and would not improve with lower tolerance settings.

Finally, before moving on to a discussion of the results, we wish to make a comment with regards to the coordinate system employed and the flow direction imposed. Within the periodic unit-cells considered, the flow field is taken to be periodic in all three coordinate directions ( $X, Y, Z$ ), such that the average velocity vector makes equal angles with all coordinate axes. Karimian and Straatman [16, 29] found that taking the flow to enter the pores on such an angle is of greatest practical interest, since it represents somewhat of an average flow condition for randomly oriented pores and produces the best agreement with

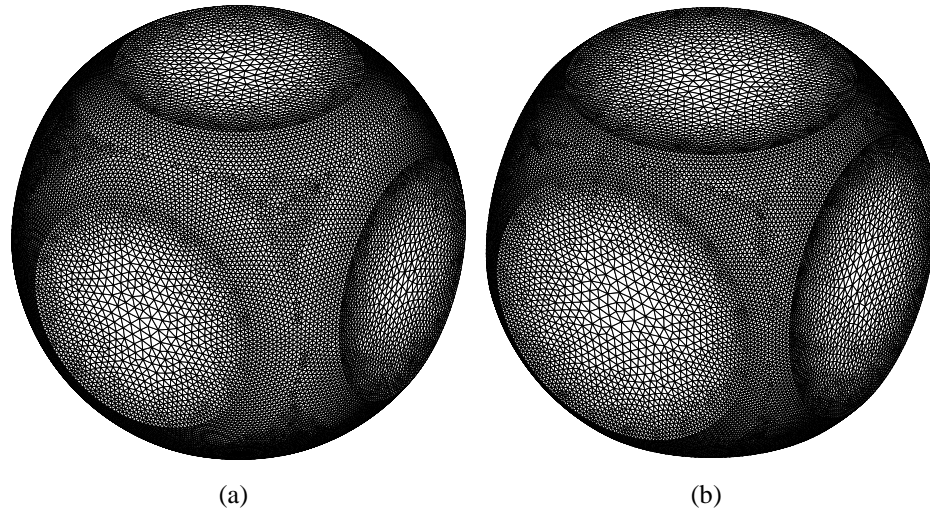


**Figure 3.4:** A plot of the tetrahedral grids used for the (a)  $\varepsilon = 0.8$  and (b)  $\varepsilon = 0.9$  cases generated with a grid size at the wall of  $\delta_w = 0.0118H$  (where  $H$  is the unit-cube size), a growth rate of 8% per row, and a maximum grid size of  $\delta_{max} = 3\delta_w$ .

experiments. Thus, all effective properties are obtained based on this macroscopic flow direction. While this coordinate system is convenient for computation and implementation of the periodic boundary conditions, it is more customary to discuss quantities in a coordinate system with the primary axis in the direction of the volume-averaged velocity vector. Therefore, we report values which have been transformed to this coordinate system, which we refer to as the ‘flow-oriented’ system  $(x, y, z)$  by the appropriate change of basis.

A grid resolution study was conducted to ensure that the presented solutions are independent of the particular grid used for the simulations. In this study, the total number of control volumes in subsequent refinements was approximately doubled until all required parameters changed by less than a specified tolerance. It was found that grid-independent solutions were obtained for grids generated using a characteristic grid size of  $\delta_w = 0.0118H$  at the wall with a growth rate of 8% per row, and a maximum grid size of  $\delta_{max} = 3\delta_w$ . These grids are shown in Fig. 3.4 for the  $\varepsilon = \{0.8, 0.9\}$  cases and contained 1,000,592 and 890,720 control volumes, respectively. Upon doubling the number of volumes in the grids, it was found that the Nusselt number was grid-independent to within 2%, while all other variables were grid-independent to within 1%, which is considered acceptable.

**Table 3.1:** Summary of the dimensionless permeabilities obtained numerically for  $\varepsilon \in \{0.80, 0.85, 0.90\}$ .

Porosity, $\varepsilon$	$K/d^2$
0.80	$9.09 \times 10^{-3}$
0.85	$1.24 \times 10^{-2}$
0.90	$1.70 \times 10^{-2}$

### 3.5 Results for Momentum Closure

Based on the momentum closure model described previously, the permeability and non-Darcy drag tensors are obtained across the range of porosity and Reynolds numbers considered. Considering steady, uniform flow in the  $x$ -direction, the closed volume-averaged momentum equation, Eq. 3.24, reduces to

$$-\frac{d\langle p \rangle^f}{dx} = \frac{\mu_f \langle u \rangle}{K_{xx}} + \frac{\mu_f \langle u \rangle F_{xx}}{K_{xx}}, \quad (3.46)$$

which is essentially an extended version of Darcy's law where the non-Darcy drag term has been left in general terms with  $F_{xx}$  characterizing the deviation from Darcy's law. In fact,  $F_{xx}$  represents the ratio of the non-Darcy term to the Darcy term. Rearranging Eq. 3.46 to solve for  $F_{xx}$ , we find

$$F_{xx} = -\frac{K_{xx}}{\mu_f \langle u \rangle} \frac{d\langle p \rangle^f}{dx} - 1, \quad (3.47)$$

which can be used to compare results for  $F_{xx}$  obtained from the closure problems with the corresponding pressure drop data to assist in validating the proposed model.

Upon transformation to the flow-oriented coordinate system, the permeability tensor is diagonal with  $K_{xx} = K_{yy} = K_{zz} = K$ . The permeabilities computed for each porosity are summarized in Table 3.1, and are represented non-dimensionally by  $K/d^2$  as suggested by the dimensionless momentum equation. In Fig. 3.5,  $F_{xx}$  is plotted as a function of Reynolds number for each of the three porosities as it is obtained from the solution of the momentum closure problem as well as directly from the computed pressure drop via Eq. 3.47, where

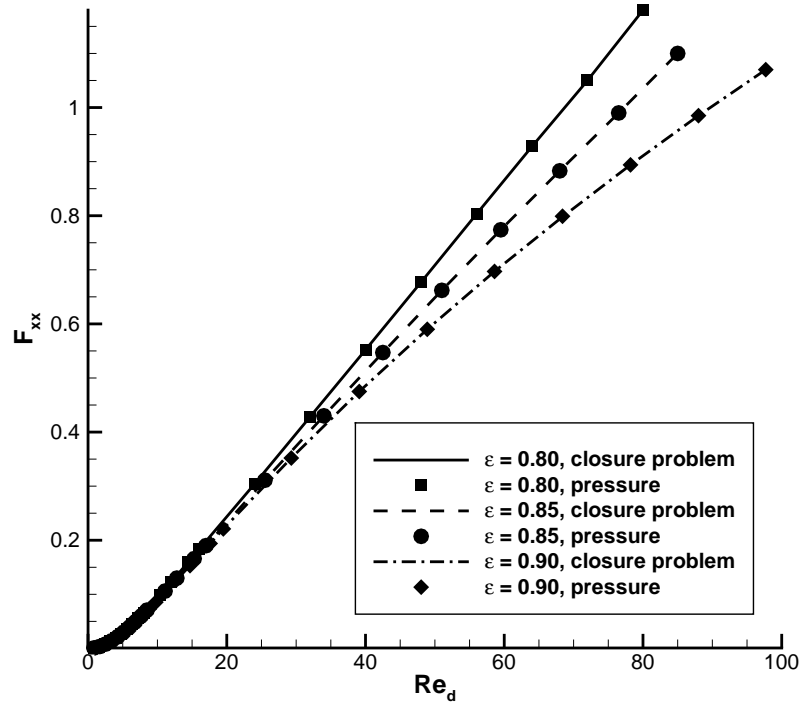


**Figure 3.5:** Plot of the non-Darcy drag term,  $F_{xx}$ , as a function of the Reynolds number obtained from the solution of the momentum closure problem in comparison to results obtained directly from the computed pressure field.

the permeabilities used to non-dimensionalize the pressure drop are those computed from the closure problem. Figure 3.5 shows excellent agreement between the results obtained from the closure problem and from the flow solution, indicating the solution to the closure problem indeed captures the required information regarding the pressure drop.

Additionally, it is observed that, in general, the non-Darcy drag term does not grow linearly with Reynolds number as it would if the second term in Eq. 3.46 was quadratic with respect to velocity, as in the Darcy-Forchheimer equation. Rather, we notice non-linear behaviour at both low and high Reynolds numbers. At low Reynolds numbers, this can be due to the effects of weak inertia [19–21] leading to a non-Darcy term that is quadratic with respect to velocity (such that the second term in Eq. 3.46 is cubic with respect to velocity). Karimian and Straatman [29] observed a similar trend at low Reynolds numbers for uni-directional flow in idealized graphite foams. Interestingly, we also observe a non-linear trend at higher Reynolds numbers, particularly for  $\epsilon \in \{0.85, 0.90\}$ .

While it is clear that there are indeed non-linear effects related to weak inertia, Fig. 3.5 indicates that for  $Re_d < 10$ , where the effects of weak inertia are most prominent, the magnitude of the non-Darcy term is less than 10% of the Darcy term. Thus, moderate errors in characterizing  $F_{xx}$  in this region, such as considering it to be a linear function, will not have a great impact on the overall pressure drop since the Darcy term is strongly dominant. To explore the relationship between the non-Darcy drag term and Reynolds number further, we have obtained models using least-squares fits for the Reynolds number ranges  $Re_d < 10$  and  $Re_d \geq 10$ , given generally by the polynomial

$$F_{xx} = a_0 + a_1 Re_d + a_2 Re_d^2 + \dots + a_n Re_d^n. \quad (3.48)$$

To ensure a physically reasonable model, with a zero non-Darcy term at zero Reynolds number,  $a_0 = 0$  for the region  $Re_d < 10$ . Results for the coefficients,  $a_n$ , along with the maximum error between the model and the actual data, are summarized in Tables 3.2 and 3.3 for linear and quadratic fits, respectively. Note that the error is given in absolute terms, since  $F_{xx}$  represents the ratio of the non-Darcy to Darcy terms, and is thus a convenient metric for the error as it is relative to the size of the Darcy term. As expected, the quadratic fits yield less error than the linear fits for all cases, since it is a higher-order model. Generally, the improvement is by an order of magnitude, except for the  $\varepsilon = 0.80$ ,  $Re_d \geq 10$  case which is close to being linear, such that the linear fit gives good results. Also, we may note that in all of the higher Reynolds number cases there are multiple  $a_n$  coefficients involved, indicating that the non-Darcy drag term cannot be adequately described as a simple  $Re_d$  relationship as commonly assumed. Further tests using linear least-squares fits over the full range of Reynolds numbers, corresponding to Forchheimer's assumption that the deviation from Darcy's law is linear, indicate that the error is higher than the previously considered cases.

Overall, it is clear that considering the non-Darcy term to be a quadratic function of

**Table 3.2:** Summary of the polynomial coefficients for the linear least-squares fits for the non-Darcy drag term,  $F_{xx}$ , along with the associated maximum absolute error.

$\varepsilon$	$Re_d$	$a_0$	$a_1$	Max. Error
0.80	$< 10$	0	$6.99 \times 10^{-3}$	$1.02 \times 10^{-2}$
0.80	$\geq 10$	$-6.54 \times 10^{-2}$	$1.55 \times 10^{-2}$	$3.74 \times 10^{-3}$
0.85	$< 10$	0	$6.99 \times 10^{-3}$	$1.15 \times 10^{-2}$
0.85	$\geq 10$	$-3.67 \times 10^{-2}$	$1.35 \times 10^{-2}$	$1.66 \times 10^{-2}$
0.90	$< 10$	0	$7.41 \times 10^{-3}$	$1.31 \times 10^{-2}$
0.90	$\geq 10$	$8.47 \times 10^{-3}$	$1.13 \times 10^{-2}$	$3.84 \times 10^{-2}$

**Table 3.3:** Summary of the polynomial coefficients for the quadratic least-squares fits for the non-Darcy drag term,  $F_{xx}$ , along with the associated maximum absolute error.

$\varepsilon$	$Re_d$	$a_0$	$a_1$	$a_2$	Max. Error
0.80	$< 10$	0	$1.46 \times 10^{-3}$	$8.27 \times 10^{-4}$	$2.21 \times 10^{-3}$
0.80	$\geq 10$	$-5.92 \times 10^{-2}$	$1.51 \times 10^{-2}$	$4.95 \times 10^{-6}$	$3.18 \times 10^{-3}$
0.85	$< 10$	0	$1.46 \times 10^{-3}$	$8.27 \times 10^{-4}$	$1.33 \times 10^{-3}$
0.85	$\geq 10$	$-5.72 \times 10^{-2}$	$1.48 \times 10^{-2}$	$-1.44 \times 10^{-5}$	$3.64 \times 10^{-3}$
0.90	$< 10$	0	$1.80 \times 10^{-3}$	$7.30 \times 10^{-4}$	$1.84 \times 10^{-3}$
0.90	$\geq 10$	$-5.71 \times 10^{-2}$	$1.49 \times 10^{-2}$	$-3.48 \times 10^{-5}$	$3.15 \times 10^{-3}$

Reynolds number, in separate low and high  $Re_d$  regimes, produces the best results. Considering the term to be a linear function of  $Re_d$  in the two flow regimes separately results in a substantial increase in error, however, relative to the size of the Darcy term, the error in  $F_{xx}$  is of the order  $10^{-2}$  or less which may be acceptable for some purposes. It also been shown that the common assumption that  $F_{xx}$  is a simple linear function of Reynolds number (leading to the Darcy-Forchheimer equation), is not particularly accurate, as previously indicated for weak inertia flows [19–21].

One may also consider how the present results for the permeability and non-Darcy drag term compare with data from experiments involving real graphite foams, for which the present model is an idealization. In general, it can be assumed that the ideal results will differ from experimental results due an imperfect characterization of the geometry. Karimian and Straatman [16] explored this issue for graphite foams and developed methods to calibrate idealized results to experimental results by considering pore blockage and solid-phase size variations. Although we do not consider such calibrations in this work, we find

it necessary to point out that this is an additional step involved in closure modelling when the idealized geometry varies from the actual geometry. The more realistic the geometric idealization is, however, the better the results from the closure problem may be. In fact, since the idealized geometry usually produces more desirable results, it is in the interest of material scientists to strive to manufacture materials which approach the homogeneity of the idealized models.

## 3.6 Results for Energy Closure

### 3.6.1 Dispersion conductivity

In general, the dimensionless effective conductivity tensor, scaled by the porosity, is diagonal and takes on the form  $\mathbf{k}_{fe}/(\epsilon k_f) = \mathbf{I} + \mathbf{k}_d/k_f$ . Thus, since this tensor is simply the addition of the identity tensor and the dimensionless dispersion conductivity tensor, it suffices to simply discuss the dispersion tensor. Also, since we are considering the flow-oriented coordinate system in which the bulk flow is in the  $x$ -direction, we may state by symmetry that  $(\mathbf{k}_d)_{yy} = (\mathbf{k}_d)_{zz}$  and simply discuss the axial ( $x$ ) and transverse ( $y$  and  $z$ ) dispersion conductivities.

Generally, the dispersion conductivity in both the axial and transverse directions is considered to be a simple function of the Péclet number,  $Pe_d$  [30–32], while, more recently, Kuwahara et al. [33, 34] have considered the dispersion conductivity to also be a function of porosity. The present results indicate that in general the dispersion conductivity is not well characterized by the Péclet number alone, rather it is a function of the Reynolds and Prandtl numbers separately, as well as the solid fraction  $(1 - \epsilon)$ . As such, we propose a model for the dimensionless dispersion conductivity as

$$\frac{k_d}{k_f} = a_0 Re_d^{a_1} Pr^{a_2} (1 - \epsilon)^{a_3}, \quad (3.49)$$

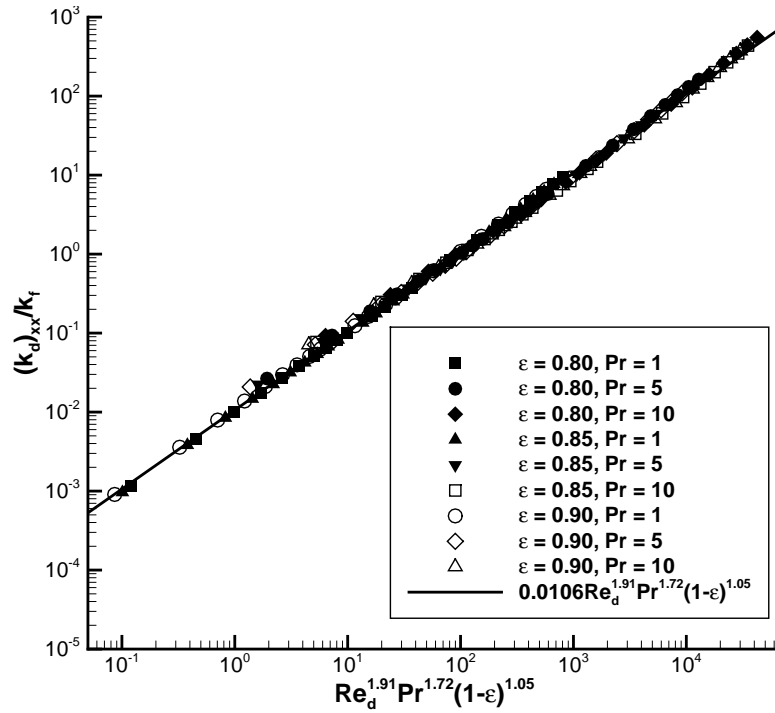


**Figure 3.6:** A plot of the dimensionless axial thermal dispersion conductivity as a function of  $Re_d^{a_1} Pr^{a_2} (1 - \epsilon)^{a_3}$ , where the coefficients  $(a_1, a_2, a_3)$  are obtained using a least-squares fit of the data.

where  $k_d$  may represent either the axial or transverse dispersion conductivity while the coefficients  $(a_0, a_1, a_2, a_3)$  are found using least-squares. In Fig. 3.6, the axial dispersion conductivity is plotted as a function of the dimensionless group  $Re_d^{1.91} Pr^{1.72} (1 - \epsilon)^{1.05}$ , obtained by a least-squares fit of the data, which shows excellent collapse of the data onto a single line. This confirms the fact that for the geometry under consideration, the axial dispersion conductivity cannot be simply considered a function of  $Pe_d^n$ . In this case we find the axial dispersion conductivity has a slightly stronger dependence on the Reynolds number than the Prandtl number as well as a roughly linear relationship with respect to the solid fraction,  $1 - \epsilon$ .

The transverse dispersion conductivity is plotted as a function of  $Pe_d$  in Fig. 3.7. In this case, performing a least-squares fit to Eq. 3.49 over the full range of the data does not result in a good fit, since there exist different behaviours within different Péclet number regimes. For  $Pe_d < 10$ , we find that the transverse dispersion conductivity is adequately

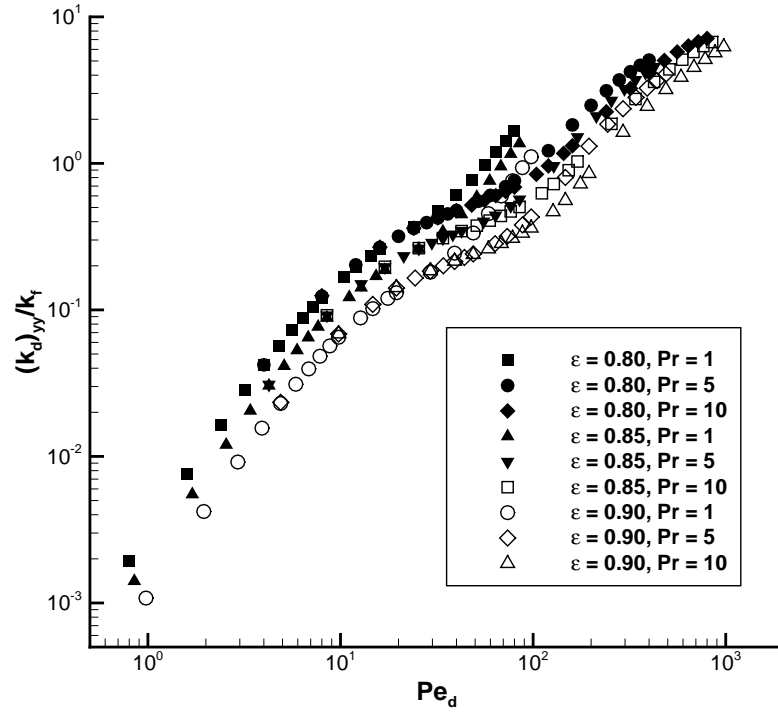
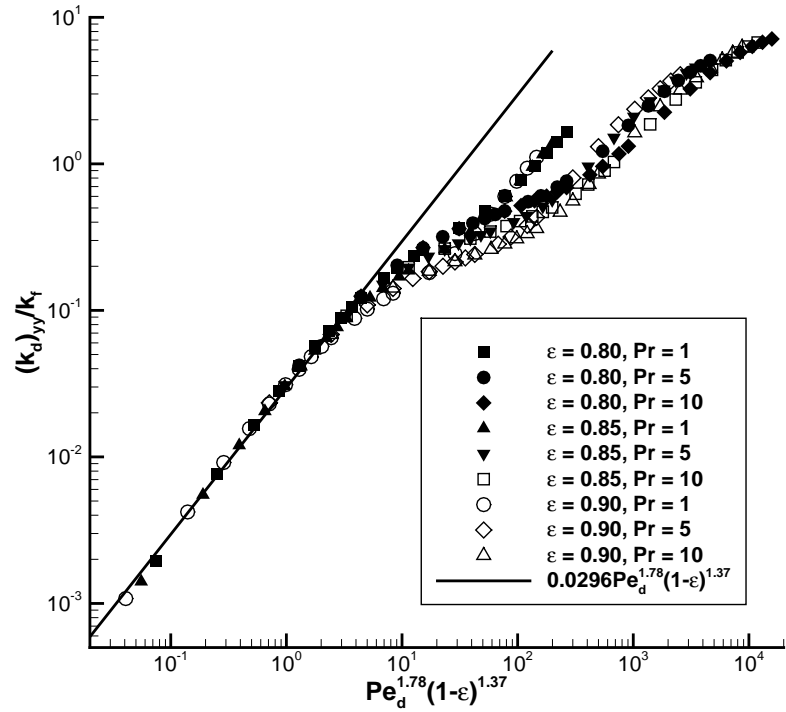


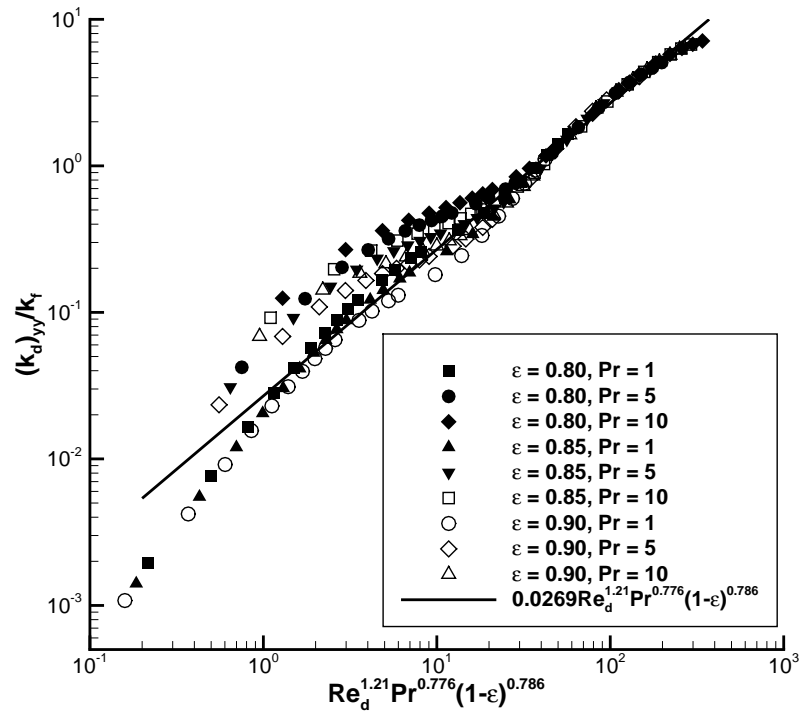
**Figure 3.7:** A plot of the dimensionless transverse thermal dispersion conductivity as a function of  $Pe_d$ .

described by the Péclet number and the solid fraction (i.e. setting  $a_1 = a_2$  in Eq. 3.49). In Fig. 3.8(a) the transverse dispersion conductivity is plotted as a function of the dimensionless group  $Pe_d^{1.78}(1 - \varepsilon)^{1.37}$ , which is found using a least-squares fit of the data for which  $Pe_d < 10$ . In this case we find good collapse of the data onto a single line at low Péclet numbers. At higher Péclet numbers, the Reynolds and Prandtl numbers needed to be considered separately in order to obtain a good fit. Results for the transverse dispersion conductivity as a function of the dimensionless group  $Re_d^{1.21}Pr^{0.776}(1 - \varepsilon)^{0.786}$  are plotted in Fig. 3.8(b). The least-squares fit in this case was obtained using data for which  $Re_d^{1.21}Pr^{0.776}(1 - \varepsilon)^{0.786} > 30$ . In this region we find generally good collapse of the data, but we also note that at the highest Péclet numbers, a different behaviour appears to be emerging.

Overall, the dispersion behaviour discovered in this work has proven to be relatively complex in comparison to the relatively simple  $Pe_d^n$  models typically observed in most of



(a)



(b)

**Figure 3.8:** Plots of the dimensionless transverse thermal dispersion conductivity as a function of the dimensionless groups  $Pe_d^{1.78}(1-\epsilon)^{1.37}$  and  $Re_d^{1.21} Pr^{0.776}(1-\epsilon)^{0.786}$ , obtained by least-squares fits for the regimes (a)  $Pe_d < 10$  and (b)  $Re_d^{1.21} Pr^{0.776}(1-\epsilon)^{0.786} > 30$ , respectively.

the literature. It is believed that much of this is due to the fact that the geometry and flow is fully three-dimensional and relatively complex in comparison to arrays of rods as is often studied in the dispersion literature.

### 3.6.2 Convecting velocity

To study the dimensionless convecting velocity,  $\bar{\mathbf{u}}^*$ , it is convenient to define the convecting velocity modification  $\bar{\mathbf{u}}'^* = \bar{\mathbf{u}}^* - \langle \mathbf{u} \rangle^*$ . The component of the convecting velocity in the  $x$ -direction is plotted in Fig. 3.9 as a function of  $Pe_d$ . Results indicate asymptotic behaviour at low Péclet numbers, followed by a gradual decrease and subsequent increase with increasing  $Pe_d$ . Overall we have found that  $\bar{\mathbf{u}}'^*$  decreases with porosity for a fixed Prandtl number. For a fixed porosity, we find very similar behaviour for  $Pr = 5$  and  $Pr = 10$ , with a smaller velocity modification being observed for  $Pr = 1$ . It is interesting to find that the convecting velocity modification is quite significant (up to 40% of the magnitude of the extrinsic velocity), given the fact that it is generally neglected when conducting volume-averaged simulations.

### 3.6.3 Interfacial Nusselt number

Next, we present results for the interfacial Nusselt number, defined by Eq. 3.45c. Results are plotted as a function of the Péclet number in Fig. 3.10. Here we note asymptotic behaviour at low  $Pe_d$ , representing the effects of molecular diffusion [16]. The low- $Pe_d$  asymptote is higher with decreasing porosity. At lower Péclet numbers, it appears that for each porosity the behaviour is independent of the Prandtl number, whereas for  $Pe_d > 40$  the Nusselt number behaviour depends on the Prandtl number. Thus, for the  $Pe_d < 40$  a model of the form  $Nu_{fs} = (a_1 + a_2 Pe_d^{a_3})(1 - \varepsilon)^{a_4}$  is proposed. A least-squares fit then reveals that a good model is

$$Nu_{fs} = (33.3 + 0.51 Pe_d^{0.85})(1 - \varepsilon)^{0.42}, \quad (3.50)$$

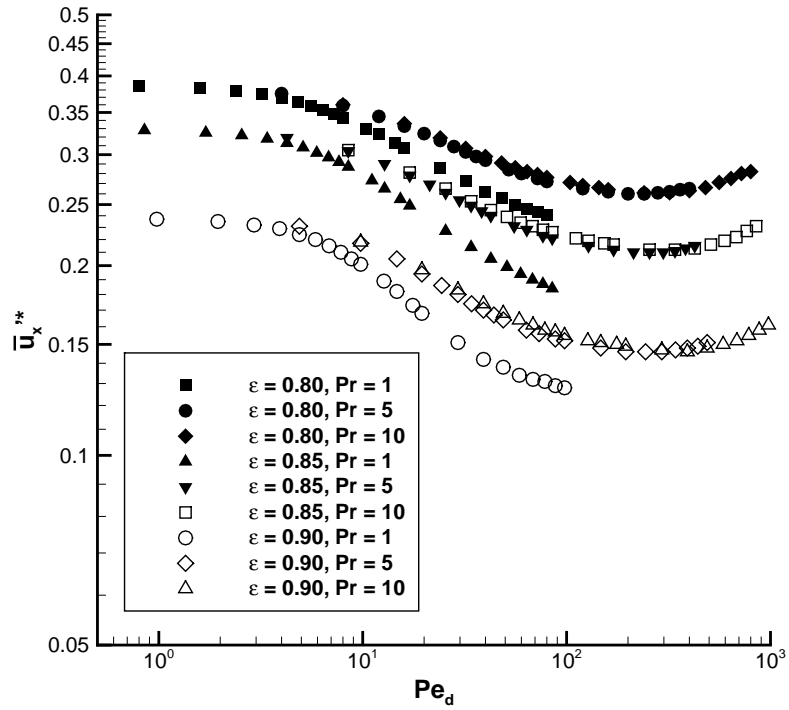


**Figure 3.9:** A plot of the dimensionless convecting velocity modification in the flow direction as a function of the Péclet number.

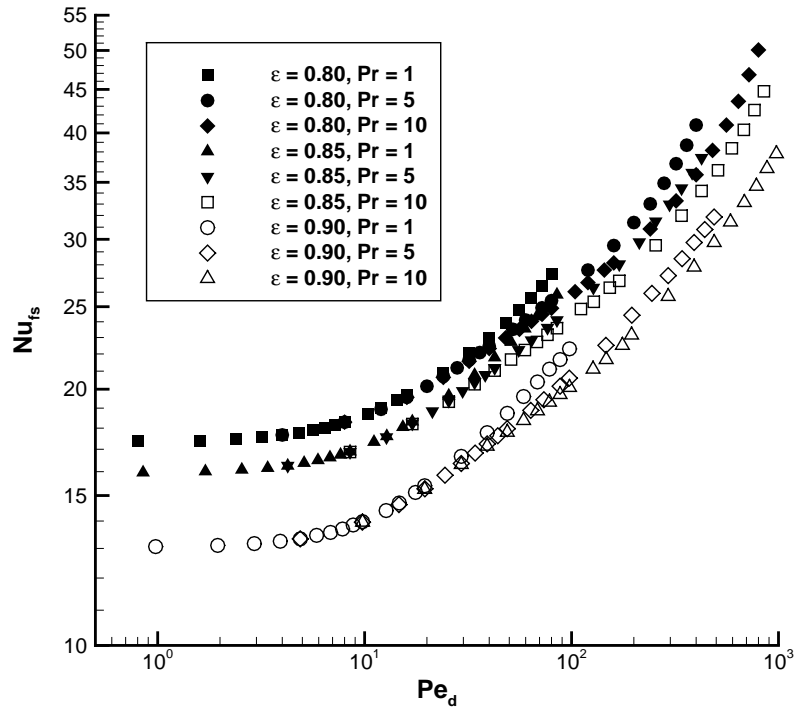


**Figure 3.10:** Plot of the interfacial Nusselt number as a function of the Péclet number.

which has a maximum error of 4.9% relative to the computed Nusselt numbers. It has been found that a model of this form is unsuitable for  $Pe > 40$ , thus a model of the form  $Nu_{fs} = (a_1 Pr^{a_2} + a_3 Re_d^{a_4} Pr^{a_5})(1 - \varepsilon)^{a_6}$  is proposed. A least-squares fit of the  $Pe_d > 40$  data reveals that a good model is

$$Nu_{fs} = (32.0Pr^{0.077} + 1.18Re_d^{0.68}Pr^{0.38})(1 - \varepsilon)^{0.42}, \quad (3.51)$$

which has a maximum error of 4.4% relative to the computed Nusselt numbers. Straatman et al. [5] proposed a model for the interfacial Nusselt number using volume-averaged simulations calibrated to experimental results. Their model took the form  $Nu_\ell = CRe_\ell^m Pr^n$ , where  $\ell$  is the appropriate characteristic length, in this case, an equivalent particle diameter. The exponents  $m$  and  $n$  were found in that work to be  $m = 0.27$  and  $n = 0.33$ . Thus, we have found a stronger dependence on Reynolds number and a similar dependence on Prandtl number in comparison to the study of [5]. In our work we also found a non-zero asymptote at low Péclet numbers, which is physically reasonable, but difficult to determine using experimental results and a calibrated volume-averaged model. Karimian and Straatman [16] also observed a non-zero Nusselt number asymptote in their study of heat transfer in graphite foams using direct pore-level simulations.

### 3.7 Comparison of Dispersion Models

With the closure relations developed, we may implement them into a volume-averaged algorithm to obtain results for bulk flow and heat transfer behaviour. Here, we use the finite-volume algorithm proposed by Betchen et al. [12] to solve the volume-averaged equations in order to compare results using our newly developed thermal dispersion model in comparison to results using the model of Calmidi and Mahajan [15], in which the dispersion conductivity is linear with respect to the Péclet number. Although this model was developed for aluminum foams, it has also been employed by Straatman et al. [5] for graphite foams

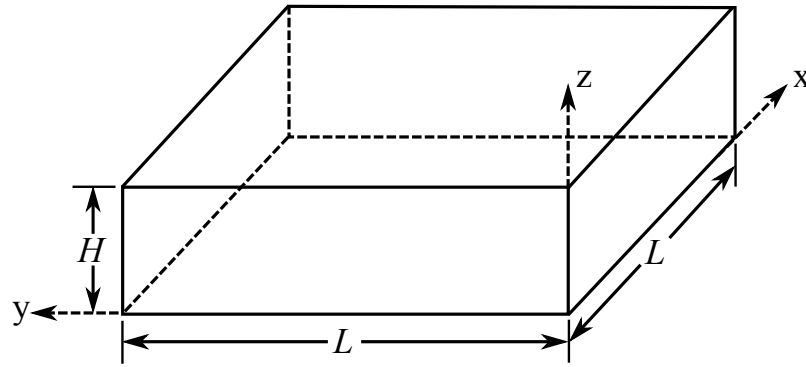


**Figure 3.11:** Schematic diagram of the domain under consideration for the volume-averaged simulations.

since no models had been developed specifically for these materials. To isolate the effects of thermal dispersion on the volume-averaged temperature fields, we use the present model for the Nusselt number in conjunction with the two different dispersion models. Note that the effective solid conductivity is obtained from the analytical model proposed by Yu et al. [14] and the convecting velocity is obtained directly from Fig. 3.9, since the flow field is essentially a plug flow.

The particular configuration under consideration in this section consists of a block of graphite foam in a sealed channel, heated from below, with dimensions  $L \times L \times H$ , as shown in Fig. 3.11. Note that we do not consider the fluid regions upstream and downstream of the porous block, since, as shown by Straatman et al. [5], these sections have little effect on the final solution. In this case,  $L/d = 100$  and  $H/d = 12$ , similar to the case considered in [5]. Also, we have chosen  $\varepsilon = 0.85$ , such that  $K/d^2 = 1.24 \times 10^{-2}$ . To highlight the dispersion effects, we have chosen the working fluid to be water at 300 K, which has a relatively high Prandtl number of  $Pr = 5.8$  and a solid-to-fluid conductivity ratio of  $k_s/k_f = 2447$ , which is sufficiently high for the present model to be applicable. The domain was discretized using 30 control volumes in each direction, with some refinement towards the boundaries. A grid resolution study indicated that doubling the total number of control volumes within the domain resulted in less than 0.2% change in pressure drop and overall heat transfer, so it is concluded that the results are independent of the particular grid employed.

The dimensionless boundary conditions on the velocity field are summarized as

$$\langle \mathbf{u} \rangle^*|_{x^*=0} = \mathbf{i}, \quad \nabla \langle \mathbf{u} \rangle^*|_{x^*=L/d} = \mathbf{0}, \quad \langle \mathbf{u} \rangle^*|_{y^*=0} = \mathbf{0}, \quad (3.52a,b,c)$$

$$\langle \mathbf{u} \rangle^*|_{y^*=L/d} = \mathbf{0}, \quad \langle \mathbf{u} \rangle^*|_{z^*=0} = \mathbf{0}, \quad \langle \mathbf{u} \rangle^*|_{z^*=H/d} = \mathbf{0}. \quad (3.52d,e,f)$$

The dimensionless pressure is simply set to zero at  $x^* = L/d$  and is extrapolated at all other boundaries. The dimensionless boundary conditions on the temperature fields are summarized as

$$\theta_f|_{x^*=0} = 0, \quad \frac{\partial \theta_f}{\partial x^*}|_{x^*=L/d} = 0, \quad \frac{\partial \theta_f}{\partial y^*}|_{y^*=0} = 0, \quad (3.53a,b,c)$$

$$\frac{\partial \theta_f}{\partial y^*}|_{y^*=L/d} = 0, \quad \theta_f|_{z^*=0} = 1, \quad \frac{\partial \theta_f}{\partial z^*}|_{z^*=H/d} = 0, \quad (3.53d,e,f)$$

$$\frac{\partial \theta_s}{\partial x^*}|_{x^*=0} = 0, \quad \frac{\partial \theta_s}{\partial x^*}|_{x^*=L/d} = 0, \quad \frac{\partial \theta_s}{\partial y^*}|_{y^*=0} = 0, \quad (3.53g,h,i)$$

$$\frac{\partial \theta_s}{\partial y^*}|_{y^*=L/d} = 0, \quad \theta_s|_{z^*=0} = 1, \quad \frac{\partial \theta_s}{\partial z^*}|_{z^*=H/d} = 0. \quad (3.53j,k,l)$$

Results are obtained for two Reynolds numbers,  $Re_d \in \{50, 100\}$ , using the two different dispersion models and are presented in terms of the average Nusselt number, defined as

$$\begin{aligned} \overline{Nu} &= \frac{q_{tot}d}{k_f A_b (T_w - T_{in})} \\ &= \left(\frac{d}{L}\right)^2 \int_{x^*=0}^{x^*=L/d} \int_{y^*=0}^{y^*=L/d} \left( \frac{(\mathbf{k}_{fe})_{zz}}{k_f} \frac{\partial \theta_f}{\partial z^*} + \frac{(\mathbf{k}_{se})_{zz}}{k_f} \frac{\partial \theta_s}{\partial z^*} \right)_{z^*=0} dx^* dy^*. \end{aligned} \quad (3.54)$$

The Nusselt number results, summarized in Table 3.4, indicate that at  $Re_d = 50$  the difference between the two dispersion models is relatively small, whereas at  $Re_d = 100$  the difference is much more significant. This is also illustrated in the contour plots of the dimensionless fluid temperature in each case, given in Figs. 3.12 and 3.13, which show that the new dispersion model results in more conduction within the fluid in comparison to the model of Calmidi and Mahajan [15], with this effect being stronger in the  $Re_d = 100$  case.

**Table 3.4:** Summary of the average Nusselt number computed using the two dispersion models for  $Re_d \in \{50, 100\}$  and the percent difference between them.

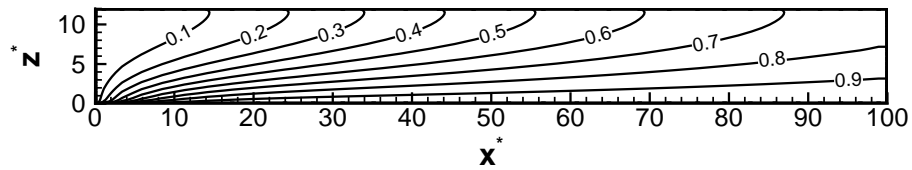
$Re_d$	$\overline{Nu}$ (Calmidi and Mahajan model [15])	$\overline{Nu}$ (present model)	Percent difference
50	35.7	36.8	3.4
100	55.0	61.8	12.4

Further calculations with  $H/d$  doubled showed that the difference in the average Nusselt number for the two dispersion models was greater.

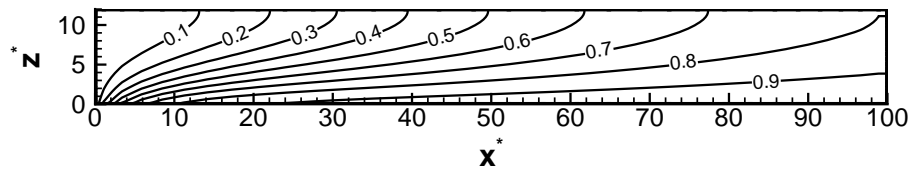
In summary, the results obtained using the volume-averaged model indicate that there is a significant difference between the present dispersion model and the model of Calmidi and Mahajan [15] when applied to graphite foams. It appears that at lower Reynolds numbers, the difference between the two models is much less, which explains why the Calmidi and Mahajan [15] model gave good results for the cases considered by Straatman et al. [5]. It is concluded, however, that as the Reynolds number and block height are increased, it becomes important to use a model developed specifically for graphite foams, such as the one proposed in this work. It should also be noted that if the interfacial Nusselt number correlation is calibrated to match experimental data, resulting in less heat exchange at the fluid-solid interface, the size of the dispersion term will be larger by comparison and may result in greater differences in heat transfer between the two dispersion models.

### 3.8 Summary

In this study, we have presented results for the relevant effective properties for an idealized graphite foam material which are required to close the volume averaged momentum and non-equilibrium energy equations. To close the momentum equation, we computed the permeability and the non-Darcy drag term, which lead us to conclude that the relationship between the non-Darcy drag and Reynolds number is generally non-linear, casting some doubt on the validity of the Darcy-Forchheimer approach as a general method of modelling flow in porous media. To close the energy equations, we computed the thermal disper-

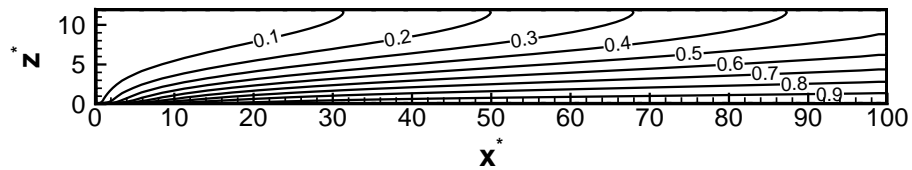


(a)

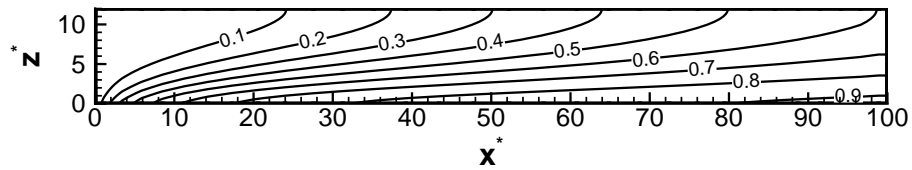


(b)

**Figure 3.12:** Contour plots of the dimensionless fluid temperature,  $\theta_f$ , along the center plane defined by  $y^* = \frac{1}{2}\frac{L}{d}$  for  $Re_d = 50$  using (a) the dispersion model of Calmidi and Mahajan [15] and (b) the present dispersion model.



(a)



(b)

**Figure 3.13:** Contour plots of the dimensionless fluid temperature,  $\theta_f$ , along the center plane defined by  $y^* = \frac{1}{2}\frac{L}{d}$  for  $Re_d = 100$  using (a) the dispersion model of Calmidi and Mahajan [15] and (b) the present dispersion model.

sion conductivity, convecting velocity, and interfacial Nusselt number. We concluded that, in general, the Péclet number alone does not adequately model the dispersion behaviour, rather, the Reynolds number, Prandtl number, and solid fraction should be considered separately. Additional results for the convecting velocity and interfacial Nusselt number have also shown behaviour which is more complicated than typically observed for porous media with simpler pore geometries. Calculations using the proposed volume-averaged model indicate that it is important to use a model specific to graphite foams to accurately model dispersion behaviour, particularly at high Péclet numbers and large block thicknesses.

## References

- [1] Bhattacharya, A. and Mahajan, R. L., 2002, “Finned metal foam heat sinks for electronics cooling in forced convection,” *J. Electron Packag.*, **124**, pp. 155–163.
- [2] Gallego, N. C. and Klett, J. W., 2003, “Carbon foams for thermal management,” *Carbon*, **41**, pp. 1461–1466.
- [3] Boomsma, K., Poulikakos, D., and Zwick, F., 2003, “Metal foams as compact high performance heat exchangers,” *Mech. Mater.*, **35**, pp. 1161–1176.
- [4] Straatman, A. G., Gallego, N. C., Thompson, B., and Hangan, H., 2006, “Thermal characterization of porous carbon foam - convection in parallel flow,” *Int. J. Heat Mass Transfer*, **49**, pp. 1991–1998.
- [5] Straatman, A. G., Gallego, N. C., Yu, Q., Betchen, L. J., and Thompson, B., 2007, “Forced convection and hydraulic losses in graphitic foam,” *J. Heat Transfer*, **129**, pp. 1237–1245.
- [6] Straatman, A. G., Gallego, N. C., Yu, Q., and Thompson, B. E., 2007, “Characterization of porous carbon foam as a material for compact recuperators,” *J. Eng. Gas Turb. Power*, **129**, pp. 326–330.
- [7] DeGroot, C. T., Straatman, A. G., and Betchen, L. J., 2009, “Modeling forced convection in finned metal foam heat sinks,” *J. Electron. Packag.*, **131**, pp. 1–10.
- [8] Sultan, K., DeGroot, C. T., Straatman, A. G., Gallego, N., and Hangan, H., 2009,

- “Thermal characterization of porous graphitic foam - convection in impinging flow,” *Int. J. Heat Mass Transfer*, **52**, pp. 4296–4301.
- [9] Leong, K. C., Li, H. Y., Jin, L. W., and Chai, J. C., 2010, “Numerical and experimental study of forced convection in graphite foams of different configurations,” *Appl. Therm. Eng.*, **30**, pp. 520–532.
- [10] Whitaker, S., 1967, “Diffusion and dispersion in porous media,” *A.I.Ch.E. J.*, **13**, pp. 420–427.
- [11] Costa, V. A. F., Oliveira, L. A., Baliga, B. R., and Sousa, A. C. M., 2004, “Simulation of coupled flows in adjacent porous and open domains using a control-volume finite-element method,” *Numer. Heat Tr. A-Appl.*, **45**, pp. 675–697.
- [12] Betchen, L. J., Straatman, A. G., and Thompson, B. E., 2006, “A nonequilibrium finite-volume model for conjugate fluid/porous/solid domains,” *Numer. Heat Tr. A-Appl.*, **49**, pp. 543–565.
- [13] DeGroot, C. T. and Straatman, A. G., 2011, “A finite-volume model for fluid flow and non-equilibrium heat transfer in conjugate fluid-porous domains using general unstructured grids,” *Numer. Heat Tr. B-Fund.*, **60**, pp. 252–277.
- [14] Yu, Q., Thompson, B. E., and Straatman, A. G., 2006, “A unit cube-based model for heat transfer and fluid flow in porous carbon foam,” *J. Heat Transfer*, **128**, pp. 352–360.
- [15] Calmidi, V. V. and Mahajan, R. L., 2000, “Forced convection in high porosity metal foams,” *J. Heat Transfer*, **122**, pp. 557–565.
- [16] Karimian, S. A. M. and Straatman, A. G., 2009, “Numerical modeling of multidirectional flow and heat transfer in graphitic foams,” *J. Heat Transfer*, **131**, pp. 052602–1–11.

- 
- [17] DeGroot, C. T. and Straatman, A. G., 2011, "Closure of non-equilibrium volume-averaged energy equations in high-conductivity porous media," *Int. J. Heat Mass Transfer*, **54**, pp. 5039–5048.
- [18] Whitaker, S., 1996, "The Forchheimer equation: a theoretical development," *Transport Porous Med.*, **25**, pp. 27–61.
- [19] Mei, C. C. and Auriault, J. L., 1991, "The effect of weak inertia on flow through a porous medium," *J. Fluid Mech.*, **222**, pp. 647–663.
- [20] Firdaouss, M., Guermond, J. L., and LeQuéré, P., 1997, "Nonlinear corrections to Darcy's law at low Reynolds numbers," *J. Fluid Mech.*, **343**, pp. 331–350.
- [21] Rojas, S. and Koplik, J., 1998, "Nonlinear flow in porous media," *Phys. Rev. E*, **58**, pp. 4776–4782.
- [22] Slattery, J. C., 1967, "Flow of viscoelastic fluids through porous media," *A.I.Ch.E. J.*, **13**, pp. 1066–1071.
- [23] Gray, W. G., 1975, "A derivation of the equations for multi-phase transport," *Chem. Eng. Sci.*, **30**, pp. 229–233.
- [24] Kaviany, M., 1995, *Principles of heat transfer in porous media*, Springer-Verlag, New York, NY, 2 ed.
- [25] Whitaker, S., 1997, *Fluid transport in porous media*, chap. 1, Springer-Verlag, Southampton, UK, pp. 1–59.
- [26] Vafai, K. and Tien, C. L., 1981, "Boundary and inertia effects on flow and heat transfer in porous media," *Int. J. Heat Mass Transfer*, **24**, pp. 195–203.
- [27] Nakayama, A., Kuwahara, F., and Kodama, Y., 2006, "An equation for thermal dispersion flux transport and its mathematical modelling for heat and fluid flow in a porous medium," *J. Fluid Mech.*, **563**, pp. 81–96.

- 
- [28] Krishnan, S., Murthy, J. Y., and Garimella, S. V., 2006, "Direct simulation of transport in open-cell metal foam," *J. Heat Transfer*, **128**, pp. 793–799.
- [29] Karimian, S. A. M. and Straatman, A. G., 2008, "CFD study of the hydraulic and thermal behavior of spherical-void-phase porous materials," *Int. J. Heat Fluid Flow*, **29**, pp. 292–305.
- [30] Taylor, G., 1953, "Dispersion of soluble matter in solvent flowing slowly through a tube," *Proc. R. Soc. A*, **219**, pp. 186–203.
- [31] Yagi, S., Kunii, D., and Wakao, N., 1960, "Studies on axial effective thermal conductivities in packed beds," *A.I.Ch.E. J.*, **6**, pp. 543–546.
- [32] Eidsath, A., Carbonell, R. G., Whitaker, S., and Herrmann, L. R., 1983, "Dispersion in pulsed systems – III Comparison between theory and experiments for packed beds," *Chem. Eng. Sci.*, **38**, pp. 1803–1816.
- [33] Kuwahara, F., Nakayama, A., and Koyama, H., 1996, "A numerical study of thermal dispersion in porous media," *J. Heat Transfer*, **118**, pp. 756–761.
- [34] Kuwahara, F. and Nakayama, A., 1999, "Numerical determination of thermal dispersion coefficients using a periodic porous structure," *J. Heat Transfer*, **121**, pp. 160–163.

# Fluid Flow in an Alveolated Duct: A Porous Media Approach<sup>†</sup>

## 4.1 Introduction

Simulation of flow in the human lung is of interest because it can provide details of the flow that cannot be measured *in vivo*. Knowledge of the flow patterns within the lung are of practical importance because of the potential impacts on respiratory drug delivery, particle deposition, and our general understanding of the relationship between lung structure and function [1]. The internal structure of the lung consists of a network of bifurcating airways that become smaller in both length and diameter with each subsequent bifurcation. Each level of bifurcation is referred to as an airway generation. The first sixteen generations are known as the conducting airways which take no part in the gas exchange process, but lead the air to the respiratory region of the lung [2]. Gas exchange occurs by passive diffusion through the thin walls of small sacs, known as alveoli, which line the airways in the respiratory region (17th generation and beyond) [2, 3].

Simulating flow in the lung is particularly challenging due to the large number of flow

---

<sup>†</sup>This chapter is an extension of the work presented in “Simulation of Flow in an Alveolated Duct within the Human Lung with Application to Porous Media” *Proceedings of the 20th Annual Conference of the CFD Society of Canada*, 2012.

paths and the wide range of length scales spanned by the various components of its structure. The zeroth generation of the airway tree is the trachea, which has a typical diameter of about two centimetres [3]. At each of the approximately 23 bifurcations, the diameter of the subsequent generation is reduced by a factor of approximately  $2^{1/3}$ , leading to diameters as small as a fraction of a millimetre [3]. There are approximately 300 million alveolar sacs in the human lung, each of which are about 0.3 mm in diameter [3]. Many computational fluid dynamics (CFD) studies have been conducted to study flow, particle deposition, as well as heat and mass transfer in the upper airways [1, 4–20]. Similarly, in the respiratory region, CFD simulations have been conducted to investigate the flow and particle transport in alveolated ducts [21–32]. Although some attempts have been made to couple computational models of flow in the upper airways to models of flow in the lower airways [15, 17], the lower airway models employed in these studies are typically quite simplified.

It has been proposed by Owen and Lewis [33], in their theoretical work on high-frequency ventilation, that the lung parenchyma can be modelled as a porous continuum. Using homogenization and volume-averaging, they developed a model to describe the flow and tissue deformation for small uniform samples of lung tissue. While the theoretical development of their model was well-founded, it depended on several effective properties of the porous lung parenchyma that were only roughly estimated and only select one-dimensional results were obtained for the flow and tissue deformations. However, it was suggested that such a macroscopic description could be coupled with models for the upper airways. This would provide a convenient way to simulate transport processes in the whole lung since full resolution in the upper airways can be obtained, while a coupled porous media model is used to account for activity the remainder of the airways and parenchyma.

Following a similar concept as that put forward by Owen and Lewis [33], it is the goal of this work to develop a porous media model for air flow in the lung parenchyma using the method of volume-averaging [34–37], which is chosen because it yields very general results

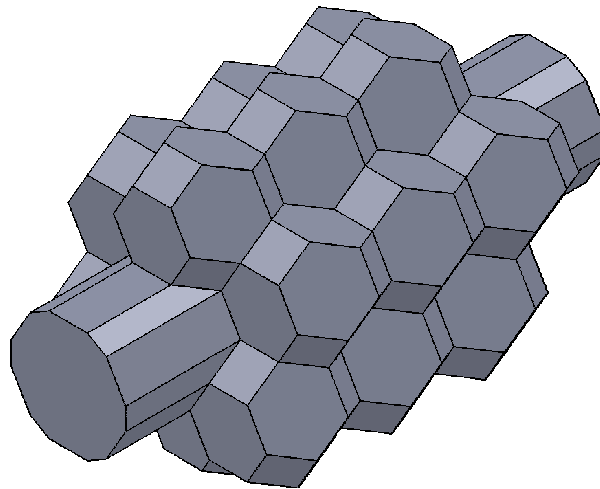


**Figure 4.1:** *A schematic diagram of an idealized geometric model of an alveolated duct.*

that are applicable to three-dimensional flows and is relatively straightforward to couple with models for the upper airways. Closure of the resulting volume-averaged momentum equation is considered theoretically, which results in a closure problem that can be solved numerically on a periodic unit-cell of the parenchyma to determine the relevant effective properties, shown in this case to be solely the permeability, or the resistance to flow. As the majority of the lung parenchyma is made up of alveolated ducts, this is taken as the pore geometry of interest. Results for the permeability are obtained using a realistic geometric idealization of an alveolated duct, shown in Fig. 4.1 which has been used previously by Kumar et al. [29, 32] to study flows in alveolated ducts. The resulting volume-averaged model is then compared to direct pore-level simulations of an alveolated duct with moving walls and some one-dimensional results are presented. The key outcome of this work is the permeability of the alveolated duct which can subsequently be used in large-scale three-dimensional simulations of flow in the lung.

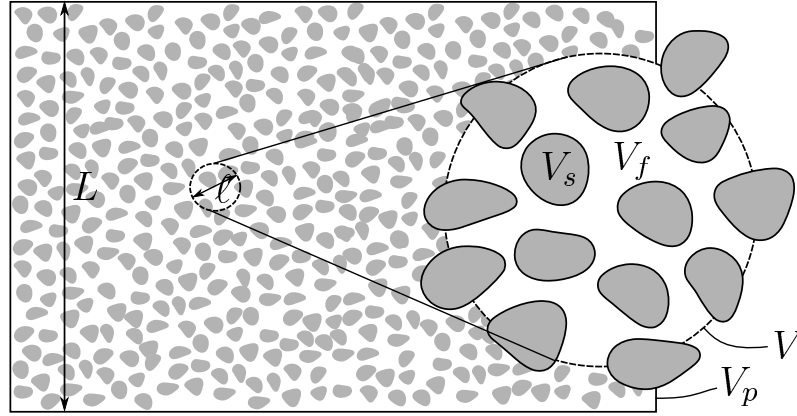


**Figure 4.2:** An illustration of a typical averaging volume,  $V$ , for an arbitrary porous medium containing fluid and solid volumes  $V_f$  and  $V_s$ , respectively.

## 4.2 Governing Equations and Closure

Flow in the airway tree and alveoli is governed by the standard continuity and Navier-Stokes equations, given by

$$\nabla \cdot \mathbf{u} = 0 \quad (4.1)$$

and

$$\rho_f \left( \frac{\partial \mathbf{u}}{\partial t} + \mathbf{u} \cdot \nabla \mathbf{u} \right) = -\nabla p + \mu_f \nabla^2 \mathbf{u}, \quad (4.2)$$

respectively, where  $\mathbf{u}$  is the fluid velocity vector,  $p$  is the pressure,  $\rho_f$  is the fluid density,  $t$  is time, and  $\mu_f$  is the fluid dynamic viscosity. Since there are far too many alveolar ducts in the human lung to consider directly, we average the above equations over a representative element of the lung parenchyma to obtain equations that can be solved for averaged quantities. For an arbitrary porous medium composed of fluid and solid constituents, shown schematically in Fig. 4.2, the definition of the extrinsic volume-average of a quantity  $\phi_k$  is given by

$$\langle \phi_k \rangle = \frac{1}{V} \int_{V_k} \phi_k dV, \quad (4.3)$$

where  $k \in \{f, s\}$  denotes the phase in which the quantity  $\phi_k$  is defined with ‘ $f$ ’ and ‘ $s$ ’ indicating the fluid and solid phases, respectively. Note that  $V_f$  and  $V_s$  are the fluid and

solid volumes, respectively, contained within the averaging volume  $V$ . For the purposes of this work, the air within the alveolated ducts represents the fluid phase while the tissue represents the solid phase. In addition to the extrinsic average, the intrinsic average is defined as

$$\langle \phi_k \rangle^k = \frac{1}{V_k} \int_{V_k} \phi_k dV, \quad (4.4)$$

which is an average over a single phase only. For the purposes of the theoretical development to follow, it is assumed that the porosity,  $\varepsilon = V_f/V$ , of the porous region may vary in both time and space. Under such conditions, the volume-averaged counterparts to Eqs. 4.1 and 4.2 are

$$\nabla \cdot \langle \mathbf{u} \rangle = -\frac{\partial \varepsilon}{\partial t} \quad (4.5)$$

and

$$\begin{aligned} \rho_f \left[ \frac{\partial \langle \mathbf{u} \rangle}{\partial t} + \nabla \cdot \left( \frac{1}{\varepsilon} \langle \mathbf{u} \rangle \langle \mathbf{u} \rangle \right) \right] = & -\varepsilon \nabla \langle p \rangle^f + \mu_f \nabla^2 \langle \mathbf{u} \rangle \\ & + \frac{1}{V} \int_{A_{fs}(t)} (-\tilde{p} \mathbf{n}_{fs} + \mu_f \nabla \tilde{\mathbf{u}} \cdot \mathbf{n}_{fs}) dA - \rho_f \nabla \cdot \langle \tilde{\mathbf{u}} \tilde{\mathbf{u}} \rangle, \end{aligned} \quad (4.6)$$

respectively, where  $A_{fs}(t)$  is the area of intersection between the fluid and solid volumes,  $V_f$  and  $V_s$ . The unit-normal vector directed from the fluid to solid phase on  $A_{fs}(t)$  is denoted  $\mathbf{n}_{fs}$ . Spatial deviations are denoted, for a generic scalar  $\phi$ , as  $\tilde{\phi} = \phi - \langle \phi \rangle^f$ . Note that  $A_{fs}$  is taken as a function of time since the walls of an alveolated duct are in motion as they expand and contract through the breathing cycle. For further details on the derivation of Eqs. 4.5 and 4.6 see Gray [34], which considers a similar case.

To close Eq. 4.6, we follow the general approach of Whitaker [38] in which transport equations for the spatial deviations are derived by subtracting Eq. 4.5, divided by  $\varepsilon$ , from Eq. 4.1 and subtracting Eq. 4.6, divided by  $\varepsilon$ , from Eq. 4.2. In this case, however, there are additional terms arising from the fact that the porosity is allowed to vary in space and time. The transport equation for the velocity deviations arising from the continuity equation is

given as

$$\nabla \cdot \tilde{\mathbf{u}} = \frac{1}{\varepsilon} \frac{\partial \varepsilon}{\partial t} - \frac{1}{\varepsilon^2} \nabla \varepsilon \cdot \langle \mathbf{u} \rangle. \quad (4.7)$$

Compared to the equation of Whitaker [38], Eq. 4.7 is quite complicated, however it can be shown through various scaling arguments that it can be simplified substantially, such that it is equivalent to that of [38]. The assumptions that are made for this analysis are summarized as:

- (i) Variations in the velocity deviations,  $\tilde{\mathbf{u}}$ , occur over the length scale of the averaging volume with length scale  $\ell$ , while variations in the volume-averaged velocity,  $\langle \mathbf{u} \rangle$ , and porosity,  $\varepsilon$ , occur over the length scale of the porous domain with length scale  $L$ ; the length scale  $\ell$  corresponds to the size of an alveolus, which has a length scale of approximately 0.3 mm [2] and  $L$  corresponds to the size of the lung which is  $O(10^{-1} \text{ m})$ .
- (ii) The velocity deviations and the volume-averaged velocity are of the same order, that is  $\tilde{\mathbf{u}} \sim O(U)$  and  $\langle \mathbf{u} \rangle \sim O(U)$ , where  $U$  is a characteristic velocity; the characteristic velocity within an alveolated duct is  $O(10^{-3} \text{ m/s})$  [21].
- (iii) The average porosity of the lung parenchyma is approximately  $\varepsilon = 0.9$  [3], such that  $\varepsilon \sim O(1)$  and the deviation from this value is small ( $\Delta\varepsilon \ll 1$ ).
- (iv) The time scale of a breath cycle,  $t_b$ , is of the order of seconds; the time scale of the porosity variations is the same.

With these assumptions, which are all physiologically-based, the order of magnitude of each of the terms in Eq. 4.7 may be estimated. On this basis of assumptions (i) and (ii), it can be said that

$$\nabla \cdot \tilde{\mathbf{u}} \sim O\left(\frac{U}{\ell}\right). \quad (4.8)$$

Adding assumptions (iii) and (iv), the orders of magnitude of the remaining terms may be

estimated as

$$\frac{1}{\varepsilon} \frac{\partial \varepsilon}{\partial t} \sim O\left(\frac{\Delta \varepsilon}{t_b}\right) \quad (4.9)$$

and

$$\frac{1}{\varepsilon^2} \nabla \varepsilon \cdot \langle \mathbf{u} \rangle \sim O\left(\frac{\Delta \varepsilon U}{L}\right). \quad (4.10)$$

Based on the length scale and characteristic velocity estimates given by assumptions (i) and (ii), respectively, the order of magnitude of the term listed in Eq. 4.8 is of the order  $10 \text{ s}^{-1}$ . Since, according to assumption (iv), the time scale,  $t_b$ , is of the order of seconds and the variation in porosity,  $\Delta \varepsilon$  is much less than one, it is clear that the term listed in Eq. 4.9 is much less than  $1 \text{ s}^{-1}$ . As a result, the term on the left side of Eq. 4.7 has been found to be much larger than the first term on the right, given the assumptions above, and may be neglected in this analysis. Comparing the term given in Eq. 4.8 to the term given in Eq. 4.10, it is clear that the term given in Eq. 4.10 is much smaller since  $\Delta \varepsilon$  is small and  $L \gg \ell$ . As a result, the last term on the right side of Eq. 4.7 may also be neglected in comparison to the term on the left. Thus, the simplified transport equation for the velocity deviations, arising from the continuity equations is

$$\nabla \cdot \tilde{\mathbf{u}} = 0, \quad (4.11)$$

as in the analysis of Whitaker [38]. Subtracting Eq. 4.6, divided by  $\varepsilon$ , from Eq. 4.2 results in

$$\begin{aligned} \rho_f \left( \frac{\partial \tilde{\mathbf{u}}}{\partial t} - \frac{1}{\varepsilon^2} \frac{\partial \varepsilon}{\partial t} \langle \mathbf{u} \rangle + \mathbf{u} \cdot \nabla \tilde{\mathbf{u}} + \tilde{\mathbf{u}} \cdot \nabla \langle \mathbf{u} \rangle^f - \frac{\nabla \varepsilon}{\varepsilon} \cdot \langle \mathbf{u} \rangle^f \langle \mathbf{u} \rangle^f \right) = & -\nabla \tilde{p} + \mu_f \nabla^2 \tilde{\mathbf{u}} \\ - \mu_f \langle \mathbf{u} \rangle \left( \frac{\nabla^2 \varepsilon}{\varepsilon} - \frac{2 \nabla \varepsilon \cdot \nabla \varepsilon}{\varepsilon^2} \right) - \mu_f \frac{2 \nabla \varepsilon}{\varepsilon} \cdot \nabla \langle \mathbf{u} \rangle - \frac{1}{V_f} \int_{A_{fs}(t)} & (-\tilde{p} \mathbf{n}_{fs} + \mu_f \nabla \tilde{\mathbf{u}} \cdot \mathbf{n}_{fs}) dA \\ & + \frac{\rho_f}{\varepsilon} \nabla \cdot \langle \tilde{\mathbf{u}} \tilde{\mathbf{u}} \rangle \end{aligned} \quad (4.12)$$

after much algebraic simplification. Let us first examine the orders of magnitude of the

terms on the left side of Eq. 4.12, under the assumptions listed previously. These are listed as:

$$\frac{\partial \tilde{\mathbf{u}}}{\partial t} \sim O\left(\frac{U}{t_b}\right), \quad (4.13)$$

$$\frac{1}{\varepsilon^2} \frac{\partial \varepsilon}{\partial t} \langle \mathbf{u} \rangle \sim O\left(\frac{\Delta \varepsilon U}{t_b}\right), \quad (4.14)$$

$$\mathbf{u} \cdot \nabla \tilde{\mathbf{u}} \sim O\left(\frac{U^2}{\ell}\right), \quad (4.15)$$

$$\tilde{\mathbf{u}} \cdot \nabla \langle \mathbf{u} \rangle^f \sim O\left(\frac{U^2}{L}\right), \quad (4.16)$$

and

$$\frac{\nabla \varepsilon}{\varepsilon} \cdot \langle \mathbf{u} \rangle^f \langle \mathbf{u} \rangle^f \sim O\left(\frac{\Delta \varepsilon U^2}{L}\right). \quad (4.17)$$

Since  $\ell \ll L$  and  $\Delta \varepsilon \ll 1$ , the terms given in Eqs. 4.16 and 4.17 are negligible in comparison to the term given in Eq. 4.15. As stated previously,  $U/\ell$  is of the order of  $10 \text{ s}^{-1}$  and the characteristic time scale,  $t_b$ , is of the order of 1 s. Thus, the term in Eq. 4.13 is an order of magnitude smaller than the term in Eq. 4.15, which is deemed small enough that it may be neglected. Since  $\Delta \varepsilon \ll 1$ , the term in Eq. 4.14 is much less than the term in Eq. 4.13, so this term may also be neglected in comparison to that in Eq. 4.15. Therefore, of all the terms on the left side of Eq. 4.12, only the third survives. Then, since

$$\frac{1}{\varepsilon} \nabla \cdot \langle \tilde{\mathbf{u}} \tilde{\mathbf{u}} \rangle \sim O\left(\frac{U^2}{L}\right), \quad (4.18)$$

the final term on the right side of Eq. 4.12 may be neglected in comparison to the surviving term on the left side.

The additional viscous terms, arising from the fact that the porosity is assumed to be spatially varying, can also be simplified. Since we have

$$\nabla^2 \tilde{\mathbf{u}} \sim O\left(\frac{U}{\ell^2}\right), \quad (4.19)$$

$$\frac{\langle \mathbf{u} \rangle \nabla^2 \varepsilon}{\varepsilon} \sim O\left(\frac{U \Delta \varepsilon}{L^2}\right), \quad (4.20)$$

$$\frac{\langle \mathbf{u} \rangle \nabla^2 \varepsilon}{\varepsilon} \sim O\left(\frac{U (\Delta \varepsilon)^2}{L^2}\right), \quad (4.21)$$

and

$$\frac{\nabla \varepsilon}{\varepsilon} \nabla \langle \mathbf{u} \rangle \sim O\left(\frac{U \Delta \varepsilon}{L^2}\right), \quad (4.22)$$

and since  $\ell \ll L$  and  $\Delta \varepsilon \ll 1$ , we can neglect all but the first viscous term, which is listed in Eq. 4.19. With these simplifications, the transport equation for the velocity and pressure deviations given by Whitaker [38] is recovered. This is given as

$$\rho_f \mathbf{u} \cdot \nabla \tilde{\mathbf{u}} = -\nabla \tilde{p} + \mu_f \nabla^2 \tilde{\mathbf{u}} - \frac{1}{V_f} \int_{A_{fs}(t)} (-\tilde{p} \mathbf{n}_{fs} + \mu_f \nabla \tilde{\mathbf{u}} \cdot \mathbf{n}_{fs}) dA. \quad (4.23)$$

The fact that the transport equation for steady problems with constant porosity is recovered is significant because it means that one may neglect any time dependence as well as any porosity variations when considering the pore-scale closure problem, under the assumptions given previously for air flow in an alveolated duct. This is quite advantageous since these additional terms would be quite challenging to deal with in a general way. Fortunately, under these limiting conditions, the transport equations for the spatial deviations reduce to those of Whitaker [38] and we may use the closure method proposed in that work. In fact, since the Reynolds number in alveolar flows is very low, one can further show that the convective term on the left side of Eq. 4.23 may also be neglected, resulting in the final form of the transport equation for the velocity and pressure deviations, given as

$$\mathbf{0} = -\nabla \tilde{p} + \mu_f \nabla^2 \tilde{\mathbf{u}} - \frac{1}{V_f} \int_{A_{fs}(t)} (-\tilde{p} \mathbf{n}_{fs} + \mu_f \nabla \tilde{\mathbf{u}} \cdot \mathbf{n}_{fs}) dA. \quad (4.24)$$

Next, the boundary conditions on Eqs. 4.11 and 4.24 must be considered. On the moving walls of the alveolated duct, the velocity deviation is expressed as  $\tilde{\mathbf{u}} = \mathbf{u} - \langle \mathbf{u} \rangle^f$ . Since the wall displacement over a breath cycle is  $O(10^{-5} \text{ m})$  over a timescale that is  $O(1 \text{ s})$ , the wall

velocity can be estimated as  $O(10^{-5}$  m/s), which is considered negligible in comparison to the bulk velocity which is typically  $O(10^{-3}$  m/s). Additionally, although the velocity field is not strictly periodic due to the volume flow into the expanding alveoli, a periodic condition can still be considered appropriate since the volume flow rate into the alveoli is typically less than 1% of that in the alveolar duct [29]. Thus, it has been shown that wall motion can be neglected within the context of the pore-level closure problem. In summary, the boundary conditions on the velocity and pressure deviations are given as

$$\tilde{\mathbf{u}} = -\langle \mathbf{u} \rangle^f, \text{ on } A_{fs} \quad (4.25a)$$

$$\tilde{\mathbf{u}}(\mathbf{x}_{in} + \Delta \mathbf{x}) = \tilde{\mathbf{u}}(\mathbf{x}_{in}), \text{ on } A_{fe} \quad (4.25b)$$

$$\tilde{p}(\mathbf{x}_{in} + \Delta \mathbf{x}) = \tilde{p}(\mathbf{x}_{in}), \text{ on } A_{fe}, \quad (4.25c)$$

where the conditions given in Eqs. 4.25b and 4.25c express the periodicity of the flow between an inflow point  $\mathbf{x}_{in}$  on  $A_{fe}(t)$  and the corresponding outflow location  $\mathbf{x}_{in} + \Delta \mathbf{x}$ . Note that  $A_{fs}$  and  $A_{fe}$  are no longer considered functions of time since it has been shown that the boundary motion can be neglected within the closure problem.

To derive the closure problem, which is to be solved on the appropriate periodic unit-cell, we first redefine the additional integral term remaining in Eq. 4.6 in terms of the permeability tensor  $\mathbf{K}$  according to

$$\frac{1}{V} \int_{A_{fs}(t)} (-\tilde{p} \mathbf{n}_{fs} + \mu_f \nabla \tilde{\mathbf{u}} \cdot \mathbf{n}_{fs}) dA = \varepsilon \mu_f \mathbf{K}^{-1} \cdot \langle \mathbf{u} \rangle. \quad (4.26)$$

Then we use the following constitutive equations, proposed by Whitaker [38] for  $\tilde{\mathbf{u}}$  and  $\tilde{p}$ :

$$\tilde{\mathbf{u}} = \mathbf{M} \cdot \langle \mathbf{u} \rangle^f + \mathbf{v} \quad (4.27a)$$

$$\tilde{p} = \mu_f \mathbf{m} \cdot \langle \mathbf{u} \rangle^f + \xi, \quad (4.27b)$$

where  $\mathbf{M}$  is a second-rank tensor and  $\mathbf{m}$  is a vector, both of which are functions of position. Whitaker [38] has shown that  $\mathbf{v}$  is zero and  $\xi$  is constant for the conditions considered herein. Thus  $\xi$  cannot pass through any integrals and is therefore inconsequential to the solution of the closure problem and is thus not considered any further. Whitaker [38] then made substitutions to separate the problem into a part which depends only on pore geometry and a part which depends on the flow field. In this work, since we are concerned with very low Reynolds number flows, this step is not necessary. Instead, we have simply neglected the inertial terms on the left side of Eq. 4.23 to arrive at Eq. 4.24. To eliminate the integral terms from the closure problems, we follow an approach similar to Whitaker [38], which is summarized by the substitutions below:

$$\mathbf{d} = \varepsilon^{-1} \mathbf{m} \cdot \mathbf{K} \quad (4.28a)$$

$$\mathbf{D} = \varepsilon^{-1} (\mathbf{M} + \mathbf{I}) \cdot \mathbf{K}. \quad (4.28b)$$

Substituting Eqs. 4.28a,b into Eqs. 4.27a,b and substituting the result into Eq. 4.23 results in the closure problem

$$\nabla \cdot \mathbf{D} = \mathbf{0} \quad (4.29a)$$

$$-\nabla \mathbf{d} + \nabla^2 \mathbf{D} + \mathbf{I} = \mathbf{0}, \quad (4.29b)$$

subject to the boundary conditions

$$\mathbf{D} = \mathbf{0}, \text{ on } A_{fs} \quad (4.30a)$$

$$\mathbf{D}(\mathbf{x}_{in} + \Delta \mathbf{x}) = \mathbf{D}(\mathbf{x}_{in}), \text{ on } A_{fe} \quad (4.30b)$$

$$\mathbf{d}(\mathbf{x}_{in} + \Delta \mathbf{x}) = \mathbf{d}(\mathbf{x}_{in}), \text{ on } A_{fe}. \quad (4.30c)$$

Now, Eqs. 4.29a and 4.29b may be solved along with the conditions listed in Eqs. 4.30a–

4.30c to determine the permeability tensor as

$$\mathbf{K} = \varepsilon \langle \mathbf{D} \rangle^f. \quad (4.31)$$

Note that for a general deforming domain,  $\mathbf{K}$  is a function of the pore geometry and thus a function of time. For general motions, this would require evaluation of  $\mathbf{K}$  for each required configuration, however, as will be seen, the characterization of  $\mathbf{K}$  as a function of time is simplified for motions where the domain is simply scaled as is typically assumed for alveolated duct flows.

With the definition of the permeability, the closed form of the volume-averaged momentum equation is then given by

$$\rho_f \left[ \frac{\partial \langle \mathbf{u} \rangle}{\partial t} + \nabla \cdot \left( \frac{1}{\varepsilon} \langle \mathbf{u} \rangle \langle \mathbf{u} \rangle \right) \right] = -\varepsilon \nabla \langle p \rangle^f + \mu_f \nabla^2 \langle \mathbf{u} \rangle - \varepsilon \mu_f \mathbf{K}^{-1} \cdot \langle \mathbf{u} \rangle, \quad (4.32)$$

where the final term in Eq. 4.6 has been neglected due to periodicity. Note that although it was found that transient and porosity gradient effects may be neglected at the pore-level closure problems, such effects may still be taken into account at the volume-averaged level through the closed volume-averaged momentum equation, Eq. 4.32.

## 4.3 Results and Discussion

### 4.3.1 Permeability Tensor

For flow in a duct where the bulk flow is in the  $x$ -direction and the walls are impermeable, the permeability tensor takes on the general form

$$\mathbf{K} = \begin{bmatrix} K & 0 & 0 \\ 0 & 0 & 0 \\ 0 & 0 & 0 \end{bmatrix}, \quad (4.33)$$

where  $K$  is the scalar permeability in the  $x$ -direction, since bulk flow transverse to the duct axis is not permitted. From a numerical perspective, however, this form poses a problem since the matrix given in Eq. 4.33 is clearly non-invertible. Thus, we assume the form

$$\mathbf{K} = \begin{bmatrix} K & 0 & 0 \\ 0 & 1/a & 0 \\ 0 & 0 & 1/a \end{bmatrix}, \quad (4.34)$$

where  $a$  is taken to be an arbitrarily large value. Thus, the inverse of the permeability tensor is given as

$$\mathbf{K}^{-1} = \begin{bmatrix} 1/K & 0 & 0 \\ 0 & a & 0 \\ 0 & 0 & a \end{bmatrix}, \quad (4.35)$$

which according to the closed volume-averaged momentum equation given in Eq. 4.32, prevents any bulk flow transverse to the axis of the duct through the very large Darcy term in these directions. Note that some care must be taken in selecting  $a$  to ensure that it is sufficiently large to serve its purpose, but not so large that it causes numerical difficulties.

Results for the permeability tensor are obtained by numerically solving Eqs. 4.29–4.30 using the finite-volume code described in Chapters 2–3 and integrating the results according to Eq. 4.31. The domain under consideration was a periodic unit-cell representing the idealized alveolated duct geometry shown in Fig. 4.1. The unit-cell geometry, taking into account the symmetry about a central plane, is shown in Fig. 4.3. Note that to solve the permeability using the proposed model requires only a single numerical solution of Eqs. 4.29 to 4.30. A grid resolution study indicated that a computational grid containing 244,331 tetrahedral volumes, refined towards walls, was sufficient to obtain a permeability tensor that is independent of the grid to less than 1%.

To promote generality of the results, the computed scalar permeability  $K$  is presented in dimensionless form as  $K/(\epsilon D_H^2)$ , where  $D_H$  is the hydraulic diameter of the central

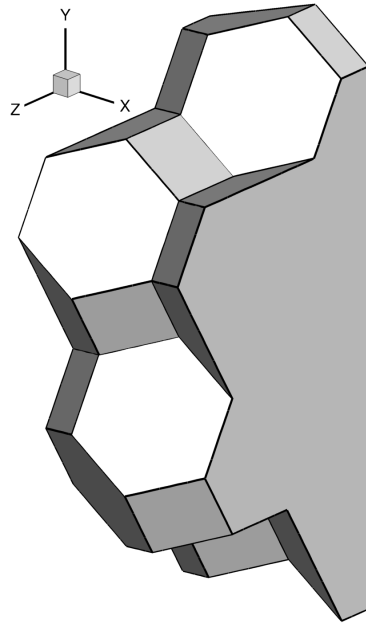


**Figure 4.3:** A schematic diagram of a periodic unit-cell of the idealized geometric model of an alveolated duct.

duct. Scaling the results by the hydraulic diameter is convenient because it allows the time-varying nature of the volume-averaged flow to be simplified as a time-varying permeability where the dimensionless permeability is constant but the hydraulic diameter of the duct changes. The permeability is also scaled by the porosity since we do not wish to specify a particular porosity for this model, since the choice of porosity depends on the nature of the system being modelled at a volume-averaged level. Numerical results confirm the form of the permeability tensor given in Eq. 4.33 and show that  $K/(\epsilon D_H^2) = 9.46 \times 10^{-3}$ .

### 4.3.2 Verification of the Porous Media Model

In order to verify the proposed porous media model of flow in an alveolated duct and the validity assumptions underlying the theoretical basis of the model, transient simulations were conducted using ANSYS<sup>®</sup> CFX, Release 13.0, to compare the model predictions with direct CFD calculations in an expanding and contracting alveolar duct geometry. A one-dimensional version of Eq. 4.32, neglecting any macroscopic velocity gradients, results

in

$$\rho_f \frac{\partial \langle u \rangle^f}{\partial t} = - \frac{\partial \langle p \rangle^f}{\partial x} - \frac{\varepsilon \mu_f \langle u \rangle^f}{K}, \quad (4.36)$$

where all averages have been converted to intrinsic averages and a constant porosity is assumed for the purposes of this verification exercise. Multiplying Eq. 4.36 by  $D_H^2$  and solving for  $K/(\varepsilon D_H^2)$  results in

$$\frac{K}{\varepsilon D_H^2} = \frac{\mu_f \langle u \rangle^f}{D_H^2} \left[ - \frac{d \langle p \rangle^f}{dx} - \rho_f \frac{\partial \langle u \rangle^f}{\partial t} \right]^{-1}, \quad (4.37)$$

where the terms on the right side of Eq. 4.37 may be obtained directly from CFD calculations to verify that the results match the modelled  $K/(\varepsilon D_H^2)$  expression.

The CFD calculations are conducted using the full alveolated duct geometry shown in Fig. 4.1. At the inlet a uniform velocity profile was specified such that the Reynolds number based on the hydraulic diameter of the duct was  $Re_{D_H} = 0.01$  in the initial undeformed geometry. At the outlet a specified average static pressure of zero was imposed. At all other walls, the velocity was taken to be the velocity of the walls, i.e. a no-slip, no-penetration condition relative to the walls. All boundary surfaces were moved as a simple sinusoidal scaling of the domain, according to

$$\mathbf{x}(t) = \mathbf{x}_0 [1 + \Lambda_w \sin(\omega t)], \quad (4.38)$$

where  $\mathbf{x}(t)$  is the position of a point at time  $t$ ,  $\mathbf{x}_0$  is the location of the corresponding point in its initial configuration at time  $t = 0$ ,  $\Lambda_w$  is the amplitude of the wall motion, and  $\omega$  is the angular frequency of the motion. For the cases considered here, the amplitude of the motion is taken to be  $\Lambda_w = \{0.125, 0.25\}$  and the angular frequency is taken such that the Womersley number,  $Wo = D_H/2\sqrt{\rho_f \omega/\mu_f} = 0.01$ . Note that the choice of parameters for these verification cases is not motivated by the study of a specific physiological process, rather we seek to choose parameters that are of the correct magnitude for the process of

**Table 4.1:** Summary of the maximum and average percent errors between the modelled value of  $K/(\epsilon D_H^2)$  and the value obtained using transient simulations in an alveolated duct and Eq. 4.37.

$\Lambda_w$	Max. % Error	Avg. % Error
0.125	1.3	1.0
0.250	4.5	1.9

breathing to test the modelling assumptions. For example, we do not claim that a constant velocity imposed at the entrance of the alveolated duct necessarily represents the breathing process as it occurs physiologically, rather it represents a simplified problem with the correct magnitude of the key parameters such that the assumptions of the model may be tested.

Results for the difference between the predicted dimensionless permeability in comparison to those obtained from the transient simulations and applying Eq. 4.37 at each timestep are summarized in Table 4.1. This shows that the modelled value of the dimensionless permeability matches well with the value obtained directly from the transient simulations conducted in the alveolated duct. Given the combined discretization errors of the permeability calculation and the direct CFD calculation, the agreement between the two cases for the  $\Lambda_w = 0.125$  case is regarded as excellent. For the  $\Lambda_w = 0.250$  case, the agreement is not as close, but is certainly quite reasonable. Considering that the simplified porous media model, which requires fairly basic calculations to solve, is able to match the results of a complex CFD calculation to within less than 5% at a large amplitude of motion, this approach has clear utility. Taking these results together implies that the theoretical development proposed in this work is indeed sound and that transient effects can be neglected within the closure problems. Further it shows that the impact of the alveolar expansion on the permeability is conveniently characterized through non-dimensionalization by the hydraulic diameter such that  $K/(\epsilon D_H^2)$  is a constant value throughout the transient expansion/contraction process as  $D_H$  changes.

### 4.3.3 One-dimensional Results for Flow in an Alveolated Duct

In this section, results are presented for one-dimensional flow in an alveolated duct, up to a terminal alveolus. In one dimension, the volume-averaged continuity equation, Eq. 4.5, reduces to

$$\frac{\partial \langle u \rangle}{\partial x} = -\frac{\partial \varepsilon}{\partial t}, \quad (4.39)$$

while the volume-averaged momentum equation, Eq. 4.32 reduces to

$$\rho_f \left[ \frac{\partial \langle u \rangle}{\partial t} + \frac{2 \langle u \rangle}{\varepsilon} \frac{\partial \langle u \rangle}{\partial x} \right] = -\varepsilon \frac{\partial \langle p \rangle^f}{\partial x} + \mu_f \frac{\partial^2 \langle u \rangle}{\partial x^2} - \frac{\varepsilon \mu_f \langle u \rangle}{K}, \quad (4.40)$$

where the porosity is considered to be a function of time, but constant in space for the purposes of this analysis. Defining the dimensionless groups

$$x^* = \frac{x}{D_H} \quad (4.41a)$$

$$u^* = \frac{\langle u \rangle}{U} \quad (4.41b)$$

$$p^* = \frac{\langle p \rangle^f}{\rho_f U^2} \quad (4.41c)$$

$$t^* = \frac{\omega t}{2\pi}, \quad (4.41d)$$

where  $U$  again represents a characteristic velocity, Eqs. 4.39 and 4.40 become

$$\frac{\partial u^*}{\partial x^*} = -\frac{2}{\pi} \frac{Wo^2}{Re_{D_H}} \frac{\partial \varepsilon}{\partial t^*} \quad (4.42)$$

and

$$\frac{2}{\pi} \frac{Wo^2}{Re_{D_H}} \frac{\partial u^*}{\partial t^*} + \frac{2u^*}{\varepsilon} \frac{\partial u^*}{\partial x^*} = -\varepsilon \frac{\partial p^*}{\partial x^*} + \frac{1}{Re_{D_H}} \frac{\partial^2 u^*}{\partial x^{*2}} - \frac{1}{Re_{D_H}} \left( \frac{K}{\varepsilon D_H^2} \right)^{-1} u^*, \quad (4.43)$$

respectively, where

$$Wo = \frac{D_H}{2} \sqrt{\frac{\rho_f \omega}{\mu_f}} \quad (4.44)$$

is the Womersley number and

$$Re_{D_H} = \frac{\rho_f U D_H}{\mu_f} \quad (4.45)$$

is the Reynolds number based on the hydraulic diameter of the central duct. Results are then to be obtained for an alveolated duct, where at  $x^* = 0$  there is a terminal alveolus such that  $u^* = 0$  and the pressure is the alveolar pressure  $p_a$ , or in dimensionless form  $p_a^*$ . To solve the problem described above the porosity and hydraulic diameter of the duct must be known as functions of time in order to properly define all of the parameters appearing in Eqs. 4.42 and 4.43. Let us assume both vary sinusoidally as

$$\frac{\varepsilon(t^*)}{\varepsilon_0} = 1 + \Lambda_\varepsilon \sin(2\pi t^*) \quad (4.46)$$

and

$$\frac{D_H(t^*)}{D_{H,0}} = 1 + \Lambda_{D_H} \sin(2\pi t^*), \quad (4.47)$$

respectively, where  $\varepsilon_0$  and  $D_{H,0}$  are the mean porosity and duct diameter and  $\Lambda_\varepsilon$  and  $\Lambda_{D_H}$  are the dimensionless amplitudes of the changes in porosity and diameter. Solving Eq. 4.42 using Eq. 4.46 and the boundary condition at  $x^* = 0$  results in a solution for  $u^*$  as

$$u^*(x^*, t^*) = -4 \frac{Wo^2}{Re_{D_H}} \varepsilon_0 \Lambda_\varepsilon \cos(2\pi t^*) x^*, \quad (4.48)$$

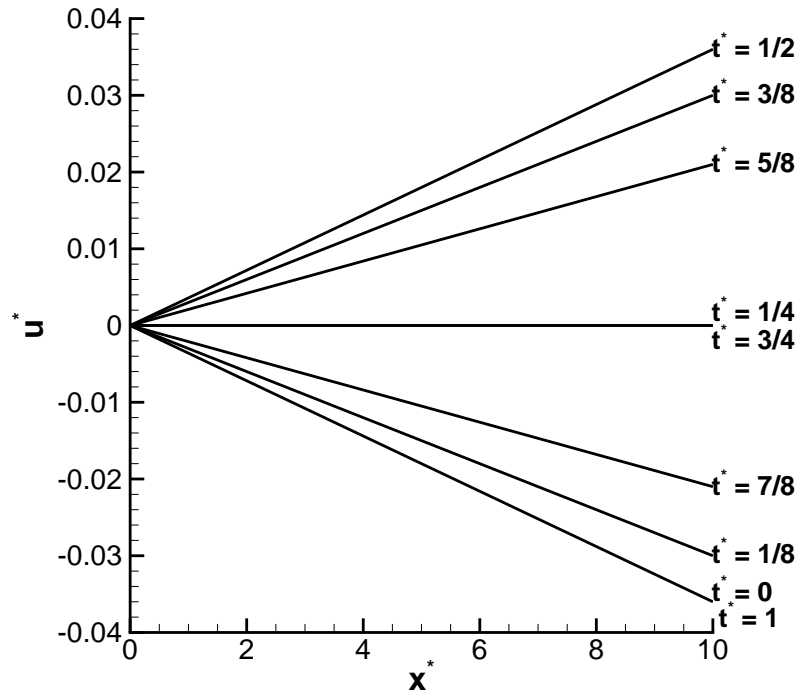
where both the Reynolds and Womersley numbers are functions of time, since they depend on  $D_H$ . This result shows that the velocity is linear in  $x^*$  such that the viscous term in Eq. 4.43 is zero, and the equation for  $\partial p^* / \partial x^*$  can be reduced to

$$\frac{\partial p^*}{\partial x^*} = -\frac{1}{\varepsilon} \left[ \frac{2 Wo^2}{\pi Re_{D_H}} \frac{\partial u^*}{\partial t^*} + \frac{2u^*}{\varepsilon} \frac{\partial u^*}{\partial x^*} + \frac{1}{Re_{D_H}} \left( \frac{K}{\varepsilon D_H^2} \right)^{-1} u^* \right], \quad (4.49)$$

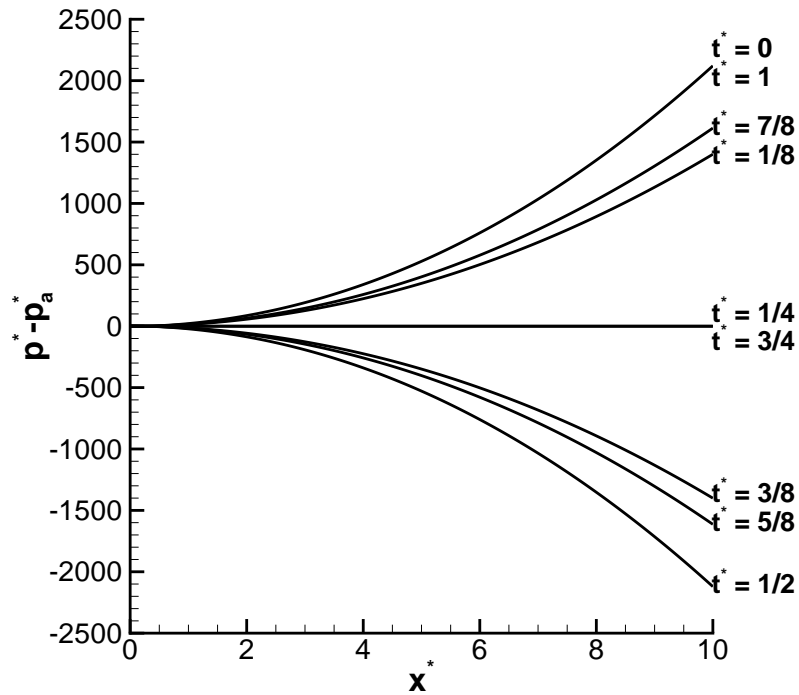
where all quantities on the right side of Eq. 4.49 are known for a given time, such that it can be numerically integrated to obtain pressure profiles for given instants in time. For the present results the initial Womersley and Reynolds numbers, that is the Womersley and Reynolds numbers at time  $t^* = 0$ , are taken to be  $Wo = Re_{DH} = 0.01$ . The initial porosity is taken to be  $\epsilon_0 = 0.9$ , which is a typical value for the lung parenchyma [3]. The amplitudes of the porosity and diameter variations are taken to be  $\Lambda_\epsilon = 0.1$  and  $\Lambda_{DH} = 0.25$ . Using these parameters, the dimensionless velocity profiles at selected times are plotted in Fig. 4.4a. Integrating Eq. 4.49 with respect to  $x^*$  using a variable-step Runge-Kutta method results in the pressure profiles shown in Fig. 4.4b up to  $x^* = 10$ .

As would be expected, this figure shows the same pressure profile,  $p^* - p_a^* = 0$ , at  $t^* = 1/4$  (maximum duct size and porosity) and  $t^* = 3/4$  (minimum duct size and porosity), since the fluid velocity is zero. Next, let us compare the pressure profiles at dimensionless times  $t^* = 1/8$  and  $t^* = 3/8$ . In these cases, all of  $u^*$ ,  $\partial u^*/\partial t^*$ , and  $\partial u^*/\partial x^*$  are of opposite sign, such that the first and third terms in Eq. 4.49 are of opposite sign and the second term is of the same sign. Thus, it appears that the convection term in Eq. 4.49 has a negligible influence on the pressure field since it is of opposite sign for the times considered, while no difference was observed in the pressure profile. A similar observation is made by comparing the pressure profiles at  $t^* = 5/8$  with those at  $t^* = 7/8$  and those at  $t^* = 0$  with those  $t^* = 1/2$ . Finally, the differences between the pressure profiles at  $t^* = 1/8$  and  $t^* = 7/8$  as well as at  $t^* = 3/8$  and  $t^* = 5/8$  warrants some discussion. Here, although all of the terms on the right side of Eq. 4.49 are of opposite sign when comparing the two sets of times, the hydraulic diameter of the duct and the porosity are smaller for the  $t^* = 5/8$  and  $t^* = 7/8$  cases, so the pressure increases more rapidly with  $x^*$ .

Comparing the present results with the one-dimensional results of Owen and Lewis [33] for their ‘alveolar capsule’ boundary conditions at lower oscillation frequencies, we find a favourable qualitative agreement. As in the present work, the velocity field was found to be a linear function of position, while pressure increased more rapidly. Note that a quantitative



(a)



(b)

**Figure 4.4:** A plot of (a) the dimensionless velocity and (b) the difference between the dimensionless pressure and the dimensionless alveolar pressure,  $p^* - p_a^*$ , as functions of the dimensionless coordinate  $x^*$  for initial Womersley and Reynolds numbers (at  $t^* = 0$ ) of  $Wo = Re_{DH} = 0.01$ ,  $\epsilon_0 = 0.9$ ,  $\Lambda_\epsilon = 0.1$ , and  $\Lambda_{DH} = 0.25$ .

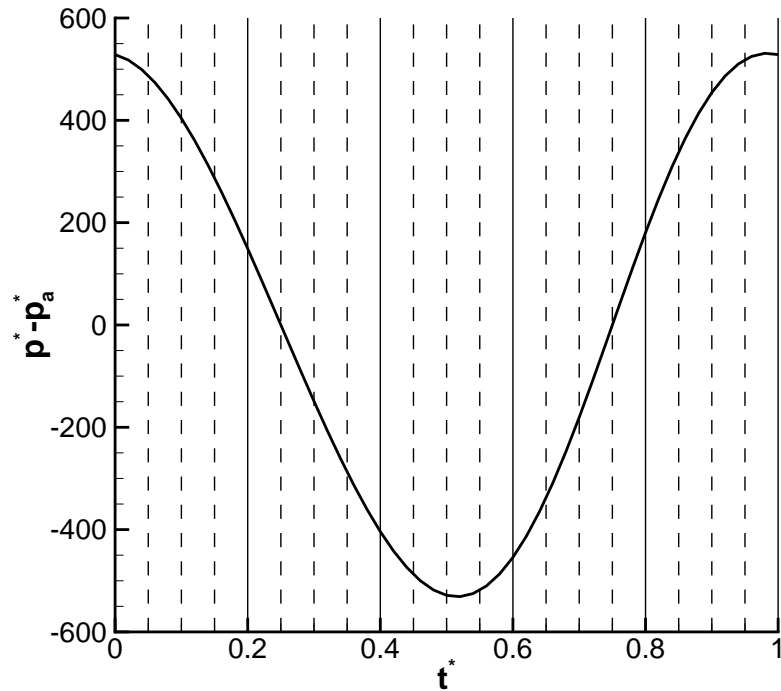


**Figure 4.5:** A plot of the difference between the dimensionless pressure and the dimensionless alveolar pressure,  $p^* - p_a^*$ , as a function of the dimensionless time,  $t^*$  at  $x^* = 5$  for initial Womersley and Reynolds numbers (at  $t^* = 0$ ) of  $Wo = Re_{DH} = 0.01$ ,  $\epsilon_0 = 0.9$ ,  $\Lambda_\epsilon = 0.1$ , and  $\Lambda_{DH} = 0.25$ .

comparison with the results of Owen and Lewis [33] is not attempted since they also solved the displacement of the solid tissue and used a very simplified estimate of the permeability.

One final point of interest is that the maximum and minimum values of pressure do not occur at peak expansion and peak contraction as might be expected. Rather, the minimum pressure occurs after peak expansion and the maximum pressure occurs before peak contraction, as shown in Fig. 4.5 for the point  $x^* = 5$ . This implies that after reaching peak expansion, there is a time lag before the minimum pressure is reached, but also that the pressure begins decreasing again before it reaches peak expansion.

## 4.4 Conclusions

In conclusion, a theoretically-based closure model has been applied to the study of air flow in an alveolated duct. The closure model is based upon the derivation of a transport equa-

---

tion for the spatial deviations of velocity and pressure and the use of constitutive equations to transform these terms into terms depending on volume-averaged quantities. There are several difficulties that are faced due to the transient nature of the flow and the assumption that porosity may vary in space and time, however, it is shown using rigorous scaling arguments that these factors may be ignored at the closure level and that the closure problem that must be solved reduces to that for a fixed, constant porosity medium. The resulting closure problem has been solved to obtain the permeability of the alveolated duct geometry, the scaling assumptions were verified using direct simulation of flow in an expanding and contracting alveolated duct, and some one-dimensional results for flow in an alveolated duct were presented using the proposed volume-averaged model. The key outcomes of this work are the permeability of the alveolated duct, which enables volume-averaged simulations to be conducted in large, three-dimensional regions of the lung parenchyma, as well as the simplified closure method which allows the permeability to be obtained for alveolated ducts in a straightforward manner.

## References

- [1] Tawhai, M. H. and Lin, C.-L., 2010, “Image-based modeling of lung structure and function,” *J. Magn. Reson. Imaging*, **32**, pp. 1421–1431.
- [2] West, J. B., 2008, *Respiratory Physiology: The Essentials*, Lippincott Williams & Wilkins, Baltimore.
- [3] Weibel, E. R., 1963, *Morphometry of the human lung*, Springer-Verlag, New York.
- [4] Comer, J. K., Kleinstreuer, C., Hyun, S., and Kim, C. S., 2000, “Aerosol transport and deposition in sequentially bifurcating airways,” *J. Biomech. Eng.*, **122**, pp. 152–158.
- [5] Gemci, T., Ponyavin, V., Chen, Y., Chen, H., and Collins, R., 2008, “Computational model of airflow in upper 17 generations of human respiratory tract,” *J. Biomech.*, **41**, pp. 2047–2054.
- [6] Zhang, Z., Kleinstreuer, C., and Kim, C. S., 2001, “Flow structure and particle transport in a triple bifurcation airway model,” *J. Fluids Eng.*, **123**, pp. 320–330.
- [7] Zhang, Z. and Kleinstreuer, C., 2002, “Transient airflow structures and particle transport in a sequentially branching lung airway model,” *Phys. Fluids*, **14**, pp. 862–880.
- [8] Zhang, Z. and Kleinstreuer, C., 2003, “Species heat and mass transfer in a human upper airway model,” *Int. J. Heat Mass Transfer*, **46**, pp. 4755–4768.
- [9] Luo, H. Y. and Liu, Y., 2008, “Modeling the bifurcating flow in a CT-scanned human lung airway,” *J. Biomech.*, **41**, pp. 2681–2688.

- 
- [10] Lin, C., Tawhai, M. H., Lennan, G. M., and Hoffman, E. A., 2009, "Multiscale simulation of gas flow in subject-specific models of the human lung," *IEEE Eng. Med. Biol. Mag.*, **28**, pp. 25–33.
- [11] Nowak, N., Kakade, P. P., and Annapragada, A. V., 2003, "Computational fluid dynamics simulation of airflow and aerosol deposition in human lungs," *Ann. Biomed. Eng.*, **31**, pp. 374–390.
- [12] Zhang, Z., Kleinstreuer, C., and Kim, C. S., 2008, "Airflow and nanoparticle deposition in a 16-generation tracheobronchial airway model," *Ann. Biomed. Eng.*, **36**, pp. 2095–2110.
- [13] Walters, D. K. and Luke, W. H., 2010, "A method for three-dimensional Navier-Stokes simulations of large-scale regions of the human lung," *J. Fluids Eng.*, **132**, pp. 051101–1–8.
- [14] van Ertbruggen, C., Hirsch, C., and Paiva, M., 2005, "Anatomically based three-dimensional model of airways to simulate flow and particle transport using computational fluid dynamics," *J. Appl. Physiol.*, **98**, pp. 970–980.
- [15] Ma, B. and Lutchen, K. R., 2006, "An anatomically based hybrid computational model of the human lung and its application to low frequency oscillatory mechanics," *Ann. Biomed. Eng.*, **34**, pp. 1691–1704.
- [16] Nazridoust, K. and Asgharian, B., 2008, "Unsteady-state airflow and particle deposition in a three-generation human lung geometry," *Inhal. Toxicol.*, **20**, pp. 595–610.
- [17] Comerford, A., Förster, C., and Wall, W. A., 2010, "Structured tree impedance outflow boundary conditions for 3D lung simulations," *J. Biomech. Eng.*, **132**, pp. 081002–1–10.

- 
- [18] Yin, Y., Choi, J., Hoffman, E. A., Tawhai, M. H., and Lin, C.-L., 2010, "Simulation of pulmonary air flow with a subject-specific boundary condition," *J. Biomech.*, **43**, pp. 2159–2163.
- [19] Walters, D. K. and Luke, W. H., 2011, "Computational fluid dynamics simulations of particle deposition in large-scale multigenerational lung models," *J. Biomech. Eng.*, **133**, pp. 011003–1–8.
- [20] Saksono, P. H., Nithiarasu, P., and Sazonov, I., 2012, "Numerical prediction of heat transfer patterns in a subject-specific human upper airway," *J. Heat Transfer*, **134**, pp. 031022–1–9.
- [21] Ma, B. and Darquenne, C., 2011, "Aerosol deposition characteristics in distal acinar airways under cyclic breathing conditions," *J. Appl. Physiol.*, **110**, pp. 1271–1282.
- [22] Tsuda, A., Henry, F. S., and Butler, J. P., 1995, "Chaotic mixing of alveolated duct flow in rhythmically expanding pulmonary acinus," *J. Appl. Physiol.*, **79**, pp. 1055–1063.
- [23] Darquenne, C. and Paiva, M., 1996, "Two- and three-dimensional simulations of aerosol transport and deposition in alveolar zone of human lung," *J. Appl. Physiol.*, **80**, pp. 1401–1414.
- [24] Lee, D. Y. and Lee, J. W., 2003, "Characteristics of particle transport in an expanding or contracting alveolated tube," *J. Aerosol Sci.*, **34**, pp. 1193–1215.
- [25] Karl, A., Henry, F. S., and Tsuda, A., 2004, "Low Reynolds number viscous flow in an alveolated duct," *J. Biomech. Eng.*, **126**, pp. 420–429.
- [26] Sznitman, J., Heimsch, F., Heimsch, T., Rusch, D., and Rösgen, T., 2007, "Three-dimensional convective alveolar flow induced by rhythmic breathing motion of the pulmonary acinus," *J. Biomech. Eng.*, **129**, pp. 658–665.

- 
- [27] Tsuda, A., Henry, F. S., and Butler, J. P., 2008, "Gas and aerosol mixing in the acinus," *Respir. Physiol. Neuro.*, **163**, pp. 139–149.
- [28] Sznitman, J., Heimsch, T., Wildhaber, J. H., Tsuda, A., and Rösgen, T., 2009, "Respiratory flow phenomena and gravitational deposition in a three-dimensional space-filling model of the pulmonary acinar tree," *J. Biomech. Eng.*, **131**, pp. 031010–1–16.
- [29] Kumar, H., Tawhai, M. H., Hoffman, E. A., and Lin, C.-L., 2009, "The effects of geometry on airflow in the acinar region of the human lung," *J. Biomech.*, **42**, pp. 1635–1642.
- [30] Harding, E. M. and Robinson, R. J., 2010, "Flow in a terminal alveolar sac model with expanding walls using computational fluid dynamics," *Inhal. Toxicol.*, **22**, pp. 669–678.
- [31] Li, Z. and Kleinstreuer, C., 2011, "Airflow analysis in the alveolar region using the lattice-Boltzmann method," *Med. Biol. Eng. Comput.*, **49**, pp. 441–451.
- [32] Kumar, H., Tawhai, M. H., Hoffman, E. A., and Lin, C.-L., 2011, "Steady streaming: A key mixing mechanism in low-Reynolds-number acinar flows," *Phys. Fluids*, **23**, pp. 041902–1–21.
- [33] Owen, M. R. and Lewis, M. A., 2001, "The mechanics of lung tissue under high-frequency ventilation," *SIAM J. Appl. Math.*, **61**, pp. 1731–1761.
- [34] Gray, W. G., 1975, "A derivation of the equations for multi-phase transport," *Chem. Eng. Sci.*, **30**, pp. 229–233.
- [35] Whitaker, S., 1997, *Volume Averaging of Transport Equations*, chap. 1, Fluid Transport in Porous Media, Springer-Verlag, Southampton, UK, pp. 1–59.
- [36] Whitaker, S., 1967, "Diffusion and dispersion in porous media," *A.I.Ch.E. J.*, **13**, pp. 420–427.

- 
- [37] Whitaker, S., 1969, "Advances in theory of fluid motion in porous media," *Ind. Engin. Chem.*, **61**, pp. 14–28.
- [38] Whitaker, S., 1996, "The Forchheimer equation: A theoretical development," *Transport Porous Med.*, **25**, pp. 27–61.

# Conjugate Fluid-Porous Flows with Moving Boundaries: Application to the Human Lung<sup>†</sup>

## 5.1 Introduction

The ability to simulate flow in the lung is of great interest to the medical community because of the potential advancements in respiratory drug delivery, particle deposition, etc. that can be attained with detailed knowledge of the flow patterns within the lung [1]. The air-filled portion of the lung can be separated into two main regions: (i) the conducting region, which consists of a network of bifurcating airways that transport air to the respiratory region, and (ii) the respiratory region, where gas exchange occurs by passive diffusion through the thin walls of the alveolar sacs which surround the respiratory airways [2]. As an inherently multi-scale problem, simulation of flow in the whole lung remains an extremely challenging task. Length scales range from the order of centimetres at the trachea to a fraction of a millimetre in the alveoli [2]. Additionally, there are approximately 300 mil-

---

<sup>†</sup>This chapter is an extension of the work presented in “Towards a Porous Media Model of the Human Lung” *Proceedings of the 4th International Conference on Porous Media and its Applications in Science, Engineering and Industry*, 2012 and published in AIP Conference Proceedings 1453, 6974, 2012.

lion alveolar sacs in the human lung [2], which cannot possibly be considered individually when simulating processes in the lung.

Computational fluid dynamics (CFD) simulations of flow have been conducted in both the upper airways [1, 3–19] and alveolated ducts within the respiratory region [20–31], however, there is great difficulty in connecting the results at the two levels in order to simulate processes in the whole lung. As computational power has increased over the years, the total number of airway segments considered in upper airway simulations has increased from seven [3] to over 1400 [4] (although the computational mesh was not sufficiently refined in this case to have grid-independent results). However, as the total number of airway segments in a full 23-generation airway tree would be more than 16 million, it is clear that simulations in a fully-resolved airway tree are well out of reach since hundreds of billions of mesh elements would be required to adequately discretize the domain [12, 18]. Thus, in order to simulate transport processes in the full lung, simplified models for the smaller conducting airways and the respiratory region are required. Several innovative methods for simulating more branches of the airway tree have been devised including those that simulate small subsections of the airway tree and use the outlet condition of one subunit as the input to the next subunit [10, 11], the use of partially resolved airway trees [4, 12], and the coupling of 3D CFD models for the upper airways with 1D resistance models for the lower airways [1, 9]. It is also worthwhile to note that even with advancements in computational abilities leading towards more detailed simulations in more extensive airway tree geometries, any physical description of the small-scale lung geometry may only be considered as an approximation, therefore, it is logical to consider applying approximate methods in modelling such regions of the lung. In the previous chapter, the theoretical development of a porous media model for flow in alveolated ducts within the human lung was described, which represents a reasonable candidate for an approximate model for processes in the respiratory region.

In light of the preceding discussion, it is the goal of this work to extend the capabili-

ties of the computational model described in Chapter 2 such that it is capable of solving problems in conjugate fluid-porous domains with moving grids and to demonstrate that the human lung geometry can be considered in this manner, where the upper airway tree is considered as a fluid region and the lower airways and alveoli are considered as a porous region. First, the governing equations will be outlined and the basic numerical method for solving the problem on moving grids, including the method of solving the mesh motion, are described. Next, the setup of the problem is discussed, including the method for obtaining the lung geometry from computed tomography (CT) images, details of creating a meshed lung model, parameter estimation, and boundary conditions. Finally, results are presented using the coupled fluid-porous description of the lung and the proposed numerical method. The results of this work constitute a platform for conducting simulations of transport in moving conjugate fluid-porous domains, which has been demonstrated using a realistic geometry of the human lung. The case involving the lung serves to illustrate the robustness of the model on a complicated geometry and also introduces a novel and potentially useful modelling paradigm for simulating processes in the lung upon further validation and possible calibration with experimental results.

## 5.2 Governing Equations and Numerical Methods

In this work, the lung is considered as a conjugate fluid-porous domain, where the fluid region is a truncated airway tree and the porous region is the remainder of the lung. In the fluid region, the flow is governed by the continuity and Navier-Stokes equations, while in the porous region it is governed by their volume-averaged counterparts. At the interface between the fluid and porous regions, the equations are coupled by appropriate interface conditions which ensure a balance of fluxes across interfaces, as well as a balance of viscous and pressure forces. The basic numerical approach taken in this work follows that presented in Chapter 2, which has been shown to be an effective method of coupling fluid and porous

regions where general unstructured grids are required to discretize the domain of interest.

Since breathing is driven by the motion of the boundary of the lung, the computational mesh must be considered to be moving for the cases under consideration in this work. Thus, modifications to the original method proposed in Chapter 2 must be made in order to formulate the method in an arbitrary Lagrangian-Eulerian (ALE) framework. Writing the governing mass and momentum equations for the fluid region in integral form, taking into account the mesh motion, results in [32, 33]

$$\int_{\partial\Omega} \mathbf{u} \cdot \mathbf{n} dS = 0 \quad (5.1)$$

and

$$\frac{\partial}{\partial t} \int_{\Omega} \rho_f \mathbf{u} dV + \int_{\partial\Omega} \rho_f \mathbf{u} (\mathbf{u} - \mathbf{u}_s) \cdot \mathbf{n} dS = - \int_{\partial\Omega} p \mathbf{n} dS + \int_{\partial\Omega} \mu_f \nabla \mathbf{u} \cdot \mathbf{n} dS, \quad (5.2)$$

where  $\Omega$  denotes an arbitrary control volume in space bounded by the control surface  $\partial\Omega$ . Differential elements of the control volume and control surface are denoted  $dV$  and  $dS$ , respectively, and the unit-normal vector to the surface  $\partial\Omega$  is denoted  $\mathbf{n}$ . The field variables  $\mathbf{u}$  and  $p$  denote the velocity vector and pressure, respectively, while  $\rho_f$  and  $\mu_f$  are the density and dynamic viscosity of the fluid. Finally,  $\mathbf{u}_s$  is the velocity of the control surface, which is used to account for mesh motion. Note that the mesh motion does not change the continuity equation since the fluid is considered to be incompressible [32].

Similarly, the integral forms of the mass and momentum equations presented in the previous chapter are, for a moving control volume, given as

$$\int_{\partial\Omega} \langle \mathbf{u} \rangle \cdot \mathbf{n} dS = - \int_{\Omega} \frac{\partial \varepsilon}{\partial t} dV \quad (5.3)$$

and

$$\begin{aligned} \frac{\partial}{\partial t} \int_{\Omega} \rho_f \langle \mathbf{u} \rangle dV + \int_{\partial\Omega} \frac{\rho_f}{\varepsilon} \langle \mathbf{u} \rangle (\langle \mathbf{u} \rangle - \mathbf{u}_s) \cdot \mathbf{n} dS = - \int_{\partial\Omega} \varepsilon \langle p \rangle^f \mathbf{n} dS + \int_{\partial\Omega} \mu_f \nabla \langle \mathbf{u} \rangle \cdot \mathbf{n} dS \\ - \int_{\Omega} \frac{\varepsilon \mu_f}{K} \langle \mathbf{u} \rangle dV, \end{aligned} \quad (5.4)$$

where  $\langle \mathbf{u} \rangle$  denotes the extrinsically volume-averaged velocity vector and  $\langle p \rangle^f$  denotes the intrinsically averaged pressure, according to the standard definitions of volume-averaged quantities [34, 35]. In this case, the permeability tensor,  $\mathbf{K}$ , is assumed to be diagonal such that the scalar permeability  $K$  may be used. Note that one might consider using a tensor permeability to bias the flow in the direction of ducts, however, for the purposes of this work it is assumed that the orientation of the ducts is random such that the flow has no preferred direction within the parenchyma. Also, as discussed in the previous chapter, the Forchheimer drag term is neglected since the Reynolds number in the lung parenchyma is very low. Furthermore, for simplicity of the governing equations, the porosity has been assumed to vary temporally, but not spatially, although the addition of a spatially varying porosity is relatively straightforward to implement numerically after expansion of the differential form of the convection term by the product rule. The variation in porosity will be further discussed in Sec. 5.3.4 which deals with the estimation of physical parameters of the lung parenchyma. Note that the porous-fluid interface conditions are the same as those for a fixed mesh, discussed in Chapter 2, and thus are not described here.

One final consideration when calculating flows on moving meshes is that one must ensure that the surface velocity,  $\mathbf{u}_s$ , is selected in such a way that volume is conserved in order to avoid artificial mass sources in the domain. This concept is expressed through the ‘geometric conservation law’ (GCL) [32, 33, 36–38], which is given as

$$\frac{\partial}{\partial t} \int_{\Omega} dV - \int_{\partial\Omega} \mathbf{u}_s \cdot \mathbf{n} dS = 0. \quad (5.5)$$

Discretization of Eqs. 5.1 to 5.4 is carried out in the same way as for a stationary mesh using a spatially second-order finite-volume method, as in Chapter 2, with the appropriate modifications to the transient and convection terms to account for the changing cell volume and control surface velocity [32, 33]. For the moving grid calculations presented herein, a first-order backward Euler method was used for the transient terms, which are discretized for a general scalar,  $\phi$ , as

$$\frac{\partial}{\partial t} \int_{\Omega} \phi dV = \frac{\phi_P V_P - \phi_P^o V_P^o}{\Delta t}, \quad (5.6)$$

where  $\phi = \rho_f \mathbf{u}$  in the fluid region and  $\phi = \rho_f \langle \mathbf{u} \rangle$  in the porous region,  $\phi_P^o$  indicates the value of  $\phi$  at the previous timestep at the centroid of the control volume  $P$ , and  $V_P$  and  $V_P^o$  are the volumes of control volume  $P$  at the current and previous timesteps, respectively. Additionally, the mass flux through a discrete control surface, which was calculated as  $\dot{m}_{ip} = \rho_f \langle \hat{\mathbf{u}} \rangle \cdot \mathbf{n}_{ip} A_{ip}$  for fixed meshes, is now computed as

$$\dot{m}_{ip} = \rho_f \langle \hat{\mathbf{u}} \rangle \cdot \mathbf{n}_{ip} A_{ip} - \rho_f \mathbf{u}_{s,ip} \cdot \mathbf{n}_{ip} A_{ip}, \quad (5.7)$$

to account for the motion of the control surface through which the mass flux is calculated, where  $\mathbf{u}_{s,ip}$  is the surface velocity at the integration point  $ip$  and  $\mathbf{n}_{ip}$  is the unit normal vector to the discrete control surface at  $ip$  with area  $A_{ip}$ .

Geometric conservation is enforced by computing the surface velocity in such a way that the discretized form of Eq. 5.5 is satisfied to machine precision, i.e.

$$\frac{V_P - V_P^o}{\Delta t} = \sum_{ip=1}^{N_{ip}} \mathbf{u}_{s,ip} \cdot \mathbf{n}_{ip} A_{ip} = \sum_{ip=1}^{N_{ip}} \frac{\delta V_{ip}}{\Delta t}, \quad (5.8)$$

where  $N_{ip}$  is the number of discrete control surfaces surrounding  $P$  and  $\delta V_{ip}$  is the volume swept by the motion of the discrete control surface containing  $ip$  from the previous timestep

to the current timestep. Thus, selecting

$$\mathbf{u}_{s,ip} \cdot \mathbf{n}_{ip} A_{ip} = \frac{\delta V_{ip}}{\Delta t} \quad (5.9)$$

for all control surfaces guarantees the satisfaction of the GCL since the sum of all swept volumes equals the change in volume represented on the left side of Eq. 5.8. Note that the GCL has been shown using a first-order backward Euler discretization of the transient terms, however, this may be extended to higher order temporal schemes if desired.

In addition to discretization of the governing equations, a procedure for updating the locations of the mesh nodes, based on prescribed boundary motions, is required. Several strategies have been proposed that fall into the class of ‘spring-analogy’ methods which considers the mesh edges as tension springs [38, 39] or torsion springs [40, 41] in order to solve for the nodal displacements. Spring analogy methods, however, will eventually fail given large enough boundary displacements [42]. To accommodate larger mesh motions, algorithms have been proposed which use a linear elasticity analogy [42, 43], which are exceptionally robust but also computationally expensive. For the purposes of this work, the motion of the mesh nodes is determined by numerically solving Laplace’s equation with a variable diffusion coefficient and Dirichlet conditions on all domain boundaries [44], which is reasonably robust for large deformations, is relatively straightforward to implement, and is not overly expensive computationally. The Laplace equation, given by

$$\nabla \cdot (\Gamma \nabla \mathbf{v}) = \mathbf{0}, \quad (5.10)$$

where  $\Gamma$  is the mesh stiffness and  $\mathbf{v}$  is the mesh displacement, is discretized using a cell-centred finite-volume method, similar to that used to solve all other transport equations. Since the resulting displacements are stored at the cell centres, they must be interpolated to the nodal locations in order to reposition the nodes. Although using a nodal formulation may be a more natural choice for this problem, no particular difficulties were encountered

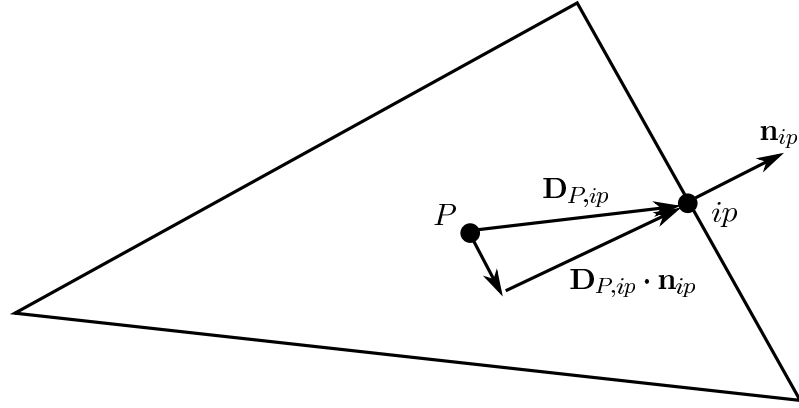


**Figure 5.1:** An illustration of a control volume,  $P$ , with the relevant geometric parameters for evaluating the normal derivative noted.

as a result of the cell-centred formulation employed in this work. The mesh stiffness,  $\Gamma$ , is taken to be inversely proportional to the cell volume such that larger cells absorb more of the motion and smaller cells move more like a rigid body. Since  $\Gamma$  is different for each control volume, an approach similar to that for diffusion across a fluid-porous interface is adopted. Discretization of Eq. 5.10 using the finite-volume method, for a control volume  $P$  results in

$$\sum_{ip=1}^{N_{ip}} \Gamma_P \nabla \mathbf{v}|_{ip} \cdot \mathbf{n}_{ip} A_{ip} = \mathbf{0}, \quad (5.11)$$

where again  $ip$  refers to the integration points surrounding the volume  $P$ . The gradient term is given as

$$\begin{aligned} \nabla \mathbf{v}|_{ip,P} \cdot \mathbf{n}_{ip} = & \frac{\mathbf{v}_{nb} - \mathbf{v}_P}{(\mathbf{D}_{P,ip} \cdot \mathbf{n}_{ip}) - \frac{\Gamma_P}{\Gamma_{nb}} (\mathbf{D}_{nb,ip} \cdot \mathbf{n}_{ip})} + \frac{(\mathbf{D}_{nb,ip} - (\mathbf{D}_{nb,ip} \cdot \mathbf{n}_{ip}) \mathbf{n}_{ip})}{(\mathbf{D}_{P,ip} \cdot \mathbf{n}_{ip}) - \frac{\Gamma_P}{\Gamma_{nb}} (\mathbf{D}_{nb,ip} \cdot \mathbf{n}_{ip})} \cdot \nabla \mathbf{v}|_{nb} \\ & - \frac{(\mathbf{D}_{P,ip} - (\mathbf{D}_{P,ip} \cdot \mathbf{n}_{ip}) \mathbf{n}_{ip})}{(\mathbf{D}_{P,ip} \cdot \mathbf{n}_{ip}) - \frac{\Gamma_P}{\Gamma_{nb}} (\mathbf{D}_{nb,ip} \cdot \mathbf{n}_{ip})} \cdot \nabla \mathbf{v}|_P, \quad (5.12) \end{aligned}$$

where the first term on the right side of Eq. 5.12 can be treated implicitly, while the remaining terms are explicit, and the relevant geometric parameters are shown in Fig. 5.1 for the volume  $P$ . Note the definitions of the displacements are  $\mathbf{D}_{P,ip} = \mathbf{x}_{ip} - \mathbf{x}_P$  and  $\mathbf{D}_{nb,ip} = \mathbf{x}_{ip} - \mathbf{x}_{nb}$ , where  $\mathbf{x}_{ip}$ ,  $\mathbf{x}_P$ , and  $\mathbf{x}_{nb}$  are the positions of the integration point, cell

centre of  $P$ , and cell centre of  $nb$ , respectively.

## 5.3 Problem Setup

### 5.3.1 CT Image Segmentation

Low-dose whole lung CT images obtained from a single breath hold with a 1.25 mm slice thickness were obtained from the ELCAP Public Lung Image Database (<http://www.via.cornell.edu/databases/lungdb.html>). From these images, a three-dimensional representation of the airway tree, up to a certain bifurcation, and a representation of the remaining lung volume were required. The truncated airway tree was extracted using the segmentation software ITK-SNAP [45], however, only a limited number of bifurcations were captured to prevent the segmented volume from leaking into regions of the lung outside of the airways. The resulting segmentation was exported as a stereolithography (STL) file and was smoothed and decimated (to reduce the total number of facets) using MeshLab (<http://meshlab.sourceforge.net/>).

The remaining lung volume was segmented by first using the automatic threshold segmentation feature in OsiriX [46], however, due to limitations in the segmentation algorithm, it was not possible to exclude the airway tree from the segmented volume. Thus, the airways were manually removed from the segmented volume and any geometric problems were manually repaired. The segmentation obtained in OsiriX was then exported as a new image series and segmented using ITK-SNAP [45], which produced significantly smoother surfaces than OsiriX. Again, MeshLab was used to smooth and decimate the exported faceted surface.

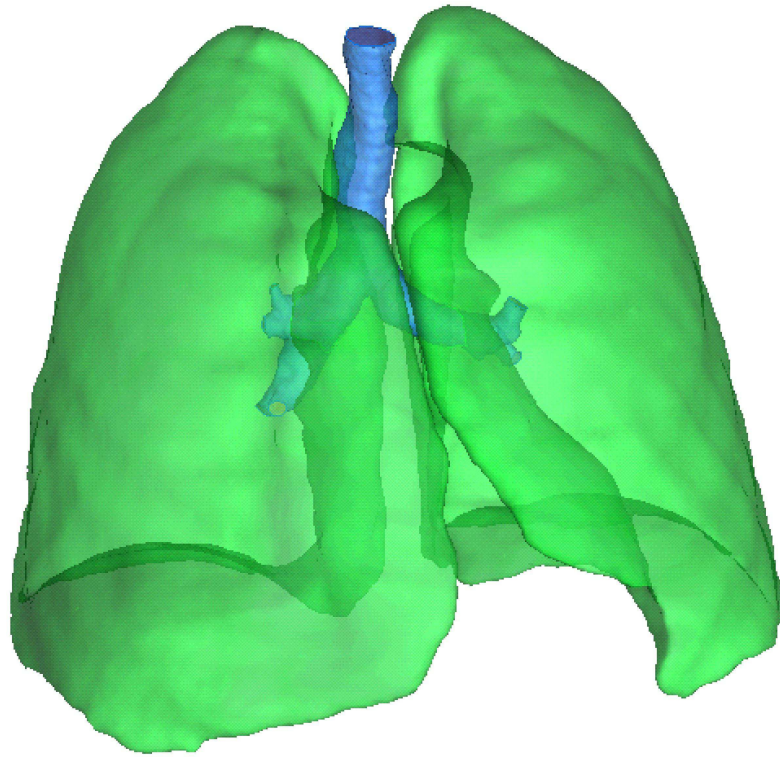


**Figure 5.2:** *An illustration of the combined airway tree (blue) and the lung surfaces (green).*

### 5.3.2 Geometric Model and Meshing

After segmentation, the STL surfaces generated for the airway tree and the remaining lung volume were imported into ANSYS<sup>®</sup> ICEM CFD, Release 13.0, to be combined, further cleaned up, and meshed for CFD simulations. The airway and lung volume surfaces were first intersected and the portion of the lung surface penetrated by the airway tree was removed. Additionally, the ends of the airway tree branches and trachea were modified such that they formed flat surfaces. The resulting surface model is shown in Fig. 5.2. From this figure, it is obvious that the CT images did not include details of the mouth and larynx. If one were to conduct simulations of purely inspiratory flow in a truncated airway tree, this configuration would not necessarily pose a problem since a standard inlet boundary condition could be applied where the trachea is truncated. However, in this case, a full breathing cycle with both inspiratory and expiratory flow is to be considered and the flow is to be driven by the motion of the boundary. Therefore, the opening where the trachea is

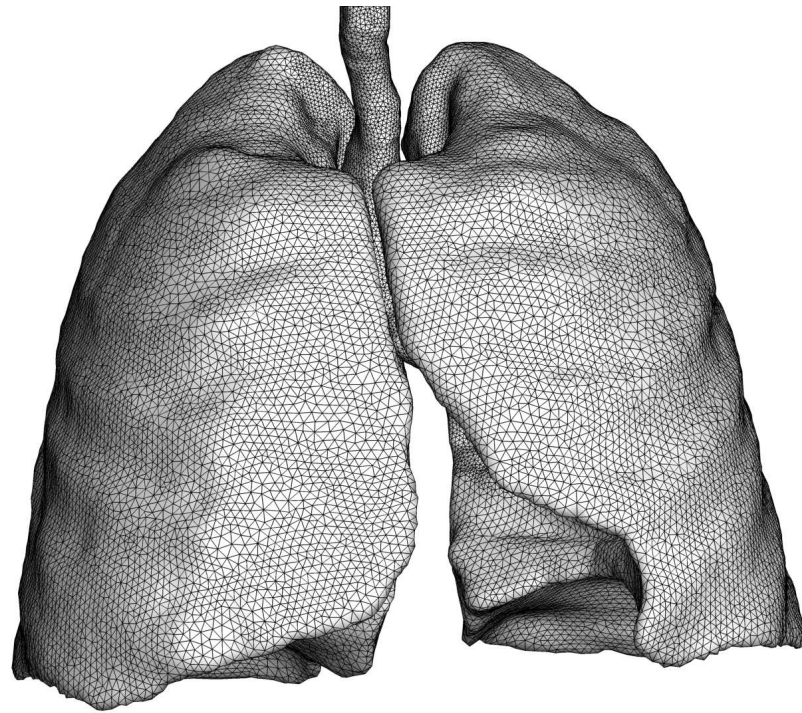
truncated must allow both inflow and outflow, possibly simultaneously when the bulk flow is changing direction. As a result, the trachea was extended somewhat to allow the flow to develop more fully before exiting the domain and a hemispherical cap was added to mimic expansion to an open environment. Treatment of this boundary will be discussed further in Sec. 5.3.5.

The resulting geometric model was meshed in ANSYS® ICEM CFD, Release 13.0, using tetrahedral volumes that were refined near fluid-porous interfaces as well as at the airway walls and the lung boundary. The meshed model is shown in Figs. 5.3a and 5.3b which show the main lung volume and the trachea extension, respectively.

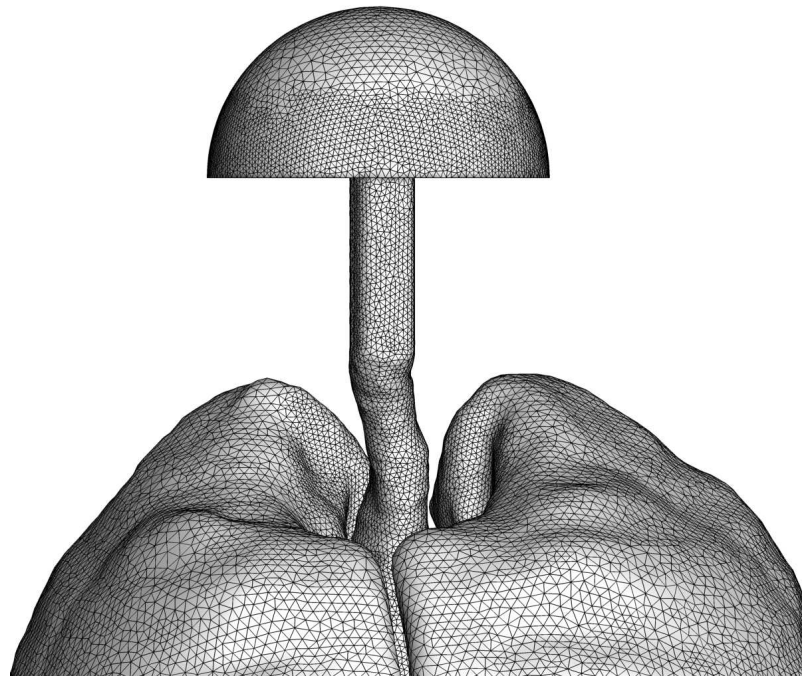
### 5.3.3 Grid Motion

To provide boundary conditions for Eq. 5.10, an estimate of the breathing rate and the nature of the lung motion is required. For the test cases considered, a breathing rate of 12 breaths per minute was chosen, which is within the normal range of breathing rates [47]. The motion of the lung, which drives breathing, is a result of the motion of the diaphragm, a thin sheet of muscle located along the bottom surface of the lung [47]. Although there is also motion of the ribcage, it has been shown that the magnitude of the motion of the diaphragm is somewhat larger [48]. Thus, for simplicity, it is assumed for the purposes of this work that all motion is driven by the diaphragm and that the magnitude of its motion is 1.5 cm, consistent with normal breathing [47]. It is found that this specification of the lung motion results in a tidal volume of approximately 400 mL, which is slightly smaller than the typical tidal volume of 500 mL given by West [47], thus represents light breathing. It should be noted at this point that the lung motion is simply a boundary condition to the mesh motion algorithm and is thus easily modified if one wishes to explore more elaborate specifications of its motion to better reflect reality.

Although it has been stated that the mesh motion at the diaphragm should be 1.5 cm, the mesh motion must be specified on all boundaries in order to solve for the motion of



(a)



(b)

**Figure 5.3:** Plots of the computational meshes for the lung geometry showing (a) the main lung mesh and (b) the trachea extension.

the interior nodes. In this case, the motion of all boundaries nodes is taken to be in the  $z$ -direction, where the flat surface where the trachea was cut lies in the  $xy$ -plane. The magnitude of the displacement should be 1.5 cm at the base of the lung, whereas at the top of the lung it should be zero. Thus, an appropriate variation between these two values must be specified. To avoid motion of the truncated airways, the motion is blended between a value of zero and 1.5 cm in the region below the truncated airways. To avoid bunching of nodes below the airway tree, the magnitude of the displacement is blended sigmoidally and is adjusted such that centre of the sigmoid function moves with the displacement. With all of these considerations taken into account the magnitude of the mesh displacement for a given time step on the boundaries is given by

$$d_i = [1 + \exp(100(z + z_o))]^{-1} \frac{d_{max}}{2} \omega \sin(\omega t_i) \Delta t_i \quad (5.13)$$

where  $d_{max}$  is the maximum displacement occurring at the base of the lung (1.5 cm in this case),  $\omega$  is the angular frequency of the breathing motion,  $\Delta t$  and  $t_i$  are the timestep size and time value at the timestep  $i$ , and  $z_o$  is an offset value, given by

$$z_o = 0.3 - \frac{1}{2} \sum_{i=1}^n \frac{d_{max}}{2} \omega \sin(\omega t_i) \Delta t_i \quad (5.14)$$

where  $n$  is the current timestep number. Figure 5.4 illustrates the sigmoidal blending factor  $[1 + \exp(100(z + z_o))]^{-1}$  as a function of the  $z$  coordinate in relation to the fully inflated lung geometry, where the offset,  $z_o$ , is at its base value of 0.3.

### 5.3.4 Parameter Estimation

According to Weibel's idealized 'Model A' lung geometry, more than three quarters of the volume of air in the lung resides in generations 20 to 23, which are fully alveolated ducts or alveolar sacs [2]. Further, almost 90% of the air resides in generations 17 to 23 which have at least some degree of alveolation [2]. Thus, a logical approximation for the

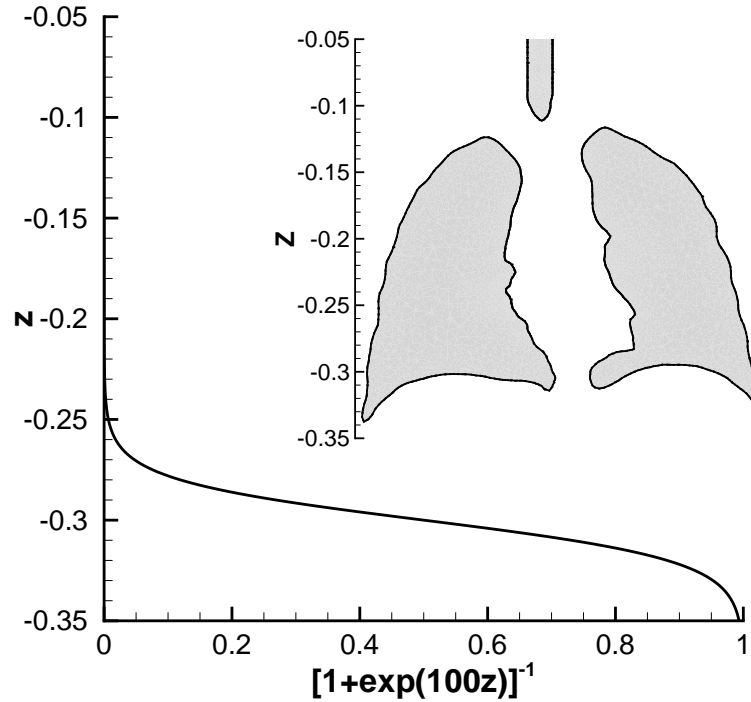


**Figure 5.4:** Plots the blending factor for the lung motion with reference to a 2D section of the lung in its maximally inflated state.

permeability of the lung parenchyma is the permeability of an alveolated duct, which has been determined numerically in the previous chapter. Taking a volume-weighted average of the airway diameters in generations 17 to 23 given by Weibel [2] yields an average diameter of 0.43 mm. Using this average diameter and the previous result for the dimensionless permeability yields an estimate for the average permeability of the lung parenchyma of  $K/\varepsilon = 1.75 \times 10^{-9} \text{ m}^2$ , where the porosity remains to be determined.

According to Weibel [2], only 10% of the parenchyma is composed of tissue and the remainder is composed of air. This leads naturally to an estimate of the porosity as  $\varepsilon = 0.9$ , which means the permeability is  $K = 1.58 \times 10^{-9} \text{ m}^2$ . Note that this estimate is for the airway diameter at mean inflation, so it will change with expansion and contraction of the lung. For the purposes of this work it will be assumed that the porosity and hydraulic diameter of the duct vary sinusoidally with time, according to

$$\varepsilon = \varepsilon_0[1 + \Lambda_\varepsilon \cos(\omega t)] \quad (5.15)$$

and

$$D_H = D_{H,0}[1 + \Lambda_{D_H} \cos(\omega t)], \quad (5.16)$$

where  $\varepsilon_0$  and  $D_{H,0}$  are the porosity and hydraulic diameter at mean inflation and  $\Lambda_\varepsilon$  and  $\Lambda_{D_H}$  are the dimensionless amplitudes of the changes in porosity and hydraulic diameter, respectively. This leads to the permeability as a function of time, given as

$$K = K_0[1 + \Lambda_\varepsilon \cos(\omega t)][1 + \Lambda_{D_H} \cos(\omega t)]^2, \quad (5.17)$$

where  $K_0$  is the permeability at mean inflation, i.e.  $K_0 = 1.58 \times 10^{-9} \text{ m}^2$ . According to studies by Sznitman et al. [24] and Harding and Robinson [28], the volume of an alveolated duct changes by approximately 15% from minimum to maximum inflation, indicating that the length scale of the duct changes by about 5%. Accordingly, the amplitude of the change in duct diameter is taken to be  $\Lambda_{D_H} = 0.025$ . The amplitude of the porosity change is much more difficult to determine accurately, although it is expected to be reasonably small. Thus, for the purposes of the present study  $\Lambda_\varepsilon$  is taken to be zero, although with more information the porosity change can be taken into account using the equations outlined previously.

### 5.3.5 Boundary Conditions

The walls of the airway tree are considered as fixed no-slip, impenetrable walls, such that all velocity components may be set to zero and the pressure is extrapolated from the interior of the domain to the boundary. Note that the walls of the extended trachea and the flat lower surface of the hemispherical cap are treated in the same way as fixed walls. The lung boundary is considered to be a moving no-slip, impenetrable wall and the velocity components are selected such that there is no mass flux through any of the control surfaces on the moving walls. On the moving walls, the pressure is also extrapolated from the interior of the domain.

At the open boundary, i.e. the curved portion of the hemispherical cap, the derivatives of

all velocity components normal to the boundary are set to zero. When the fluid is exiting the domain, a constant static pressure is specified, whereas when the fluid enters the domain, a constant dynamic pressure is specified, as recommended by Mathur and Murthy [49] for open boundaries. Mathematically, this condition is stated as

$$p_b = \begin{cases} p_\infty, & \dot{m}_b \geq 0 \\ p_\infty - \frac{1}{2}\rho_f u_b^2, & \dot{m}_b < 0 \end{cases}, \quad (5.18)$$

where  $u_b$  is the magnitude of the velocity at the boundary,  $\dot{m}_b$  is the mass flux through the boundary control surface, and  $p_\infty$  is a specified ambient pressure. Note that  $u_b$  is obtained from the mass flux at the integration point on the boundary as  $u_b = \dot{m}_b/(\rho_f A_b)$ , where  $A_b$  is the area of the boundary control surface.

## 5.4 Results and Discussion

### 5.4.1 Parameters of Study

The model for air flow in the human lung described in the previous sections was run for five full breath cycles to ensure any initial transient behaviour was dissipated and results were extracted from the final full breath cycle computed. For the purposes of the results to be presented, the time  $t = 0$  corresponds to the beginning of the final breath cycle. The computational mesh, shown previously in Fig. 5.3 contained 911,156 tetrahedral control volumes. In this section, results will be presented for the maximum pressure difference across the domain, representing the pressure drop from the trachea to the most distal alveolus, as well as pressure contours on the surface of the lung and velocity vectors in a plane intersecting the bifurcation from the trachea to the main bronchi. Although detailed experimental data for comparison is not yet available, connections will be made with typical values for pressure drop in the lung.

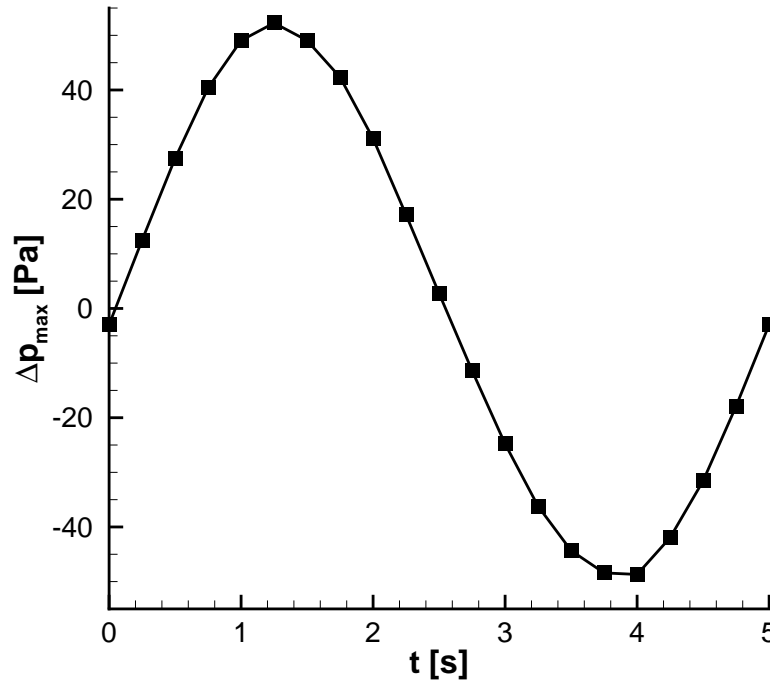


**Figure 5.5:** A plot of the maximum pressure difference within the domain as a function of time, where  $t = 0$  represents the beginning of the breath cycle at maximum inflation.

#### 5.4.2 Alveolar Pressure

Figure 5.5 shows the maximum pressure difference across the domain, representing the pressure drop from the inlet surface to the most distal alveolus, where the pressure difference is maximum. Note the maximum magnitude of the alveolar pressure shown in this figure is just over 50 Pa, which is the correct order of magnitude for a healthy lung which has a pressure drop on the order of 1 cm H<sub>2</sub>O (98 Pa) for normal breathing [47]. Since the breathing simulated here is light breathing with only 80% of the tidal volume as compared to normal breathing, this is indeed the correct magnitude for the pressure drop. Certainly, this increases confidence in the validity of this approach and the method of estimating the permeability, although experimental verification should be pursued in the future.

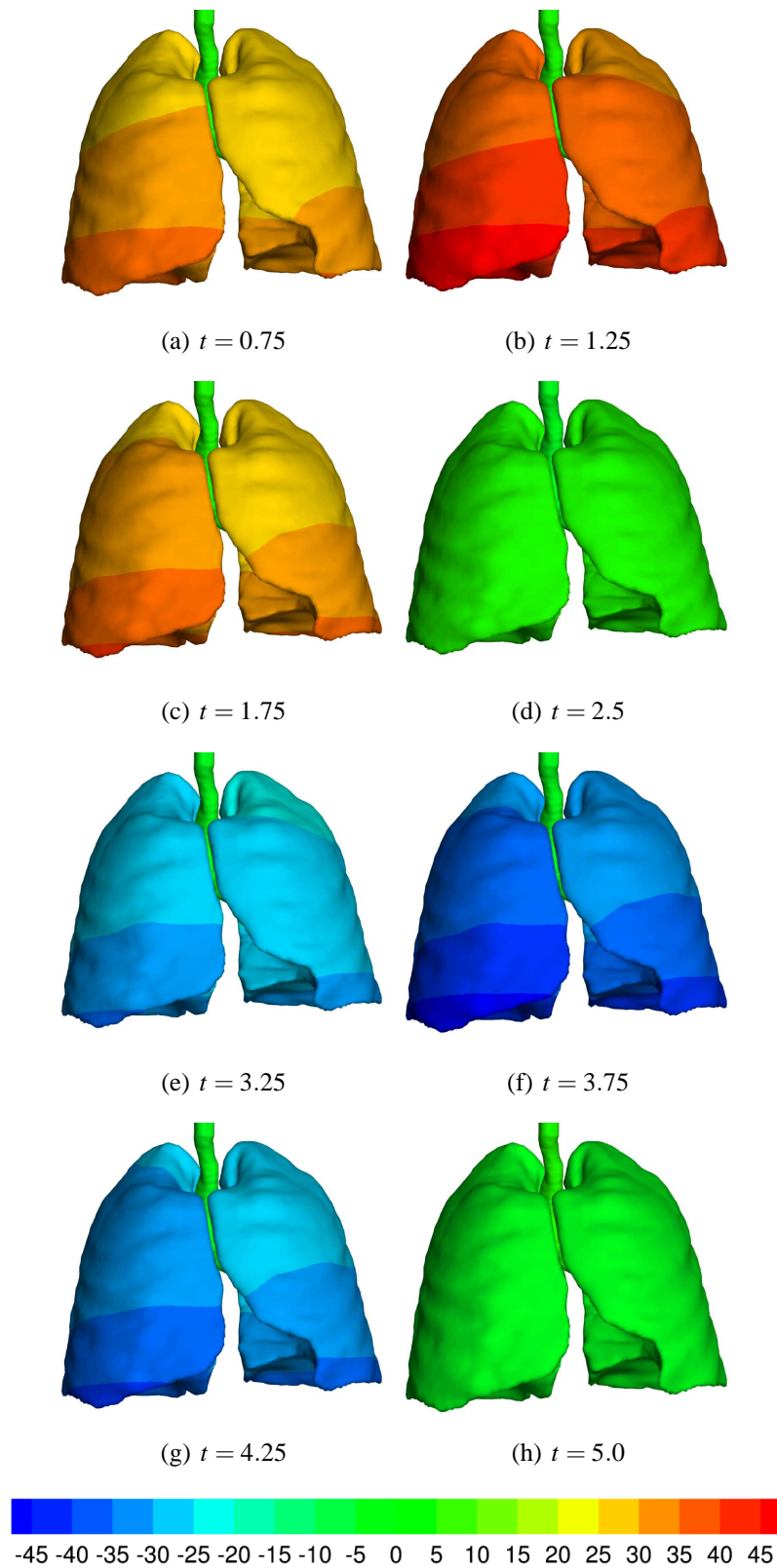


**Figure 5.6:** Contour plots of the pressure in Pascals for the times (a) 0.75, (b) 1.25, (c) 1.75, (d) 2.5, (e) 3.25, (f) 3.75, (g) 4.25, (h) 5.0 seconds from the beginning of the breath cycle.

### 5.4.3 Pressure Field

Contour plots of the pressure on the surface of the lung model are given in Fig. 5.6 for various times within the breath cycle. This figure illustrates the higher pressures exhibited during expiration near the diaphragm where the lung motion is largest in Figs. 5.6a-c. In its fully contracted state, shown in Fig. 5.6d, and in its fully expanded state, shown in Fig. 5.6h, the pressure is nearly zero everywhere since there is no net flow in or out of the lung. In Figs. 5.6e-g it is shown that the pressure is lower near the base of the lung as the air is drawn into the lung. In all cases, it can be seen that the pressure within the trachea is similar.

### 5.4.4 Velocity Field

Velocity vectors at two time points are shown in Fig. 5.7 in an  $xz$ -plane that intersects a portion of the trachea and the region where the trachea bifurcates into the main bronchi. Figures 5.7a,b show the vectors for the time  $t = 1.25$  s from the beginning of the breath cycle (peak expiratory flow rate) while Figs. 5.7c,d show the vectors for the time  $t = 3.75$  s from the beginning of the breath cycle (peak inspiratory flow rate). These figures show the velocity magnitude dropping significantly after the main bronchi bifurcate, such that the velocity vectors are hardly visible. Within the porous region, the velocity is clearly very small as expected for the respiratory region. Note the bursts of velocity shown in Figs. 5.7a,c which occur where the slice intersects a smaller airway included in the fluid region.

### 5.4.5 Comparison with Direct CFD Approach

With the results presented, it is important to put into perspective the advantages of the proposed approach to simulating processes in the lung. In comparison to direct simulations in truncated airway trees, the proposed approach has the clear advantage of being able to consider both an upper airway tree and the remainder of the lung through the porous media

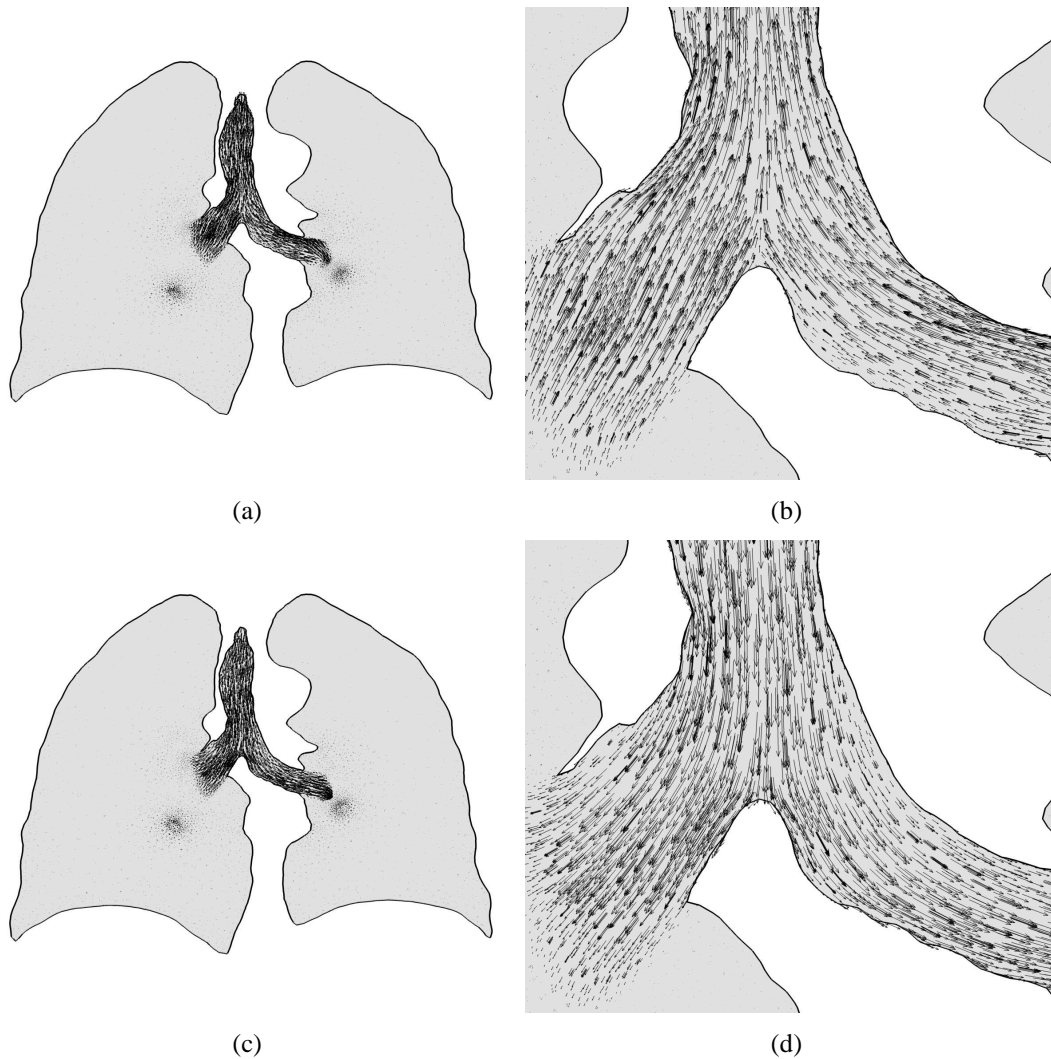


**Figure 5.7:** Contour plots of velocity vectors in the  $xy$ -plane, at times (a,b) 1.25 and (c,d) 3.75 s from the beginning of the breath cycle.

model. Additionally, the computational cost of adding the porous region is significantly less than adding enough airway branches to the direct CFD model to capture the full lung or any significant part of the respiratory region. Note that the current model employed 911,156 control volumes and that a fully-resolved airway tree would require an estimated 720 billion control volumes [12, 18].

As another comparison, consider the recent work of Gemci et al. [4] which simulated 1433 individual airway branches across 17 generation of the human lung. While this is far from the more than 100,000 branches actually present in 17 airway generations, the

6.7 million control volumes used to discretize the domain (the upper limit possible on the given hardware) was far from sufficient for obtaining grid independent results. To estimate the number of control volumes actually required, consider the work of Yin et al. [17] who were able to obtain grid-independent results in a realistic 4-5 generation airway geometry using 4.6 million control volumes. Recently, Walters and Luke [12] proposed a novel stochastic coupling method to reduce the number of flow paths that must be simulated directly, although up to 4.3 million control volumes were still required to discretize an 8-generation airway tree model. Although the proposed method is also somewhat computationally expensive, taking on the order of three to four days of computational time (depending on convergence criteria, timestep selection, etc.) to compute five full breath cycles using 32 processors in parallel, there still appears to be an advantage in terms of reduced computational requirements that can be attained in comparison to the previously mentioned approaches. Even with significant grid refinement and the addition of several more airway generations, it is doubtful that the current model would need to approach the number of control volumes required for reasonably extensive airway tree computations and certainly not the requirements for a full airway tree model.

## 5.5 Summary and Future Directions

In summary, this chapter presented the development of a numerical method for computing flows in conjugate fluid-porous domains with moving boundaries. While the method is general and can be used to solve a wide range of problems in porous media, its robustness has been demonstrated using a complex, physiologically-realistic geometry of the human lung. This case was selected because it is believed that a coupled fluid-porous model of the lung provides a convenient method of simulating processes in the full lung that is considerably more efficient than simulating flow in large airway trees, since as the airways become smaller and more numerous, the computational costs increase dramatically. Additionally,

the details of the flow in very small airways and alveoli are not generally of interest, rather their bulk behaviour is sought. Thus, a porous media approach appears logical.

In the future, it is foreseen that this modelling paradigm will prove useful for modelling transport processes in the lung for applications such as respiratory drug delivery. While this work serves to introduce this new approach, it is expected that future work will be directed at experimental validation and calibration of the model, improved specification of the boundary motion using imaging and/or solid mechanics techniques, and the addition of more transport models for particle and species transport.

## References

- [1] Tawhai, M. H. and Lin, C.-L., 2010, “Image-based modeling of lung structure and function,” *J. Magn. Reson. Imaging*, **32**, pp. 1421–1431.
- [2] Weibel, E. R., 1963, *Morphometry of the human lung*, Springer-Verlag, New York.
- [3] Comer, J. K., Kleinstreuer, C., Hyun, S., and Kim, C. S., 2000, “Aerosol transport and deposition in sequentially bifurcating airways,” *J. Biomech. Eng.*, **122**, pp. 152–158.
- [4] Gemci, T., Ponyavin, V., Chen, Y., Chen, H., and Collins, R., 2008, “Computational model of airflow in upper 17 generations of human respiratory tract,” *J. Biomech.*, **41**, pp. 2047–2054.
- [5] Zhang, Z., Kleinstreuer, C., and Kim, C. S., 2001, “Flow structure and particle transport in a triple bifurcation airway model,” *J. Fluids Eng.*, **123**, pp. 320–330.
- [6] Zhang, Z. and Kleinstreuer, C., 2002, “Transient airflow structures and particle transport in a sequentially branching lung airway model,” *Phys. Fluids*, **14**, pp. 862–880.
- [7] Zhang, Z. and Kleinstreuer, C., 2003, “Species heat and mass transfer in a human upper airway model,” *Int. J. Heat Mass Transfer*, **46**, pp. 4755–4768.
- [8] Luo, H. Y. and Liu, Y., 2008, “Modeling the bifurcating flow in a CT-scanned human lung airway,” *J. Biomech.*, **41**, pp. 2681–2688.
- [9] Lin, C., Tawhai, M. H., Lennan, G. M., and Hoffman, E. A., 2009, “Multiscale sim-

- ulation of gas flow in subject-specific models of the human lung,” *IEEE Eng. Med. Biol. Mag.*, **28**, pp. 25–33.
- [10] Nowak, N., Kakade, P. P., and Annapragada, A. V., 2003, “Computational fluid dynamics simulation of airflow and aerosol deposition in human lungs,” *Ann. Biomed. Eng.*, **31**, pp. 374–390.
- [11] Zhang, Z., Kleinstreuer, C., and Kim, C. S., 2008, “Airflow and nanoparticle deposition in a 16-generation tracheobronchial airway model,” *Ann. Biomed. Eng.*, **36**, pp. 2095–2110.
- [12] Walters, D. K. and Luke, W. H., 2010, “A method for three-dimensional Navier-Stokes simulations of large-scale regions of the human lung,” *J. Fluids Eng.*, **132**, pp. 051101–1–8.
- [13] van Ertbruggen, C., Hirsch, C., and Paiva, M., 2005, “Anatomically based three-dimensional model of airways to simulate flow and particle transport using computational fluid dynamics,” *J. Appl. Physiol.*, **98**, pp. 970–980.
- [14] Ma, B. and Lutchen, K. R., 2006, “An anatomically based hybrid computational model of the human lung and its application to low frequency oscillatory mechanics,” *Ann. Biomed. Eng.*, **34**, pp. 1691–1704.
- [15] Nazridoust, K. and Asgharian, B., 2008, “Unsteady-state airflow and particle deposition in a three-generation human lung geometry,” *Inhal. Toxicol.*, **20**, pp. 595–610.
- [16] Comerford, A., Förster, C., and Wall, W. A., 2010, “Structured tree impedance outflow boundary conditions for 3D lung simulations,” *J. Biomech. Eng.*, **132**, pp. 081002–1–10.
- [17] Yin, Y., Choi, J., Hoffman, E. A., Tawhai, M. H., and Lin, C.-L., 2010, “Simulation

- of pulmonary air flow with a subject-specific boundary condition,” *J. Biomech.*, **43**, pp. 2159–2163.
- [18] Walters, D. K. and Luke, W. H., 2011, “Computational fluid dynamics simulations of particle deposition in large-scale multigenerational lung models,” *J. Biomech. Eng.*, **133**, pp. 011003–1–8.
- [19] Saksono, P. H., Nithiarasu, P., and Sazonov, I., 2012, “Numerical prediction of heat transfer patterns in a subject-specific human upper airway,” *J. Heat Transfer*, **134**, pp. 031022–1–9.
- [20] Tsuda, A., Henry, F. S., and Butler, J. P., 1995, “Chaotic mixing of alveolated duct flow in rhythmically expanding pulmonary acinus,” *J. Appl. Physiol.*, **79**, pp. 1055–1063.
- [21] Darquenne, C. and Paiva, M., 1996, “Two- and three-dimensional simulations of aerosol transport and deposition in alveolar zone of human lung,” *J. Appl. Physiol.*, **80**, pp. 1401–1414.
- [22] Lee, D. Y. and Lee, J. W., 2003, “Characteristics of particle transport in an expanding or contracting alveolated tube,” *J. Aerosol Sci.*, **34**, pp. 1193–1215.
- [23] Karl, A., Henry, F. S., and Tsuda, A., 2004, “Low Reynolds number viscous flow in an alveolated duct,” *J. Biomech. Eng.*, **126**, pp. 420–429.
- [24] Sznitman, J., Heimsch, F., Heimsch, T., Rusch, D., and Rösgen, T., 2007, “Three-dimensional convective alveolar flow induced by rhythmic breathing motion of the pulmonary acinus,” *J. Biomech. Eng.*, **129**, pp. 658–665.
- [25] Tsuda, A., Henry, F. S., and Butler, J. P., 2008, “Gas and aerosol mixing in the acinus,” *Respir. Physiol. Neuro.*, **163**, pp. 139–149.

- [26] Sznitman, J., Heimsch, T., Wildhaber, J. H., Tsuda, A., and Rösgen, T., 2009, “Respiratory flow phenomena and gravitational deposition in a three-dimensional space-filling model of the pulmonary acinar tree,” *J. Biomech. Eng.*, **131**, pp. 031010–1–16.
- [27] Kumar, H., Tawhai, M. H., Hoffman, E. A., and Lin, C.-L., 2009, “The effects of geometry on airflow in the acinar region of the human lung,” *J. Biomech.*, **42**, pp. 1635–1642.
- [28] Harding, E. M. and Robinson, R. J., 2010, “Flow in a terminal alveolar sac model with expanding walls using computational fluid dynamics,” *Inhal. Toxicol.*, **22**, pp. 669–678.
- [29] Li, Z. and Kleinstreuer, C., 2011, “Airflow analysis in the alveolar region using the lattice-Boltzmann method,” *Med. Biol. Eng. Comput.*, **49**, pp. 441–451.
- [30] Ma, B. and Darquenne, C., 2011, “Aerosol deposition characteristics in distal acinar airways under cyclic breathing conditions,” *J. of Appl. Physiol.*, **110**, pp. 1271–1282.
- [31] Kumar, H., Tawhai, M. H., Hoffman, E. A., and Lin, C.-L., 2011, “Steady streaming: A key mixing mechanism in low-Reynolds-number acinar flows,” *Phys. Fluids*, **23**, pp. 041902–1–21.
- [32] Demirdžić, I. and Muzaferiya, S., 1995, “Numerical method for coupled fluid flow, heat transfer and stress analysis using unstructured moving meshes with cells of arbitrary topology,” *Comput. Methods Appl. Mech. Engrg.*, **125**, pp. 235–255.
- [33] Demirdžić, I. and Perić, M., 1990, “Finite volume method for prediction of fluid flow in arbitrarily shaped domains with moving boundaries,” *Int. J. Numer. Meth. Fl.*, **10**, pp. 771–790.
- [34] Gray, W. G., 1975, “A derivation of the equations for multi-phase transport,” *Chem. Eng. Sci.*, **30**, pp. 229–233.

- 
- [35] Whitaker, S., 1997, *Volume Averaging of Transport Equations*, chap. 1, Fluid Transport in Porous Media, Springer-Verlag, Southampton, UK, pp. 1–59.
- [36] Thomas, P. D. and Lombard, C. K., 1979, “Geometric conservation law and its application to flow computations on moving grids,” *AIAA J.*, **17**, pp. 1030–1037.
- [37] Demirdžić, I. and Perić, M., 1988, “Space conservation law in finite volume calculations of fluid flow,” *Int. J. Numer. Meth. Fl.*, **8**, pp. 1037–1050.
- [38] Venkatakrisnan, V. and Mavriplis, D. J., 1996, “Implicit method for computation of unsteady flows on unstructured grids,” *J. Comput. Phys.*, **127**, pp. 380–397.
- [39] Batina, J. T., 1990, “Unsteady Euler airfoil solutions using unstructured dynamics meshes,” *AIAA J.*, **28**, pp. 1381–1388.
- [40] Farhat, C., Degand, C., Koobus, B., and Lesoinne, M., 1998, “Torsional springs for two-dimensional dynamic unstructured fluid meshes,” *Comput. Methods Appl. Mech. Engrg.*, **163**, pp. 231–245.
- [41] Murayama, M., Nakahashi, K., and Matsushima, K., 2002, “Unstructured dynamic mesh for large movement and deformation,” *AIAA Paper*, **2002-0122**.
- [42] Yang, Z. and Mavriplis, D. J., 2007, “Mesh deformation strategy optimized by the adjoint method on unstructured meshes,” *AIAA J.*, **45**, pp. 2885–2896.
- [43] Truong, A. H., Oldfield, C. A., and Zingg, D. W., 2008, “Mesh movement for a discrete-adjoint Newton-Krylov algorithm for aerodynamic optimization,” *AIAA J.*, **46**, pp. 1695–1704.
- [44] Ž Tuković and Jasak, H., 2012, “A moving mesh finite volume interface tracking method for surface tension dominated interfacial fluid flow,” *Computers & Fluids*, **55**, pp. 70–84.

- 
- [45] Yushkevich, P. A., Piven, J., Hazlett, H. C., Smith, R. G., Ho, S., Gee, J. C., and Gerig, G., 2006, "User-guided 3D active contour segmentation of anatomical structures: significantly improved efficiency and reliability," *Neuroimage*, **31**, pp. 1116–1128.
- [46] Rosset, A., Spadola, L., and Ratib, O., 2004, "OsiriX: an open-source software for navigating in multidimensional DICOM images," *J. Digit. Imaging*, **17**, pp. 205–216.
- [47] West, J. B., 2008, *Respiratory Physiology: The Essentials*, Lippincott Williams & Wilkins, Baltimore.
- [48] Werner, R., Ehrhardt, J., Schmidt, R., and Handels, H., 2008, "Modeling respiratory lung motion - a biophysical approach using finite element methods," *Proc. SPIE*, **6916**, pp. 69160N–1–11.
- [49] Mathur, S. R. and Murthy, J. Y., 1997, "Pressure boundary conditions for incompressible flow using unstructured meshes." *Numer. Heat Tr. B-Fund.*, **32**, pp. 283–298.

## Summary

### 6.1 Summary of the Present Work

In this work, computational methods for analyzing fluid flow and heat transport in porous media and determining the relevant effective properties were developed. There were two major application areas selected in this work, metal foams and the human lung, to demonstrate the robustness and utility of the proposed models in complex porous domains and pore shapes. In addition to the development of the computational methods, useful data for closure parameters was generated and a novel modelling paradigm for simulating transport processes in the human lung was proposed.

In Chapter 2, a finite volume-based computational method was proposed for simulating fluid flow and heat transfer in conjugate fluid-porous domains. This work involved the development of novel fluid-porous interface conditions in order to ensure that the method was robust for all flow speeds and grid types. Special attention was given to the accurate estimation of diffusive and advective fluxes at interfaces, ensuring a balance of pressure forces and viscous stresses across the interface, as well as pressure-velocity coupling. The resulting model has been shown to be very robust and accurate for all test cases considered.

In Chapter 3, closure of the volume-averaged momentum and energy equations were studied using a unique constitutive equation-based approach for flow and heat transfer in

an idealized graphite foam pore geometry using extensive numerical simulations. While the main motivation of this work was to generate correlations that enable volume-averaged simulations to be conducted, several interesting aspects of the flow physics in such porous media were elucidated. First, the existence of a non-linear drag term, proportional to the cube of the volume-averaged velocity, for flows in the weak inertia regime was confirmed. Second, as a consequence of considering a more complicated pore geometry than much of the literature, it was found that the dispersion behaviour was much more complicated. While the dispersion conductivity is typically considered to be a function of the Péclet number (the product of the Reynolds and Prandtl numbers), it was found in this work that the Reynolds and Prandtl numbers must be considered as separate influences in order to obtain a good fit with the data. Finally, the importance of selecting a dispersion model specifically formulated for the porous medium of interest was demonstrated using volume-averaged calculations.

In Chapter 4, closure of the volume-averaged momentum equation was considered for flow in an alveolated duct within the human lung. Although this is an unsteady problem, it was shown using detailed scaling arguments based on physiologically reasonable orders of magnitude that the closure problem reduces to that of the steady case and that any changes in the permeability due to unsteadiness can be taken into account by the appropriate scaling of the permeability tensor. The assumptions underlying the theoretical model were tested using direct CFD calculations to confirm their validity. Finally, some selected one-dimensional results for flow in an alveolated duct were presented using the volume-averaged model developed.

In Chapter 5, a conjugate-fluid porous model for computing air flow in the human lung was proposed using the results obtained in Chapter 4 for the permeability of the lower airways and lung parenchyma. The geometry under consideration was based on publicly available CT image sets that were segmented to extract a truncated airway tree and the remainder of the lung volume. In order to allow the motion of the lung boundary to drive

the flow, the computational model developed in Chapter 2 was extended to an arbitrary Lagrangian-Eulerian framework for moving meshes. The resulting model was tested with the physiologically-realistic lung model to demonstrate the ability of the computational method to solve such a complex flow configuration. Further, this work sets up a new modelling paradigm for simulating transport in the human lung which is believed to be of significant value with the appropriate validation and calibration, which is suggested as future work.

To conclude, this work has led to the development of a useful numerical tool for solving fluid flow and heat transfer in complex geometries using general moving unstructured grids. It has also extended the state of the art when it comes to closure of volume-averaged equations and has produced new insights in this area. Finally, a novel coupled fluid-porous methodology for modelling flow has been proposed which has great potential as a tool for modelling transport in the lung with further development.

## 6.2 Summary of Contributions

**1. Development of a numerical method for computing fluid flow and heat transfer in conjugate fluid-porous domains using general moving unstructured grids.** In Chapter 2, the development of a finite volume-based numerical method was described that enables the solution of fluid flow and heat transfer problems in the presence of fluid-porous interfaces on unstructured grids. Prior to the development of this method, there were no computational methods capable of accurately solving such problems when employing unstructured grids. In the present work, novel interface conditions were proposed to ensure accurate estimates of diffusive and advective fluxes as well as pressure forces at fluid-porous interfaces. Additionally, the coupling of the pressure and velocity fields was considered to ensure that no decoupling occurred at interfaces. The resulting model has been shown to be robust for all flow speeds considered and is successful in maintaining accu-

racy on all grid types. This is a very important development as many practical situations involve coupled fluid-porous domains with geometric complexities that necessitate the use of unstructured grids. This numerical method was further extended in Chapter 5 in order to handle moving grids using an arbitrary Lagrangian-Eulerian approach, such that moving boundary problems may also be solved. This is an important development, particularly for biomedical applications where domain motion is common.

**2. Characterization of the effective flow and thermal properties of graphite foams.** In Chapter 3, results were obtained for all of the relevant effective flow and thermal properties of a high-conductivity graphite foam material such that volume-averaged calculations may be conducted for devices incorporating this material. In addition to establishing these useful correlations for use in volume-averaged calculations, this study was the first to consider closure of volume-averaged equations using a constitutive equation-based approach in a three-dimensional geometry for non-creeping flows. Thus, it has been shown that this approach is appropriate for such geometries and flow configurations, indicating that similar characterizations are possible for other high-conductivity porous materials.

**3. Elucidation of flow and thermal physics for flow through a complex pore shape.** In Chapter 3, in addition to the development of correlations for effective properties, several interesting phenomena were uncovered. First, the existence of non-linear pressure drop behaviour in the weak inertia flow regime was confirmed for this particular geometry. Additionally, it was observed that while the literature typically considers the thermal dispersion conductivity to be a function of the Péclet number, substantially better fits to the data were obtained by considering the Reynolds and Prandtl numbers as separate influences. Finally, it was found that the spherical void phase material considered in this work exhibits substantially different dispersion behaviour as compared to reticulated metal foams and that this difference has a meaningful impact on the volume-averaged results. Taken together, these conclusions are very important to those conducting volume-average simulations involving graphite foams, or more generally, any high-conductivity porous material.

**4. A novel application of porous media theory and closure methods to flow in an alveolated duct.** In Chapter 4, flow in an alveolated duct was considered using a porous media approach and closure of the resulting volume-averaged momentum equation was considered. Typical closure methods are not compatible with moving domains or varying porosities, however, in this work the transport equations governing the pore-level velocity and pressure spatial deviations were carefully simplified using physiologically-based scaling arguments. This led to the conclusion that at the closure level one may neglect transient effects and the effects of porosity gradients. The assumptions underlying the theoretical part of this work were then tested using direct simulations, which were in good agreement with the given results. Thus, this work serves to show the important fact that a steady closure model may be used for alveolar flows and proposes that properly scaling the permeability tensor allows transient effects to be included in volume-averaged simulations. Additionally, it provides a value for the permeability of an alveolated duct that can be used to conduct volume-averaged simulations of flow in the lung.

**5. Proposal of a new conjugate fluid-porous approach for modelling transport in the human lung.** In Chapter 5, a new modelling paradigm for simulating flows in the human lung was proposed, wherein the upper airway tree is considered directly as a fluid region and the remainder of the lung is considered as a coupled porous region. Test cases were shown to demonstrate that the proposed numerical method could indeed solve this complicated flow problem for a physiologically realistic lung model based on segmented CT images. Although full validation of this model is beyond the scope of this work, it is believed that the proposed approach will be useful for computing transport in the whole lung upon experimental validation and calibration.

### 6.3 Suggestions for Future Work

**1. Investigation of effective properties in other porous materials.** In this work, all of the effective flow and thermal properties of graphite foam were obtained and the permeability of an alveolated duct was determined. Clearly, this is only a small subset of all of the porous materials in existence. Thus, a practical suggestion for future work is to use the closure methods described in this work to investigate the effective properties of other porous materials such as aluminum or copper metal foams and biological tissues including bone, muscle, solid tumours, etc. Such work would have an immediate impact on the quality of volume-averaged simulations that may be conducted, which could have a significant impact on the design of porous devices or the study of medically-relevant processes.

**2. Investigation of effective properties at interface regions.** In this work, a comprehensive investigation of the effective flow and thermal properties of graphite foam was conducted for transport processes in regions of the porous medium where the macroscopic properties, such as porosity, are uniform and interface effects are negligible. Thus, it would be an interesting topic for future research to investigate the impact of porous-fluid and porous-solid interfaces on the results for the effective properties of porous materials using the closure models discussed in this work. At porous-fluid interfaces phenomena such as stress-jump [1, 2] could be investigated and more insight into the heat convection and conduction processes at the interface could be obtained. At porous-solid interfaces, further insight into the conduction and thermal dispersion processes could be gained [3]. Such advancements in the mathematical treatment of interfaces will undoubtedly serve to improve the accuracy of the volume-averaged description of transport in porous media and may readily be incorporated into existing numerical methods for porous media flows, such as the one proposed in this work.

**3. Incremental improvement of the porous media model of the human lung.** While significant progress was made towards a porous media description of transport in the human lung, this modelling philosophy is still in its early stages. As a result, there are several

improvements that can be made to the model in an incremental fashion in order to gradually increase the extent to which it replicates a real human lung. One such improvement is to segment more generations of the airway tree to determine at which point the benefits of computing the flow directly are sufficiently small that a transition to a porous media model is appropriate. Additionally, improvements could be made to the specification of the lung motion using either calculations of the tissue motion with given material properties and applied loads, using medical imaging to determine the motion of the lung as a function of time, or a combination of both approaches [4, 5].

**4. Experimental validation and calibration of the porous media lung model.** Since full experimental validation and calibration of the porous media model of the human lung was beyond the scope of the present work, it is recommended that future work is directed at collaborating with medical imaging experts in order to perform as much validation and subsequent model calibration as possible with current techniques.

**5. Study of other transport processes in the lung using volume-averaged simulations.** The volume-averaged simulations presented in this work were focused on the air flow process within the human lung. With this model in place, it becomes relatively straightforward to study other relevant transport processes, such as gas exchange, heat transfer, and particle transport in a similar, volume-averaged framework with relatively minor additions to the model proposed in this work.

**6. Medical applications of volume-averaged simulations of transport in the human lung.** This work presented a volume-averaged method for analyzing air flow in the human lung. As discussed above, it is relatively straightforward to extend this model to include other relevant transport processes. A fairly long-range goal for the extension of this work, which will require substantial research effort, is to find applications of such methods in the medical field. While the proposed model certainly facilitates the study of transport processes and may lead to new knowledge, it would be very interesting to work towards such models playing an active role in the medical field. Some possible applications include

optimizing drug delivery, surgical planning, and diagnostics.

**7. New applications of porous media theory in the biomedical field.** While this work focused primarily on the lung as a porous biological tissue, there are certainly many other biological systems of interest that can be modelled as porous domains. For example, thermal ablation is a process by which cancerous tissue is destroyed using thermal energy [6–8]. Such a process is ideally suited to being considered as a porous system. If this process can be accurately modelled using porous media theory, there are immediate applications in planning and optimizing the ablation procedure to minimize extraneous cell death around the cancerous region. Another interesting biomedical application of porous media is macromolecule transport through arterial walls [9, 10]. Since this work introduced a new method for simulating conjugate fluid-porous systems using unstructured grids, many problems that were previously too geometrically complex can now be solved, and represent an interesting possibility for future work.

## References

- [1] Ochoa-Tapia, J. A. and Whitaker, S., 1995, “Momentum transfer at the boundary between a porous medium and a homogeneous fluid – I. Theoretical development,” *Int. J. Heat Mass Transfer*, **38**, pp. 2635–2646.
- [2] Costa, V. A. F., Oliveira, L. A., and Baliga, B. R., 2008, “Implementation of the stress jump condition in a control-volume finite-element method for the simulation of laminar coupled flows in adjacent open and porous domains,” *Numer. Heat Tr. B-Fund.*, **53**, pp. 383–411.
- [3] Sahraoui, M. and Kaviany, M., 1994, “Slip and no-slip temperature boundary conditions at the interface of porous, plain media: Convection,” *Int. J. Heat Mass Transfer*, **37**, pp. 1029–1044.
- [4] Eom, J., Xu, X. G., De, S., and Shi, C., 2010, “Predictive modelling of lung motion over the entire respiratory cycle using measured pressure-volume data 4DCT images, and finite-element analysis,” *Med. Phys.*, **37**, pp. 4389–4400.
- [5] Werner, R., Ehrhardt, J., Schmidt, R., and Handels, H., 2008, “Modeling respiratory lung motion - a biophysical approach using finite element methods,” *Proc. SPIE*, **6916**, pp. 69160N–1–11.
- [6] Mahjoob, S. and Vafai, K., 2009, “Analytical characterization of heat transport through biological media incorporating hyperthermia treatment,” *Int. J. Heat Mass Transfer*, **52**, pp. 1608–1618.

- 
- [7] Gupta, P. K., Singh, J., and Rai, K., 2010, “Numerical simulation for heat transfer in tissues during thermal therapy,” *J. Therm. Biol.*, **35**, pp. 295–301.
- [8] Peng, T., O’Neill, D. P., and Payne, S. J., 2011, “A two-equation coupled system for determination of liver tissue temperature during thermal ablation,” *Int. J. Heat Mass Transfer*, **54**, pp. 2100–2109.
- [9] Yang, N. and Vafai, K., 2006, “Modeling of low-density lipoprotein (LDL) transport in the artery—effects of hypertension,” *Int. J. Heat Mass Transfer*, **49**, pp. 850–867.
- [10] Khakpour, M. and Vafai, K., 2008, “Critical assessment of arterial transport models,” *Int. J. Heat Mass Transfer*, **51**, pp. 807–822.

# Additional Code Validation and Test Problems

## A.1 One-dimensional porous plug flow

In this validation problem, a one-dimensional version of the porous plug problem presented in Chapter 2 and shown in Fig. 2.4, is solved. In this case the computational domain is  $x \in [0, 3]$  with a porous region  $x \in [2, 3]$  and fluid regions  $x \in [0, 1)$  and  $x \in (2, 3]$ . The domain is meshed using three-dimensional hexahedral control volumes, however, there is only one volume in each of the  $y$ - and  $z$ -directions with symmetry conditions on  $y$ - and  $z$ -planes such that the problem reduces to being one-dimensional. In the  $x$ -direction, six control volumes are used; two in each fluid region and two in the porous region. Since this is a one-dimensional flow, the continuity equations in the fluid and porous regions imply  $u = \langle u \rangle = U$ , where  $U$  is a constant. Here we take  $U = 1$ . In the fluid region, this implies pressure is constant in both the upstream and downstream regions. In the porous region, we assume  $c_f = 0$  such that Darcy's law is valid, which implies a linear pressure profile with respect to  $x$ . Specifying the outlet pressure to be  $p = 0$  and assuming a continuous pressure

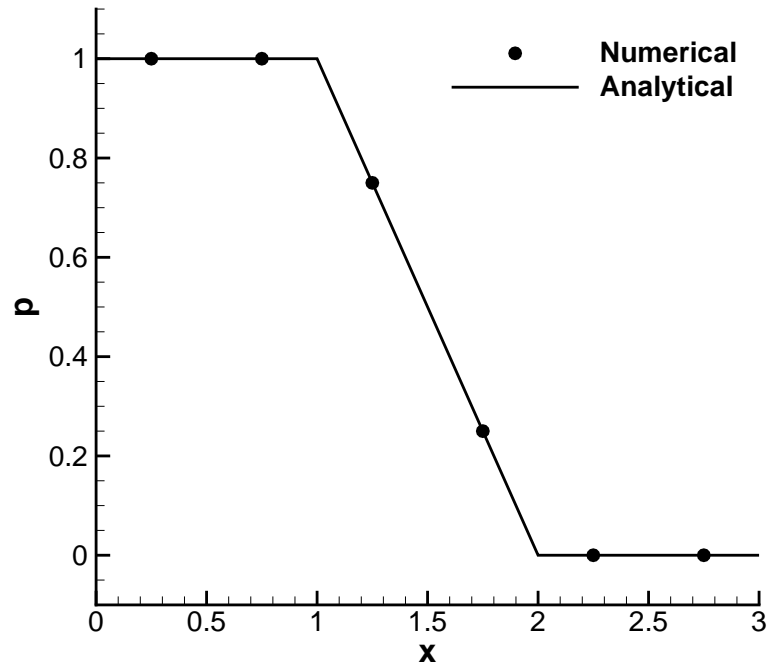


**Figure A.1:** A plots of the results for the one-dimensional porous plug case obtained using six control volumes in comparison to the analytical solution.

at interfaces gives the following analytical solution for pressure:

$$p(x) = \begin{cases} \frac{\mu_f U}{K}, & x \in [0, 1) \\ -\frac{\mu_f U}{K}(x-2), & x \in [1, 2) \\ 0, & x \in [2, 3] \end{cases} . \quad (\text{A.1})$$

Numerical results are obtained with the proposed numerical method using a Dirichlet condition on velocity at the inlet ( $u = U$ ) and a Neumann condition at the outlet ( $\partial u / \partial x = 0$ ). On pressure, a Neumann condition was specified at the inlet (inlet pressure extrapolated from interior) and a Dirichlet condition was imposed at the outlet ( $p = 0$ ). The numerical results are plotted in Fig. A.1 for  $K = \mu_f = U = 1$  in comparison to the analytical solution given in Eq. A.1. Results show excellent agreement with the analytical solution and have a maximum relative error of  $4.0 \times 10^{-6}$ , which indicates that the algorithm and interface conditions are working properly.

## A.2 One-dimensional non-equilibrium heat transfer<sup>†</sup>

In this validation problem, we solve the non-equilibrium energy equations for a special one-dimensional case with no flow component to ensure that the energy equations are solved properly. Note that we make no claim that this is a physically relevant problem; it is simply designed to test the code. In this problem, we consider steady one-dimensional heat transfer between the fluid and solid components of a porous medium. At the origin, the body is insulated. At the other end of the domain,  $x = L$ , there is a finite temperature difference between the fluid and solid constituents. For simplicity, and to enable an analytical solution, constant properties are assumed. Since advection is neglected, this problem serves to verify the diffusion and exchange components of the code.

The two governing energy equations are given as

$$k_{fe} \frac{d^2 \langle T_f \rangle^f}{dx^2} + h_{fs} a_{fs} (\langle T_s \rangle^s - \langle T_f \rangle^f) = 0 \quad (\text{A.2})$$

and

$$k_{se} \frac{d^2 \langle T_s \rangle^s}{dx^2} - h_{fs} a_{fs} (\langle T_s \rangle^s - \langle T_f \rangle^f) = 0. \quad (\text{A.3})$$

Boundary conditions are given as

$$\left. \frac{d \langle T_f \rangle^f}{dx} \right|_{x=0} = 0, \quad (\text{A.4})$$

$$\left. \frac{d \langle T_s \rangle^s}{dx} \right|_{x=0} = 0, \quad (\text{A.5})$$

$$\langle T_f \rangle^f \Big|_{x=L} = T_{f,L}, \quad (\text{A.6})$$

and

$$\langle T_s \rangle^s \Big|_{x=L} = T_{s,L}. \quad (\text{A.7})$$

---

<sup>†</sup>Thanks to Juan Carlos Morales of ANSYS Canada Ltd. for suggesting this test problem.

Rearranging and combining Eqs. A.2 and A.3 results in

$$\frac{d^2 \langle T_f \rangle^f}{dx^2} - \frac{d^2 \langle T_s \rangle^s}{dx^2} - \frac{h_{fs} a_{fs} (k_{fe} + k_{se})}{k_{fe} k_{se}} (\langle T_f \rangle^f - \langle T_s \rangle^s) = 0. \quad (\text{A.8})$$

For convenience, we let  $\phi = \langle T_f \rangle^f - \langle T_s \rangle^s$  such that the governing differential equation becomes

$$\frac{d^2 \phi}{dx^2} - A^2 \phi = 0, \quad (\text{A.9})$$

where  $A^2 = [h_{fs} a_{fs} (k_{fe} + k_{se})] / [k_{fe} k_{se}]$ . The boundary conditions then become

$$\left. \frac{d\phi}{dx} \right|_{x=0} = 0 \quad (\text{A.10})$$

and

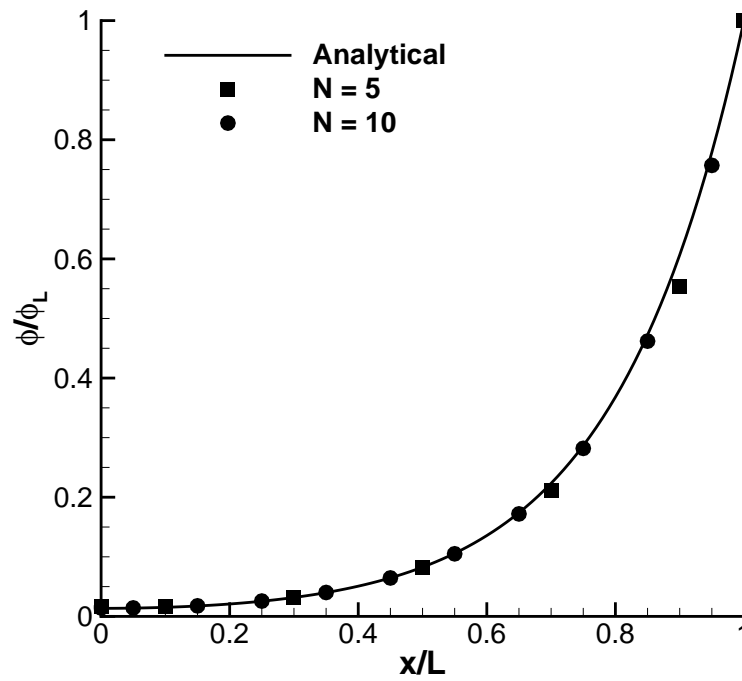
$$\phi|_{x=L} = \phi_L = T_{f,L} - T_{s,L}. \quad (\text{A.11})$$

The differential equation given by Eq. A.8 with boundary conditions given by Eqs. A.10 and A.11 has a simple analytical solution given by

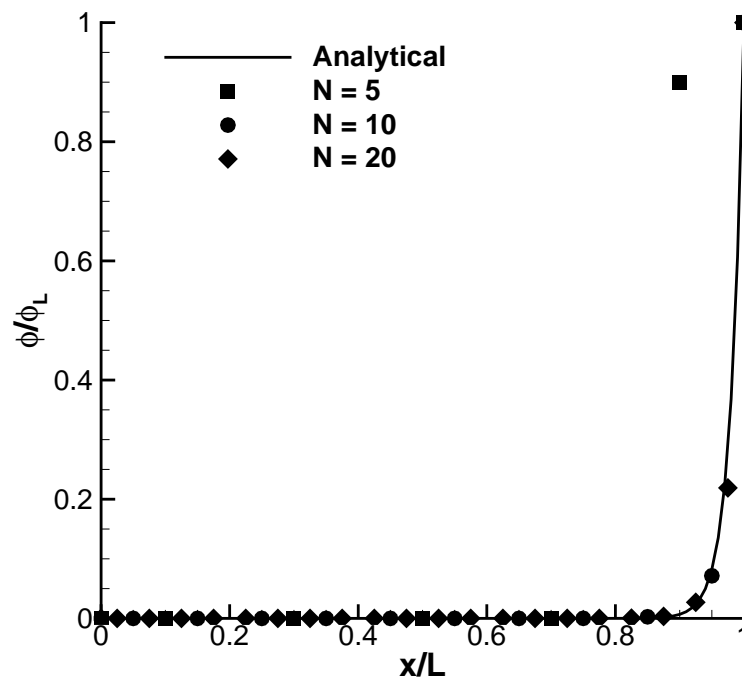
$$\phi(x) = \phi_L \frac{\cosh(Ax)}{\cosh(AL)}. \quad (\text{A.12})$$

To test the code using this problem, we choose a unit length domain ( $L = 1$ ) with a unit temperature difference at  $x = L$  ( $\phi_L = 1$ ) for convenience. Two values of  $A$  are selected such that  $A \in \{5, 50\}$ . Three different grid resolutions are selected with 5, 10, and 20 control volumes in the  $x$ -direction to examine the effects of the grid density. Since the code is three dimensional, the control volumes are hexahedra, however, since there is only one volume in the  $y$ - and  $z$ -directions with symmetry conditions on the  $xy$ - and  $xz$ -planes the problem is reduced to a single dimension.

In Fig. A.2(a), results obtained from the code are compared to the analytical solution for  $A = 5$ . This figure indicates that reasonable results are obtained using only five con-



(a)



(b)

**Figure A.2:** Plots of the dimensionless temperature difference  $\phi/\phi_L$  as a function of the dimensionless position  $x/L$  for two values of the parameter  $A$ , namely, (a)  $A = 5$  and (b)  $A = 50$  for different grid densities.

control volumes (maximum percentage error: 8.9%) and that very good results are obtained with ten control volumes (maximum percentage error: 2.7%). Although not shown in Fig. A.2(a), results were also obtained using 20 control volumes which showed the error was further reduced (maximum percentage error: 0.7%). In the case where  $A = 5$ , it is clear that neither the diffusion or interstitial exchange mechanisms are strongly dominant. The temperature difference imposed at  $x = L$  is diffused through the domain and is reduced towards  $x = 0$  due to the interstitial exchange mechanism. For  $A = 5$  the fluid and solid do not come to thermal equilibrium at any point within the domain. For larger values of  $A$ , the interstitial exchange mechanism is more dominant and thermal equilibrium may be achieved.

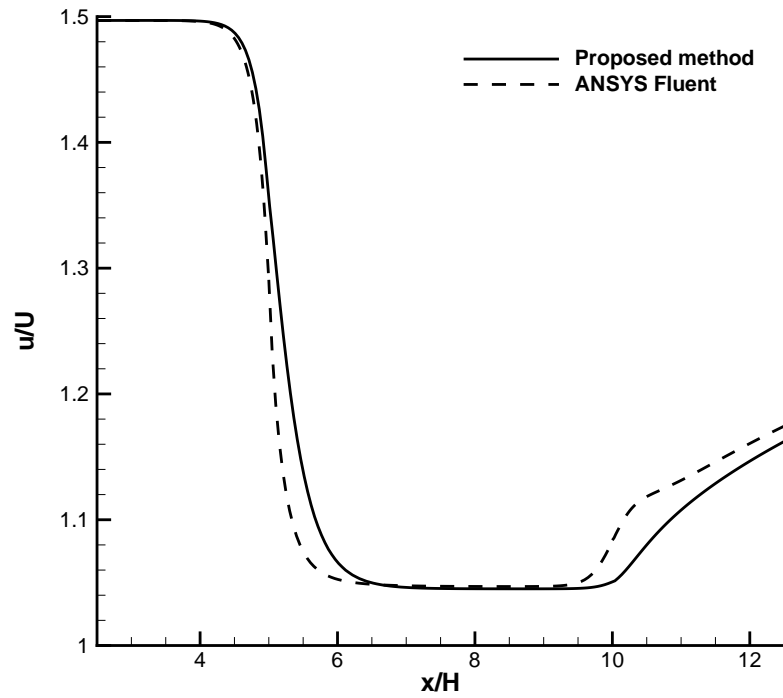
Next we consider results for  $A = 50$ , which are shown in Fig. A.2(b). In this case, thermal equilibrium conditions are attained a short distance from  $x = L$  as the interstitial exchange mechanism is strongly dominant over diffusion. In this case, the profile of the temperature difference is very steep near  $x = L$  which is clearly not captured using only five control volumes. Using 10 or 20 control volumes, it appears that the analytical solution is accurately matched. In this case, using a percentage difference is misleading since many of the values are very close to zero, so instead the absolute difference is discussed. For the cases using 10 and 20 control volumes, the maximum absolute error is below 0.07, however it is clear that the shape of the analytical solution cannot be reconstructed in either case due to insufficient data points where the value of  $\phi/\phi_L$  is changing rapidly. In this case, it would be prudent to refine the grid towards this end of the domain since the temperature gradients are so high.

### A.3 Comparison of porous plug results with those from ANSYS Fluent

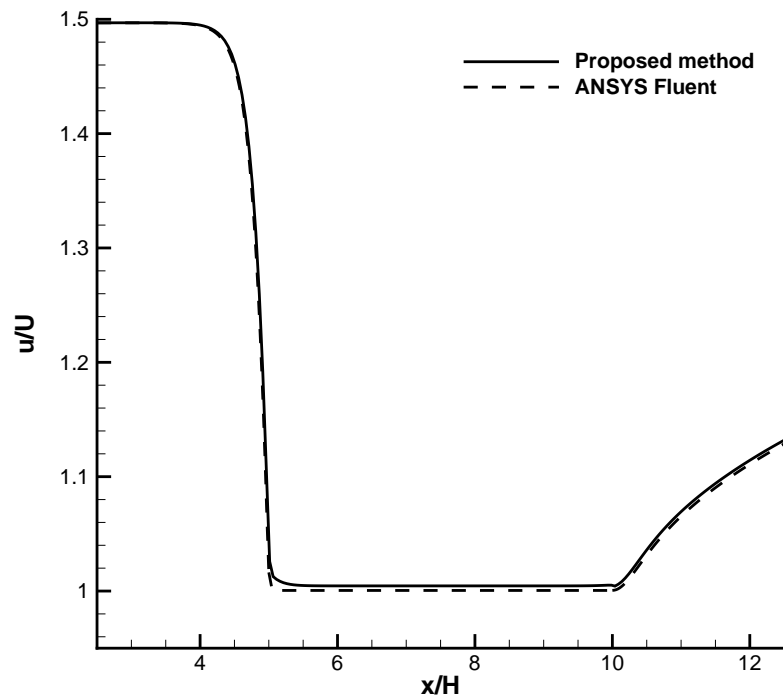
In order to demonstrate the usefulness of the proposed method of considering flow in conjugate fluid-porous domains, the porous plug case considered in Chapter 2 is also solved using ANSYS<sup>®</sup> Fluent, Release 13.0, a popular commercial software package for performing computational fluid dynamics simulations, and the results are compared with those from the proposed model. The grids used for the Fluent simulations are identical to those used for the simulations conducted using the proposed model. All solver parameters in Fluent were selected to be as similar as possible to those specified in the proposed code. Results for two Darcy numbers,  $Da \in \{10^{-2}, 10^{-5}\}$ , which represent the two extremes considered in Chapter 2 are plotted in Fig. A.3.

For the higher Darcy number,  $Da = 10^{-2}$ , there are significant differences between the present results and the results from Fluent, particularly in the vicinity of the fluid-porous interface. Since the Fluent solution does not exhibit any spurious oscillations near the interface, it is clear that some sort of special condition has been applied to assist in maintaining coupling at the interface, however the Fluent documentation does not specify what sort of condition may be applied. At the outlet, the Fluent solution exhibits unusual behaviour as fluid accelerates out of the porous plug. It appears that the rate of acceleration is increasing, which does not make physical sense since this increase in velocity along the centreline is due to momentum diffusion away from the walls as the flow redevelops from essentially a plug flow at the exit of the porous block. At the lower Darcy number,  $Da = 10^{-5}$ , good agreement between the present results and the results from Fluent is obtained.

Thus, it appears that the interface conditions imposed in Fluent are able to produce a good solution at low Darcy numbers where the velocity profile changes sharply at the interface. In cases where the Darcy number is higher and the velocity changes more gradually



(a)



(b)

**Figure A.3:** Plots of the streamwise velocity component for the porous plug problem at  $Re_H = 1000$  and (a)  $Da = 10^{-2}$  and (b)  $Da = 10^{-5}$  computed using the proposed method and ANSYS Fluent. Note that these cases were run using the same hexahedral grids used for the cases presented in Chapter 2.

as it enters and exits the porous plug, it does not appear that the results obtained using Fluent are particularly accurate near interfaces. In such cases, it appears beneficial to consider a more rigorous approach to treating fluid-porous interfaces, such as the method proposed in this work.

## VITA

**Name:** Christopher T. DeGroot

**Post-secondary Education and Degrees:** The University of Western Ontario  
London, Ontario, Canada  
2009–2012 Ph.D.

The University of Western Ontario  
London, Ontario, Canada  
2008–2009 M.E.Sc.

The University of Western Ontario  
London, Ontario, Canada  
2004–2008 B.E.Sc.

**Honours and Awards:** Mitacs  
Elevate Postdoctoral Fellowship  
September 2012–August 2014

Natural Sciences and Engineering Research Council (NSERC)  
Alexander Graham Bell Canada Graduate Scholarship (Doctoral)  
May 2009–April 2012

Natural Sciences and Engineering Research Council (NSERC)  
Postgraduate Scholarship (Master's)  
May 2008–April 2009

**Related Work Experience:** Teaching Assistant  
Department of Mechanical and Materials Engineering  
The University of Western Ontario  
2008–2012

Lecturer  
Department of Applied Mathematics  
The University of Western Ontario  
Fall 2011

Research Assistant  
Department of Mechanical and Materials Engineering  
The University of Western Ontario  
2006–2012

**Journal Publications:**

DeGroot, C. T., Straatman, A. G. (2012). Numerical results for the effective flow and thermal properties of idealized graphite foam. *J. Heat Transfer*. **134**, 042603.

DeGroot, C. T., Straatman, A. G. (2011). A finite-volume model for fluid flow and nonequilibrium heat transfer in conjugate fluid-porous domains using general unstructured grids. *Numer. Heat Transfer B-Fund.* **60**, 252–277.

DeGroot, C. T., Straatman, A. G. (2011). Closure of non-equilibrium volume-averaged energy equations in high-conductivity porous media. *Int. J. Heat Mass Transfer* **54**, 5039–5048.

DeGroot, C. T., Gateman, D., Straatman, A. G. (2010). The effect of thermal contact resistance at porous-solid interfaces in finned metal foam heat sinks. *J. Electron. Packag.* **132**, 041007.

Sultan, K., DeGroot, C. T., Straatman, A. G., Gallego, N. C., Hangan, H. (2009). Thermal characterization of porous graphitic foam – Convection in impinging flow. *Int. J. Heat Mass Transfer* **52**, 4296–4301.

DeGroot, C. T., Straatman, A. G., Betchen, L. J. (2009). Modeling forced convection in finned metal foam heat sinks. *J. Electron. Packag.* **131**, 021001.

**Book Chapters:**

DeGroot, C. T., Straatman, A. G. (2012). Thermal dispersion in high-conductivity porous media in *Numerical Analysis of Heat and Mass Transfer in Porous Media*, Springer-Verlag, Berlin.

**Conference Proceedings:**

DeGroot, C. T., Straatman, A. G. (2012). Towards a porous media model of the human lung. Proceedings of the 4th International Conference on Porous Media and its Applications in Science, Engineering and Industry, Potsdam, Germany, June 17–22. Published in *AIP Conference Proceedings* 1453, 69–74, 2012.

DeGroot, C. T., Straatman, A. G. (2012). Simulation of flow in an alveolated duct within the human lung with application to porous media. Proceedings of the 20th Annual Conference of the CFD Society of Canada, Canmore, Canada, May 9–11.

DeGroot, C. T., Straatman, A. G. (2011). A comparison of thermal dispersion behaviour in high-conductivity porous media of various pore geometries, Proceedings of the 7th International Conference on Diffusion in Solids and Liquids, Algarve, Portugal, June 27–29. Published in *Defect and Diffusion Forum* **326-328**, 308–312, 2012.

---

DeGroot, C. T., Straatman, A. G. (2011). Interface conditions for finite-volume-based models of flow in conjugate fluid-porous domains. Proceedings of the 19th Annual Conference of the CFD Society of Canada, Montreal, Canada, April 27–29.

DeGroot, C. T., Straatman, A. G. (2010). A finite-volume model for flow in conjugate fluid-porous domains with moving grids. Proceedings of the 18th Annual Conference of the CFD Society of Canada, London, Canada, May 17–19.

DeGroot, C. T., Straatman, A. G. (2009). Closure of the volume-averaged transport equations for flow through high-conductivity porous materials. Proceedings of the 17th Annual Conference of the CFD Society of Canada, Ottawa, Canada, May 3–5.

DeGroot, C. T., Straatman, A. G. (2008). Modeling thermal dispersion in 2D cylinder arrays. Proceedings of the 16th Annual Conference of the CFD Society of Canada, Saskatoon, Canada, June 9–11.

DeGroot, C. T., Betchen, L. J., Straatman, A. G. (2007). Forced convection in aluminum foam finned heat sinks. Proceedings of the 15th Annual Conference of the CFD Society of Canada, Toronto, Canada, May 27–31.